Universidad de Concepción
Facultad de Ingeniería
Departamento de Ingeniería Química

The role of doping in tannin-derived carbon materials for electrochemical applications

Tesis presentada al Departamento de Ingeniería Química de la Facultad de Ingeniería de la Universidad de Concepción para optar al grado de Doctor en Ciencias de la Ingeniería con mención en Ingeniería Química.

By : Oscar Pinto Burgos

Supervised by : Dr. Juan Matos Lale

Dr. Romel Mario Jiménez

Concepción, Chile, 2024

To know is to understand

how the smallest thing is linked to the whole,

how no one thing

can be understood without the context of the whole.

Alan Sokal

ACKNOWLEDGMENTS

I would like to express my sincere gratitude to Dr. Juan Matos and Dra. Po Shan Poon for their valuable feedback, support and encourage along this doctoral journey. To Dr. Romina Romero, who introduced me to the fascinating and challenging world of scientific research, I will always remember her telling me what a pleasure it would be to meet at a congress when we were old, back when I decided to pursue the doctoral path. Thank to her passion for science and encouragement to pursue this path, I am where I am today. To all the people at *Institut Jean Lamour*, I want to express my heartfelt gratitude for your advice and assistance in navigating the challenges of immigrating to France without speaking French at all. I have fond memories of the vacations, parties, raclette gatherings, outings, and numerous activities we enjoyed together, which made living abroad a truly enjoyable experience. Knowing that I had a place to call home in a small town in the heart of the French forest it is truly comforting. Special mention must be made to Dr. Jimena Castro-Gutierrez, whose patience and availability in teaching me the fundaments and technical knowledge of electrochemical capacitors characterization were essentials in obtaining the main results of this doctoral research. I am deeply grateful for her support, not only in scientific matters but also in personal challenges during my time abroad. Her friendship is invaluable, and I hope it will endure despite the temporal and spatial distance between us. I also want to express my gratitude to Dr. Romel Jimenez, who reached out to me and agreed to participate in this research when it was already well advanced. Without this noble act, I would not have been able to complete this doctoral thesis. To my friends and housemates from the Lientur's, who supported and tolerated me during the toughest times of my doctoral journey, thank you for your unwavering friendship. I will always cherish the memories of our evenings filled with meaningful conversations or gibberish talks over beverages. It is good to know that I have friends who will answer the call when the beacons are lit and Gondor calls for aid.

To my family, especially my mother and niece, I want to express my deepest gratitude for the unconditional love you have shown me. Your presence in my life is a source of immense comfort and strength, I cherish you both more than words can say, and I truly do not know where I would be without one of you two.

This doctoral journey would not have been possible without the support and contributions of these people, and for that, I will be eternally and truly grateful.

This research was financial support by ANID - Subdirección de Capital Humano/Doctorado, # 2019/21190633, ANID-ANILLO project ATE220014, ANID-FONDEF project 19I10003, and ANID-FONDECYT project 1220228.

ABSTRACT

There is a growing and urgent demand for eco-friendly, high-power devices, especially in portable applications like portable electronics or hybrid-electric/electric vehicles (H/EVs). Electrochemical energy storage systems are highly sought after in this regard. The main technologies currently available are Li-ion batteries and electrochemical capacitors (ECs), each offering distinct yet often complementary performance characteristics. Meanwhile, the former stores the energy mainly through chemical pathways, the latter stores the charge via physical process where the electric double layer is a key parameter. The ECs' storage process is rapid, highly reversible, and exhibits minimal effects on device performance over numerous charge/discharge cycles, making them advantageous in the long term. However, ECs face the drawback of low specific energy, prompting scientific efforts to enhance this value without compromising power.

One promising approach to achieve this enhancement is through heteroatom doping of carbon materials. In this context, tannins, a polyphenolic compound frequently derived from tree bark, serve as a suitable precursor due to their auto-condensation reactions, leading to a well-connected porosity network and high reactivity, enabling the incorporation of functionalities.

In this context, this doctoral research focuses on the study of the relationship between pore size distribution, surface chemistry, and electrochemical performance of tannins-derived carbon materials as electrodes in electrochemical capacitors, with an emphasis on surface modification with oxygen, nitrogen and/or boron. Advanced characterization techniques such as adsorption-desorption isotherms, and X-ray photoelectron spectroscopy (XPS) were employed to analyze the structure and chemistry of the carbon materials. Additionally, electrochemical tests were conducted to evaluate their energy storage capacity, power density and overall electrochemical performance.

The research establishes tannins-derived carbon materials as effective electrodes for electrochemical capacitors. Chemically activated tannins-derived carbon materials exhibit a linear correlation between capacitance and specific surface area, optimizing electrochemical performance with energy densities reaching 4.4 $W \cdot h \cdot kg^{-1}$ at 1.1 $kW \cdot kg^{-1}$.

The hydrothermal carbonization doping method successfully incorporates nitrogen or boron into tannins-derived carbon materials, introducing significant alterations to tailored chemical and morphological modifications. Without doping agents, hydrothermal carbonization leads to carboxylic acid-dominated surface chemistry, limiting electric double layer formation. Boron incorporation moderately enhances electrochemical performance. Meanwhile, nitrogen doping significantly improves surface chemistry and textural properties after CO_2 activation, enhancing electrochemical performance. The top-performing material achieves remarkable energy density of 6.0 $W \cdot h \cdot kg^{-1}$ at 1.3 $kW \cdot kg^{-1}$, retaining nearly 96% of initial energy storage after 30,000 cycles.

TABLE OF CONTENTS

LIST OF FIGURES

LIST OF TABLES

NOMENCLATURE

A_{BET}	BET Surface area
a_0	Ion effective size
BO	Burn-off
b	Pore radius
C	Capacitance
C_H	Helmholtz layer capacitance
C_{Dif}	Diffusive layer capacitance
C_{EDL}	Electric double layer capacitance
C_{PsC}	Pseudocapacitance
C_T	Total capacitance
DFT	Density functional theory
DMS	Disordered mesoporous carbon
d	Double layer thickness
e	Electric charge of one electron
EC_s	Electrochemical capacitors
EDL	Electric double layer
ESR	Equivalent series resistance
E	Applied voltage
f	Frequency
F	Faraday constant
HTC	Hydrothermal carbonization
IHP	Inner Helmholtz plane
I	Current flow
I_0	Applied current
k_B	Boltzmann constant
L_0	Average pore size
n_i	ions per unit of volume
NLDFT	Non-linear density functional theory
OHP	Outer Helmholtz plane
OMC	Ordered mesoporous carbon
P	Power density
P	Pressure
P^0	Vapor pressure
PZC	Point of zero charge
R	Gas constant
q	Electric charge
q_∞	Non-limited ion diffusion charge
q_T	Total charge
R_S	Electrolyte resistance
R_{CT}	Charge-transfer resistance
SSA	Specific surface area
T	Temperature
t	Time
t_D	Discharge time
V	Applied voltage
V_T	Total volume
$V_{u\mu}$	Ultramicropore volume
$V_{s\mu}$	Supermicropore volume
V_{meso}	Mesopore volume
w	Pore width
$w_{u\mu}$	Ultramicropores
$w_{s\mu}$	Supermicropore
w_{meso}	Mesopore
XPS	X-ray photoelectron spectroscopy
Z	Impedance
Z_R	Real part of the impedance
Z_i	Imaginary part of the impedance
z_i	Formal charge of the ion

Greek letters

α	Transfer coefficient for electron exchange	ρ_e	Local electric charge density
ϵ_0	Vacuum permittivity	υ	Scan rate for cyclic voltammetry
ϵ_r	Dielectric constant of the solvent	ϕ	Phase angle
η	Overpotential from the equilibrium	ψ	Electric potential
λ	Adjustable parameter for NLDFT model	ω	Angular frequency

1 INTRODUCTION

The over raising CO_2 emissions, global warming, and the development of new technologies have generated a fast-growing market of portable electronic devices and hybrid electric vehicles. Additionally, there is an increasing and urgent demand for environmentally friendly and high-power devices, and as the industrial, and the scientific community have been explored the existing and variety of emerging options for clean and safe energy sources, the energy storage systems have become a key concept to improve in order to meet these new challenges on energy matters [1–3]. The energy storage systems may be classified into four generalized categories, namely mechanical energy storage (e.g., pumped-hydro), chemical energy storage (e.g., petrochemical fuels) electrochemical energy storage (e.g., batteries, capacitors, and fuel cells), and electrical energy storage (e.g., superconducting magnets). However, the requirements for energy storage are widely varying and diverse, and driven primarily by the specific application, and there is no single bullet to address the impending needs for electrical energy storage. Hence, a diverse multi-portfolio strategy is best suited to develop a multitude of storage technologies and systems [2].

In case of portable applications, such as portable electronics or hybrid-electric/electric vehicles (H/EVs), the use of solutions based on electrochemical energy storage systems is well-desired [3,4]. The main available technologies are currently the Li-ion batteries and electrochemical capacitors (EC_s), where both offer different but often complementary performance characteristics [4,5]. Meanwhile, the former store the energy through chemical pathways (transformation of chemical bonds via electrochemical redox reactions), the latter store the charge via physical process (electrostatic charge at the electrode/electrolyte interface) [6,7]. Since no chemical or phase changes are taking place, the EC_s storage process is fast and highly reversible, and in the long term the charge/discharge cycle can be repeated with minor effects on the performance of the electric device [8].

As a matter of fact, the main advantage of EC_s is their long lifetime given that they may reach up to 20000 charge-discharge cycles with less than a 10% drop in performance retention, while batteries have an average lifespan between 500-3000 cycles [4]. Conversely, the main disadvantage of ECs is their low specific energy due to the lack of chemical reactions. Thus, ECs are not able to store large capacities compared to batteries, but they may play complementary functions. On this context, research and industrial developments for EC_s are essentially oriented to improving the device's energy density through the design of new electrode materials, new electrolytes, and even new electrochemical concepts [9].

Regarding to electrode materials, microporous carbons are the primary materials used to make EC_s electrodes. They may be derived from sustainable, natural, abundant, and low-to-moderate-cost resources, which are important factors for industrial applications and the transition to the use of sustainable materials [8–10].

The main advantages of carbon materials are their versatility that allow to match the material characteristic to a given application (e.g. flexible or stationary electrodes), and even to tailor the nanostructure porosity and surface chemistry according to the specific requirements [11].

One promising approach to achieve the energy enhancement without losing power performance is through heteroatom doping of carbon materials. It has been demonstrated that heteroatom doping (oxygen, nitrogen or boron) can improve the electrochemical performance of carbon materials through the addition of defects that alter the material conductivity and allow faradaic contributions [1,12,13]. Although, it is noteworthy that heteroatom's synergetic effect depends on the relative location of the heteroatoms rather than their concentration [14].

In particular, tannins, a polyphenolic compound often obtained from tree bark, have demonstrated to be an excellent precursors for the elaboration of carbon-based electrodes for ECs [15–17]. The ability to generate auto condensation reactions makes tannins an attractive alternative to produce high-added-value materials [18,19]. Also, the presence and high reactivity of -OH groups allows the addition of other atoms or functionalities.

In this context, this doctoral research focuses on the study of the relationship between pore size distribution, surface chemistry, and electrochemical performance of tannins-derived carbon materials as electrodes in electrochemical capacitors, with an emphasis on surface chemistry modification through tailored doping of oxygen, nitrogen and/or boron. Advanced characterization techniques such as adsorption isotherms, and X-ray photoelectron spectroscopy (XPS) among others were employed to analyze the structure and chemistry of the carbon materials. Additionally, electrochemical tests were conducted to evaluate their energy storage capacity, power density and overall performance. It is expected that this doctoral thesis leads to advance the understanding of the factors influencing the electrochemical performance of carbon-based electrochemical capacitors using tannins as precursor material, as well as the effect of heteroatom addition. Moreover, the obtained results can contribute to the improvement of electrochemical capacitors and accelerate their adoption as a more efficient and sustainable energy storage technology in various fields of application.

2 BACKGROUND

2.1 Electrochemical energy storage

Electrical energy storage systems (EES) have been the subject of intense study as they constitute an essential element in the development of sustainable energy technologies. Electrical energy generated from renewable resources such as solar radiation or wind has proven to provide great potential to meet our energy needs in a sustainable manner. It would reduce not only our dependence on fossil fuel but also pollutant emission responsible for global warming [2,20] However, these renewable energy technologies generate electricity intermittently and thus require efficient and reliable electrical energy storage (EES) methods. Among the EES, electrochemical capacitors and batteries are the predominant electrochemical energy systems commercially available [2]. Energies obtained from the intermittent renewable sources such as solar, tide, and wind energy, customer electronics like laptop computers, personal digital assistant (PDA), global positioning system (GPS), portable media players, hand-held devices, and photovoltaic systems as well as the grid power buffers all require batteries or/and ECs for efficient energy storage [21–23]. Moreover, greatly improved EES systems are required to enable the widespread use of hybrid electrical vehicles (HEV), plug-in hybrids, and all-electric vehicles [4,24]. Therefore, the development of improved EES systems will be critical.

The performances of electrical energy storage devices can be assessed by comparing their energy density (in W-h kg^{-1}) and power density (in W kg^{-1}). **Figure 2-1** shows the so-called Ragone chart plotting the energy density versus the power density of different kind of batteries and electrochemical capacitors. Batteries exhibit relatively high energy density but low power density, attributed to the slow kinetics of their chemical reactions. For instance, lithium-ion batteries, highlighted in green in **Figure 2-1**, have an energy density ranging from 100 to 265 W·h kg^{-1}, yet their main drawback is their power density that hardly surpasses 1 kW kg^{-1}. In contrast, electrochemical capacitors (ECs) can operate in a wide range of power densities. Generally, ECs have energy densities below 20 W·h kg^{-1}, but boast high power densities exceeding 10 kW kg^{-1}, reaching values 10 to 100 times greater than the batteries [25]. However, when compared to conventional gasoline and hydrogen combustion engines, which offer very high specific power and energy densities, both batteries and ECs fall short. Gasoline, for instance, has a specific energy of 12.3 kW·h kg^{-1} and can provide 3.700 kW kg^{-1} considering a typical 30% internal combustion engine efficiency [26]. Nevertheless, these internal combustion engines raise concerns regarding fossil fuel dependency and environmental pollution. Thus, the major challenge for ECs and batteries is to achieve high power and high energy densities, as illustrated by the “star” marked goal in **Figure 2-1**.

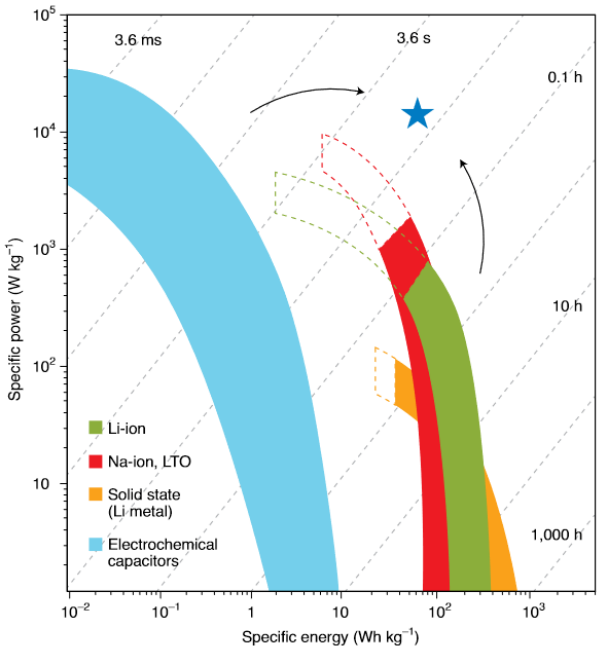

Figure 2-1 Ragone plot illustrating specific energy and power trends for various batteries types (green area for Li-ion, red area for Na-ion, and yellow area for Li-metal batteries), and electrochemical capacitors (blue area), with the star indicating the direction toward improved performance, obtained from [1].

Nowadays, intensive research efforts have been devoted to improve both energy density and power density by innovating new materials, engineering unique nanostructures, developing highly ion-conductive electrolytes and creating both energy and power boosting configurations for ECs [9,12,13,27,28]. Particularly, the efforts for research and development in ECs have been focused on increasing the energy density from two approach. As exposed in **section 2.1.1**, the energy density of ECs is given by the capacitance and the operation voltage window, according to **Eq. 2-3**. For enlarging the voltage window, non-aqueous ionic liquids electrolytes can be selected due to their higher decomposition potential window than the aqueous electrolytes [29]. On the other hand, to improve capacitance, the electrode modifications are the main target. Nanostructures are tailored to improve their specific surface area and develop a controlled pore size distribution, allowing for improved ion storage mechanisms [13,28,30]. On this matter, carbon materials are the most popular material to made ECs electrodes, which could typically have a surface area about 1000 $m^2 \cdot g^{-1}$ [11], resulting in specific capacitance over 100 $F \cdot g^{-1}$ [10,28]. Although there are multiple materials that improve the aforementioned capacitance values, such as oxides of transition metals [31], carbide-derived carbons (MXenes) [32], almost all large-scale produced commercial ECs are made from coconut shells-derived activated carbon. The limitation to use any of these reported favorable ultra-high-energy density materials are their associated high cost and difficulty of production in a medium-large scale [27,33]. On this context, there is still a need to develop high-energy densities capacitors that bridge the gaps of power density and energy density between batteries and ECs with suitable conditions to scale-up their production.

2.1.1 General principles on electrochemical capacitors

Electrochemical capacitors (EC_s) store energy in an electrostatic field rather than in chemical form as batteries. The main differences between the electrochemical storage mechanism are illustrated in **Figure 2-2**. Commonly, ECs consists of two parallel electrodes soaked in an electrolyte solution and separated by a dielectric material. Its charging establishes from an electric potential difference between the electrodes, which causes ions to migrate toward the electrode surface of opposite polarity.

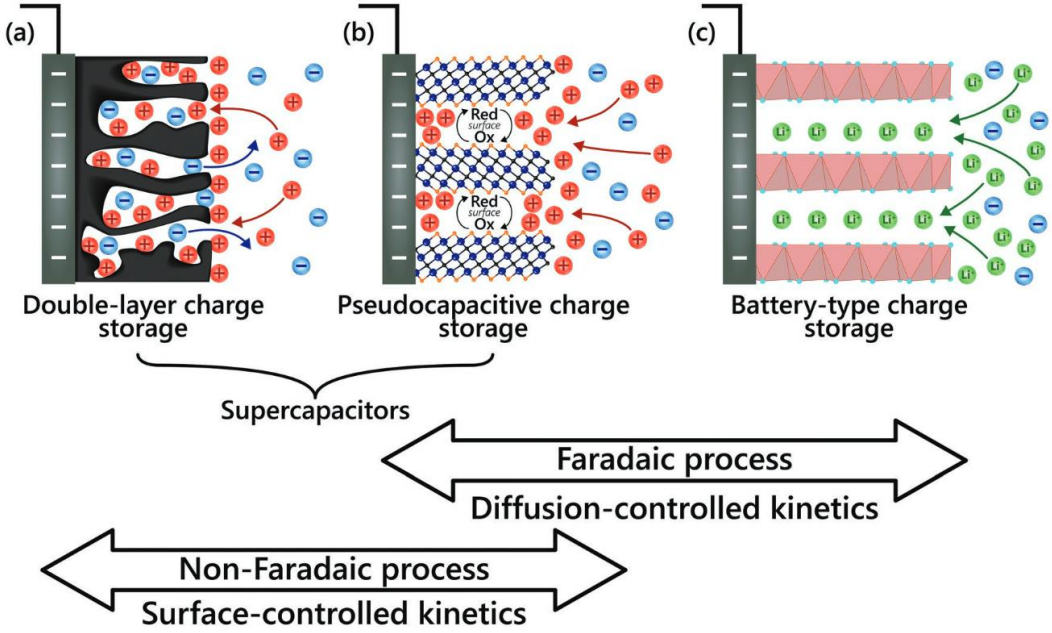

Figure 2-2 Illustration of the electrode processes occurring at a) electrical double-layer capacitance, b) pseudocapacitive, and c) faradaic electrodes as in batteries, obtained from [20].

Typically, a flat plate capacitor obeys **Eq. 2-1**, where capacitance ($\boldsymbol{C}$) is measured in Farads (F), $\boldsymbol{\varepsilon_0}$ is the permittivity of vacuum, and $\boldsymbol{\varepsilon_r}$ is the solution permittivity. The geometry includes the overlapping surface of the electrode ($\boldsymbol{A}$), and the effective thickness ($\boldsymbol{D}$) of the electric double layer (EDL) [34].

$$C = \frac{\varepsilon_r \varepsilon_0 A}{D} \qquad \textbf{Eq. 2-1}$$

Therefore, it would be noticed that capacitance is directly proportional to the surface area and contrariwise proportional to the distance. However, in the case of porous material, the foregoing is partially right according to the expose on section 2.1. In addition to the EDL capacitance, an extra capacitance can also exist within the electrode itself.

For carbon materials, especially, an extra capacitance in series, as is shown in **Eq. 2-2**, should be taken into account due to the density of states of the electrode material, where C_{EDL} is the capacitance of the double layer (**section 2.2.1**), and C_Q is the quantum capacitance (see section **2.2.2**).

$$\frac{1}{C} = \frac{1}{C_{EDL}} + \frac{1}{C_Q} \qquad \textbf{Eq. 2-2}$$

Two primary attributes of any electrochemical energy storage are its energy density (E), and power density (P), described according to **Eq. 2-3** and **Eq. 2-4**, respectively. Thus, the overall performance of the electrochemical capacitor is influenced by two main factors: (i) the choice of the electrode material, which defines the capacitance, and (ii) the electrolyte utilized, which limits the operating voltage (V).

$$E = \frac{1}{2} C V^2 \qquad \textbf{Eq. 2-3}$$

$$P = \frac{E}{t_D} \qquad \textbf{Eq. 2-4}$$

Currently, the most widespread materials used in EC_s are carbon materials produced from a wide variety of carbonization and activation processes, using raw materials ranging from conventional activated carbons [8,10] through to the more sophisticated carbon materials, such as hollow-carbon spheres, carbon nanotubes or even graphene-kind materials. In all these instances, electrodes have a high specific surface area (SSA) between 500 to 3500 $m^2\,g^{-1}$, and the possibility of manipulating their surface topology according to the precursor and synthesis method [9,33].

On the other hand, electrolytes are classified into three broad groups: (i) aqueous, (ii) salts dissolved in organic solvents, and (iii) ionic liquids. The aqueous electrolyte, such as acids (H_2SO_4) or bases (KOH) have the advantage of high ionic conductivity (~ 600 mS cm^{-1}). However, they have a restricted voltage range of 1.23 V due to the electrochemical breakdown of water [29]. Organic electrolytes allow the use of cell operating voltages up to 2.7 V, but they have a conductivity with at least an order of magnitude lower than aqueous electrolytes [27]. Similarly, ionic liquids are promising electrolytes for EC_s due to their wide electrochemical stability window (between 3 and 6 V), but they have an even lower ionic conductivity than organic electrolytes [29]. Generally, the ionic liquids have an ionic conductivity between 0.1 and 15 mS cm^{-1}. The issue with voltage operation is that it is proportional to the density energy of EC_s according to exposed by **Eq. 2-3**, which is currently the principal disadvantage of these devices [1], as it was discussed in section 2.1. However, the use of electrolytes with a lower ionic conductivity has an impact on electrochemical series resistance (ESR).

The ESR values determines the power capability, and ultimately, the final application of the storage unit. It depends on: (i) intrinsic structure of the electrode material, (ii) interfacial resistance between the electrode material and the current collector, (iiI) ionic diffusion through the electrolyte solution and into the pores, and (iv) the electrolyte ionic resistance.

As showed before, the energy density is proportional to the square of the voltage window, while the ESR is inversely proportional to the cell's power capability [35]. Therefore, a careful selection of suitable electrolytes is crucial in constructing high-performance EC_s.

Another important consideration at the electrolyte and electrode selection, it is to match the size of the electrolytes ions with the pore size in the porous materials [29]. As a general rule, the smaller the ion size, more surface area is available to the ions. Given that aqueous electrolytes have smaller ion sizes tan organic electrolytes and even ionic liquids, it is expected that they provide higher specific capacitance. As a matter of fact, capacitance values ranging from 100 to 400 F g^{-1} are reported in aqueous electrolytes, while for organic electrolytes and ionic values these values rounded between 120 – 150 F g^{-1} [27].

As mentioned before, capacitance arises from the potential dependence of the surface density of charges stored electrostatically (non-faraidic) at the electrode-electrolyte interface. The accumulated charge is the result of an excess or deficit of conduction-band electrodes at or in the near-surface region of the interface, altogether with a counterbalancing charge densities of accumulated cations or anions of the electrolyte on the solution side of the double-layer [34]. The former is commonly called quantum capacitance (C_Q), while the second is the electric-double layer capacitance (C_{EDL}). However, a third phenomenon is also can been noticed, with a completely different charge storage mechanism. It arises from electron transfer at the interfaces (e.g., chemisorption and/or redox reactions), and it is commonly named as pseudocapacitance (C_{PsC}), as illustrated at the beginning of this section in **Figure 2-2**. It has been found that carbon materials with a significant proportion of heteroatoms or surface functionalities can exhibit significant pseudocapacitance [36–39], and also hydrogen electro-sorption [40]. Such behavior and the essential details of its impact on capacitance are explained in the following sections.

2.1.2 Electric double layer (EDL) theory

The concept of a double layer theory corresponds to a model consisting of two array layers of opposite charges, separates by a small distance. In 1853, Helmholtz developed the first theoretical model. He proposed that in a charged surface (electrode), the counter-ions would be attracted from the solution (electrolyte) to the interface where they would form a sheet of countercharge that balances the charge on the electrode [27,34]. However, Helmholtz's model describes in a simple way the double layer and does not predict the dependence of capacitance with voltage. Posteriorly, Gouy proposed that ions on the solution side of the double layer would not remain static in a compact array. They would be subject to the effects of thermal fluctuation according to the Boltzmann principle, which also depends on the electrostatic and chemisorption energy [41]. Chapman gave the full mathematical approach of the Gouy diffuse layer model in 1913. It based on the combined application of Boltzmann and Poisson equation, and it described the relation of the ionic space charge density in the interfacial region to the second derivative of electric potential ($\boldsymbol{\psi}$), according to the distance from the electrode surface [34]. The key of the Gouy-Chapman model is the Poisson-Boltzmann equation (**Eq. 2-5**), where ϵ_r is the dielectric constant of the solvent, ϵ_0 is the vacuum permittivity (8.85×10^{-12} F m^{-1}), and ρ_e is the local electric charge density described by **Eq. 2-6**, where k_B is the Boltzmann constant, n_i is the number of cations or anions per unit of volume, z_i is the formal charge of the ion and e is the electric charge of one electron (1.60×10^{-19} C).

$$\nabla^2\psi = \frac{\rho_e}{\epsilon_r\epsilon_0} \qquad \textbf{Eq. 2-5}$$

$$\rho_e = \sum n_i z_i e \exp\left(\frac{-z_i e\psi}{k_B T}\right) \qquad \textbf{Eq. 2-6}$$

Additionally, Chapman anticipated the approach taken by Debye and Hückel and derived the Debye length (L_D) for a $z{:}\,z$ electrolyte (**Eq. 2-7**), which is frequently taken as a measure of diffusive-layer thickness. Despite the ability to explain the EDL behavior made it for the Gouy-Chapman model, this treatment has a serious problem, given that it overestimates the capacitance on the double-layer. Therefore, Stern proposed in 1924 (5) the existence of two regions: (i) the inner region with an ion distribution that could be treated as an adsorption process according to Langmuir's adsorption isotherms, and (ii) the outer region, that could be treated as a diffusive region according to the Gouy-Chapman model.

$$L_D = \left(\frac{\epsilon_r\epsilon_0 k_B T}{2nz^2e^2}\right)^{0.5} \qquad \textbf{Eq. 2-7}$$

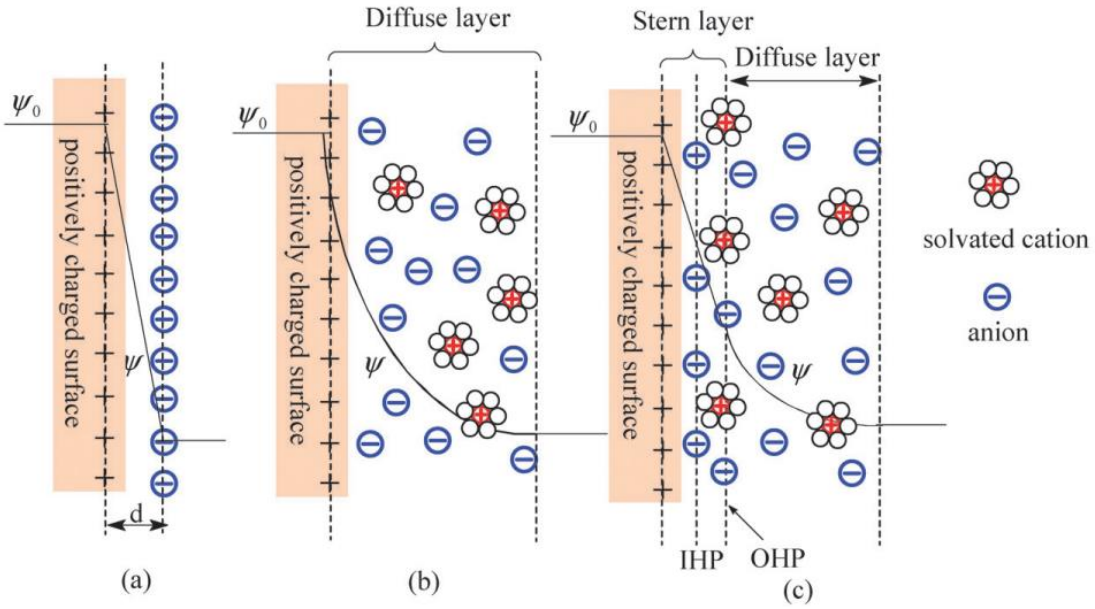

Figure 2-3 Models of the electric double layer at a positively charged surface (a) the Helmholtz model, (b) the Gouy-Chapman model, and (c) the Stern model showing the IHP and OHP plane according to the BDM model, obtained from [10].

Thus, the Stern model is a combination of the Helmholtz model and the Gouy-Chapman model, and the reciprocal of the double layer capacitance (C_{EDL}) in the interface is the harmonic sum of the capacitance of the inner region (C_H), called Helmholtz layer, and the capacitance of the outer region (C_H), called the diffusive layer, according to **Eq. 2-8**. Therefore, the overall capacitance of the EDL will be determined by the lower value of these two capacitances. In the case of dilute solutions, the minimum capacitance occurs at the minimum value of C_{Dif}, which occurs when the electrode is uncharged, and the measured potential of the electrode is called the potential of zero charge (PZC) [42]. The PZC depends on both electrode and electrolyte. At the PZC point, the differential capacity of the electrode typically exhibits a local minimum [43]. Further, Graham modified the EDL model and proposed that some ionic or uncharged species can penetrate the Stern layer. The ions can also lose their solvation shell as they approach the electrode.

$$\frac{1}{C_{EDL}} = \frac{1}{C_H} + \frac{1}{C_{Dif}} \qquad \textbf{Eq. 2-8}$$

Following these improvements on the EDL theory, Bockris Devanathan and Müller, also proposed an improve Stern model, that they called BDM model. In this BDM model, the attached molecules on the electrode would have a fixed alignment to the surface. This inner layer (IHP) displays a strong electric field orientation, depending on the charge, and it has a significant influence on the permittivity of the solvent that varies with field strength. The IHP passes through the center of these molecules. The solvated ions are outside the IHP layer, and they form an outer layer (OHP).

Specifically, the OHP layer passes through the center of these ions, and the diffusive layer is the region beyond the OHP layer, as is shown in **Figure 2-3 C**. Although some others models have been proposed subsequently, the BDM model is the currently accepted model. However, it has to be noted that electrodes in EC_s are generally porous materials, and the pores width have a comparable size to EDL thickness. This leads that the diffusive layer overlapping from opposites surfaces, and consequently a redistribution of the diffusive layer. This phenomenon may contribute to an enhanced double-layer capacitance that cannot be explained using the classical parallel-plate capacitance models formerly described. In this context, an alternative approach for modeling the EDL in porous materials was proposed by Huang et al. in 2008 [44,45] . The authors developed a heuristic model based on density functional theory (DFT) calculations, which considers the curvature of the pore walls as depicted in **Figure 2-4**. For macropores (w > 50 nm), the capacitance is well-described by the traditional double layer approach. Meanwhile, the pore curvature should be considered for mesopores (2 < w < 50 nm) and micropores (w < 2 nm) for a more accurate estimation of capacitance. In the case of mesopores, a cylindrical geometry with a radius b_j is assumed, whereby the solvated counterions approach the pore wall to form an electric double cylinder capacitor (EDCC). For micropores, a cylindrical geometry is also used, but with a radius b_i, the solvated or desolvated counterions line up to form electric wire-in cylinder capacitor (EWCC) because of the space in the micropores not allow the formation of an inner cylinder. In this case, the key quantity is no longer the thickness of the double layer ($\boldsymbol{D}$), but rather the radius of the inner cylinder $\boldsymbol{a_0}$, which is the effective size of the counterions.

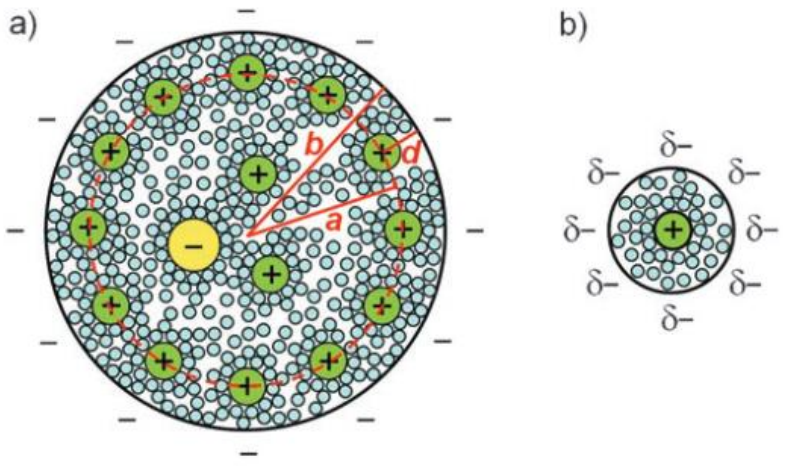

Figure 2-4 Schematic diagram of a) a negatively charged mesopore with solvated counterions arrangement in a cylindrical way, and b) a negatively charged micropore with solvated counterions in a wire arrangement, obtained from [44].

On this way, the capacitance of the electric double layer is given by **Eq. 2-9**, where $\boldsymbol{b}$ is the pore radius, $\boldsymbol{a_0}$ is the effective size of the counterions, and $\boldsymbol{D}$ is the effective thickness of the electric double layer.

$$C_{EDL} = \sum \frac{\varepsilon_{r,micro}\varepsilon_0 A_{i,micro}}{b_i \ln(b_i/a_0)} + \sum \frac{\varepsilon_{r,meso}\varepsilon_0 A_{j,meso}}{b_j \ln(b_j/(b_j - D)} + \sum \frac{\varepsilon_{r,macro}\varepsilon_0 A_{k,macro}}{D} \quad \textbf{Eq. 2-9}$$

This extension to the classical double layer model has been shown to apply to a range of carbon materials and electrolytes. It supports the anomalous capacitance increase in porous materials with pores below 1nm [30]. As well as the partial desolvation of ions before they come into fine micropores, as it is discussed in **section 2.2.1**.

2.2 Carbon materials in electrochemical capacitors

Carbon has a unique electronic structure, including an intermediate electronegatively and fourfold bonding possibilities in saturated valence interactions. As a result, it is considered unusual in the number of its allotropic structures, and the diversity of structural forms. Furthermore, it exhibits some semiconductor properties and the band structures of its various forms are an attractive research field. Carbon has four crystalline (ordered) allotropes: diamond (sp^3 bonding), graphite (sp^2), carbyne (sp) and fullerenes (distorted sp^2) [8]. Meanwhile, two of them are naturally found on earth (graphite and diamond), the others form of carbon are synthetic. For ECs purposes, the majority of carbon materials are derived from carbon-rich precursors by heat treatment in inert or controlled atmospheres (carbonization). The resulting properties are dependent on a number of critical factors: (i) the raw material, which could be natural (e.g., coconut shell, wood, bark, coal), petroleum-derived (e.g., acetylene, ethylene, aromatic hydrocarbons) or synthetic polymers; (ii) dominant aggregation state during carbonization (gas, solid or liquid), (iii) processing conditions (e.g. pressure, temperature, residence time) [8], being the most important parameters their specific surface area, pore size distribution, pore connectivity, electrical conductivity and surface chemistry [33].

A wide range of carbon materials can be used as electrodes in ECs. The most investigated currently are graphene, carbon nanotubes (NCT), hollow-spheres, carbon aerogels, whereas the most widely used in industry is activated carbon (AC). A brief summary is provided in **Table 2-1**, and more information about the preparation, properties and performance of carbon materials can be found in the reviews made by Pandolfo et al. [8], Chen et al. [46], Gu et al. [47] or Frackowiak et al. [33], to name few. Actually, carbon materials used as electrode in ECs is a very popular research field, especially over the last decade. For instance, according to Web of Science, the total number of research papers until November 2019 is 3.803 (keywords used in title: carbon, capacitor, or supercapacitor) and they represent 30.94 % of the total reported literature for the topic “carbon electrochemical” (keywords used in topic: carbon electrochemical). Moreover, and as mentioned above, activated carbons are the most widely used carbon materials. Generally, the process employed to increase the surface area and porosity from a carbonized precursor is referred to as activation. Varying the carbon precursor and activation conditions (temperature, time, activate agent and gaseous environment) offers flexibility and control over the resulting porosity, pore size distribution and chemical nature of the internal surfaces [8,11,48]. The activation process can be placed into two general categories: “physical” and “chemical” activation, where differences on the morphology of the material can be appreciated, as it shows in **Figure 2-5**, published by Yang et al. [49]. The “physical” activation entails the modification of raw material by controlled gasification, and it is usually carried out between 700 to 1100 °C in the presence of a suitable oxidizing current flow such as steam, carbon dioxide, air, or a mixture of these gases.

Table 2-1 Use of different carbon materials used as electrodes in ECs.

Carbon material	Description	Method	Carbon precursor	SSA [a] ($m^2 g^{-1}$)	Electrolyte	Cw ($F g^{-1}$)	Ref.
HCS	Zeolite-templated hollow core mesoporous carbons	CVD	Acetonitrile	2205	Net_4BF_4 in acetonitrile	146	[50]
AC	AC submitted to pre-pyrolysis step	Chemical activation	Lignin	2233	KOH 6M	237	[51]
AC	Chemical activation with KOH	Chemical activation	Tree bark	1018	Na_2SO_4	191	[52]
N-doped graphene	Carbonization, followed by etching of the template	Polymerization and carbonization	Dopamine / montmorillonite composite	401	$EMImBF_4$	128	[53]
rGO	Exfoliation under low-temperature and vacuum	Low temperature carbonization	Graphite	368	KOH 5.5 M	264	[54]
SWCNT	SWCNT sprayed onto PET substrates	Comercial SWCNT	N.A.[b]	N.A.[b]	H_3PO_4 (gel electrolyte)	120	[55]

[a] SSA estimated by BET. [b] N.A. = not available information.

During gasification, pore volume and surface area of the material increase by virtue of a controlled carbon burn-off and the elimination of residual pyrolysis products (from **Eq. 2-10** to **Eq. 2-12**) [49,56].

$$C + CO_2 \rightarrow 2CO \qquad \textbf{Eq. 2-10}$$

$$C + 2CO \rightarrow C + O_2 \qquad \textbf{Eq. 2-11}$$

$$C + O_2 \rightarrow CO_2 \qquad \textbf{Eq. 2-12}$$

The burn-off degree is, perhaps, the most important factor governing the quality of the activated carbon and it is controlled by temperature and activation time. A high degree of activation is achieved by an increased burn-off, but it may be along with a decrease in carbon strength, a much lower density, reduced yield and excessive pore widening [57].

On the other hand, “chemical” activation is usually carried out altogether with carbonization at slightly lower temperatures (400 – 700 °C), and involves primarily the dehydrating action of agents such as phosphoric acid, zinc chloride and potassium hydroxide [58]. Post-activation washing of the carbon is usually required to remove residual reactants as well as any inorganic residue that originates from the carbon precursor or is introduced during activation.

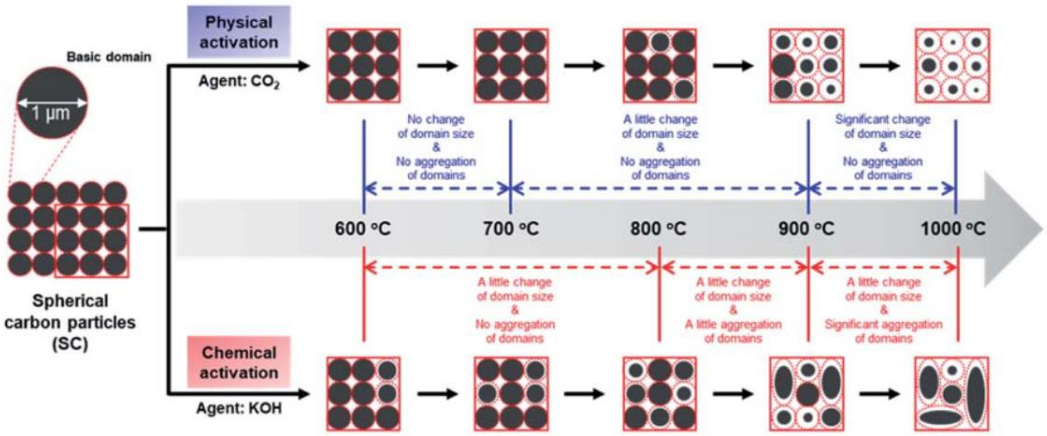

Figure 2-5 Changes in the morphologies of physical and chemical activated carbon materials according to the activation temperature, obtained from [49].

The KOH activation is one of the most popular activating agent, but it is a complex process that involved several redox reactions between the carbon matrix and KOH [59,60] (from **Eq. 2-13** to **Eq. 2-15**), followed by potassium intercalation/insertion and expansion of the structure [58] (**Eq. 2-16** and **Eq. 2-17**).

$$2KOH \rightarrow K_2O + H_2O \qquad \textbf{Eq. 2-13}$$

$$H_2O + C \rightarrow CO + H_2 \qquad \textbf{Eq. 2-14}$$

$$CO + H_2O \rightarrow CO_2 + H_2 \qquad \textbf{Eq. 2-15}$$

$$CO_2 + K_2O \rightarrow K_2CO_3 \qquad \textbf{Eq. 2-16}$$

$$K_2CO_3 + 2C \rightarrow 2K + 3CO \qquad \textbf{Eq. 2-17}$$

Exceptionally high-surface area materials (up to 2500 $m^2\ g^{-1}$) with narrow pore size distribution have been prepared by KOH activation [51,52,60–62]. In the case of H_3PO_4, carbonization and activation generally proceed simultaneously at lower temperatures than KOH activation [63]. Another route for the preparation of carbon materials is the chemical pre-treatments. As example, the most famous is the modified Hummers method [64]. It consists in the preparation of graphite oxide, which is then exfoliated to graphene oxide, and ultimately converted to graphene (or reduced graphene oxide) by heat treatment. Another pre-treatment is hydrothermal (HTC) or solvothermal carbonization. It consists in heat treatment of an aqueous or organic solution/dispersion of organic material under autogenous pressure at 150 - 350 °C [65,66].

The carbon products (named hydrochars) generally exhibit uniform chemical and structural properties as well as significant and tunable content of oxygen, nitrogen, sulfur as well as boron when using dopant-containing additives in this step [39,66–68].

The purpose to functionalized carbon with a variety of heteroatoms and regulate their content is to produce donor states in the electronic structure and tailor the conductivity as well as modify the surface polarity and electron donor/acceptor affinity according to the electrolyte [12,69]. Additionally, the capacitance of carbon materials can be enhanced through faradaic reaction between selected functional groups and the electrolyte [28,37,70]. For example, the article published by Hulicova-Jurcakova et al. [71] showed that the specific capacitance of nitrogen-enriched carbon materials obtained via ammonia treatment was three times higher than that of non-enriched parent materials. On the same context, the published work by Lee et al. [38] study the effect of nitrogen-doped reduced graphene N-RGO, where it was possible to differentiate the pseudocapacitance contributions from the electric double layer capacitance showing that nitrogen groups increase both capacitance in the case of H_2SO_4 as electrolyte but in the case of KOH, only the pseudocapacitance increases while the electric double layer capacitance diminishes. Additionally, the study by Pognon et al. [72] shows that introduction of catechol groups improve the specific capacitance of activated carbon from 150 to 250 F g^{-1}. However, in some cases, the introduction of these functionalized groups entails an unstable pseudocapacitance and the reduction of cyclability due to irreversible reactions [7,12,37].

To understand the role of functional groups over the capacitive performance of carbon materials, it is necessary to clarify the exact nature of those in the carbon materials, as it is discussed in section 2.2.2. On this context, the utilization of feedstocks with high content of oxygen or nitrogen offers the opportunity to achieve electrode improvement without the use of extra chemicals or additional steps to obtain a tailored material. Zhang et al. [73] made a hierarchical porous carbon from lignin via the traditional carbonization with a subsequent chemical activation using KOH. The resulting carbon had a BET specific surface area of 3775 $m^2 g^{-1}$ and narrow pore size distribution with micropores close to 1 nm and mesopores between 2 and 4 nm. The maximum specific capacitance reached 286.7 F g^{-1} at 0.2 A g^{-1} using an 6M aqueous solution of KOH.

A similar methodology was used by Yu et al. [51], they studied the effect of pre-pyrolysis before activation on the electrochemical performance, and observed an improvement in the development of micropores and graphitization degree of the lignin-derived carbon. Although pre-pyrolysis resulted in a lower total surface area, the carbon material obtained had a higher specific capacitance (261 F g^{-1} at 1 A g^{-1}) than that obtained by a directly activation method (218 F g^{-1} at 1 A g^{-1}). Wang et al. [62] used phenol formaldehyde resins obtained from bark liquefaction as carbon precursors, which were chemical activated using KOH.

The resulting carbon had a high surface area (2359 $m^2\ g^{-1}$), composed of ultramicropores (< 0.7 nm), micropores (close to 1 nm), and small-size mesopores (2-5 nm) with an oxygen content of 6 wt% in the form of C=O, O-C-O and O=C-O groups. The capacitance was 370 F g^{-1} at 0.1 A g^{-1} and 251 F g^{-1} at 10 A g^{-1}.

Another raw material less explored as carbon precursor, are tannins. Although, throughout the course of this doctoral research an increased interest has been notice. They are commonly obtained from tree bark (e.g., Acacia auriculiformis, Pinus pinaster or Pinus radiata) [16,74], and have a very suitable chemical structure for electrochemical purposes, as covered in **section 2.3**.

2.2.1 EDL capacitance at the porous carbon/electrolyte interface

As mentioned in **section 2.1.1**, the overall capacitance ($\boldsymbol{C}$) of an electrochemical capacitor obeys **Eq. 2-2**, if pseudocapacitance can be neglected. Additionally, the capacitance of the double layer ($\boldsymbol{C_{EDL}}$) could be calculated, as a first approach, using **Eq. 2-1**. As a consequence, it can be seen that $\boldsymbol{C_{EDL}}$ is directly proportional to the surface area and inversely proportional to the EDL thickness (D). Experimental research has shown, as a general trend, that capacitance increases as the specific surface area (SSA) increases. However, at relatively high SSA values (up to 2000 $m^2\ g^{-1}$) on carbon materials, it has been observed that capacitance tends to a plateau [75,76], as observed in **Figure 2-6 A**.

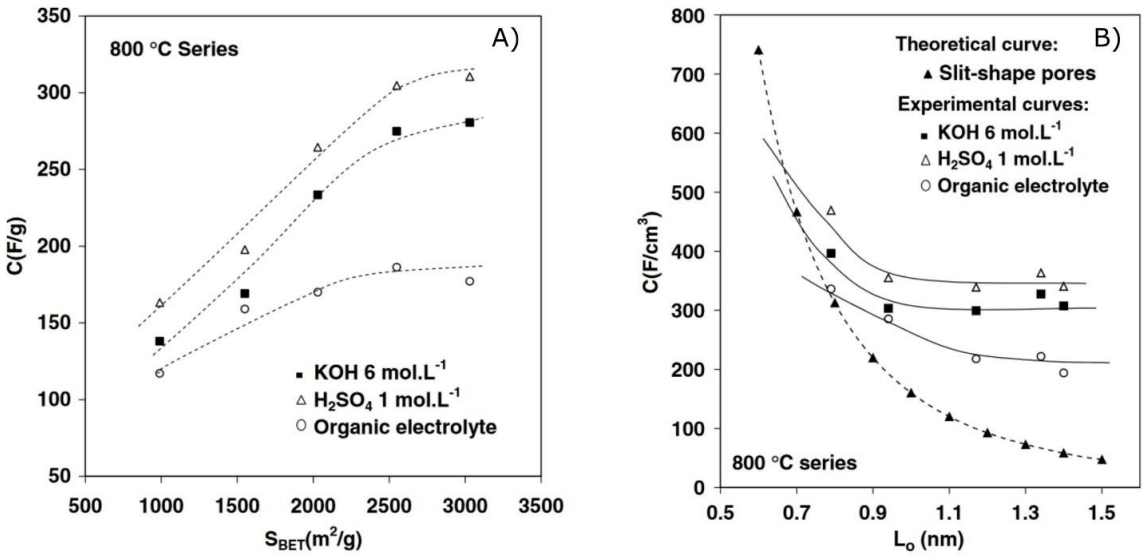

Figure 2-6 A) Gravimetric capacitance in aqueous and organic electrolytes (1 M $TEABF_4$ in acetonitrile) obtained from GCD curves at 100 mA g^{-1}, and B) Relationship between the volumetric capacitance and pore size for the same experimental data, obtained from [76].

This is because at this point, the increase of surface area is related to the widening of the already existing pores, rather than the generation of new pores [57]. As the pore size increases, the interaction between the adsorbed ions and the surface of the electrode becomes weak as well the D tends to increases. As a result, there is a decrease on capacitance values as it is shown in **Figure 2-6 B**, where the trend is observed no matter the ion sizes. Actually, this was the main subject studied by Chmiola et al. [30], when in 2006 observed an increases on capacitance for carbon materials with average pore size below 1 nm, which behavior was corroborated by following researches [76,77].

Charge storage in pores smaller than the size of solvated electrolytes ions was fully evidenced using carbide-derived carbons (CDC) with a narrow pore size distribution [30]. The CDCs, with an average pore size ($\boldsymbol{L_0}$), tunable with accurate less than 0.5 nm, where used to study the ion adsorption in pores of average size between 0.6 and 1.0 nm using 1.5 M solution of tetraethylammonium tetrafluoroborate in acetonitrile (organic electrolyte). The cation size, $(CH_3CH_2)_4H^+$ is 0.68 nm, while the anion BF_4^- is 0.33 nm. The authors reported a trend of decreasing volumetric capacitance as the pore size decreases until reach close to 1 nm, as exposed in **Figure 2-7**. However, as the pore size approached the ion size, the trend reversed and there was a sharp increase in capacitance below 1 nm, even for sizes smaller than those of solvated ions. This capacitance increase was attributed to the distortion of the ion solvation shell, leading to a closer ion approach to the carbon surface, and a decrease of the double layer thickness. Subsequently, Largeot et al. [77] obtained similar results for CDCs electrodes using an ionic liquid with cation and anion sizes of 0.7 nm and 0.76 nm, respectively. In this context, Huang et al. [44,45] contributed to the development of a heuristic model, as mentioned in **section 2.1.2**, which is based on DFT calculations and previous experimental data.

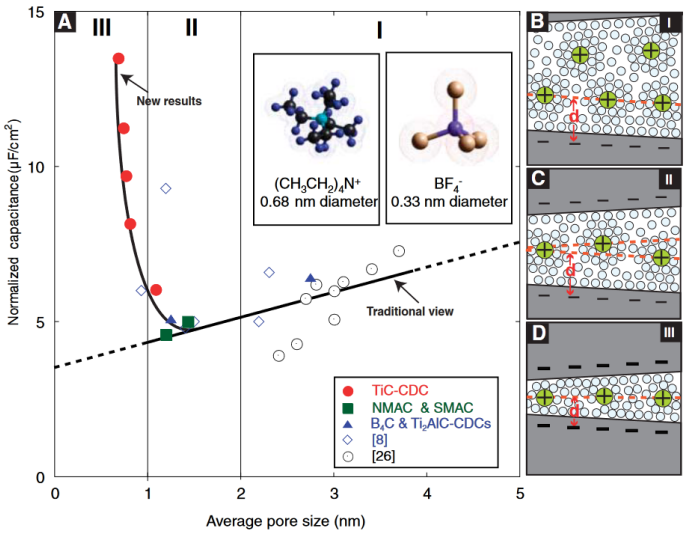

Figure 2-7 Capacitance normalized by A_{BET} versus average pore size and (B to D) drawings of solvated ions residing in decreasing pore sizes, obtained from [30].

The main contribution of this work was the **Eq. 2-9**, which is extended to all types of electrolytes regardless of the carbon used as electrode. This model allows one to correlate parameters such as pore size distribution, specific surface area, Debye length, electrolyte concentration, and dielectric constant, as well as solute ion size, which may lead to more systematic optimization of carbon properties through carefully designed experiments. The fitting with experimental data indicates that ions tend to be desolvated before entering in sub-nanometer pores as well ionic liquids, while aqueous electrolyte ions can retain their hydration shell. For instance, this model was applied on the work of Lota et al. [78] for 6M KOH as electrolyte and activated carbon electrodes.

The effective size of counterions (a_0) calculated was 1.64 ± 0.83 Å, which is in good agreement with the size of hydrated K+, between 1.38 Å and 1.46 Å, depending on the number of coordinates water molecules [50]. It is important to note that the value a_0 is at least an order of magnitude smaller than carbon pore size (between 1.06 nm and 1.45 nm). Thus, the desolvation effect of aqueous electrolytes remains unclear due to the lack of materials with pore sizes that are closer to the corresponding ion size. Moreover, because ions are flexible species with a variable diameter, and since pores in carbon-materials are distributed around an average value, the researchers should always be careful in interpreting such data, and should not expect that it will be possible to obtain perfect quantitative correlations [27].

Be that as it may, the capacitance behavior of carbon materials is essentially related to the sub nanometric pores. However, it has been also demonstrated that mesopores are needed for the fast transport of ions [15,48], which finally impact on the power density of carbon materials. On this matter, Vaquero et al. [48] studied the electrochemical behavior of different carbon materials with a wide range of textural properties using electrolytes from different nature and size. The carbon materials were tested using 1 M H_2SO_4, from low to high scan rates in cycling voltammetry (CV) assays (see section 2.4), and evidencing a dependence of capacitance with this parameter, as expected.

However, remarkable differences were observed on capacitance retention depending on the textural properties of the carbon materials. The mesoporous carbon with pores size between 2 and 6 nm shown a capacitance retention close to 69 % from scan rate of 10 to 100 mV s^{-1}. Conversely, the strictly microporous carbon (pore size below 2 nm) had a capacitance retention close to 27 % under the same test conditions. Likewise, where electrolytes with bigger size were tested, microporous carbon had important distortions from what it is expected of ECs. This behavior may be explained by the pore saturation due to a bigger size of the bulky ions than the pore. As a consequence, on the last decade, it will be an improvement on the textural target of carbon materials for electrochemical purposes focused on hierarchically, which is based on the promise that a combination of micro and mesoporous will bring the gap between energy and power density.

Actually, the study of Castro-Gutiérrez et al. [15] used ordered mesoporous carbon activated through CO_2 to evaluate the importance of pore connectivity. They actually found that carbon materials with a combination of mesopores and micropores shown the best performance on capacitance with an adequate balance between energy and power density.

On a practical point of view, such findings should also allow the correct design for specific applications of ECs: for longer discharge times when energy density is at a premium, such as in hybrid electric vehicles, extremely narrow pores should prove optimal; but for pulse power applications, increasing the pore size might be beneficial. Furthermore, tuning carbon porosity and designing carbon materials with a large volume of narrow but short pores may allow improve both energy and power density.

As summary, the relevance on this matter, it is that texture is a key parameter to develop electrochemical capacitors with outstanding performance that can bring the gap between energy and power density, where a match between the pore size and the electrolyte is fundamental altogether with a well development connectivity that allow the fast transport of ions.

2.2.2 Influence of surface chemistry and electric properties of carbon materials over capacitance.

As discussed in **section 2.1.1**, capacitance arises from the potential dependence of the surface density of charges stores electrostatically (non-Faradaic) at the electrode/electrolyte interface. This accumulated charge is the result of an excess or a deficit of conduction-band electrons at or in the near-surface region of the electrode in tandem to counterbalancing charge densities of accumulated cations or anions of the electrolyte on the solution side of the double layer. On the previous section, it was shown that the electric double layer capacitance (C_{EDL}) is related to the accessible surface area of the electrode in contact with electrolyte ions, where the morphology of the electrode material and the match between the pore size and the electrolyte are the crucial parameters.

However, carbon materials, such as graphene, have semiconductor properties and a relatively low density of states near the Fermi level due to its orthogonal π and π^* orbitals, which do not overlap each other [79]. Thus, graphene acts as a zero band-gap semiconductor, which nature results in high leakage currents and power dissipation. Xia et al. [43] measured the differential capacitance of graphene electrodes, and they founded that capacitance exhibits a V shape as a function of electrode potential having quantum capacitance as its source. The authors concluded that this V shape has a quantum mechanical origin and it results from the free-electron gas behavior in the basal plane of graphene, which shows a pronounced minimum close to the PZC [27]. The PZC varies according to the surface chemistry, and although pristine carbon material serves as a conceptual starting point, chemical defects, native or tailored, may play a critical role in modifying and optimize carbon materials electronic properties, such as conductivity [69,80].

They can enhance chemical activity through redox reactions [81], modification of surface charge and accessibility to ions [37,82]. Furthermore, introduce defects and covalent binding with heteroatoms, functionalities and even molecules onto the surface of carbon materials, as illustrated in **Figure 2-8**, are effective ways to open the band gap near to the Fermi level of pristine carbon materials through an introduction of sp^3-hybridization on the neighbor carbon atoms [70,79,83,84]. Specifically, the presence of heteroatoms changes the electron and hole carrier concentrations of the electrode at thermal equilibrium. The n-type doping (heteroatoms with higher electron valence than carbon) contributes free electrons on the surface, while p-type doping (heteroatoms with lower electron valence than carbon) creates a vacancy of electrons.

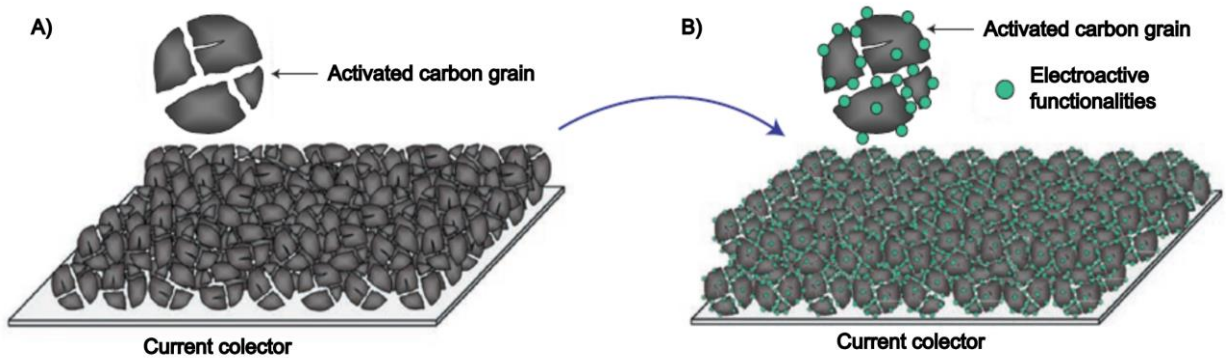

Figure 2-8 Schematic depicting the addition of electroactive functionalities onto the surface of carbon particles.

Because of that, heteroatom doping of carbon materials is an interesting approach to enhance the performance of carbon materials for electrochemical purposes. The final amount and the type of functionality on the carbon surface depend, as usual on carbon materials, on the precursor and the synthesis method, being carefully selective with both parameters due to heteroatom's synergetic effect depends on the relative location of the heteroatoms rather than their concentration [14].

Among the heteroatom functionalities found in carbon materials, the most abundant are the oxygen-containing groups. They are mostly present on the edge of carbon , more specifically at the edges of basal planes graphitic structures, in the form of hydroxyl (-OH), carbonyl (C=O), and carboxyl (-COOH) moieties [83,85,86], as depicted in **Figure 2-9 A**. For carbon materials obtained from renewable materials, such as tannins, the presence of oxygen is almost unavoidable. Due to the above, the role of oxygen functionalities is one of the most explored topics in heteroatom doping for electrochemical applications [36,37,87]. These functionalities play a crucial role as they can enhance the wettability of the materials and induce faradaic contributions through electron transfer [12]. However, it should be noted that the presence of oxygen functionalities can also lead to a decrease in surface conductivity [37].

Specifically, carboxylic acids species has demonstrated undesirable effects due to its strong polarity, leading to a leak current through catalytic effects and causing steric hindrance due to its large molecular structure [88], but also can induce faradaic reactions in basic conditions , as depicted in **Figure 2-10 A**. Additionally, carboxylic groups on the carbon surface are thermally unstable and present non-reversible reactions [12,89], therefore they are considered less preferable when compared to phenols or quinones groups.

The literature suggests that quinone groups could be of crucial importance in high-energy density capacitors. Quinones are electrochemically active through reversible two-electron and proton-coupled electron transfers with hydronium ions, especially in acidic solutions, enhancing the faradaic contributions of oxygen-containing carbon materials [17,36,90]. Given its reaction (**Figure 2-10 A**), in theory, they can provide two times higher energy storage than the other oxygen functionalities. Besides, quinones allow for an expanded potential window, exhibit good chemical stability, and do not negatively impact the cycling stability of the electrode [90].

Carboxyl and phenol groups are electrochemically active in both acidic and basic medias, involving a single electron transfer during their respective electrochemical reactions [36], and therefore their contribution are similar. They also have a key role on the wettability of carbon surface, decreasing the mass transfer resistance [37].

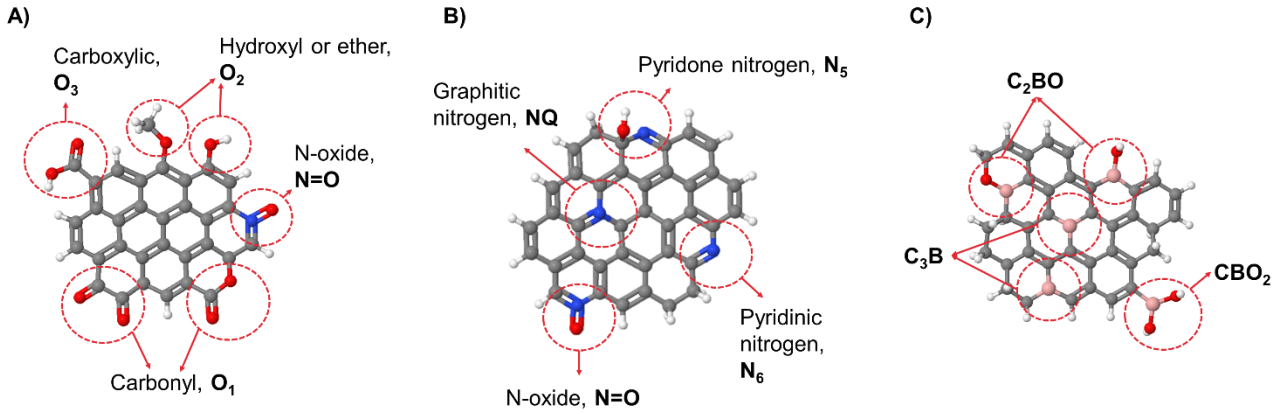

Figure 2-9 Representative functionalities for A) Oxygen, B) Nitrogen and C) Boron heteroatoms presented on carbon materials.

The nitrogen, as element, has one more electron than carbon. However, the electron-donor properties as n-type doping, on the N-doped carbon surface rely on the position of nitrogen into the carbon matrix. There is four kind of nitrogen classified as: (i) pyridinic nitrogen (N_6) that includes amides, aromatic amines, protonated amines, and pyridines; (ii) pyridine-like nitrogen (N_5) that includes pyrrolic-N, and pyridones; (iii) quaternary or graphitic nitrogen (N_Q); and (iv) nitrogen oxide (N=O), as exemplified in **Figure 2-9 B**. The nature of nitrogen functionalities differs depending on the temperature of heat treatment used on carbon material synthesis.

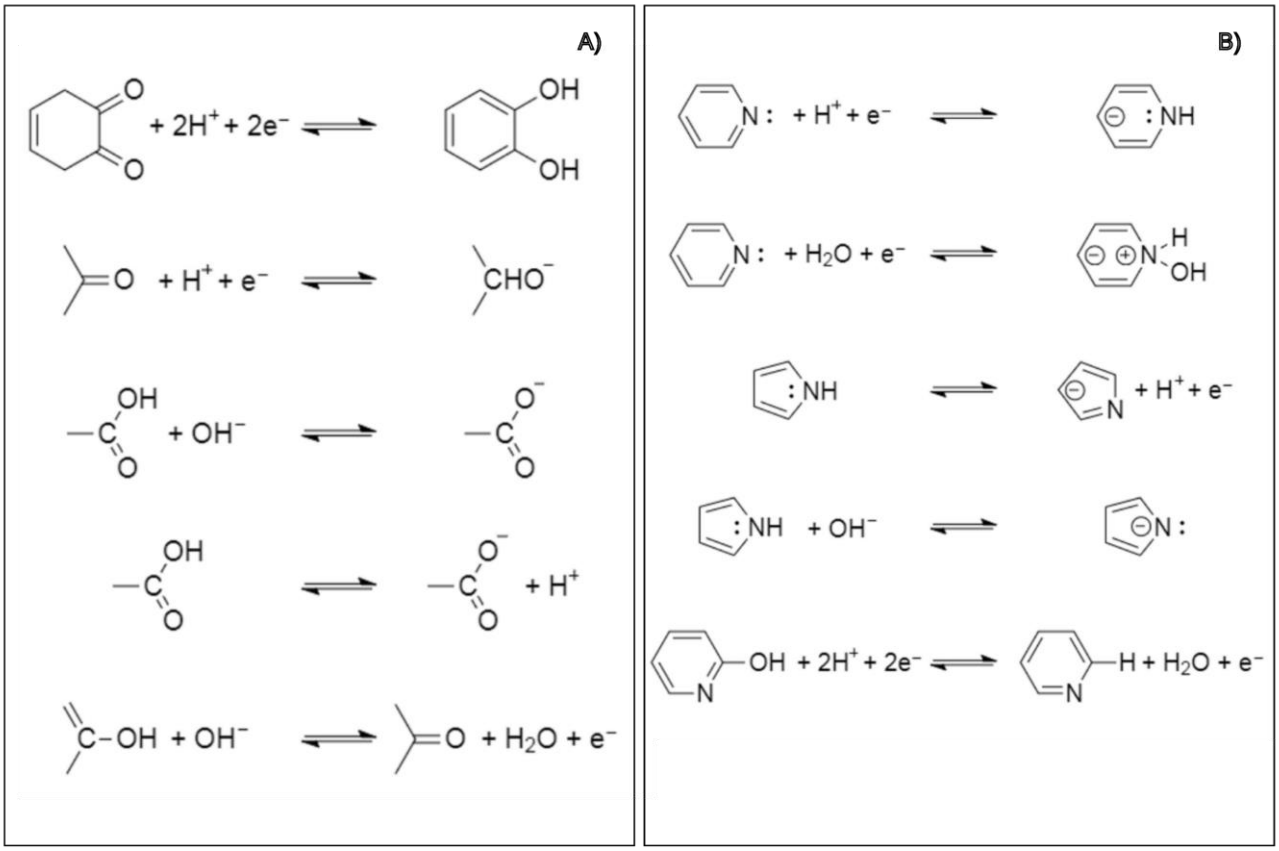

Figure 2-10 Oxygen and nitrogen surface functionalities commonly associated with the enhanced performance of carbon-based ECs. Proposed reactions for A) oxygen and B) nitrogen, obtained from [17].

It is expected that pyridinic nitrogen dominate in temperatures ranging from 400 and 700°C, while pyridones, pyrrolic nitrogen and quaternary nitrogen dominate at higher temperatures. Generally, at lower temperature nitrogen tends to appear on the edge of the carbon lattice with a localized charge, whereas at higher nitrogen is rather located within the aromatic ring with a delocalized charge [91]. Each configuration has a specific role in the enhancement of the properties of the carbon material. For instance, the negatively charged pyridinic nitrogen (N_6) has a relatively larger dipole moment that improves wettability of the electrode and reduce the charge transfer resistance between electrolyte and electrode [92], and also allow redox reactions in both acidic and alkaline electrolyte, as depicted in **Figure 2-10 B**. Moreover, protonated N_6 can be transformed into N_Q during the electrochemical charge-discharge storage process [12]. The pyrrolic-N, which is also negatively charged, plays a similar role in improving the wettability and faradaic contributions [71].

Moreover, it has been demonstrated that the pseudocapacitive behavior of N-doped carbon materials may be different depending if they are tested as positive or negative electrode, at least in acidic aqueous electrolyte [93]. This fact can be attributed to the fast and efficient faradaic reactions between pyridinic-N, pyrrolic/pyridine-N, and H^+ at the negative electrode–electrolyte interface.

The positively charged quaternary nitrogen (N_Q) and pyridinic C-N-O contribute a pair of electrons in the conductive π-π system, which results in an improved electron transfer across the electrode-electrolyte interface and enhances the electronic conductivity, through modifications of the carbon material band gap. Actually, first principles studies show that quantum capacitance of N-doped graphene can be enhanced proportionally with some nitrogen functionalities [70,84,94]. As depicted in **Figure 2-11**, the graphitic nitrogen (N_Q) and pyridinic nitrogen (N_6) alters the density of states (DOS) of the graphene layer with a consequently enhance of quantum capacitance [94] . Meanwhile, pyrrolic nitrogen does not have influence on the electric properties of graphene.

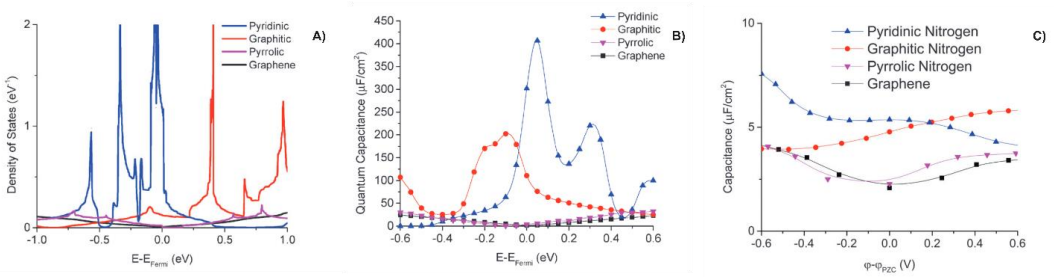

Figure 2-11 A) Density of states, DOS; B) Quantum capacitance, and C) total volumetric capacitance for a mole fraction of each nitrogen functionalities in a graphene layer, modeled from DFT calculations and CMD simulations using 1.0 NaCl as electrolyte in a graphene wall of 5 nm, obtained from [94].

On the other hand, boron has one less electron than carbon and a smaller atomic radius, thereby its expected p-type doping. Although, in the same way as nitrogen, this relies on the bonding configuration of boron. While boron is doped into the carbon matrix, the π electrons are redistributed which softens the C−C bonds and strengthens the C−O bonds upon oxygen adsorption [95].

There is three possibles configurations of boron into the carbon matrix, which are: BC_3, BC_2O, and BCO_2 as illustrated in **Figure 2-9 C**. BC_3 has an important role on the electric modifications of the carbon framework. This configuration can be found in the carbon lattice and its three valence electrons are bounded each one to a single carbon atom. Therefore, the fermi level shift toward the valence band and result in higher charge carrier concentration and density of states at the Fermi level, collectively enhancing the conductivity and the electrons acceptance of the carbon framework [84], among other properties. The BC_2O is founded on the edge of the carbon lattice and can enhance the electrochemical storage through both electrical conductivity and faradaic contributions, while it has been proposed that BCO_2, also founded on the edge of the carbon lattice, only contributes through faradaic contributions due to their localized charge [96]. The reactive B−O groups make the surface hydrophilic and lead to the higher electrochemically active surface area, although the measured surface area is found to be lower in B-doped carbon structures than in its pristine counterpart [97]. Significantly, the incorporation of boron into the carbon matrix results in an increased oxygen content, primarily attributed to the prevalence of BC_2O and BCO_2 functionalities, which stand out as the most abundant boron functionalities observed on carbon materials [14,96,98,99].

It is postulated that the faradaic contributions arising from redox reactions involving these functionalities are achieved by the oxygen in both acidic and alkaline electrolytes. Consequently, the enhanced electrochemical performance of B-doped carbon materials can be attributed to the faradaic contributions facilitated by the oxygen functionalities, as well as the improved electric double-layer (EDL) capacitance resulting from B-substitution into the carbon framework.

As summary, the surface chemistry modifications allow enhance the electric properties of carbon materials, significantly influencing their electrochemical performance. Through deliberate doping of oxygen, nitrogen, and boron onto the carbon surface, these modifications induce noteworthy alterations in the material's charge storage and transport characteristics, where the heteroatom’s synergetic effect depends on the relative location of the heteroatoms rather than their concentration.

2.3 Tannins as carbon precursor

The origin of the word “tannins” can be traced back to the properties of a wide range of natural organic substances used to tan animal skins to make leather. From ancient times, the term was used indistinctly but with the advances of analytical techniques in the twentieth century the vail of tannins was revealed [100]. Nowadays, tannins are defined as polyphenolic secondary metabolites of higher plants, that can be found in the bark or leaves of plants as well as in fruit and seeds, being their main role to protect the unit from external damages, i.e., UV-light, insects, herbivores, or bacterial and fungal infections [16,101]. Commonly, tannins are classified according their structural characteristic and chemical properties in four categories (**Figure 2-12**): (i) gallotannins, (ii) ellagitannins, (iii) complex tannins, (iv) and condensed tannins [100].

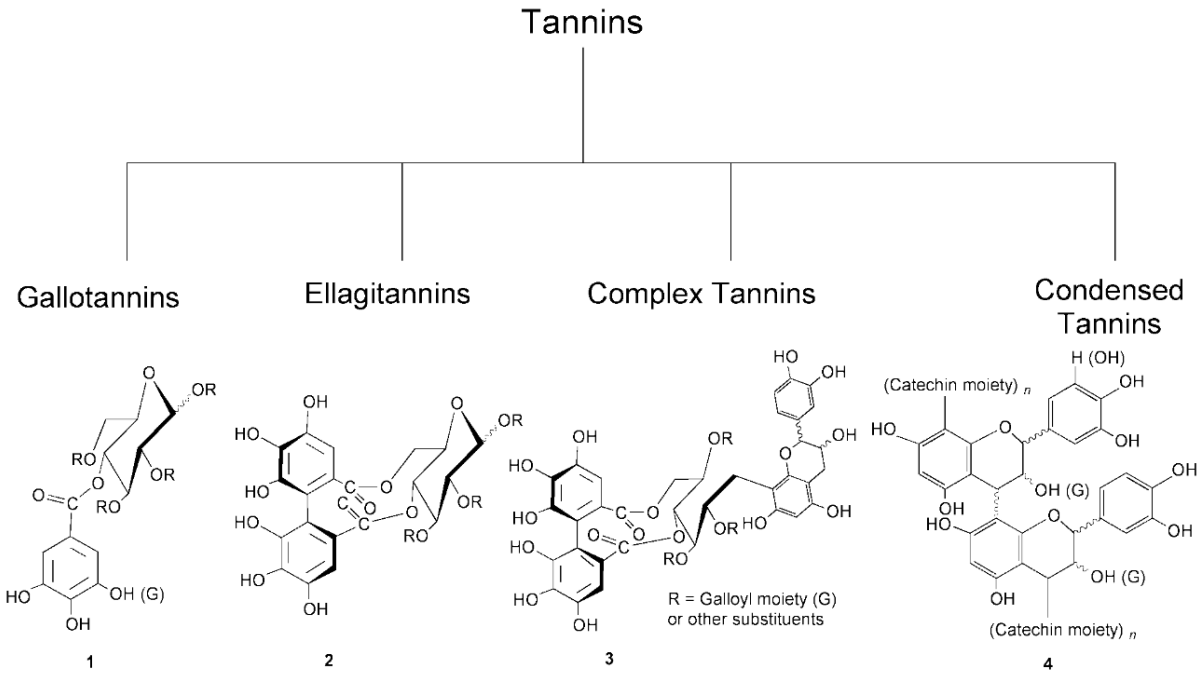

Figure 2-12 Tannins classification according their structural characteristics, obtained from [100].

Generally, gallotannins, ellagitannins and complex tannins are hydrolysable tannins, which are of great interest in the leather industry, and resins field for eco-friendly adhesives [74]. However, they have a limited interest related to carbon materials because of their limited crosslinking properties and low carbon yield after carbonization [16]. Conversely, condensed tannins are easily crosslinked and even they are able to auto-condense in the presence of some catalyst [102]. Additionally, they maintain their original structure and morphology when submitted to pyrolysis, and they can have relative high carbon yields (around 50 wt. %). However, due to their aromatic nature, the carbonization of tannins leads to a non-graphitizable carbon, commonly called glassy carbon.

Condensed tannins are extracted mainly from tree bark such as quebracho, mimosa or pine [16], and they have been used to obtain a wide range variety of high added-value materials. Usually, the synthesis of porous materials using tannins involves some aldehyde to perform the crosslinking and to obtain a resin-like materials [17,19,74], in a similar way that phenol-formaldehyde resins. From here, depending on the kind of crosslinking synthesis used is possible to obtain multiples kind of foams [19,103,104] or gels [105,106]. Moreover, tannins have the ability to perform auto condensation reactions, which enable their polymerization without the addition of a crosslinker [107,108].

Another remarkable feature of condensed tannins is given by their phenolic nature that allows them good chemical reactivity. They have a strong ability to complex transitions metals [109,110] , that have been used to prepare metal-carbon hybrids materials. They can be easily prepared by submitting tannins to hydrothermal conditions into an aqueous solution of the proper salt, followed by a carbonization of the resultant material. Actually, the evidence suggests that is possible to obtain different kinds of metal-carbon hybrids materials depending on the metal-salt used in tannins. For instance, the work of Braghiroli et al. [110] shows that is possible use tannins as precursor to obtain different kind of metal-carbon porous materials using V, Cr, Ni and Fe salts. In the case of V and Cr salts, the carbonization leads to nanoparticles, while for Ni and Fe salts leads to hollow microspheres. In particular, for Fe-tannins derived carbon material, it was found that after carbonization the iron exist as magnetite (Fe_2O_3), and, in a less proportion, as element (Fe). Additionally, the presence of iron induced the partial graphitization of carbon. Similar works are found related to dope tannins with other elements, specifically, nitrogen [68], which was added in a similar way into the tannins matrix by hydrothermal carbonization, using in this case, an aqueous solution of ammonia. It was found that nitrogen content reach values between 3-6 wt.% after pyrolysis, depending on the synthesis conditions, and as it was discussed in the previous section, there is nitrogen functionalities would improve the electrochemical performance of carbon materials.

Although tannins have been researched as precursors for carbon materials for many years, there has not been so much work related to their use in energy-related fields. Actually, the work made by Amaral-Labat et al. [111], published in 2012, was one of the first published research on this matter, in which carbon cryogels obtained from freeze-drying and pyrolysis of tannins-formaldehyde organic gels were characterized for their use in electrochemical capacitors. Another work made by Braghiroli et al. [112], published in 2015, explored the use of tannins doped with nitrogen through different hydrothermal carbonization synthesis, in a similar way that their earlier work published in 2012 [68] mentioned previously, just that in this case, the carbon materials were characterized in terms of their performance for their use as electrodes in electrochemical capacitors.

Previous to the begin of this research, just a few articles were devoted to the use of tannins as carbon precursor for energy-related field such as batteries [113], electrochemical capacitors [114–116], fuel cells [117], and even electrochemical sensors [118], according to the survey performed on the search engine Scopus. Since that, a few interesting paths have been explored related to tannins as carbon materials precursor for electrochemical-related devices, which are summarizes in the review of Castro-Gutierrez et al. [17]. For instance, a prominent research line is the use of ordered and disordered mesoporous carbon synthesized from tannins as carbon material to investigate the relevance of pore connectivity in the limitations of ion transport and power density on electrochemical capacitors [15,119], as illustrated in the **Figure 2-13**. In these studies published in 2019 [15] and 2021 [119], the carbon materials were synthesized using water-assisted mechano-synthesis, where the disordered mesoporous carbons (DMCs) were obtained mixing tannins, water and a surfactant (Pluronic F127®) in a weight ratio of 1:1:1, respectively. Meanwhile, the ordered mesoporous carbons (OMCs) were obtained by just changing the weight ratio at 2:0.75:1.75, respectively. The mixtures were submitted into a planetary milling machine filled with agate balls. Then, the material obtained was directly submitted to carbonization at 900 °C by 1 h, and subsequently activated under CO_2 flow at the same temperature but varying the time of the activation.

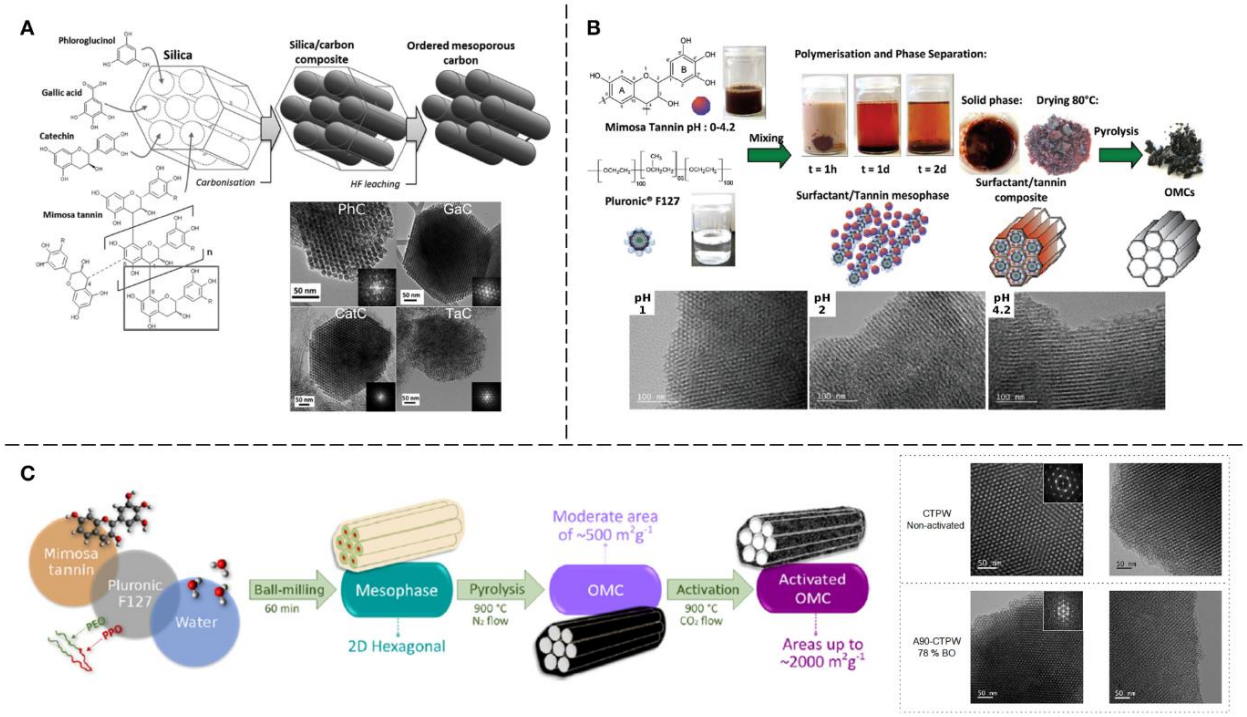

Figure 2-13 Synthesis of OMCs from tannins by: (A) hard-templating carried out using other biomass-derived phenolic molecules, and B) soft-templating trough phase separation, and C) mechanosyntesis using a surfactant, obtained from [17].

Both materials have a similar surface area development according to the burn-off evolution, and also similar surface chemistry, being their main difference the mesoporous structure. The electrochemical cells were tested in aqueous (H_2SO_4) and organic electrolytes ($TEABF_4$/ACN). Counterintuitive, the ordered structure improves the diffusion in aqueous electrolytes with small size ions, while the disordered structure enhances the diffusion on large size ions with an improvement on the electrochemical performance of the organic electrolyte. These differences are boosted when they are tested at high-power conditions. On the same line, tannins-derived OMCs were used to investigate the activation regime influence over their electrochemical performance, which main results were published in 2022 by Castro-Gutierrez et al. [120]. In this study, the CO_2 activated OMCs were compared with KOH activated OMCs, where a wide range of KOH:OMCs ratio was explored to cover a proper range of surface area and porosity development to compare the results with the CO_2 activated OMCs. One of the main differences is the higher apparent water affinity of the samples activated with CO_2 compared to those activated with KOH. The above could be related to the heterogeneities in surface chemistry evolution of the samples, such as the presence of different kind of functional groups in the neighborhood of active sites and their relative position on the same or in opposite pore walls. Additionally, according to the hysteresis loops scanning analysis of the N_2 adsorption-desorption isotherms, the KOH-OMCs materials exhibit low pore connectivity, which can hinder the water access to the active sites into the pores. As a result of these differences, the KOH activated samples showed a high capacitance at low current density (49 F g^{-1} at 0.5 A g^{-1}). However, as the current density increases there is a significant decay in capacitance associated with diffusion limitations, with a capacitance retention below 20% at 40 A g^{-1}. In contrast, although the CO_2 activated samples showed lower values of capacitance (close to 37 F g^{-1} at 0.5 A g^{-1}), the values remain almost constant even at high current densities. It is important to note, that this research was a derivative work of some results addressed in this doctoral research and exposed in the **section 5.1**, where microporous chemical activated carbon materials derived from tannins were tested as electrodes in electrochemical capacitors [121].

As exposed briefly in this section, tannins have proven to be an excellent precursor material for the elaboration of tailored carbon materials, not only for the classical uses of carbon materials, such as adsorbents, but also for high-value added uses, such as energy-related applications. The advantages of tannins over other materials rely mainly on their ability to auto-condensate to build high blocks of a homogeneous polymer and their phenolic nature, which gives them a good chemical reactivity that allows the formation of complexes with metals or doping with molecules, functionalities, or heteroatoms, which can be used to modify the electrochemical properties of the carbon materials.

2.4 Electrochemical characterization

2.4.1. Potentiostatic methods: Cyclic voltammetry

Cyclic voltammetry (CV) has become a very popular technique for initial electrochemical studies of new systems and has proven to be very useful in obtaining information about complicated electrode reactions. The CV refers to sweeping the potential with time and recording the potential-current curve. Usually, the potential varies linearly with time at a specific sweep rate that depend on the electrochemical cell studied. In the case of electrochemical capacitors, the sweep rates used ranging from 1 mV s^{-1} to 2 V s^{-1} [122]. An ideal capacitor would exhibit a rectangular curve when current is plotted as a function of the potential window, as observed in **Figure 2-14 A**. During charging, the sharp increase in current at the beginning of the cycle is due to the rapid formation of the electric double layer (EDL) and it remains constant as the potential window increases because no Faradaic reaction occurs. Given the reversible nature of the EDL formation mechanism, the CV curve during discharge obtained when potential window decreases is the exact inverse of the charging curve. Evidently, the CV curves of the real electrochemical capacitors deviate from the ideal one, and those that present pseudocapacitance performance, also display peaks that are attributed to the reversible response a redox pair immobilized on the electrode surface, as shown in **Figure 2-14 B**. On the other side, battery-like electrodes show remarkable peaks as depicted in **Figure 2-14 C**. Once a material electrode has been decided based on their profile, then becomes pertinent to use the correct techniques and formulas for evaluating and reporting the electrochemical performance, as exposed in multiples publications [20,123,124]. For further details related the fundaments of CV please refer [123,125].

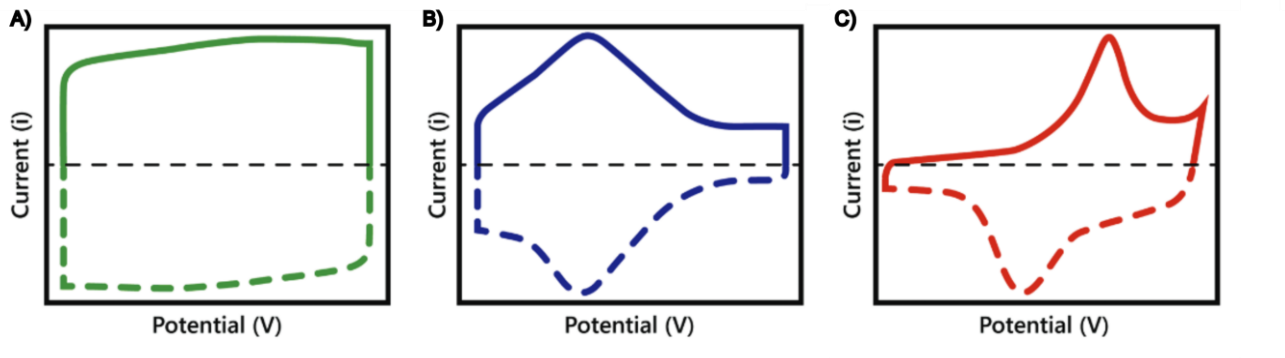

Figure 2-14 Archetypal cyclic voltammogram behavior of the three main types of electrodes A) electrical double layer, B) pseudocapacitive-type, and C) battery, obtained from [20].

In this research, the CV curve obtained at different sweep rates was utilized to differentiate the electric double layer from faradaic contributions, commonly named pseudocapacitance contributions. This was performed using the Trassatti's method [126]. On this methodology it is assumed that the charge (q) on the voltametric assay has the following dependences to the scan rate (υ):

$$\boldsymbol{q = q_{\infty} + a_1 \upsilon^{-1/2}} \qquad \textbf{Eq. 2-18}$$

$$\boldsymbol{\frac{1}{q} = \frac{1}{q_T} + a_2 \upsilon^{1/2}} \qquad \textbf{Eq. 2-19}$$

where a_1 and a_2 are constants, $\boldsymbol{q_{\infty}}$ is the non-limited by ion diffusion charge ($\upsilon \to \infty$) and $\boldsymbol{q_T}$ is the total charge of the cell ($\upsilon \to 0$). If the measurements are made under the same conditions, they can be applied in capacitance terms as follows:

$$\boldsymbol{C_{(\upsilon)} = a_1 \upsilon^{-1/2} + C_{EDL}} \qquad \textbf{Eq. 2-20}$$

$$\boldsymbol{\frac{1}{C_{(\upsilon)}} = a_2 \upsilon^{1/2} + \frac{1}{C_T}} \qquad \textbf{Eq. 2-21}$$

where C_T is assumed to be the total capacitance and C_{EDL} is the capacitance that arises from the electric double layer (non-limited by ion diffusion). Additionally, it is assumed that the total capacitance is given by:

$$C_T = C_{PsC} + C_{EDL} \qquad \textbf{Eq. 2-22}$$

where C_{PsC} is the capacitance that arises from faradaic contributions. To illustrate the values obtained from this method, the **Figure 2-15** depicts the anticipated linear regression for the fitted data, where the intercept with the y-axis indicates the C_{EDL} value and the inverse of C_T for each graph, respectively.

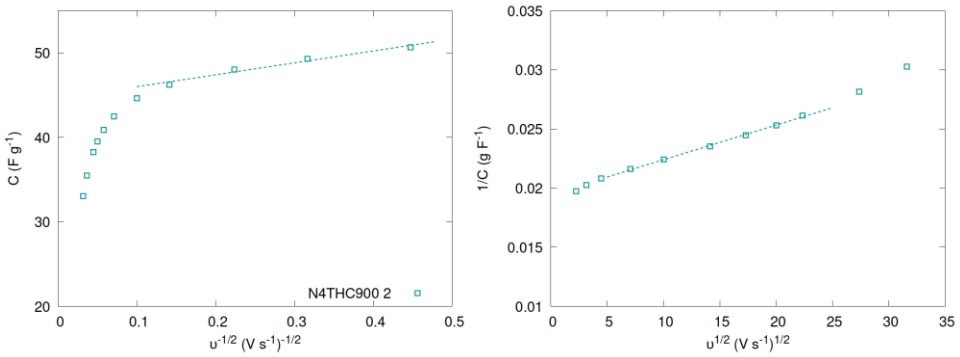

Figure 2-15 Dependence of capacitance as a function of the scan rate to differentiate pseudocapacitance (C_{PsC}) and double-layer capacitance (C_{EDL}) according to Trassatti's method.

2.4.2. Galvanostatic methods: Galvanostatic charge-discharge

The galvanostatic charge-discharge (GCD) technique is a fundamental method employed in electrochemical studies to analyze the energy storage properties of various energy storage devices, including electrochemical capacitors, pseudo-capacitors, and batteries. This technique involves applying a constant current to the device, either during the charging or discharging phase, and monitoring the resulting voltage changes over time. According to energy storage mechanism, an important difference between capacitor and battery is that the charge and discharge voltage of an electrochemical capacitor always linearly increases and decreases, respectively with the time due to their surface-controlled charge storage nature. In contrast, an ideal battery normally has a constant voltage during discharge or charge process due to its phase transformation process. Galvanostatic charge-discharge results can directly represent the capacitive and battery behavior, respectively. GCD is the most widely used technique to reliably evaluate the performance of ECs and batteries while clearly distinguishing one from another. Typical discharge curves in **Figure 2-16** show that both electric double layer capacitance systems (red line) and pseudocapacitance systems (black line) have a linear relation of voltage versus discharge time at a constant discharge current as discussed above but the former possesses a sharper slope than the latter due to its smaller capacitance and shorter discharge time. The capacitance is a constant value in an ideal capacitor, indicating a potential-independent capacitance. Nevertheless, a typical discharge curve of a battery presents distinct characteristics (blue line), which displays a prominent voltage plateau with different polarization zones as marked. This characteristic S-shaped curve resulting from phase transition followed by a sharp voltage drop by concentration polarization for batteries can be used to distinguish itself from other systems. Moreover, for capacitors, the charge and discharge curves at the same current should have a mirror or symmetric manner, which means a small voltage hysteresis. From this analysis, the capacitance, energy density and power density, and leakage/self-discharge rate values obtained are well acceptable as the most reliable and standard results for ECs and batteries [5,20].

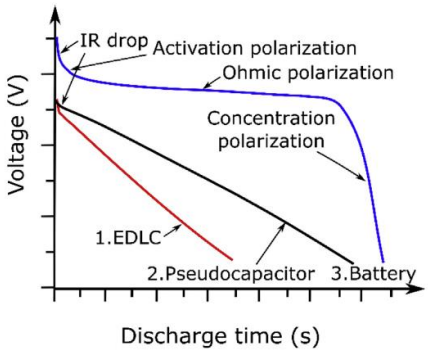

Figure 2-16 Typical GCD discharge curve for EDLC (red line), pseudocapacitor (black line), and battery (blue line), obtained from [5].

2.4.3. Electrochemical impedance spectroscopy

Impedance ($\boldsymbol{Z}$), refers to the amount of the opposition to current flow ($\boldsymbol{I}$) that takes place under an applied voltage ($\boldsymbol{E}$) within an electrical circuit, as described in **Eq. 2-23**. It is impacted by the nature of the electrolyte, as well as the electrolyte-electrode interface, and morphology or composition of the electrode materials.

$$\boldsymbol{Z = E/I} \qquad \textbf{Eq. 2-23}$$

The electrochemical impedance spectroscopy (EIS) response arises from the sinusoidal applied voltage, according to **Eq. 2-24**, where $\boldsymbol{\omega}$ is the angular frequency ($\boldsymbol{\omega = 2\pi f}$), applied while controlling its frequency ($\boldsymbol{f}$, in Hz).

$$\boldsymbol{E(t) = E_{app} + |E_0| \sin(\omega t)} \qquad \textbf{Eq. 2-24}$$

The current response follow the Butler-Volmer model described in **Eq. 2-25**, where $\boldsymbol{\alpha}$ is the transfer coefficient for electron exchange, $\boldsymbol{\eta}$ is the overpotential from the equilibrium potential ($\boldsymbol{E(t) - E_q}$), $\boldsymbol{n}$ is the number of electrons transferred, $\boldsymbol{T}$ is the temperature in Kelvin, $\boldsymbol{F}$ is the Faraday constant, and $\boldsymbol{R}$ is the gas constant. Additionally, the current correlates to the frequency of the applied current ($\boldsymbol{I_0}$), as described in **Eq. 2-26**, but with a phase shift ($\boldsymbol{\phi}$), which magnitude depends on the specific circuit elements. In order to obtain reliable results, the applied frequency should cover a wide range, typically from 1 mHz to 100 kHz [127].

$$\boldsymbol{I = I_0(e^{\frac{-\alpha nF}{RT}\eta} - e^{\frac{(1-\alpha)nF}{RT}\eta})} \qquad \textbf{Eq. 2-25}$$

$$\boldsymbol{I(t) = I_0 \sin(\omega\, t + \phi)} \qquad \textbf{Eq. 2-26}$$

In general, given the sinusoidal nature of the experiment, the impedance contains a real, and an imaginary part, as described in **Eq. 2-27**, and the phase angle can be obtained from **Eq. 2-28**. At this point, is fair to say that impedance is a kind of generalized resistance, and the phase angle expresses the balance between capacitive and resistive components in the circuit. For instance, a pure resistance is given by $\phi = 0$, and a pure capacitance is given by $\phi = \pi/2$, and for mixtures, intermediate phase angles are observed [128].

$$\boldsymbol{Z(\omega) = Z_R + Z_i = |Z|(\cos\phi + j\sin(\phi))} \qquad \textbf{Eq. 2-27}$$

$$\boldsymbol{\tan\phi = \frac{Z_i}{Z_R}} \qquad \textbf{Eq. 2-28}$$

The variation of the impedance with frequency can be displayed in different ways. A useful way to represent the data is using the Bode plot, where $\boldsymbol{log|Z|}$ or $\boldsymbol{\phi}$ are both plotted against $\boldsymbol{log(\omega)}$. However, the most useful and used representation is the Nyquist plot, due to one can estimate the nature and behavior of the system on a qualitative, and simple way [122,127–129]. The Nyquist plot is formed by the real part of the impedance (Z_r or Z') on the abscissa axis, and the negative value of the imaginary part (Z_i or Z'') on the ordinate axis, an illustrative example with the main regions and parameters estimation can be appreciated in the **Figure 2-17**. At low values of impedance (high frequencies), the electric circuit is limited by diffusion. Thus, only charge transfer process remains and the impedance could be described by:

$$\left(Z_r - R_s - \frac{R_{CT}}{2}\right)^2 + Z_i^2 = \left(\frac{R_{CT}}{2}\right)^2 \qquad \textbf{Eq. 2-29}$$

Hence, Z_r vs Z_i should give a circular plot centered at $Z_r = R_s + R_{CT}/2$, and $Z_i = 0$, having a radius of $R_{CT}/2$, where R_S represent the electrolyte resistance and R_{CT} is the resistance to the charge transfer, where small semicircles represent kinetic fast charge transfer for the electrode material. Commonly, one semicircle is observed in the Nyquist plot, but could also be two or even three semicircles at low frequencies, indicating multiple independent resistances. For instance, a second arc can take place from adsorption/desorption of ions at the electrode-electrolyte interface [130]. In the middle frequencies, there is a second region where diffusion of charge and mass transfer at the electrode-electrolyte interface begins to dominate. At this point, a characteristic line with a 45° angle appears, known as the Warburg region. The frequency range of the Warburg region depends on the materials under study, and deviations from the ideal case can be found. When the linear line with 45° extends at lower frequencies, it is called semi-infinite Warburg impedance, revealing battery behavior. Conversely, Nyquist plot can also depict finite space Warburg impedance, which means a slope that tends to infinite runs parallel to $-Z_i$, and is defined as pure capacitance behavior.

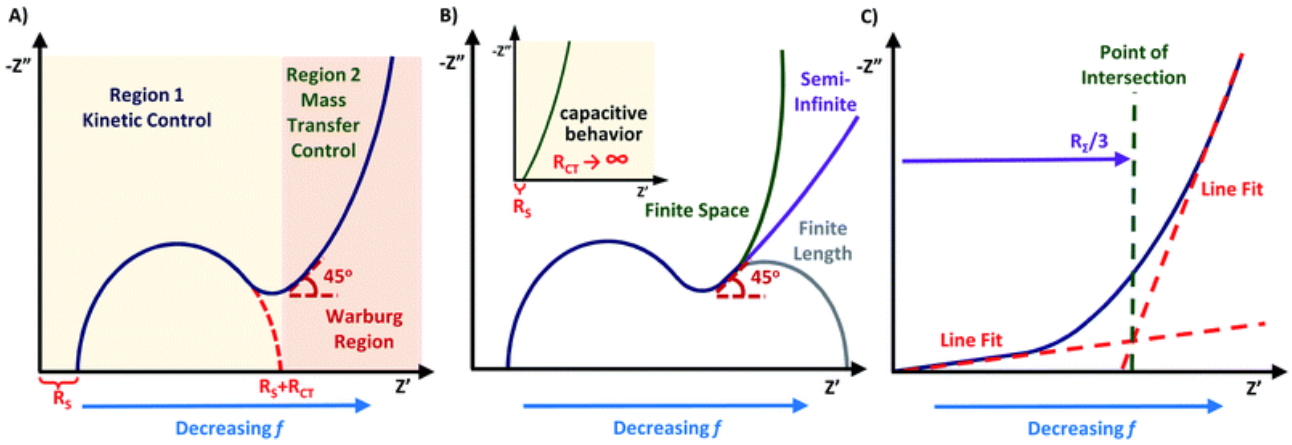

Figure 2-17 Nyquist plot with key regions labelled and estimation of the main parameters.

3 HYPOTHESIS AND OBJECTIVES

3.1 Hypothesis

Based on the comprehensive analysis of the state of art, this doctoral research proposes that is viable to manipulate both the porous texture and surface chemistry of carbon materials derived from tannins, and to elucidate how these properties impact the electrochemical performance of the obtained carbon materials when used in electrochemical capacitors. Specifically, it is possible to alter the surface chemistry through the doping of heteroatoms, such as nitrogen and boron, into the oxygen-carbon matrix of tannins and subsequently enhancing the surface area through chemical or physical activation.

3.2 Main objective

The main objective of this doctoral research is to investigate the feasibility of manipulating the surface chemistry of the oxygen-carbon matrix of tannins through the introduction of heteroatoms, such as nitrogen or boron, and to control the surface area through activation to understand how both surface chemistry and porous texture alter the electrochemical performance of the obtained tannins-derived carbon materials when used in electrochemical capacitors.

3.3 Specific objectives

1. To explore chemical and physical activation to enhance the surface area of tannins-derived carbon materials.
2. To evaluate the introduction of heteroatoms, specifically nitrogen and boron, into the oxygen-carbon matrix of tannins through hydrothermal carbonization using controlled concentrations of boric acid and aqueous ammonia solutions.
3. To elucidate the textural, morphological and chemical surface properties of the so-obtained carbon materials derived from tannins.
4. To evaluate the impact of modified surface chemistry and increased surface area on the electrochemical performance of the carbon materials when utilized in electrochemical capacitors.

4 METHODOLOGY

Based on the proposed objectives, this study aims to explore through experimental assays the role of pore development and surface chemistry by heteroatom doping in tannin-derived carbon materials using the work diagram flow illustrated in **Figure 4-1**. In this context, the synthesis of carbon materials through activation process will be done as follows. Firstly, tannins-derived carbon materials will be submitted to flash pyrolysis to remove the volatile fraction, then chemically activated with KOH at different ratios to understand the pore development and their influence on electrochemical performance. Secondly, to introduce the controlled presence of heteroatoms in the carbon matrix, the hydrothermal step will be used in the synthesis of carbon materials where controlled concentrations of boric acid and aqueous ammonia will be used as source of boron and nitrogen, respectively. Subsequently, the pore development of the so-obtained carbon materials will be done by physical activation using CO_2 as activating agent at different conditions to obtain a wide range of burn-off and pore development. The synthesized carbon materials will be characterized in order to quantify their physical and chemical properties (surface area, chemical structure, among others) and relate these to their electrochemical behavior (cyclability, capacitance, equivalent series resistance) to estimate the role of doping in the electrochemical performance of tannins-derived carbon materials.

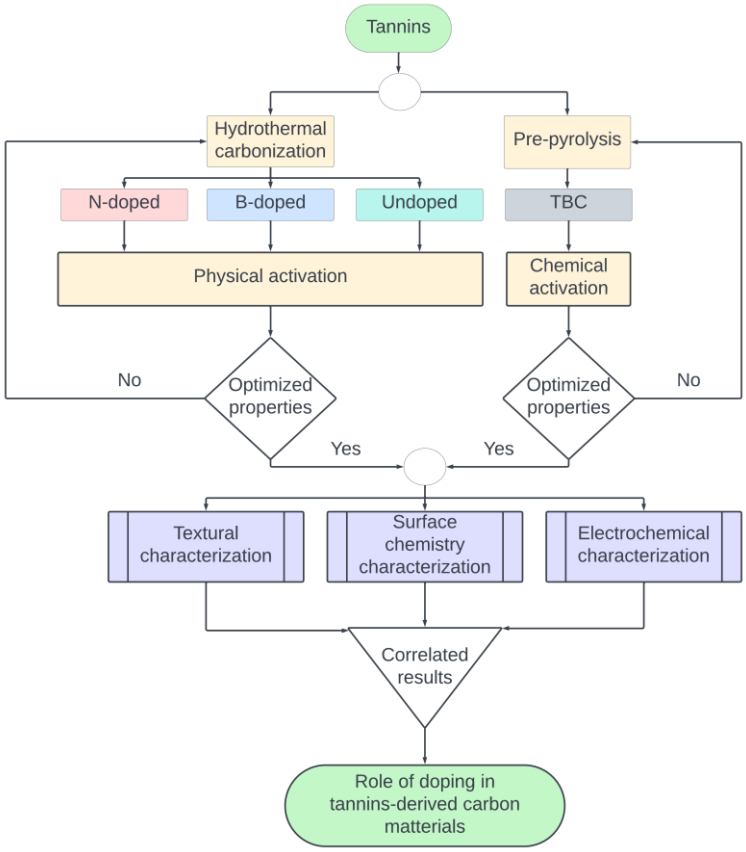

Figure 4-1 Workflow diagram of the present scientific research.

4.1 Carbon materials synthesis

4.1.1 Oxygen functionalized tannins-derived carbon materials synthetized through chemical activation.

Tannins were submitted to fast pyrolysis using a fluidized bed bench-scale reactor as is described in Moore et al. [131]. Tannins were dosed through a screw feeder and then pneumatically transported into the reactor using a nitrogen flow rate of 6 mL min^{-1}. Quartz sand (30-50 mesh) was used as fluidized bed material. Nitrogen was used as a gas carrier with a flow rate of 9 mL min^{-1}. The hot gas filter was kept at 400°C, and the temperature range studied in the reactor was bounded between 400 °C and 600 °C. The residence time of vapors varied between 1.0 and 2.6 s, depending on the reactor temperature. The pyrolysis products retained in the reactor and hot gas filter were collected, weighed, and kept separately for further analysis. Gravimetric mass balance (XB 3200C, Precisa) was established based on biochar collected from both reactor and hot-gas filter. According to the results obtained in the study of Pinto et al. [132], the carbon materials obtained at 550 °C was used as precursor to chemical activation, and labelled as TBC. Prior to activation, the TBC samples were crushed and sieved to a roughly unimodal distribution of particles sizes. The proximate analysis of TBC, including moisture determination by heating at 100°C for 2h, ash estimation by heating at 550°C for 14 h, and volatiles by heating at 850°C for 7 min, was performed.

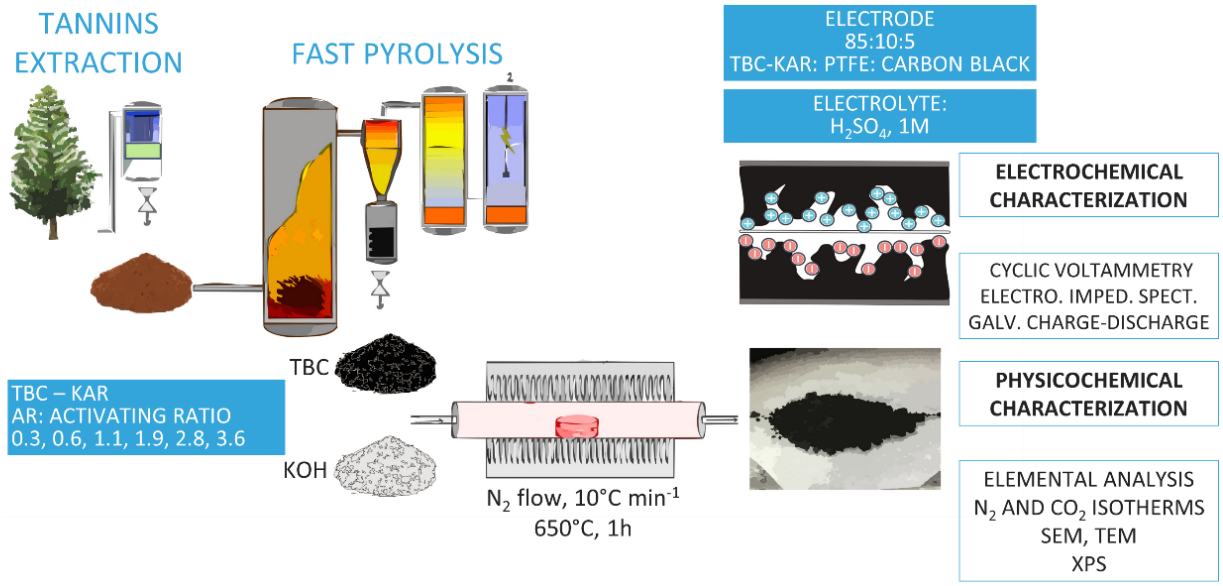

Figure 4-2 Schematic representation for the synthesis of oxygen functionalized tannins-derived carbon materials obtained through pre-pyrolysis and chemical activation.

In a typical synthesis, 1 g of TBC was mechanically mixed with KOH granules (Merck > 85 % purity) by grinding in a mortar until a homogeneous particle size was observed, then put in a mullite sample holder and subjected to a thermal treatment at 650 °C for 1 h, under a flow of 100 mL min^{-1} of N_2, using a heating rate of 10°C min^{-1} in using a Nabertherm R 50/125.

The ACs were labelled as TBC-KAR, where AR is the activating ratio on a weight basis defined as the mass of KOH per gram of TBC. The ratio of KOH:TBC used were 0.3, 0.6, 1.1, 1.9, 2.8, and 3.6, and a sample was subjected to the same thermal treatment in the absence of activating agent, labelled as TBC-K0.

4.1.2 Surface chemistry modification through nitrogen or boron doping.

Tannins were submitted to hydrothermal carbonization (HTC) as illustrated in Figure 4-3. In a typical synthesis, 1 g tannin was added to 9 mL of the corresponding solution according to shown in **Table 4-1** for boron doped tannins and **Table 4-2** for nitrogen doped tannins (for details refer to **section 8.3**, **Appendix C**). These values correspond to 4 and 8 mmol of the doped element per gram of tannin. The solution was stirred for at least 15 min at room temperature, and then submitted to HTC at 190°C for 18 h. For the sake of comparison, tannins-derived hydrochars were also synthesized using distillate water. These materials were labelled as B4THC, B8THC, N4THC, N8THC, and THC, respectively. The hydrochars so-obtained were filtered to separate the solid from the liquid phase, washed with distilled water, and dried under vacuum (80 °C, overnight). This procedure was repeated multiples times to obtain enough material to perform the post-treatments. The hydrochars were ground using an agate mortar until obtain a fine, and homogeneous powder, and sieved to determine their particle size distribution (**Figure 8-1** on Appendix section).

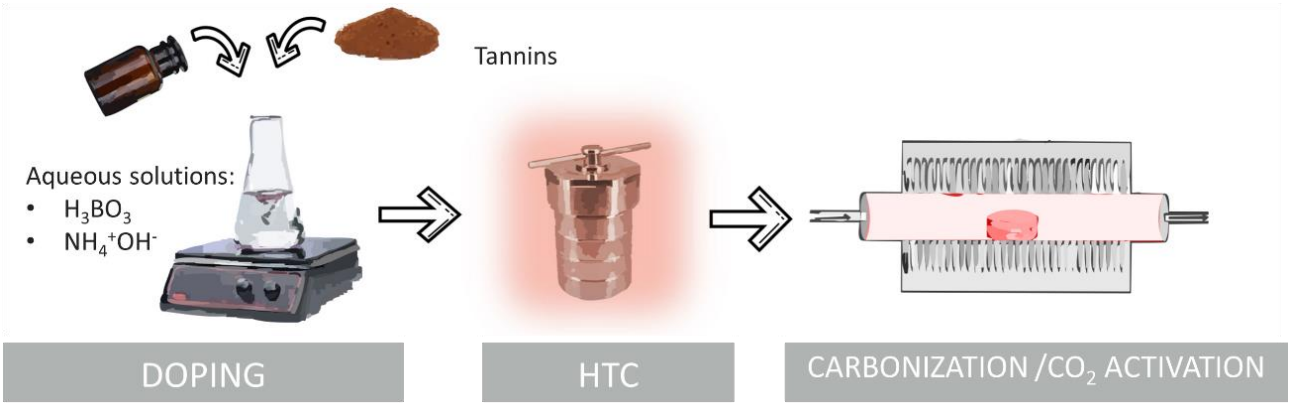

Figure 4-3 Schematic for the doped carbon materials synthesis using hydrothermal carbonization and posteriorly carbonization and CO_2 activation.

Table 4-1 Tannins and boron quantities used on the synthesis of B-doped tannins through hydrothermal carbonization.

Code	Tannins (g)	Water (mL)	Reagent	Reagent (g)	Conc. (wt.%)	Boron (g)	Boron (mmol)
B8THC	1	9	H_3BO_3	0.500	5.5	0.0874	8.086
B4THC	1	9	H_3BO_3	0.250	2.8	0.044	4.043

Then, 2 g of material were put in a mullite sample holder and submitted to pyrolysis in a Nabertherm R 50/250/12 tube furnace using a heating rate of 10°C min^{-1} from ambient temperature until reach 800 °C, which was kept by 1 h, then leave it to nature cooldown until get under 100 °C. Throughout all the procedure was used a N_2 flow of 100 mL min^{-1}. The materials were weighted before and after each pyrolysis essay in order to quantify the burn-off (BO) and assure the repeatability of those.

Finally, the carbon materials obtained from the pyrolysis step were submitted to CO_2 activation, employing a flow rate of 50 mL min^{-1}, a heating rate of 10 °C min^{-1}, ascending from ambient temperature to 800°C. The activation process was conducted for varying reaction time including 1, 2 and 4 hours, resulting in a diverse spectrum of burn-off, determined through weight measurements as previously outlined. Notably, for N4THC and N8THC, additional conditions were explored, involving a final temperature of 900°C, maintained for 1, 1.5, and 2 hours. These specific conditions aimed to further tailor the textural properties and surface characteristics of the materials, contributing to a comprehensive understanding of their electrochemical performance. The temperature and time parameters used on the pyrolysis or CO_2 activation step were added to the aforementioned labels. For instance, N8THC800 is the AC obtained from the pyrolysis step (so called non-activated), and N8THC800-2 is the AC obtained from N8THC after pyrolysis at 800 °C and further CO_2 activation at 800°C for 2 hours.

Table 4-2 Tannins and nitrogen quantities used on the synthesis of N-doped tannins through hydrothermal carbonization.

Code	Tannins (g)	Water (mL)	Reagent [a]	Reagent (mL)	$NH_4^+OH^-$ (g)	Nitrogen (g)	Nitrogen (mmol)
N8THC	1	7.70	$NH_4^+OH^-$	1.30	0.285	0.114	8.12
N4THC	1	8.35	$NH_4^+OH^-$	0.65	0.143	0.057	4.06

[a] The reagent concentration is 26.2 wt. %

4.2 Physicochemical characterization

The thermal decomposition of the materials was analyzed using a Netzsch 409 PC thermogravimetric apparatus. Approximately 50 mg of each sample was heated at a rate of 5 °C min^{-1} from 20 °C to 800 °C under a flow of helium (50 mL min^{-1}).

The textural properties of the materials were obtained from N_2 and H_2 adsorption-desorption isotherms at 77 K, and CO_2 adsorption-desorption isotherms at 273 K, acquired using a 3Flex equipment (Micromeritics). The Brunauer-Emmet-Teller (BET) surface area (A_{BET}) was obtained from the nitrogen adsorption isotherms following the IUPAC recommendations [133]. The total volume of pores ($V_{0.97}$, Gurvich volume) was determined at a relative pressure (P/P°) of 0.97. The non-local density functional theory kernel for heterogenous surface (NLDFT-HS) with a λ = 3.2 was applied to N_2+H_2 adsorption isotherms to estimate the pore size distribution (PSD), from which specific surface area (SSA), total pore volume (V_T), ultra-micropore volume ($V_{u\mu}$, pore diameter below 0.7 nm), supermicropore volume ($V_{s\mu}$, pore diameter between 0.7 and 2 nm), micropore volume ($V_\mu = V_{u\mu} + V_{s\mu}$) and mesopore volume ($V_{meso} = V_T - V_\mu$) were calculated. The choice of N_2+H_2 adsorption isotherms instead of N_2+CO_2 adsorption isotherms was made to extend the lower limit value on the PSD and to prevent potential specific interactions between CO_2 and the N-functional groups that could lead to misleading textural characterization [134,135]. The average pore width ($\langle w \rangle$) for each range was calculated by **Eq. 4-1**.

$$\langle \boldsymbol{w} \rangle = \frac{\sum_i \frac{\boldsymbol{dV}}{\boldsymbol{dw_i}} \boldsymbol{w_i} \Delta \boldsymbol{w_i}}{\sum_i \frac{\boldsymbol{dV}}{\boldsymbol{dw_i}} \Delta \boldsymbol{w_i}} \qquad \textbf{Eq. 4-1}$$

The surface chemistry and nature of carbon, oxygen, nitrogen, and boron functional groups were analyzed by X-ray photoelectron spectroscopy (XPS) using an ESCAPlus OMICRON system equipped with a non-monochromatized MgKα X-ray source (1253.6 eV), for both survey and high-resolution analysis. The survey was performed in a range from 0 to 1000 eV with an step size of 0.5 eV, dwell time of 0.2 s, and an energy step of 50 eV. The high-resolution areas was analyzed using a step size of 0.1 eV, dwell time of 0.1 s, and energy step of 20 eV. The C 1s, O 1s, N 1s, and B 1s spectrum regions were deconvoluted by assigning peaks based on Smith et al. [136], Ayiania et al. [137] for undoped and N-doped carbon materials. Meanwhile, B-doped carbon materials XPS peaks assignments were made according to Smith et al. [136], Szymanski et al. [14] and Wang et al [138]. . The deconvoluted area were optimized fitting Gaussian-Lorentzian (20:80 G:L) curves with FWMH between 1.1 and 1.3 for the main peaks, and FWMH close to 2 for the less significant curves. Elemental analysis (C, N, H, and O) was carried out using a Vario EL Cube elemental analyzer.

4.3 Electrochemical characterization

The electrochemical characterization of the ACs as electrodes for ECs was conducted using a Biologic VMP3 workstation and a symmetrical two-electrode configuration in a Swagelok cell as illustrates **Figure 4-4**. The electrode preparation involved a weight ratio of 85:10:5 of carbon material, PTFE as binder, and carbon black, respectively. Ethanol was added to ensure homogeneity, and the resulting paste was dried overnight. Disc-shaped electrodes with a 5 mm diameter and a mass load close to 10 mg cm^{-2} were cut from the paste. Prior to analysis, the electrodes were soaked in the 1 M H_2SO_4 electrolyte for at least two days to allow impregnation. The electrochemical cell assembly consists of golden current collectors, carbon electrodes, and a porous quartz fiber separator, arranged from the outermost component towards the cell center. All components are immersed in the aqueous electrolyte.

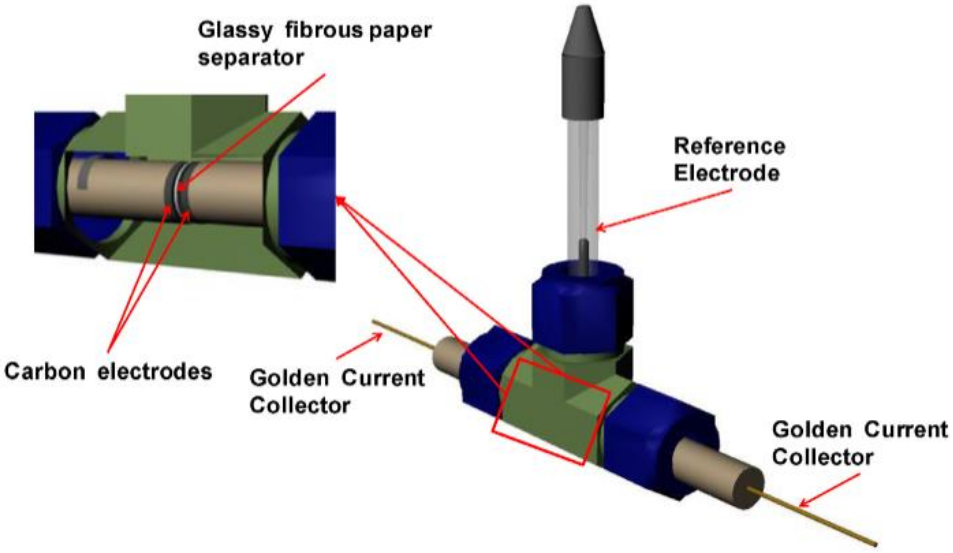

Figure 4-4 Two and three-electrode cell used for measuring electrochemical properties of carbon electrodes.

Electrochemical impedance spectroscopy (EIS) measurements were performed by applying alternating current at the open circuit potential (OCP) over a frequency range of 100 kHz to 1 mHz with a sinusoidal amplitude of 10 mV. The data obtained was used to generate the Nyquist and Bode plots. The bulk electrolyte resistance (Rs) and charge transfer resistance (RCT) were estimated fitting the data in the high-frequency region to **Eq. 2-29** [125], and the equivalent series resistance (ESR) was estimated using a linear line fit in the low-frequency region of the Nyquist plot [127].

Cyclic voltammetry (CV) experiments were conducted using a potential window of 1 V, with scan rates ranging from 5 to 1000 mV s^{-1}. The specific cell capacitance ($C_{CV,cell}$) was calculated using **Eq. 4-2**, where $\boldsymbol{I}$ is the current, $\boldsymbol{v}$ is the scan rate, $\Delta\boldsymbol{V}$ is the potential window, and $\boldsymbol{m}$ is the total mass of carbon used on both electrodes.

$$\boldsymbol{C_{CV,cell} = \frac{\int IdV}{v\,\Delta V\,m}} \qquad \textbf{Eq. 4-2}$$

The collected CV data obtained at different scan rates, were used to estimate the contributions of electric double-layer capacitance ($\boldsymbol{C_{EDL}}$) and pseudo-capacitance contributions ($\boldsymbol{C_{PsC}}$) using Trasatti's method [126], described in **section 2.4.1**.

Galvanostatic charge/discharge (GCD) cycling was also conducted within the 0 to 1 V potential window, applying a specific current from 0.5 to 40 A g^{-1}, based on the total mass of one electrode. The specific cell capacitance ($\boldsymbol{C_{GCD,cell}}$) was also determined from the GCD discharge curves using **Eq. 4-3**.

$$\boldsymbol{C_{GCD,cell} = \frac{I}{\left(\frac{dV}{dt}\right)m}} \qquad \textbf{Eq. 4-3}$$

where $\boldsymbol{I}$ is the applied current in A, m is the total mass of carbon in the electrodes, and dV/dt is the slope of the discharge curve in V s^{-1}. The dV/dt slope was calculated within the 0.4 – 1 V range after subtracting the corresponding potential drop ($\boldsymbol{iR}$) [139,140]. The capacitances obtained from GCD curves were used to calculate the specific energy ($\boldsymbol{E}$) and power ($\boldsymbol{P}$) using **Eq. 4-4** and **Eq. 4-5**, respectively. In these equations, the potential window is corrected by the corresponding $\boldsymbol{iR}$ and $\boldsymbol{t_D}$ is the time required for a complete discharge of the electrochemical cell.

$$\boldsymbol{E = \frac{1}{2} C_{GCD,cell}\, V^2\, \frac{1}{3.6}} \qquad \textbf{[W-h kg}^{\textbf{-1}}\textbf{]} \qquad \textbf{Eq. 4-4}$$

$$\boldsymbol{P = \frac{E}{t_D}\, 3600} \qquad \textbf{[W kg}^{\textbf{-1}}\textbf{]} \qquad \textbf{Eq. 4-5}$$

5 RESULTS AND DISCUSSION

5.1 Tannins-derived carbon materials obtained by chemical activation.

5.1.1 Surface chemistry and chemical composition

The bulk and surface chemical composition of the tannin-derived carbons was studied by elemental analysis (EA) and XPS, respectively. The main results are shown in **Table 5-1**, and the contribution of the deconvoluted peaks is shown on the appendix section (**Table 8-1** for C 1s, and **Table 8-2** for O 1s). As expected, the increase in KOH used in chemical activation leads to a drop in yield. The biochar prepared at 550 °C (TBC) has a high bulk oxygen content (14.8 wt%) in agreement with the phenolic nature of the tannin precursor. Oxygen-containing groups were largely eliminated during the thermal treatment at 650 °C in the absence of KOH, as suggested by the drastic reduction in the amount of surface O for TBC-K0 (O_{EA} = 7.7 wt%).

In contrast, activated biochars presented a high bulk oxygen content of 14–23 wt. % due to the insertion of oxygen atoms during KOH activation at 650 °C **(Figure 5-1 A**), associated to potassium oxides added in the intercalation/insertion steps, as discussed in **section 2.2**.

Table 5-1 Bulk and surface chemical composition obtained from elemental analysis (EA) and XPS, respectively, of tannins-derived ACs activated via chemical activation at different KOH ratios.

Carbon material	Yield (%)[a]	EA (wt. %)				XPS (wt. %)			XPS (at. %)			O_{XPS}/O_{EA}
		C	N	H	O	C	N[b]	O	C	O	C/O	
TBC	44	80.6	0.1	2.7	14.8	89.5	N.D.	10.5	91.9	8.1	8.5	0.71
TBC-K0	33 (74)	89.7	0.1	1.6	7.7	90.5	N.D.	9.5	97.2	2.8	9.2	1.23
TBC-K0.3	27 (61)	82.6	0.4	1	16.0	84.6	N.D.	15.4	88.0	12.0	5.5	0.96
TBC-K0.6	30 (69)	78.6	0.3	1.3	18.8	85.6	N.D.	15.6	88.8	12.2	5.5	0.83
TBC-K1.1	30 (69)	81.4	0.2	0.9	19.2	84.5	N.D.	15.5	87.9	12.1	5.4	0.81
TBC-K1.9	30 (68)	82.0	0.1	0.9	23.3	88.0	N.D.	12.0	90.7	9.3	7.3	0.52
TBC-K2.8	26 (58)	83.1	0.1	0.8	20.4	90.2	N.D.	9.8	92.5	7.5	9.3	0.48
TBC-K3.6	21 (48)	81.1	0.1	0.8	19.1	89.0	N.D.	11.0	91.5	8.5	8.1	0.58

[a] Total yield, activation step yield is given in brackets; [b] N.D.= non-detected.

In general, the XPS analysis showed lower values of oxygen on the surface of activated biochars (about 10–15 wt%), suggesting an enrichment of the bulk in oxygen species. As a matter of fact, the ratio O_{XPS}/O_{EA} was calculated as a measure of the oxygen functionalities distributions, i.e., a higher ratio means an enhancement of oxygen on the surface. It can be noticed that the sample TBC-K0 is the only sample where the surface oxygen content is slightly higher than the bulk content. As discussed previously, the chemical activation increases the oxygen content, however this occurs with preference on the bulk material rather than the surface, where a decrease on the O_{XPS}/O_{EA} ratio can be noticed with the increase of activating agent ratio used for activation. Consequently, higher C/O atomic ratios were obtained with a high activation ratio (AR), although it has to be noticed that the non-chemically activated materials (TBC and TBC-K0) have the highest C/O atomic ratios. In other words, at low AR, the high oxygen content and less developed porosity are consistent with the higher product yields (27–33%, Table 5-1) or activation yields (61 – 74%) observed for activated biochars prepared at AR < 2.8. In addition, a low nitrogen content was also determined by EA for all samples (**Table 5-1**), which is ascribed to amino acids leached with polyphenols during the tannin extraction step, whereas surface nitrogen was not detected by XPS.

The nature of the oxygen species was estimated through the deconvolution of the high-resolution XPS spectra of C 1s and O 1s region. **Figure 5-1 B** and **C** shows the relative atomic C 1s and O 1s contributions as a function of AR, respectively. KOH activation resulted in the introduction of oxygen species at the carbon surface compared to pristine biochar (TBC) or heat-treated carbon in the absence of KOH (TBC-K0) as evidenced by: (i) the decrease in the relative content of C-C single bonds in hydrocarbons, aromatics and aliphatic groups (peak C_1) and (ii) the increase in the contribution of oxygen-containing groups (peaks C_2, C_3 and C_4) (**Figure 5-1 B**). Regarding the nature of oxygen functionalities (**Figure 5-1 C**), the raw biochar (TBC) and the sample thermally treated at 650 °C (TBC-K0) present O_2 as the major contribution (55–60%), which is mainly associated with phenolic groups in agreement with the chemical nature of the carbon precursor. Carbonyl and quinone functionalities (O_1: 40–44%) are the second most common groups, followed by carboxyl groups (O_3). Carbonyl and quinone (O_1) groups are known to increase reversible redox reactions (especially in aqueous media), which increase the capacitance of the EC by pseudocapacitive effects [87,90,141,142]. Moreover, basic groups (O_1 and O_2) can improve the affinity of the surface electrode with the electrolyte solution used in this research, increasing the available surface area and hence improving the electrochemical performance [141,142]. In contrast, O_3 species with high polarity and acidic nature (such as carboxylic groups) may reduce ion mobility, thus increasing the resistance [141–143]. Chemical activation produced an increase in the O_1 contributions while the relative amount of O_2 decreased to ARs of 1.1, indicating the generation of electrochemically active groups (carbonyl and quinone) as the main functionalities. A higher amount of KOH (AR > 1.1) resulted in an inverse trend, i.e., the contribution of OI gradually decreased and that of OII increased.

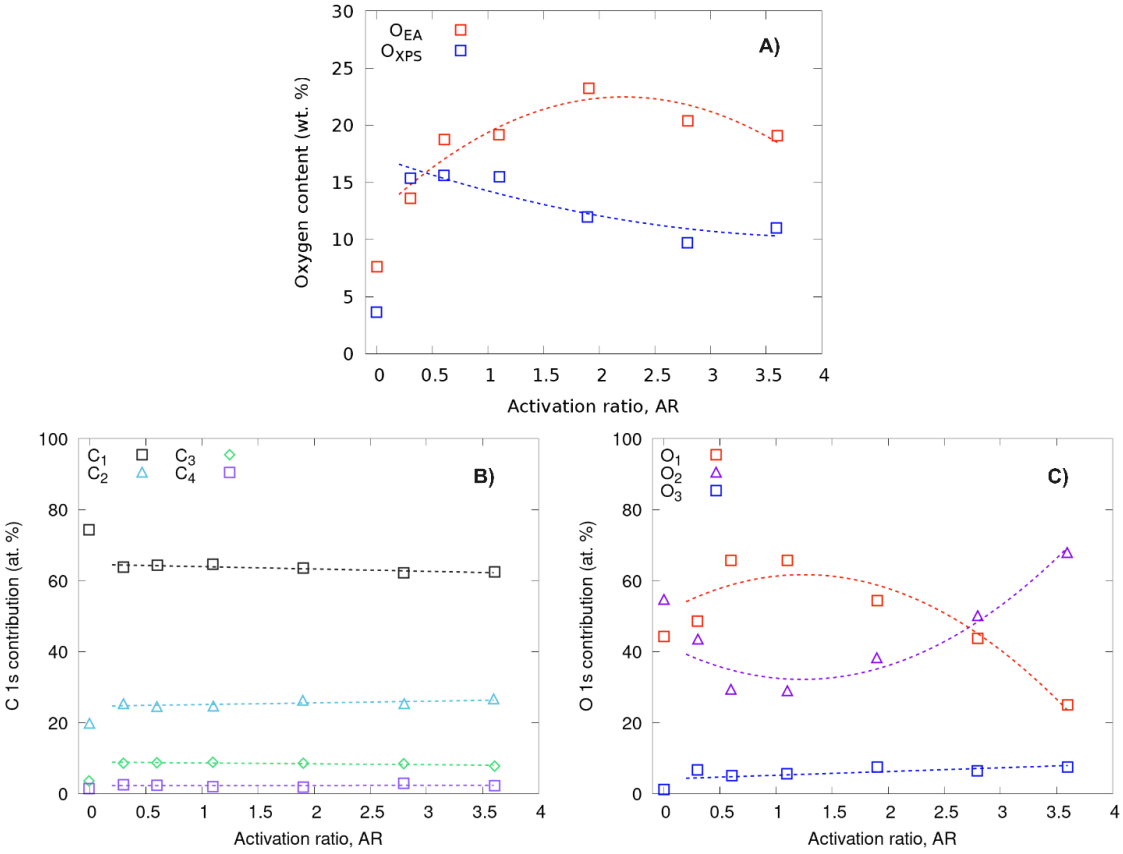

Figure 5-1 A) Bulk and surface oxygen content, B) contribution of functionalities according to deconvolution of C 1s region, and B) O 1s region, obtained from XPS of tannins-derived carbon materials chemically activated.

Indeed, phenolic species were again in majority for the most activated materials (TBC-K2.8 and TBC-K3.6). The O_3 contribution slightly increased after KOH activation and remained constant with AR (5.0–7.5 wt%). These results suggest differences in the oxidation mechanisms of the carbon surface during activation as a function of AR. The formation of elemental K and K_2CO_3 (according to equations presented in **section 2.2**), is well-known to be promoted at high AR [60,141,144,145]. Additionally, as it has been reported earlier [59,61], the thermal decomposition of KOH can lead to the selective formation of steam and carbon dioxide, which leads to the physical activation of the biochar and, consequently, to different O-containing functionalities.

The structural order of the carbon materials was studied using Raman spectroscopy, and the main results are exposed in **Figure 5-2**. As expected from the nature of the carbon precursor, the synthesis method used, and post-processing conditions, all samples exhibited the typical spectra of highly disordered carbon, where the D1 band is more intense than the G band [146,147], without significances differences on the spectra on the whole range of AR studied.

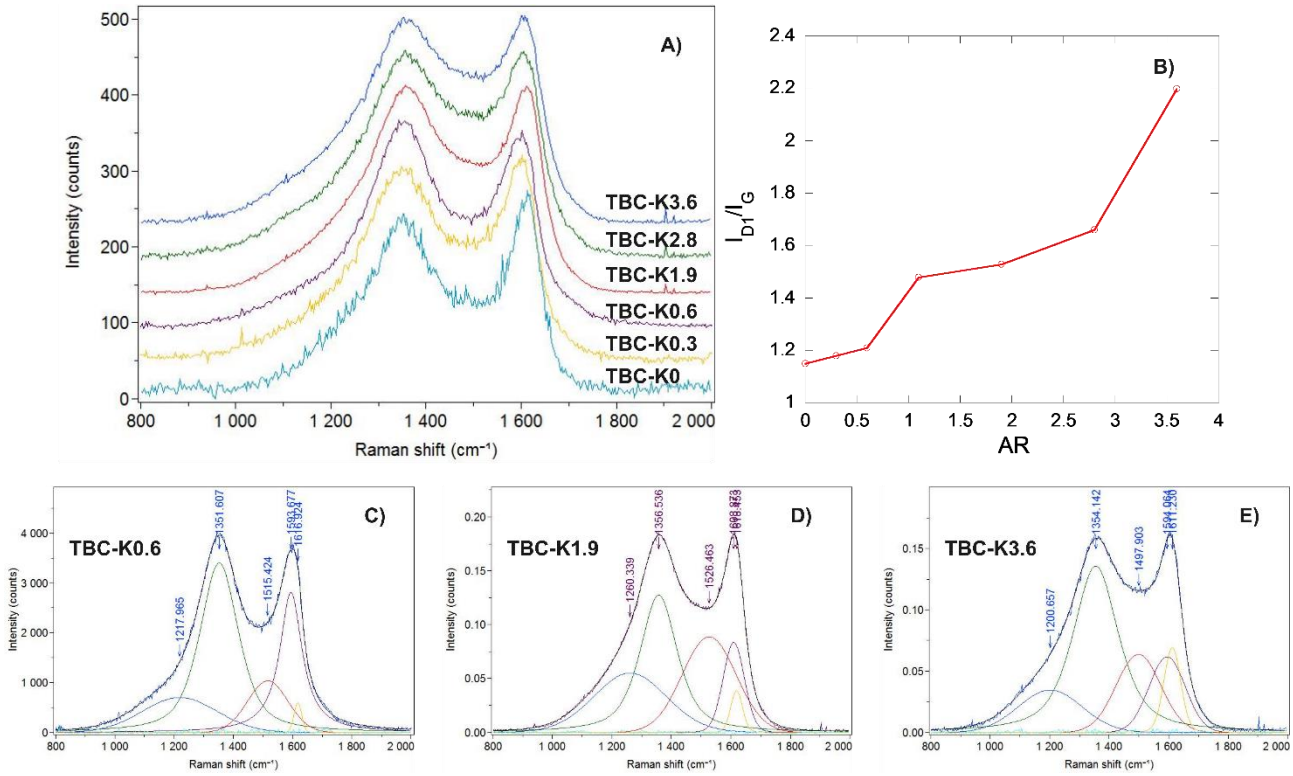

Figure 5-2 Raman spectra of tannin-derived carbon materials activated with KOH at different activating ratios, A) raw profiles for the chemically activated series of carbon materials, B) Intensity ratios of bands D1 (1350 cm^{-1}) to G (1595 cm^{-1}); C, D and E) examples of deconvolution of Raman profiles into five bands for TBC-K0.6, TBC-K1.9, and TBC-K3.6, respectively.

Due to the phenolic nature of tannins, as discussed previously on **section 2.3**, and the carbonization regime under the present experimental conditions, it is expected that the materials does have a non-graphitizable structure, and the increase in the ratio of the intensities of the D1 over the G band that show the **Figure 5-2 B** can be attributed to an increase in crystallite size and thus an enhancement of the long-range order in carbon [16,49].

TEM images were performed to study the morphology of the activated carbon materials prepared by chemical activation. For instance, the **Figure 5-3 A** shows the TEM image for the sample TBC-K1.1, where additionally to the raw image, a mapping on the carbon and oxygen distribution obtained from EDX analysis is shown, where the color green and red represent each element, respectively. Both images have shown a homogeneous distribution of the elements on the surface of the carbon matrix evidencing an appropriate distribution of the activating agent over the precursor. Apparently, a well-defined disordered with consistently randomly oriented pores morphology is observed for all the materials, and there are not significant changes with the AR. Actually, by comparing the **Figure 5-3 B**, **C** and **D**, which show the TEM images for the sample simply pyrolyzed (TBC), and the carbon materials chemically activated using AR of 1.1 (TBC-K1.1) and 3.6 (TBC-K3.6), respectively.

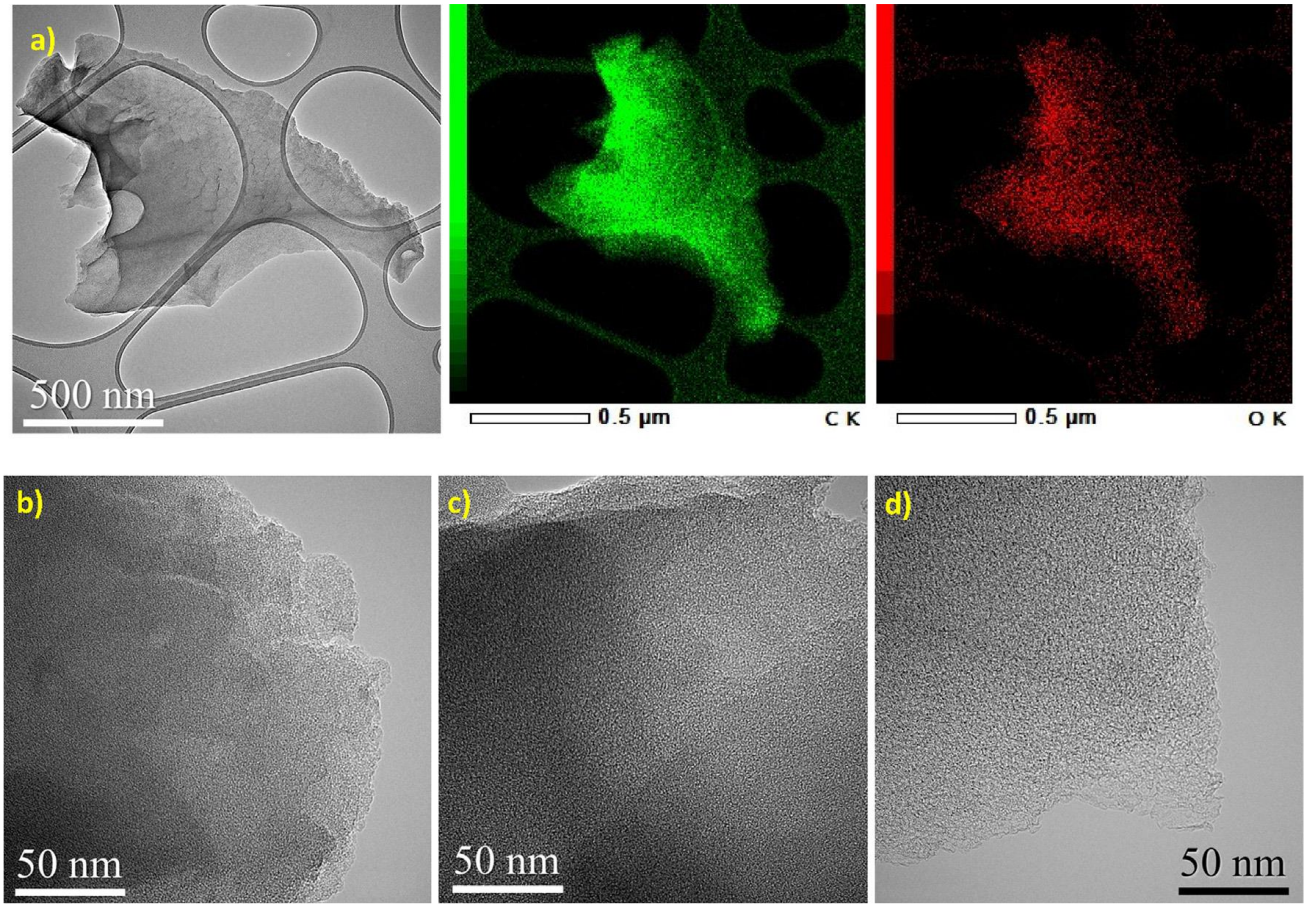

Figure 5-3 a) TEM image of TBC-K1.1 and corresponding chemical mapping of C and O; and TEM images of b) TBC, c) TBC-K1.1, and d) TBC-K3.6.

At this point, it is fair enough to establish that chemical activation did not alter the morphology of the final carbon materials, with the exception of the porosity development as discussed from the adsorption isotherms in the following section.

5.1.2 Textural properties

The N_2 adsorption–desorption isotherms of the ACs prepared from the pine tannin-derived carbon material are given in **Figure 5-4**, while the corresponding textural properties are listed in **Table 5-2**. All carbons, including non-activated biochar (TBC), exhibit type I isotherms with an almost horizontal plateau at $P/P_0 > 0.1$, indicating that the porosity is mainly associated with micropores. The sample just pyrolyzed at 550 °C (TBC) showed limited development of porosity (A_{BET} = 384 $m^2\ g^{-1}$; S_{NLDFT} = 623 $m^2\ g^{-1}$; $V_{0.97}$ = 0.17 $cm^3\ g^{-1}$). As the AR increases, a progressive enhancement in adsorption capacity is observed, leading to high values of specific surface area (A_{BET} = 2554 $m^2\ g^{-1}$ and S_{NLDFT} = 2147 $m^2\ g^{-1}$) and total pore volume ($V_{0.97}$ = 1.10 $cm^3\ g^{-1}$) for the sample activated at the highest AR (TBC-K3.6).

Table 5-2 Textural parameters estimated from both N_2 and CO_2 adsorption isotherms and product yields for the TBC series[a].

Sample	A_{BET} ($m^2\ g^{-1}$)	S_{NLDFT} ($m^2\ g^{-1}$)	$V_{0.97}$ ($cm^3\ g^{-1}$)	V_T ($cm^3\ g^{-1}$)	V_μ, ($cm^3\ g^{-1}$)	$V_{u\mu}$, ($cm^3\ g^{-1}$)	V_{meso} ($cm^3\ g^{-1}$)	‹w_{av}› (nm)	‹$w_{\mu,av}$› (nm)	‹$w_{u\mu,av}$› (nm)	Yield (%) [b]
TBC	384	623	0.17	0.21	0.18	0.12	0.02	1.81	0.69	0.52	44
TBC-K0	489	789	0.21	0.25	0.22	0.18	0.02	1.61	0.62	0.55	33 (74)
TBC-K0.3	599	1057	0.24	0.31	0.30	0.23	0.01	1.19	0.62	0.53	27 (61)
TBC-K0.6	808	1310	0.31	0.37	0.37	0.31	0.00	0.66	0.60	0.55	30 (69)
TBC-K1.1	1183	1625	0.46	0.49	0.49	0.39	0.00	0.75	0.64	0.58	30 (69)
TBC-K1.9	1783	1998	0.71	0.69	0.69	0.39	0.00	0.91	0.77	0.59	30 (68)
TBC-K2.8	2417	2190	1.04	0.97	0.92	0.27	0.04	1.22	1.02	0.58	26 (58)
TBC-K3.6	2554	2147	1.10	1.01	0.94	0.23	0.07	1.26	1.09	0.58	21 (48)

[a] V_T, V_μ, $V_{u\mu}$, V_{meso}, ‹w_{av}›, ‹$w_{\mu,av}$›, ‹$w_{u\mu,av}$› are total volume, micropore volume, ultra-micropore volume, mesopore volume, average pore size, average micropore size, average ultramicropores size, respectively, obtained by applying 2D-NLDFT-HS model to N_2 and CO_2 adsorption isotherms; [b] Total yield, and activation yield is given in brackets.

These values are higher than those reported by other authors for ACs obtained by KOH activation of biomass precursors at temperatures above 650 °C, such as human hair (1306 $m^2\ g^{-1}$) [148], hydrolyzed lignin (1660 $m^2\ g^{-1}$) [149], broad beans (655 $m^2\ g^{-1}$) [150], coffee endocarp (893 $m^2\ g^{-1}$) [151] or ginkgo shells (1775 $m^2\ g^{-1}$) [152]. Such a well-developed texture results from both chemical activation by carbon oxidation and carbon lattice expansion by intercalation of potassium, according to the activation mechanism, as described in **section 2.2**.

This progressive activation also leads to a lower product yield for materials activated at the highest AR, as can be seen in **Table 5-2**, ranging from 33% for the non-activated carbon (TBC-K0) to 21% for TBC-K3.6. Similarly, a gradual widening of the ‘‘knee” of the isotherms at low P/P^0 is evident with the increase in AR (**Figure 5-4 A**), indicating a broadening of the micropore size [133], as can be seen from the data obtained from 2D-NLDFT-HS in **Table 5-2**. Additionally, the materials with a high degree of activation, i.e., those obtained using an AR of 2.8 and 3.6, exhibited a slightly higher slope in the multilayer region due to the generation of narrow mesopores by KOH activation and micropore merging. Micropore widening is also observed in the CO_2 isotherms (**Figure 5-4 B**), where the slope at $P/P^0 > 0.01$ clearly increases at AR above 1.1. Conversely, a lower CO_2 adsorption was evidenced for ACs prepared with the highest AR, such as TBC-K2.8 and TBCK-3.6, at $P/P^0 < 0.005$. On the same line with these results, a lower contribution of ultramicropores is evident for the most activated materials, indicating a significant loss of pores of width $w < 0.7$ nm, with the consequent increase of supermicropores ($0.7\ nm < w < 2\ nm$) and mesopores, due to pore widening by KOH activation at high AR.

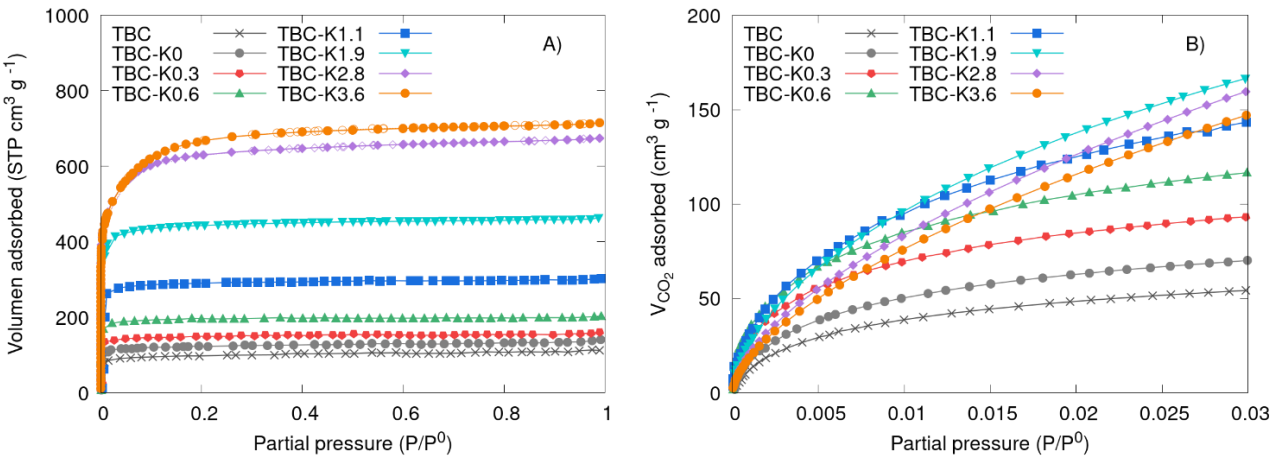

Figure 5-4 A) N_2 and B) CO_2 adsorption-desorption isotherms at -196°C for TBC-series.

Pore size is a key parameter in the design of efficient ECs, since pores that are too small are not easily impregnated by the electrolyte, and therefore these pores do not efficiently contribute to the double-layer capacitance [29,44], whereas faster ion transport through wider micropores or mesopores results in higher rate capability [119,153].

The **Figure 5-5 A** shows A_{BET} and S_{NLDFT} as a function of the activating ratio. Values of A_{BET} are lower than those of S_{NLDFT} for AR < 2.8. This is because the BET method assumes monolayer adsorption on each pore wall. It therefore underestimates the surface area of narrow micropores where only one layer is adsorbed between the two walls, and hence only one wall is considered [154]. The latter is in good agreement with the high contribution of ultramicropores (around 56–84%, **Figure 5-5 B**) determined for the pristine carbon (TBC) and activated materials with AR < 2.8. Conversely, the values of A_{BET} are lower than those of S_{NLDFT} for the most activated carbons (TBC-K2.8 and TBC-K3.6) due to multilayer adsorption in the wider pores [78,133,154,155]. The 2D-NLDFT-HS model combining N_2 and CO_2 adsorption data is known to provide a more accurate estimate of the textural parameters of ACs [156,157]. Correct interpretation of these properties will allow a better correlation between textural characteristics and the electrochemical capacitance. A maximum S_{NLDFT} of 2190 m^2 g^{-1} (**Table 5-2**) was obtained for TBC-K2.8, while a higher KOH amount did not result in a significant change in texture. **Figure 5-5 B** shows the ultra-micropore, super-micropore, micropore and mesopore volume fraction obtained by the 2D-NLDFT-HS method as a function of AR. As can be seen, the main contribution to the total volume is the microporosity ($\Phi V_{\mu} \approx 100$), with a high proportion of ultra-micropores for the low values of AR, which significantly decreases according to the AR increases in favor of the super-micropores. Moreover, the chemical activation resulted in a progressive increase of the micropore volume, as it is shown in **Figure 5-5 C** from the pore size distribution of each carbon material. A decrease in the micropore volume and a slight increase in mesopore volume are observed only for AR higher than 1.9, again due to pore widening by KOH activation.

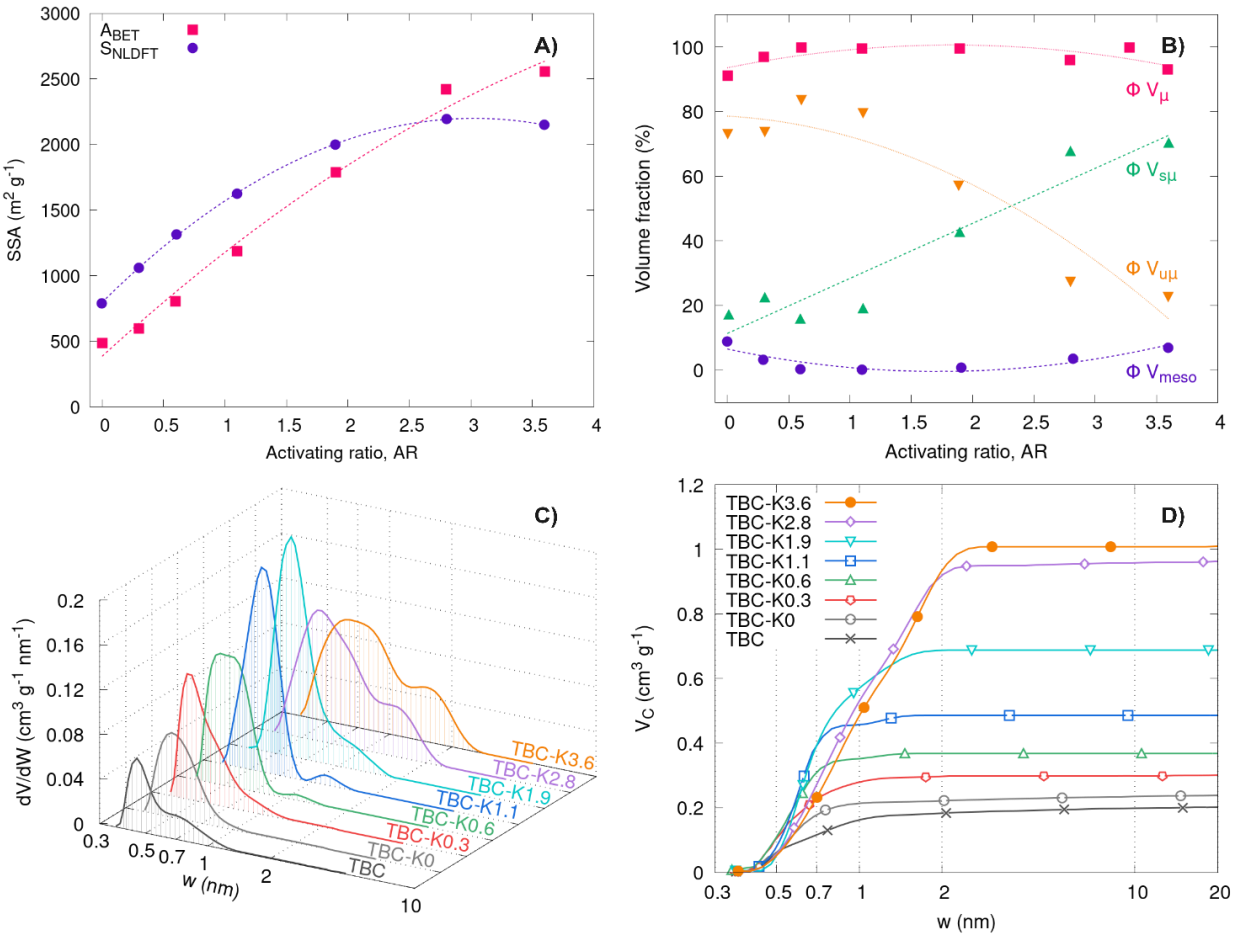

Figure 5-5 A) Specific surfaces areas determined by BET and NLDFT methods as a function of the activating ratio, B) contribution on the total volume of mesopores, micropores ultra-micropores and super-micropores, C) Pore size distribution (PSD), and D) cumulative pore volume for the TBC series of carbon materials, all values estimated from 2D-NLDFT-HS model applied to N_2 and CO_2 adsorption isotherms.

The widening of pores with increasing AR is also confirmed by the PSD calculated by the 2D-NLDFT-HS method, which reveals a shift to larger pore sizes as the activation degree increases evidencing the collapse of the carbon structure leading to a merge of pores. In the micropore range, a bimodal distribution is observed for activated samples. The main maximum shifts from 0.51 to 0.67 nm as the AR increases from 0.6 to 3.6, whereas the second pore peak is shifted from 1.1 to 1.6 nm. This second contribution to larger micropores (1 to 2 nm) is more evident for AR > 1.9. In addition, TBC-K2.8 and TBC-K3.6 show a continuous PSD over the entire range of micropores, which can promote ion diffusion through the interconnected pores and thus improve the electrochemical performance of ECs [158]. On the contrary, a low contribution of pores > 1 nm in size is observed in the PSD of non-activated or materials activated at AR below 1.9. Finally, a higher cumulative pore volume was obtained as the activating ratio increased, as can be seen in **Figure 5-5 D**.

5.1.3 Electrochemical performance

The electrochemical behavior of the activated tannins-derived carbon materials was studied in aqueous acid medium (1 M H_2SO_4) by CV under standard commercial mass loadings. The main results obtained from the capacitance–voltage curves are given in **Figure 5-6**. The ACs present a double-layer capacitive behavior with quasi-rectangular CV curves at low scan rates, which window increases as the AR increases due to the development of porosity by KOH activation. A maximum cell capacitance ($C_{CV,cell}$) of approximately 60 F g^{-1}, and thus an electrode capacitance of approximately 240 F g^{-1} ($C_e = 4C_{cell}$), was found for the sample activated using an AR of 2.8, which gave the highest SSA according to the 2D-NLDFT-HS model (S_{NLDFT}). Indeed, a clear linear correlation between C_{cell} and S_{NLDFT} was found with a determination coefficient (R^2) of 0.996 at 5 mV s^{-1} (**Figure 5-6 B**).

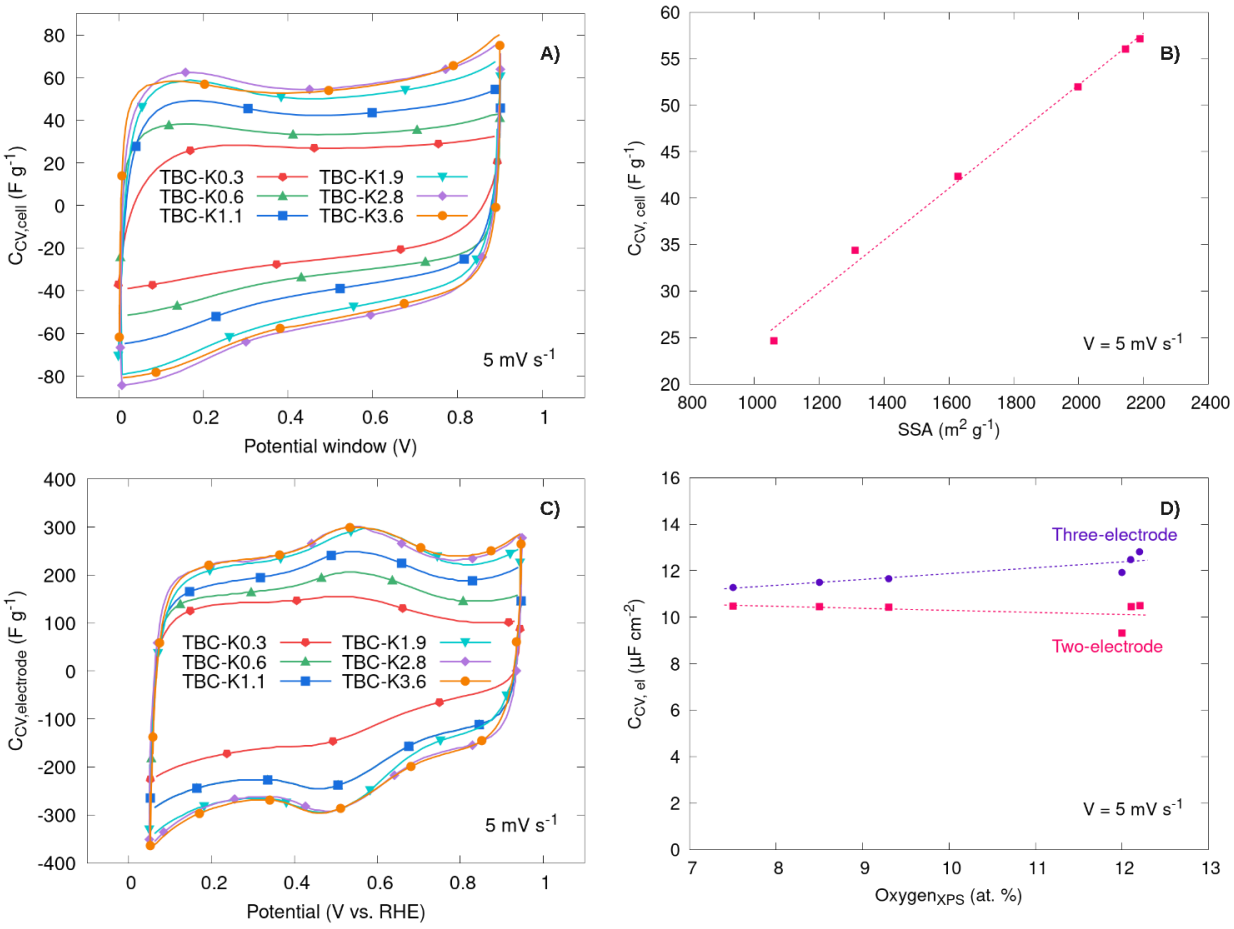

Figure 5-6 A) Curves of cell capacitance vs. voltage at scan rate of 5 mV s^{-1} obtained from symmetrical two-electrode cell, B) Cell capacitance obtained from CV curves in a two-electrode cell as a function of the specific surface area (SSA), C) Curves of cell capacitance vs. voltage at scan rate of 5 mV s^{-1} obtained from three-electrode cell using reversible hydrogen electrode as reference, and D) Specific capacitance obtained from CV curves on a two-electrode cell and CV curves on a three-electrode cell as a function of the oxygen content on the surface estimated by XPS.

A lower determination coefficient (0.915) was obtained when considering A_{BET} instead of S_{NLDFT}, illustrating a better fit of the 2D-NLDFT-HS model for the correlation of the capacitance and textural properties for this material series. Although two-electrode configurations are useful to study the performance of the materials in conditions closer to those of real capacitors, electrochemical measurements in three-electrode cells provide a better estimate of the pseudocapacitive behavior. CV tests in a conventional three-electrode system provided a better understanding of the effect of the surface chemistry on the capacitance of carbon materials. **Figure 5-6 C** shows the capacitance vs potential curves at 5 mV s^{-1} of carbons obtained at different AR. In all the cases, a redox couple appeared close to 0.5 V vs. RHE, which is ascribed to Faradaic reactions of carbonyl and quinone groups accounting for pseudocapacitance [159]

In order to match the electrochemical storage behavior to the surface chemistry, the capacitances of an electrode normalized by the S_{NLDFT} surface area, called $C_{CV,el}$, were represented as a function of the atomic oxygen content determined by XPS (O_{XPS}) (**Figure 5-6 D**). Capacitances obtained at a low scan rate (5 mV s^{-1}) were considered in order to avoid the appearance of uncompleted redox reactions (due to kinetics limitations at fast sweep rates), which would underestimate the pseudocapacitance. Normalized electrode capacitances on the two-electrode configuration at 5 mV s^{-1} present a value of ~ 10.3 mF cm^2 (with an average of 13 mF cm^2 for A_{BET}-normalized capacitances). On the same line, interfacial capacitances obtained in the three-electrode configuration at 5 mV s^{-1} presented a value around 11.9 mF cm^2 (see **Figure 5-6 D**, purple dots), which correlates well to that obtained in the two-electrode device. These values are comparable to or higher than those reported for other carbons in aqueous H_2SO_4 electrolyte, such as corn straw-based AC (~9.3 mF cm^2) [160], tannin-derived carbons (~8.6 mF cm^2) [15] or hierarchically structured activated carbon (~8.0 mF cm^2) [161], highlighting the great potential of these carbon materials for energy storage. An increase in the surface oxygen content from 7.5 to 12.2 at. % did not affect the interfacial capacitance of the electrode, even at the low scan rate of 5 mV s^{-1}.

This finding suggests a similar pseudocapacitive contribution of KOH-activated electrodes obtained at different AR with a preferential double-layer storage mechanism. Counterintuitive, one could assume that an increase in the atomic oxygen content will lead to an enhancement of the interfacial capacitance, evidencing a certain pseudocapacitive behavior of the materials. However, the slight slope indicates that double-layer formation is the main storage mechanism in good correlation with the findings obtained in a symmetric two-electrode system. Actually, a linear relationship of the interfacial capacitance ($C_{e,int}$) measured in a three-electrode cell and the surface density of oxygen and nitrogen relative to carbon, ((O + N)/C)/SNLDFT (wt.% g m2) [78,162] was also found according to the data exposed in the **Figure 5-7**. The fit of the data resulted in the following correlation (**Eq. 5-1**), with a determination coefficient of 0.751:

$$C_{e,int}(F\ m^{-2}) = \frac{C_e}{S_{NLDFT}} = (0.094 \pm 0.007) + (1.767 \pm 0.509)\frac{(\frac{O+N}{C})}{S_{NLDFT}} \qquad \textbf{Eq. 5-1}$$

From the slope in **Figure 5-7**, and according to the coefficient of the second term of **Eq. 5-1**, the pseudocapacitance effect of ACs was estimated by considering a factor of 1.77 F per % of the ratio (O + N)/C per m^2. Carbons obtained using low AR presented a more significant pseudocapacitance, with a contribution ranging from ~25% for poorly activated carbons to ~ 17% for TBC-K2.8 and TBC-K3.6 (see inset in **Figure 5-7**). The lower pseudocapacitance of the latter materials is ascribed to the loss of surface oxygen species (as evidenced by the lower values of O_{XPS}, see **Table 5-1**) during KOH activation at high AR, and the decrease in the relative content of carbonyl and quinone groups (O_1 functionalities, **Figure 5-1 C**), which are electrochemically active, as discussed in section 2.2.2.

The impact of scan rate on the capacitance was also evaluated by CV in symmetrical ECs. For instance, **Figure 5-8 A** exhibited quasi-rectangular shapes of the current density–voltage curves for TBC-K2.8 as the scan rate increases. This shows the rapid formation of the double layer for the most activated materials, which is consistent with their lower pseudocapacitance contribution. More importantly, the aforementioned materials retain about 62% of the initial cell capacitance when the scan rate increases from 5 to 100 mV s^{-1} (**Figure 5-8 B**).

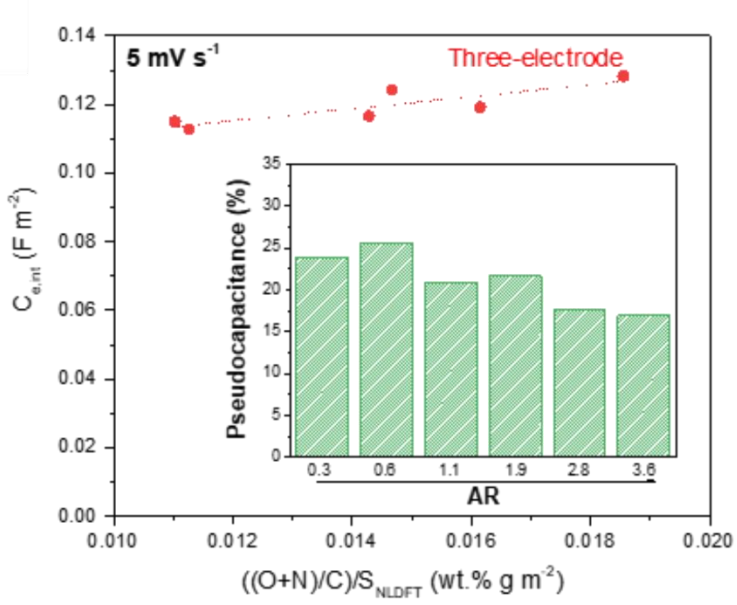

Figure 5-7 Electrode capacitance measured in a three-electrode configuration normalized by their specific surface area as a function of the (O+N)/C per S_{NLDFT} at 5 mV s^{-1}, inset: pseudocapacitance contribution (%) according to the AR.

The lower decrease of capacitance at high AR may be explained by: i) the existence of a well-connected porosity (see **Figure 5-5 C**), where wider micropores facilitate the transport of the electrolyte ions to the micropores and; ii) an improved electrical conductivity due to the lower density of oxygen species, evidenced by the lower oxygen amount per surface area of highly activated materials (**Figure 5-1 A**) and the higher C/O atomic ratio, which facilitates electron mobility to the carbon matrix. Carbon materials produced at AR < 2.8 presented a sharper loss of capacitance, except for TBC-K0.6 with a relatively high retention of 61%, comparable to that of the most activated materials. This material is a particular case where KOH activation resulted in a specific cell capacitance at high scan rates higher than, or comparable to, those of materials activated using 1.1 and 1.9 g KOH per g of biochar, respectively, despite the larger S_{NLDFT} of the latter samples.

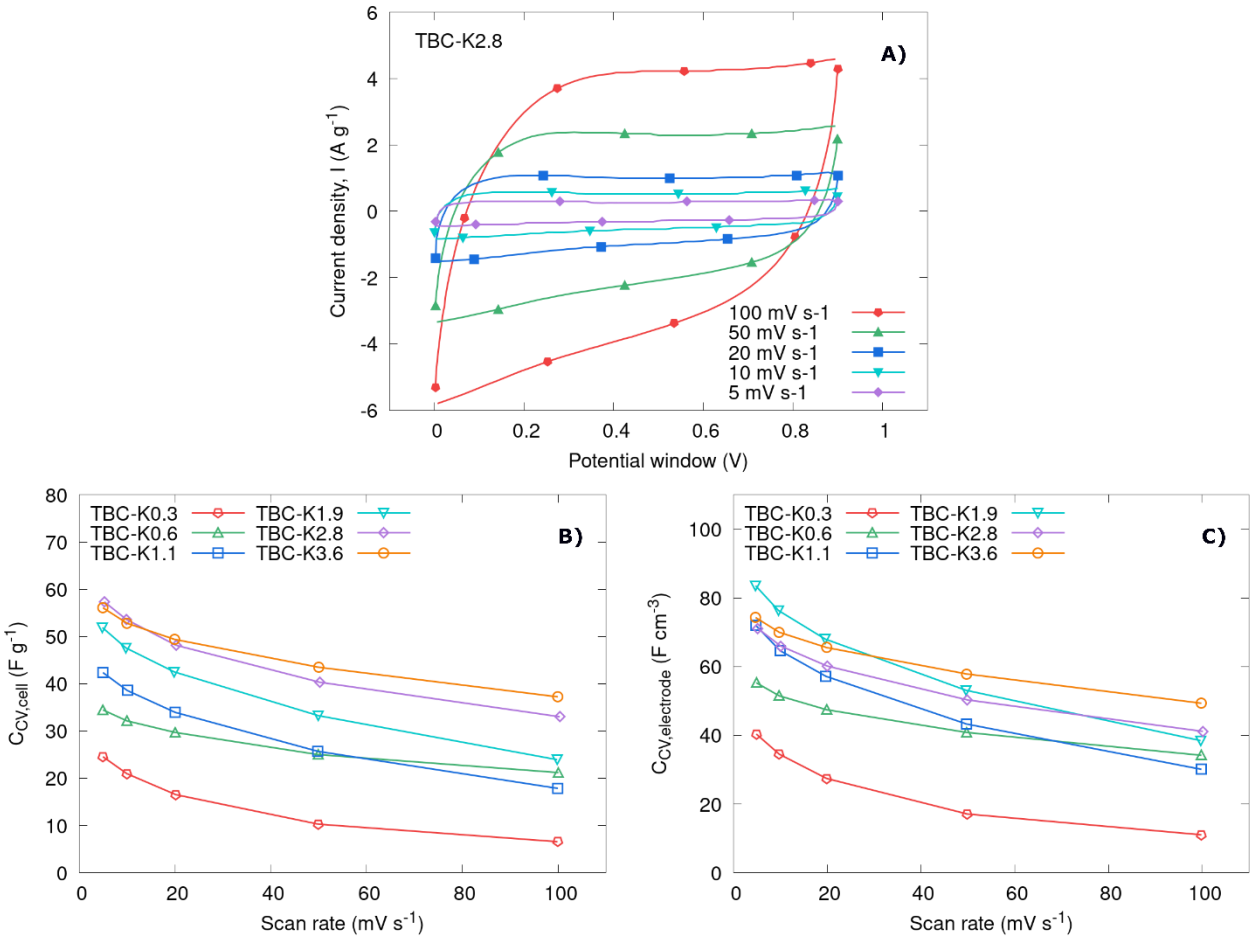

Figure 5-8 Cyclic voltammograms (CV) at different scan rates of symmetrical ECs in aqueous electrolyte (1 M H_2SO_4) for TBC-K2.8 carbon material, B) Gravimetric cell capacitance estimated from CV curves of tannins-derived carbon materials series named TBC used on a symmetrical cell, C) volumetric electrode capacitance based on electrode packing density.

Although, this larger surface area originated from the creation of ultramicropores, as evidenced by the largest values of $V_{u\mu}$ for TBC-K1.1 and TBC-K1.9 (0.39 $cm^3\ g^{-1}$) vs. TBC-K0.6 (0.31 $cm^3\ g^{-1}$), the PSD of TBC-K0.6, TBC-K1.1 and TBC-K1.9 shown a main peak centered between 0.51 to 0.58 nm, and their main difference is the higher mean pore width for the former material (0.29 vs 0.25 or 0.26 nm, respectively), which may reduce ion electrolyte resistance.

Additionally, TBC-K1.1 exhibited the lowest average pore diameter (and micropore diameter), which may produce the distortion of solvated ions, reducing the distance to the carbon surface, and as a result, this material exhibits a faster capability. **Figure 5-8 B** and **C** show the specific or gravimetric (F g^{-1}) and volumetric (F cm^{-3}) capacitances as a function of scan rate. These values were determined considering the packing density (g cm^{-3}), defined as the amount of active material per electrode volume [163]. The electrode volume was easily calculated by using the geometrical area and thickness of the electrodes. The materials with the highest porosity (TBC-K2.8 and TBC-K3.6) achieved the lowest packing densities (0.30 and 0.33 g cm^{-3}, respectively), whereas a value of about 0.4–0.42 g cm^{-3} was found for the rest of materials. Consequently, the aforementioned materials have shown a slight lower volumetric capacitance than the sample TBC-K1.9 due to overdeveloped volume. Despite these differences, the volumetric capacitance (F cm^{-3}) exhibited similar behavior to that observed for the gravimetric capacitance (F g^{-1}), where the most developed texture (AR of 2.8 and 3.6) showed the highest capacitances at faster scan rates.

The ability of ions to penetrate the porous structure of the electrodes at different frequencies was studied by EIS by applying an alternating current with an amplitude of 10 mV at OCP. The Nyquist plots of activated carbon materials in **Figure 5-9 A** show a well-defined semicircle in the high-frequency range, followed by a 45° Warburg region, and a nearly vertical line at low frequency, indicating the classical electrochemical performance of porous carbons [20,127,164]. Close inspection reveals a large Warburg region for the poorly activated material TBC-K0.3, indicating a substantial limitation of ion transport within the porous structure (diffuse layer resistance) [164]. As AR increases, the Warburg region is less evident, reaching values of ~0.7 Ω cm^2 for TBC-K2.8 and TBC-K3.6 due to the more developed porosity and enlarged pore size. These electrodes also exhibited the lowest internal resistances (0.23 and 0.38 Ω cm^{-2}, respectively), as evidenced by the lower diameter of the semicircles in **Figure 5-9 A**. These results suggest an improved electron transport in TBC-K2.8 and TBC-K3.6 electrodes, which may be related to the widening of the pores and the noticeable appearance of pores between 1 and 2 nm, but also due to the increase in the structural order when increasing AR, as shown by Raman spectroscopy results. Normalized capacitances ($C_{EIS}/C_{EIS,1\ mHz}$,) as a function of frequency are plotted in **Figure 5-9 B**. The relaxation time constant ($\tau_{0.5} = 1/f_{0.5}$), i.e., the time required to discharge 50% of the saturation capacitance, decreases from 30 to 8 s with the increase of AR from 0.6 to 3.6.

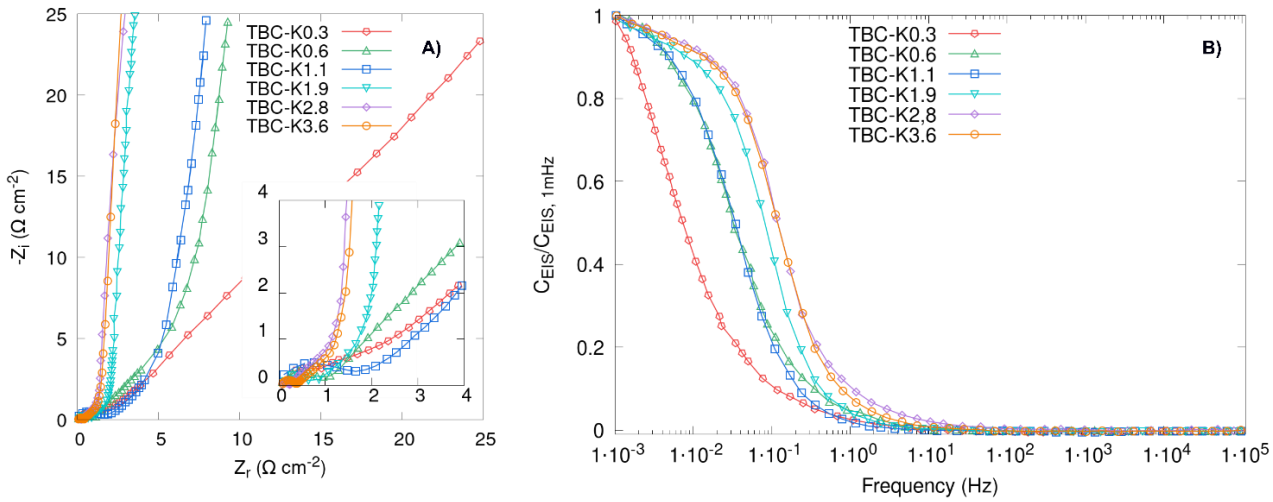

Figure 5-9 Electrochemical impedance spectroscopy (EIS) for symmetrical ECs based on TBC series as carbon material electrode and 1 M H_2SO_4 as electrolyte: A) Nyquist plot with inset focused on the region close to the origin, and B) normalized capacitance calculated from EIS vs frequency.

The faster performance of TBC-K2.8 ($\tau_{0.5}$ = 8.5 s) and TBC-K3.6 ($\tau_{0.5}$ = 8.3 s) is consistent with their larger average micropore sizes (1.02 and 1.09 nm, respectively) and adequate electron transport. These relaxation times are lower than those obtained for commercial activated carbons (~10 s), showing the applicability of the materials in realistic devices [1,165].

For a more in-depth interpretation of the electrochemical performance of activated biochars, galvanostatic charge/discharge cycling experiments were performed at different current densities. The **Figure 5-10 A** shows a comparison of the galvanostatic charge–discharge curves at 2 A·g^{-1} for all materials. The ACs exhibited quasi-triangular voltage profiles indicating the preferential electrical double-layer storage mechanism [20,139,140]. The slight deviation from the linear and symmetrical voltage profiles is due to the occurrence of Faradaic reactions by pseudocapacitance [17,20,140]. The materials prepared at high AR exhibited the lowest Ohmic drops ($\boldsymbol{iR}$) in good agreement with the lowest internal resistances estimated by EIS for these electrodes. A lower AR resulted in an increase of the $\boldsymbol{iR}$, indicating a higher electrical resistance. The capacitance retention at different current densities is displayed in **Figure 5-10 B** for carbon materials with AR > 0.3.

ECs based on TBC-K2.8 and TBC-K3.6 presented the largest $\boldsymbol{C_{GCD,cell}}$ over the entire current density window with values of 50 and 60 F g^{-1} at 0.5 A g^{-1}, respectively, which are close to those obtained by CV at 5 mV s^{-1} (~60 F g^{-1}). Similar capacitances at low current densities have been reported for other biomass-derived carbon electrodes synthesized by pyrolysis and KOH activation (see **Table 5-3**), or for porous carbons obtained from tannin by different approaches [15,67,166]. Furthermore, TBC-K2.8 and TBC-K3.6 exhibited the highest capacitance retentions (64–70%) when the current density increased up to 10 A g^{-1}.

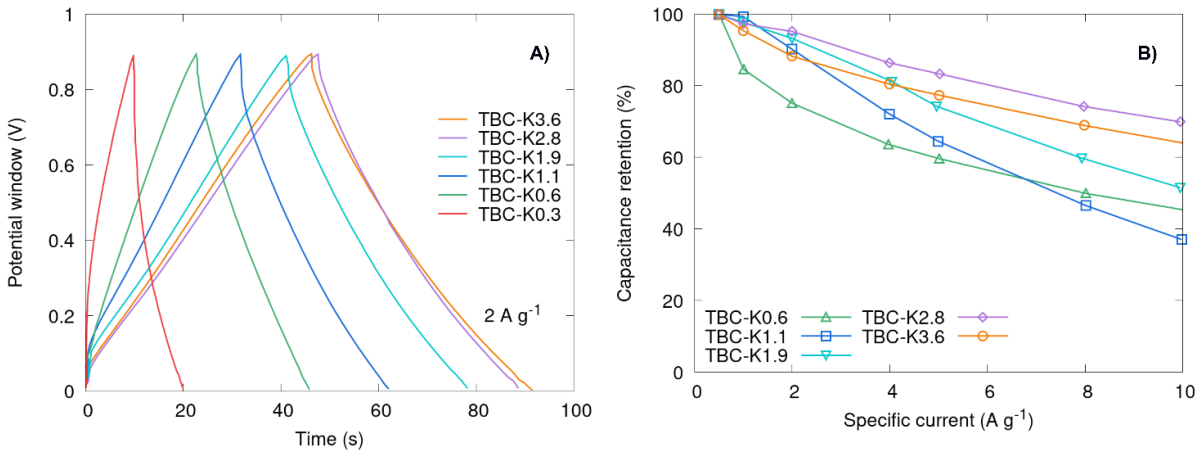

Figure 5-10 A) Galvanostatic charge-discharge (GCD) curves for symmetrical ECs based on TBC materials with a potential window of 0.9 V in 1 M H_2SO_4 at current density of 2 A g^{-1}, and B) Capacitance retention calculated from discharge GCD curves as a function of the applied current density.

These results indicate easier diffusion of ions into the pores and faster electron transport as mentioned before. Although this rate capability is not exceptional in acidic media, most of the studies reported there used electrodes with a lower effective carbon loading (or the carbon loading has not been reported). A low carbon loading leads to an overestimation of the material capacitance by reducing the diffusion distance for the ions of the electrolyte, especially at high current densities [167]. In this work, the mass loading was comparable to the commercial standard of 10 mg cm^{-2}, thus providing a realistic insight, from a technical point of view, into the electrochemical performance of these activated carbon materials derived from pine tannins.

Table 5-3 Summary of biomass-derived carbon electrodes submitted to chemical activation using KOH and their use in symmetric electrodes for ECs in H_2SO_4 electrolyte.

Precursor	Treatment	Activation	A_{BET} ($m^2 g^{-1}$)	$C_{e,1}$[a] ($F\ g^{-1}$)	$C_{e,2}$[a] ($F\ g^{-1}$)	C_{ret}[a] (%)	$C_{loading}$ ($mg\ cm^{-2}$)	H_2SO_4 (M)	Ref.
Bean dregs	Carbonization 400°C	KOH 700°C	2876	280 (0.1 A g^{-1})	165 (2.5 A g^{-1})	59	2-3	1 M	[168]
Silk fibroin	N.A.[b]	KOH 800°C	2557	264 (0.1 A g^{-1})	162 (6.2 A g^{-1})	61	N.R.[b]	1 M	[169]
Hemi cellulose-derived	Hydrothermal 200°C	KOH 700°C	2300	315 (1 A g^{-1})	182 (1 A g^{-1})	58	N.R.[b]	0.5 M	[170]
Lignin	N.A.[b]	KOH 700°C	907	165 (0.5 A g^{-1})	124 (10 A g^{-1})	75	N.R.[b]	1 M	[73]
Corn straw	Carbonization 450°C	KOH 800°C	2790	260 (0.2 A g^{-1})	130 (60 A g^{-1})	50	7.6	1 M	[160]
Tannins	Carbonization 550°C	KOH 650°C	2187	200 (0.5 A g^{-1})	120 (10 A g^{-1})	70	9	1 M	[121]

[a] $C_{e,1}$: capacitance at the low current density reported and indicated in brackets, $C_{e,2}$: capacitance at the high current density reported, C_{ret}: capacitance retention, $C_{loading}$:Carbon loading; [b] N.A.: non-applied, N.R.: non-reported.

The stability of the TBC-K2.8- and TBC-K3.6-based ECs was evaluated by a long-term charge–discharge cycling at 5 A g^{-1} (**Figure 5-11 A**). After 10,000 cycles, these systems retained 92 and 94% of their initial capacitance, respectively, evidencing the robustness of ECs based on these carbon materials. To better understand the practical use of tannin-derived activated carbon materials as EC electrodes, the leakage current and self-discharge of the most promising materials (TBC-K2.8 and TBC-K3.6) were evaluated, TBC-K1.1 was also evaluated for the sake of comparison. **Figure 5-11 B** shows the time-dependent leakage current at a cell voltage of 0.9 V, while the spontaneous OCP decays after the devices were fully charged are given in **Figure 5-11 C**. The current sharply drops over time and then reaches a steady-state value after ~500 s for the three electrodes. The devices based on TBC-K1.1, TBC-K2.8 and TBC-K3.6 present a leakage current of around 0.15–0.17 mA (~0.08–0.10 A g^{-1}) after 1 h of potential holding (inset in **Figure 5-11 B**). These values are in agreement with those reported for other AC-containing devices assembled in similar conditions (~0.2–0.4 mA) [171,172].

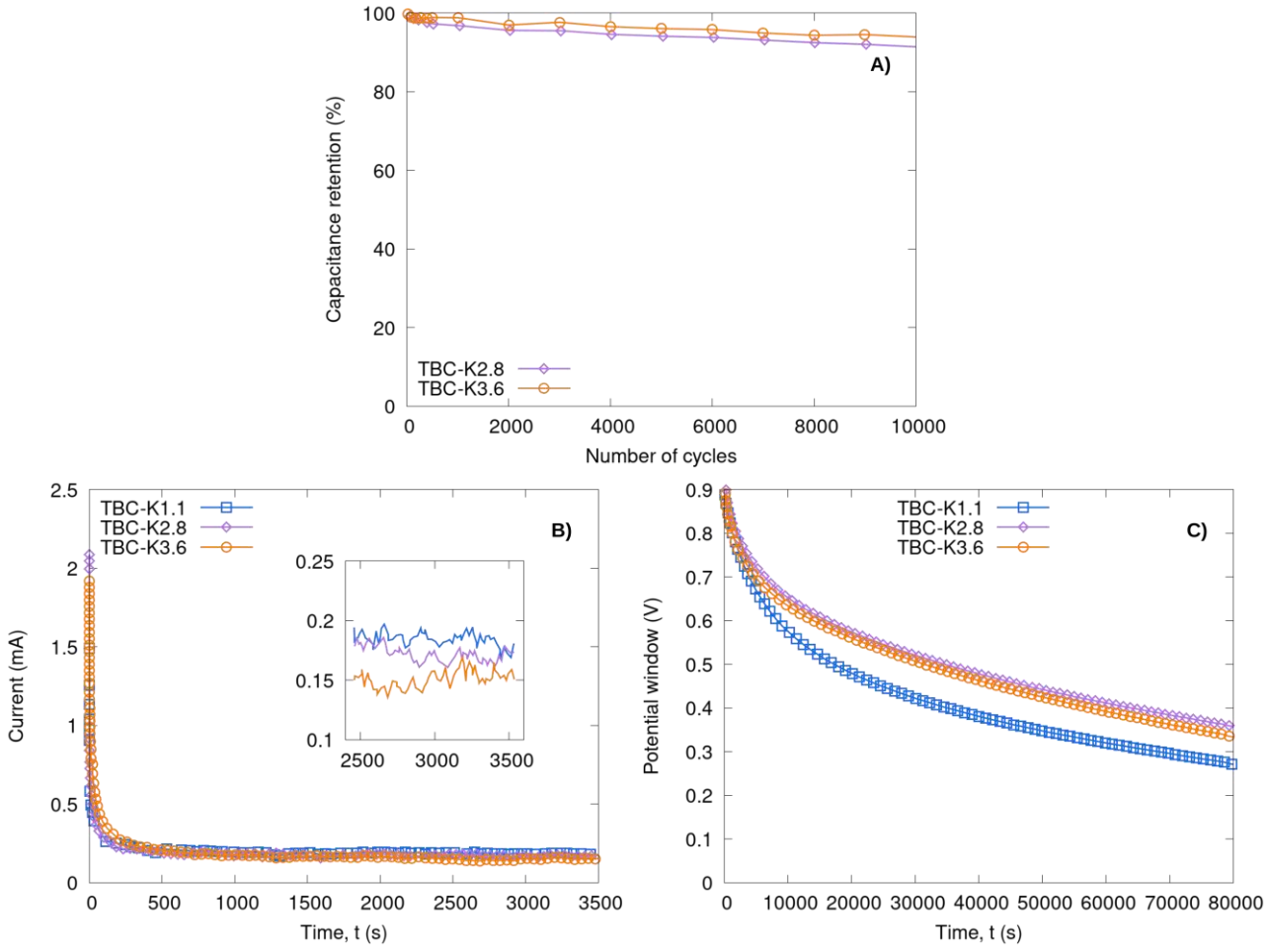

Figure 5-11 A) Cycling stability performed at 5 A g^{-1}, B) Time-dependent leakage current at 0.9 V, and C) Self-discharge curves from 0.9 V of ECs based on representative samples of TBC.

Additionally, the dissipation charge by leakage (~0.08–0.10 A g^{-1}) is 10 times lower than the charging current density (1 A g^{-1}), which shows the efficient charge of the ECs [173]. As AR increases, a slightly lower steady-state current is noticed, which can be attributed to a lesser amount of unstable oxygen-containing species, which can undergo irreversible redox reactions or serve as reactive sites for carbon electrooxidation [87,173]. Consistently, a more severe potential decay was observed for the cell based on TBC-K1.1. The time required to retain 50% of the initial voltage ($t_{0.5\,V}$) increases from ca. 6.9 h for TBC-K1.1 to 12.0 h and 13.3 h for TBC-K3.6 and TBC-K2.8, respectively. Similarly, the potential retention after 24 h of self-discharge follows the sequence: TBC-K1.1 (29%) < TBC-K3.6 (36%) < TBC-K2.8 (38%). The faster self-discharge of the former material is in good agreement with: (i) its higher content of oxygen-containing groups (O_{XPS} = 12.1 at.%); and (ii) its lower pore volume (V_{NLDFT} = 0.49 cm3 g^{-1}), which hinders charge redistribution by blocking access to the pores [174].

5.2 Hydrothermal doped tannins-derived carbon materials

5.2.1 Synthesis of N- and B-doped tannins-derived carbon materials through hydrothermal carbonization

In this section, we delve into the results of the hydrothermal carbonization synthesis of materials doped with nitrogen and boron and their subsequent carbonization as described in **section 4.1.2**. The results center around assessing how the dopants and their concentrations influence the morphological, structural characteristics, and chemical composition of the resulting carbon materials, unraveling the effect of nitrogen and boron incorporation during the hydrothermal carbonization process. The presented findings shed light on the tailored modifications achieved, providing a comprehensive understanding of how these dopants influence the resulting materials properties and chemical composition. Through an analysis of morphology, thermal behavior and chemical composition, this exploration aims to contribute valuable insights on the field of advanced materials synthesis, focused on tannins-derived carbon materials.

The alterations in the morphology of tannins-derived materials resulting from hydrothermal carbonization utilizing aqueous ammonia (coded N4THC and N8THC) or boric acid solutions (coded B4THC and B8THC) are visually depicted in the upper section of **Figure 5-12**. Additionally, the non-doped material (coded THC) is included for comparison. Meanwhile, the lower section of **Figure 5-12** presents the TEM images of the carbonized samples under a nitrogen atmosphere at 800°C for 2 hours, occupying the same position in the figure.

It is possible to observe that THC is constituted by spherical particles of approximately 500 nm. This observation aligns with the anticipated outcomes of hydrothermal carbonization [65], and specially for tannins, as demonstrated by Braghiroli et al. [175]. In their study, they observed spherical particles with diameters ranging from 200 nm to 5 µm, depending on the reaction time and temperature. It is noteworthy that the sphericity of these particles tends to increase with prolonged reaction times. Both B4THC and B8THC materials similarly showcase spherical particles with a particle size comparable to THC, indicating a lack of significant influence from boric acid on the materials morphology. In contrast, N4THC and N8THC reveal smaller, more cohesive spherical particles with an approximate diameter of 50 nm. This disparity suggests that the introduction of controlled nitrogen in the form of aqueous ammonia induces a noteworthy reduction in particle size and fosters a greater degree of particle cohesion. Nonetheless, it is crucial to note that comparable research conducted by Braghiroli et al. [54], exploring various methodologies for introducing nitrogen into tannins-derived carbon, suggests that N-doped carbon materials obtained through hydrothermal carbonization, similar to those in the present study, exhibit particle sizes comparable to the non-doped carbon materials.

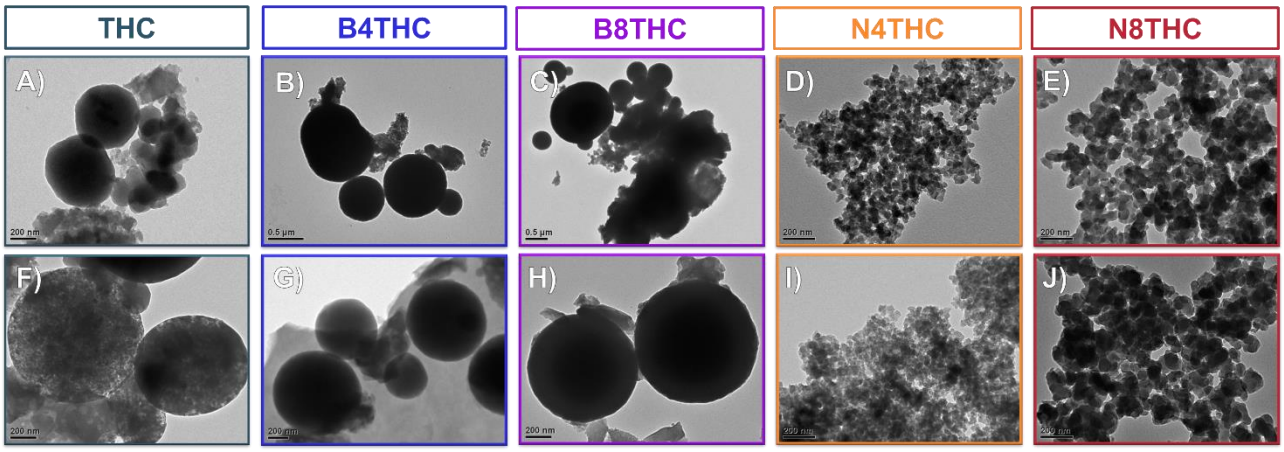

Figure 5-12 TEM images for: A-E) materials obtained from HTC step, coded from left to right as THC, B4THC, B8THC, N4THC and N8THC, and F-J) for the respective carbonized materials at 800°C.

This intriguing discrepancy might be attributed to either the inherent nature of the tannins utilized, derived from *Pinus radiata* bark in contrast to the tannins employed by Braghiroli, sourced *from Acacia mearnsii* bark (please refer to Celzard and Fierro [16]), or variations due to the quantity of aqueous ammonia utilized during the hydrothermal carbonization process. These divergent observations underline the complex interplay between the source material and the specific experimental conditions, emphasizing the need for further investigations to elucidate the factors contributing to variations in particle size in N-doped carbon materials derived from different tannin sources and processing methods.

An interesting observation arises concerning the impact of carbonization on the nanoscale architecture of the materials. The TEM images clearly illustrate that carbonization leads to the development of porosity without significant alteration to the overall morphology of all materials. This phenomenon is distinctly observed when comparing Figure 5-12 TEM images from **Figure 5-12 A** and **Figure 5-12 F**. Despite the process of carbonization, the original spherical shape and structural integrity of the materials persist, highlighting the unique ability of hydrothermal carbonization to enhance porosity without compromising fundamental morphological features [65,110]. The formation of pores enhances surface area and accessibility, crucial factors for electrochemical applications such as capacitors.

As a matter of fact, the N_2 adsorption-desorption isotherms illustrated in **Figure 5-13** reveal a notable development of nanopores as a result of carbonization, evidenced by the increased adsorbed volume at low pressures [57] in all carbonized samples compared to their pristine counterparts. Nevertheless, despite this development of porosity, there are no significant modifications in the types of isotherms exhibited by the materials post-carbonization, in accordance with the earlier observations discussed for the TEM images.

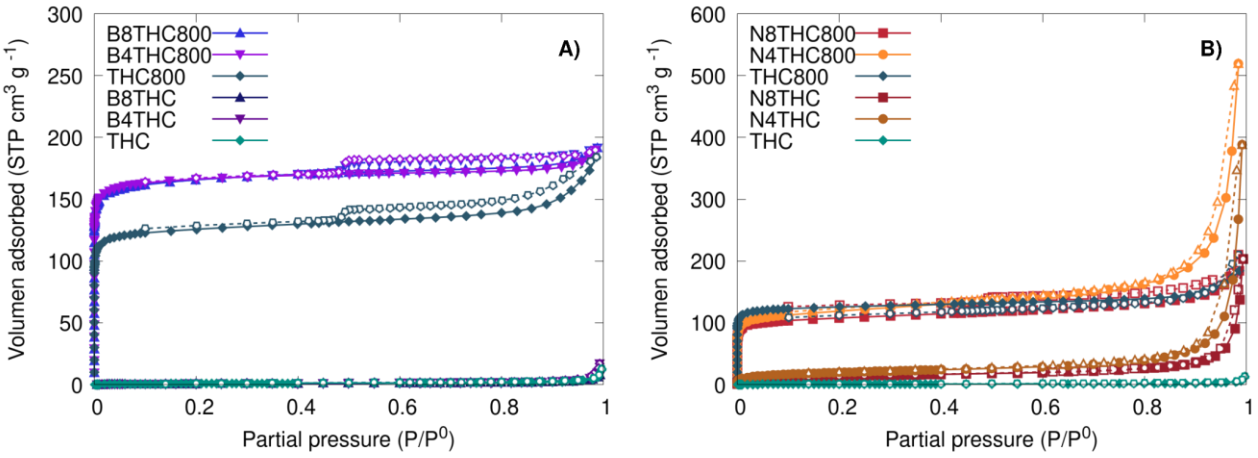

Figure 5-13 N_2 adsorption-desorption isotherms for doped tannins-derived materials. A) B-doped materials B) N-doped materials.

Moreover, in the context of doped samples, those treated with boric acid hydrothermal carbonization exhibit a similar isotherm, and closely resembling that of non-doped hydrothermally treated tannins, characterized as type I with hysteresis type 4, as depicted in **Figure 5-13 A**. Notably, the carbonization process fosters a more pronounced development of micropores in the B4THC800 and B8THC800 samples compared to the non-doped THC800 counterpart. Indeed, upon examination of **Table 5-4**, it becomes evident that both B4THC800 and B8THC800 exhibit a superior surface area compared to THC800. The values, obtained by applying the 2D-NLDF-HS model to N_2 and H_2 adsorption isotherms, reveal surface areas of 1115 and 1137 m^2g^{-1} respectively. Notably, these values surpass the surface area achieved by THC800, which stands at 992 $m^2\,g^{-1}$.

Conversely, as illustrated in **Figure 5-13 B**, the N4THC sample reveals a type III isotherms, characterized by the uptake close to the saturation pressure ($P/P^0 \approx 1$), with hysteresis type H3, and the respective carbonized sample N4THC800, displays may be classified by a type II isotherms, as a result of the micropore development, while retaining the hysteresis. Similarly, the N8THC sample mirrors the N4THC isotherm during adsorption for both pristine and carbonized sample. However, no discernible hysteresis is observed for this material. These findings underscore the role of aqueous ammonia in the hydrothermal carbonization of tannins as an agent to finely tune the textural properties of carbon materials derived from tannins. In terms of surface area, **Table 5-4** reveals that, concerning tannins-derived carbon materials obtained through hydrothermal carbonization with aqueous ammonia, both N4THC800 and N8THC800 exhibit marginally lower values compared to THC800. The specific values recorded for N4THC800 and N8THC800 are 905 and 912 $m^2\,g^{-1}$, respectively. The development of microporosity may be attributed to the initial creation of small pores, originating from the breakage of bonds within the most unstable structures, including the monomer units of tannins, as the temperature increases [176,177].

Commonly, carbonization involves three primary mechanisms: char formation, depolymerization, and fragmentation [178]. Char formation elucidates the creation of the carbon material matrix through the recombination of intra and intermolecular reactions, resulting in a higher degree of reticulation and increased thermal stability of the final product [49,178]. Simultaneously, the depolymerization and fragmentation of the raw material led to the generation of volatile compounds. The ratio of solid to volatile compounds is highly dependent on the heating rate [179]. At low heating rates (<10 °C min^{-1}), only the weakest chemical bonds break [180], minimally affecting the tannin structure, and favoring the rearrangement into a carbon matrix. In this context, the **Figure 5-14** illustrates the thermogravimetric analysis (TGA) revealing alterations of tannins materials resulting from the use of boric acid or aqueous ammonia solutions during the hydrothermal step.

An enhancement in the thermal stability of tannins is evident following hydrothermal carbonization. The untreated tannins (coded as TAN) exhibit a distinct peak at approximately 280-300 °C, attributed to the breakdown of the weakest C-C bond between the B-ring and C-ring of the monomer unit, catechin. This breakdown results in the volatilization of the B-ring compounds [176].Subsequently, there is a gradual reduction in mass losses, leading to a residual mass of approximately 43 wt.% at 800°C. This process facilitates char formation through recombination reactions between the polyphenol units, favoring the creation of a stable aromatic-like structure [132,177].

In the case of hydrothermal tannins (THC), there is a noticeable shift in the main peak to around 370-400°C, and subsequent gradual thermal degradation results in a residual mass close to 45.5 wt.%.

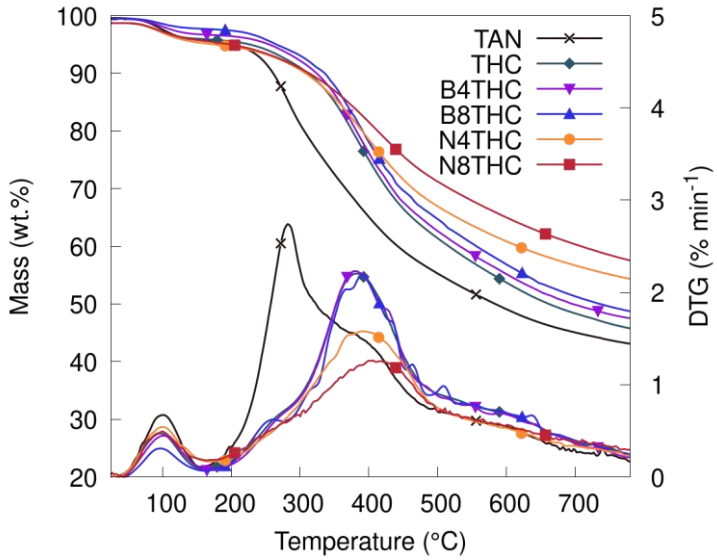

Figure 5-14 TGA and DTG characterization of the hydrothermal carbon materials obtained using aqueous ammonia (N4THC and N8THC) or boric acid (B8THC and B4THC) as doping agent, hydrothermal tannins without doping agent (THC) and tannins (TAN) as shown for comparison.

This peak is also observable in tannins treated with boric acid or aqueous ammonia solutions in the hydrothermal step, with comparable intensity in the cases of B4THC and B8THC, and a slightly lower intensity in the cases of N4THC and N8THC. The identified peak is also associated with the volatilization of B-ring compounds, corroborated by Py-GC-MS results [132,176] indicating catechol derivatives as the primary thermal products for all materials. Discrepancies in peak intensity are explicable through tannin amination, as detailed in section 2.3, leading to a higher quantity of soluble compound losses during the hydrothermal step due to the basic medium of the treatment. This basic environment enables the opening of the heterocyclic ring, amination of the B-ring, and even amination of certain C2' sites, facilitating the linkage of two distinct chains through an -NH- bridge [68,106]. Importantly, this process also contributes to an enhanced solid structure, evident in TGA results where both N4THC and N8THC exhibit a higher residual mass compared to the other materials, reaching values close to 57 wt.% and 54 wt.%, respectively. The preceding observations align with the recovery yields of materials after hydrothermal carbonization as it is shown in **Table 5-4**, with those treated with aqueous ammonia displaying the lowest yields, and also exhibiting a decrease in yield corresponding to the increase in aqueous ammonia concentration. Specifically, N4THC and N8THC have yields of 67.0 wt.% and 63.1 wt.%, respectively, which are lower than that of THC800, reaching 80.3 wt.%. Even when compared to materials treated with boric acid, both B4THC and B8THC show higher yields, reaching up to 79.4 wt.%. Nevertheless, following carbonization, all materials exhibit comparable yields, regardless of their prior treatment, within the range of 32.4 to 35.7 wt.%.

As previously discussed, carbonization significantly enhances porosity. In fact, the materials obtained after hydrothermal carbonization exhibit low surface area, with the highest value observed in N4THC reaching just 70 m^2 g^{-1}. Through the carbonization process, a substantial improvement is evident, pushing the material's surface area values close to 1000 $m^2 g^{-1}$. This development in surface area can be attributed to the volatilization of unstable structures, leading to the formation of micropores without altering the material's morphology. These unstable structures, predominantly oxygen functional groups [178], generate water vapor, hydrogen, carbon monoxide, and carbon dioxide [178,179]. In the case of phenolic materials, such as those under study, various low molecular weight compounds like phenol, catechol, or their derivatives are produced [18,176,181]. As a matter of fact, elemental analysis conducted on the materials pre and post carbonization reveals a marked decrease in oxygen content across all samples. For instance, the THC sample exhibits an oxygen content of 24.3 wt.%, which significantly reduces to 4.5 wt.% after carbonization.

In the case of materials treated with boric acid, both B4THC and B8THC present 24.7 wt.% oxygen content, and after carbonization there is a significant decrease in oxygen content. This reduction results in oxygen content values of 0.4 wt.% and 1.7 wt. % for B4THC800 and B8THC800, respectively.

Table 5-4 Elemental analysis and surface area summary for materials obtained via hydrothermal carbonization.

Sample	Yield (wt. %)	C (wt. %)	H (wt. %)	O [a] (wt. %)	N (wt. %)	B [b] (wt. %)	A_{BET} (m^2g^{-1})	S_{NLDFT} (m^2g^{-1})
THC	80.3 ± 0.6	70.3 ± 0.2	5.1 ±0.0	24.3 ± 0.3	0.3 ± 0.0	N.D.	3	--
B4THC	79.4 ± 0.4	70.0 ± 0.1	5.1 ± 0.1	24.7 ± 0.4	0.3 ± 0.0	0.9 ± 0.0	3	--
B8THC	79.4 ± 0.4	70.0 ± 0.1	4.9 ± 0.1	24.7 ± 0.4	0.3 ± 0.0	1.1 ± 0.0	3	--
N4THC	67.0 ± 1.1	70.7 ± 0.1	4.9 ± 0.1	17.9 ± 0.2	6.5 ± 0.0	N.D.	70	--
N8THC	63.1 ± 0.9	70.0 ± 0.1	4.8 ± 0.1	16.9 ± 0.4	8.3 ± 0.0	N.D.	50	--
THC800	32.4 ± 2.2	94.5 ± 0.7	0.8 ± 0.1	4.5 ± 0.8	0.2 ± 0.0	N.D.	503	992
B4THC800	34.3 ± 1.2	97.8 ± 0.5	1.0 ± 0.1	0.4 ± 0.6	0.8 ± 0.0	1.7 ± 0.1	668	1115
B8THC800	35.7 ± 0.7	96.5 ± 0.2	0.9 ± 0.0	1.7 ± 0.2	0.9 ± 0.0	2.1 ± 0.4	642	1137
N4THC800	33.2 ± 1.7	87.4 ± 0.2	1.3 ± 0.1	6.7 ± 0.3	4.6 ± 0.0	N.D.	451	905
N8THC800	35.6 ± 1.5	87.5 ± 0.3	1.5 ± 0.1	6.2 ± 0.5	4.8 ± 0.1	N.D.	420	912

[a] Estimated by difference, [b] determined by ICP

On the contrary, materials treated with aqueous ammonia exhibit lower oxygen content compared to the other materials after hydrothermal carbonization, with values of 17.9 wt. % and 16.9 wt. % for N4THC and N8THC. However, after carbonization, both aqueous ammonia treated materials reaching the highest levels recorded (6.7 wt. % for N4THC800 and 6.2 wt. % for N8THC800). It is crucial to emphasize that the primary objective of using boric acid or aqueous ammonia in the hydrothermal step is to introduce boron or nitrogen into the tannin matrix. On this regard, elemental analysis results confirm the successful incorporation of these elements in both cases. In the case of B4THC and B8THC, a similar boron content close to 1 wt. % is initially observed, which then increases after carbonization to reach levels of 1.7 wt. % and 2.1 wt. % for B4THC800 and B8THC800, respectively. For materials treated in aqueous ammonia, the nitrogen content reaches up to 6.5 wt. % and 8.3 wt. % for N4THC and N8THC, respectively. As a consequence of carbonization, in this case, the nitrogen content decreases to 4.6 wt. % and 4.8 wt.%.

This successful incorporation of doping agents not only offers valuable insights into the tailored chemical and morphological modifications induced by the hydrothermal carbonization process using controlled concentrations of aqueous ammonia or boric acid, as exposed on this section, but also opens avenues for the development of functionalized carbon materials with specific properties and their use in multiples fields such as electrocatalyst for OER in energy storage, including batteries and electrochemical capacitors, hydrogen storage, and in sensing applications [182].

In the subsequent sections, we will delve into the electrochemical performance of the carbon materials described in this section, exploring their textural properties and surface chemistry. It is crucial to note that the materials obtained were submitted to CO_2 activation to enhance their surface area, aiming for improved performance as electrodes in electrochemical capacitors.

5.2.2 Non-doped tannins-derived carbon materials characterization

In this section, we will focus on the textural properties and chemical composition of tannins subjected to hydrothermal carbonization, placing a particular emphasis on the transformative impact of CO_2 activation. The primary points of focus revolve around the effects of CO_2 activation on porosity development and alterations in surface chemistry. As discussed earlier, these aspects play a pivotal role in shaping the material suitability for electrochemical capacitors.

To clarify the impact of burn-off resulting from CO_2 activation, the sample THC800 is considered as the raw material, and therefore attributing a B.O. value of 0 wt. % to this sample. In the production of the final products, 1g of carbon materials (THC800) underwent N_2 flow at a rate of 100 mL min^{-1}, with the temperature gradually increasing from ambient temperature to reach 800°C at 10°C min^{-1}. Subsequently, a switch to CO_2 was made it, maintaining a flow rate of 50 mL min^{-1} by 1, 2 and 4 hours. The flow gas then reverted to N_2 flow during the oven cooling phase until it reached <100 °C. This procedure was iteratively conducted for each condition, yielding a minimum of 5 g for each final carbon material.

The **Table 5-5** shows the burn-off percentage, revealing a steady increase with the prolonged duration of activation. As expected, form the physical activation as detailed in **section 2.2**, there is a discernible rise in burn-off corresponding to the increased activation time. Specifically, the burn-off values escalate from 10 wt. % to 14.9 wt.%, and ultimately reach 24.9 wt. % for activation durations of 1, 2 and 4 hours, respectively.

The physical activation process exhibited minimal impact on the elemental composition of the carbonaceous materials. Notably, the only discernible difference lies in a slight and sustained increase in oxygen content, coupled with the respectively decrease in carbon content, as the activation time is extended, aligning with findings reported by Castro-Gutierrez et al. [119]. This phenomenon is attributed to the reactivity of CO2 with carbon within the matrix, leading to the generation of carbon monoxide and pyrolysis products [49,56]. Nevertheless, this alteration remains relatively marginal.

Concurrently, the results derived from X-ray Photoelectron Spectroscopy (XPS) highlight the absence of appreciable differences in the surface chemistry of the THC samples, indicating that gasification reactions extend beyond the material surface. Actually, the carbon content remains consistent, ranging between 97-98%, while the oxygen content ranging between 2-3%. Notably, the signals of the N 1s spectrum were too faint to enable a reliable quantification on these materials.

The detailed XPS deconvolution of the C 1s and O 1s spectra for the THC800 series is presented in **Appendix B 8.2.2**. The original C 1s and O 1s spectra are illustrated in **Figure 8-2**. Furthermore, **Table 8-1** provides peak assignments and area percentages for each peak in the C 1s spectrum, while **Table 8-2** presents the corresponding information for the O 1s spectrum.

Table 5-5 Burn-off, elemental analysis and XPS quantification for non-doped tannins-derived carbon materials.

Carbons	BO (%)	Elemental analysis C (wt. %)	H (wt. %)	N (wt. %)	O (wt. %)	XPS C (at. %)	N (at. %)	O (at. %)
THC800	0 [a]	94.5	0.8	0.2	4.5	97.3	N.D.	2.7
THC800-1	10.0	93.6	0.8	0.2	5.4	97.4	N.D.	2.6
THC800-2	14.9	93.3	0.7	0.2	5.8	97.2	N.D.	2.8
THC800-4	24.9	92.8	0.8	0.2	6.2	97.8	N.D.	2.2

[a] This burn-off values were assumed for the non-activated samples for the sake of comparison. The burn-off obtained for samples pyrolyzed at 800°C for 2h was 67.6 wt % for THC800.

As expected from carbon materials [136], the main peak in the C 1s spectra is observed at 284.4 eV (denoted as Csp^2), indicative of graphitic carbon, and suggesting the presence of carbon atoms arranged in a planar, hexagonal lattice structure. The spectrum also exhibits various peaks primarily associated with oxygen bonding. These include the C_2 peak at 285.5 eV, assigned to carbon atoms outside the basal planes with sp^3 hybridization. The C_3 peak at 286.4 eV is indicative of ether or hydroxyl bonding, while the C_4 peak at 287.6 eV suggests the presence of lactones or pyridines. The C_5 peak at 289.2 eV is associated with carboxylic acids, and the $C_{\pi-\pi^*}$ peak at 291 eV corresponds to HUMO-LUMO transitions related to the Csp^2 peak. In the O 1s spectrum, three main peaks are assigned at 530.9 eV, 532.3 eV, and 533.1 eV, corresponding to quinone groups, hydroxyl or ether functionalities, and carboxylic acid groups, respectively. An additional peak at 534.9 eV is assigned to chemisorbed water.

Noteworthy insights emerge from the XPS deconvolutions. In the C 1s spectra, a clear increase of the Csp^2 peak percentage area with activation time is evident, indicating an enhanced order of carbon within the structure, likely due to the evolution of gasification reactions on active sites. Improved fitting of the C 1s deconvolution is observed when excluding the C_3 peak associated with ether or hydroxyl bonding, a pattern similarly observed in the O 1s spectra, suggesting the absence of these functionalities.

The impact of oxygen functionalities on the capacitive performance of carbon materials has been extensively explored [36,37,87]. These functionalities play a pivotal role, influencing material wettability and inducing faradaic contributions through electron transfer. However, depending on their nature, they can either promote or hinder double-layer formation. Carboxylic acid, the predominant group in these materials, ranging from 49.6 at. % to 66.0 at. % depending on activation conditions, has demonstrated undesirable effects due to its strong polarity, leading to a leak current through catalytic effects and causing steric hindrance due to its large molecular structure [88]. This fact can explain, as discussed latter, the poor electrochemical behavior of these materials.

In contrast, quinone groups, representing the second-largest group in these materials with values ranging from 26.6 at. % to 37.9 at. %, are highly desirable. They exhibit electrochemical activity through reversible two-electron and proton-coupled electron transfers with hydronium ions, particularly in acidic solutions, thereby enhancing faradaic contributions [17,36,90]. Additionally, quinones facilitate an expanded potential window, demonstrate good chemical stability, and do not negatively impact electrode cycling stability [90].

The textural properties of the THC series were assessed through N_2 and H_2 adsorption-desorption isotherms, utilizing the 2D-NLDFT-HS model to estimate the pore size distribution, cumulative volume, and other pertinent parameters, as outlined in **Figure 5-15** and **Table 5-6**. As stated in the previous section, the THC carbon material exhibits a type I isotherm, indicative of a prevalence of micropores. These micropores are further enhanced through physical activation, a trend observed in the increasing nitrogen adsorbed volume at a partial pressure close to zero ($P/P^0 \approx 0$), as depicted in **Figure 5-15 A**. Similarly, there is a rise in hydrogen adsorbed volume, as illustrated in **Figure 5-15 B**. Notably, under the evaluated conditions, there is no conspicuous development of the characteristic knee at low pressures. However, a distinct N_2 uptake near the saturation pressure becomes pronounced with prolonged times of physical activation, transforming the isotherm into a type II, as can be observed for the THC800 4 carbon material. Additionally, the materials retain the H4 hysteresis observed in the raw carbon material THC800, unaffected by physical activation.

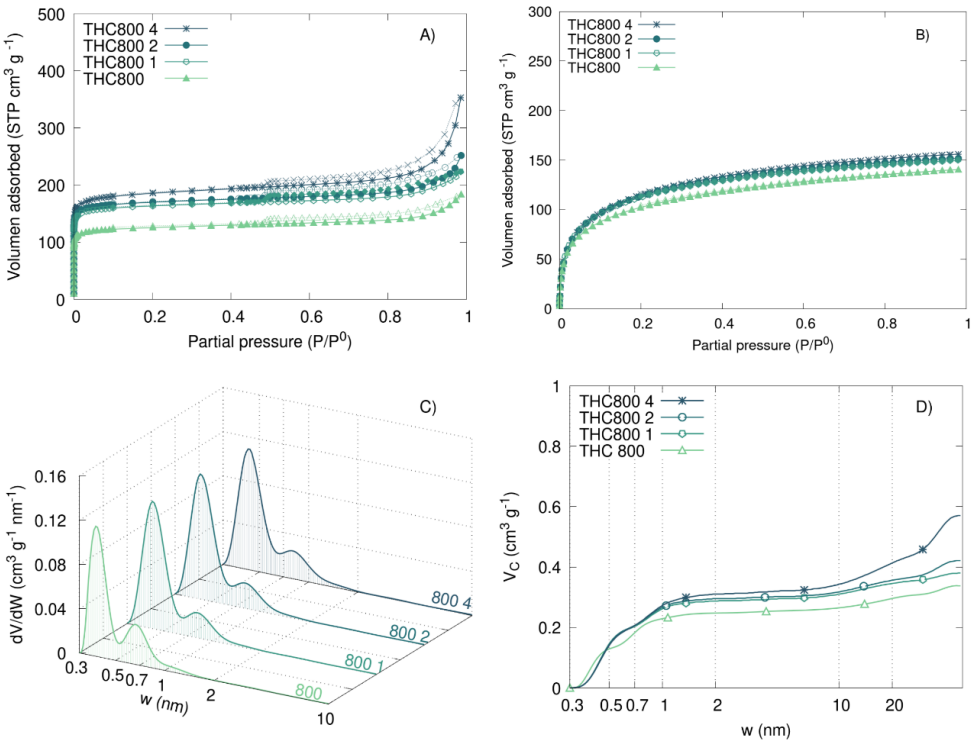

Figure 5-15 A) N_2 and B) H_2 adsorption (filled symbols)-desorption (empty symbols) isotherms at 77 K for THC series, C) Cumulative and D) Differential pore size distribution (PSD) estimated by 2D-NLDFT-HS for THC series.

Table 5-6 Textural properties obtained to apply 2D-NLDFT-HS to N_2 and H_2 adsorption isotherms of THC samples.

Carbons	A_{BET} (m^2g^{-1})	SSA (m^2g^{-1})	$V_{0.97}$ (cm^3g^{-1})	V_T (cm^3g^{-1})	‹$w_{u\mu}$› (nm)	$V_{u\mu}$ (cm^3g^{-1})	‹$w_{s\mu}$› (nm)	$V_{s\mu}$ (cm^3g^{-1})	‹w_{meso}› (nm)	V_{meso} (cm^3g^{-1})
THC800	505	992	0.173	0.339	0.5	0.182	1.0	0.065	21.7	0.091
THC800-1	655	1100	0.214	0.380	0.5	0.203	1.0	0.084	19.0	0.093
THC800-2	680	1110	0.229	0.421	0.5	0.206	1.0	0.089	22.8	0.126
THC800-4	730	1150	0.304	0.570	0.5	0.206	1.0	0.104	25.0	0.260

The pore size distribution (PSD) depicted in **Figure 5-15 C** reveals a prominent peak around 0.4 nm for all materials, characteristic of tannins-derived carbon materials [15,111] accompanied by a subtle peak in the range of 0.7 to 1 nm. Despite apparent consistency in micropore volume according to the PSD, the cumulative volume (**Figure 5-15 D**) shows a modest increase in the ultra-micropore region due to physical activation [151], with no significant variation based on activation time. Specifically, as depicted in **Table 5-6**, the ultra-micropore volume increased from 0.182 $cm^3\ g^{-1}$ for THC800 to 0.203 $cm^3\ g^{-1}$ after 1 hour of activation, reaching only 0.206 $cm^3\ g^{-1}$ after 2 hours, without a subsequent increase at 4 hours. Noteworthy differences emerge in the supermicropore region ($0.7\ nm < w < 1\ nm$), where cumulative pore volume rises from 0.065 $cm^3\ g^{-1}$ for THC800 to 0.104 $cm^3\ g^{-1}$ for THC800 4. Similarly, the mesopore zone of THC800 4 exhibits an increase in mean pore width, reaching 25.0 nm, and a mesopore volume of 0.260 $cm^3\ g^{-1}$. The pore development, while subtle under the explored physical activation conditions, translates to a moderate increase in surface area. Activation for 1 hour, for instance, leads to an approximate gain of 200 $m^2\ g^{-1}$, while prolonged activation times yield no notable surface area increase, reaching just 1150 $m^2\ g^{-1}$ for the material activated for 4 hours.

As mentioned in the concluding remarks of the preceding section, the primary objective of subjecting the carbon materials to physical activation was to enhance their surface area, with the ultimate goal to improve their potential as electrodes in electrochemical capacitors. Unfortunately, this endeavor was not successful, under the conditions evaluated for the non-doped materials, coded THC. The electrochemical behavior of these materials was assessed through cyclic voltammetry, as illustrated in **Figure 5-16 A**, employing various scan rates ranging from 5 mV s^{-1} to 1 V s^{-1}. The observed cyclic voltammograms unmistakably portray a subpar electrochemical performance.

From a positive perspective, the voltammograms reveal an absence of prominent peaks within the explored potential windows utilizing 1 M H_2SO_4 as electrolyte, suggesting the lack of significant chemical reactions. However, the capacitance values are considerably below the minimum expected for carbon materials, which is over 30 F g^{-1} per cell (120 F g^{-1} per electrodes) [13,144], even at the lowest scan rate explored (5 mV s^{-1}).

Moreover, at high scan rates, there is a distortion in the curves shapes, indicating a lack of electrical storage. Furthermore, the Trassatti's method [126] was employed to estimate the cell's capacitance, as depicted in **Figure 5-16 B** and **C**, where the intercept values indicate the double layer capacitance and the total capacitance of the cell. In both cases, the negative values indicate a lack of electrochemical storage. The lackluster performance in the electrochemical domain raises critical considerations regarding the underlying factors contributing to this outcome. The poor electrochemical response could be attributed to several factors, such as the limited development of the surface area during physical activation. However, as it can be seen on the **section 5.2.3**, carbon materials with similar textural properties have an improved electrochemical performance emphasizing the importance of surface chemistry on the electrochemical performance.

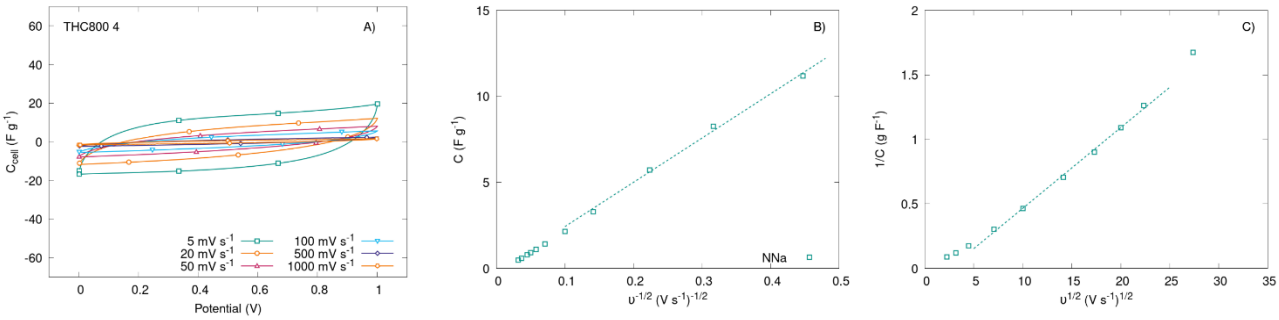

Figure 5-16 A): Cyclic voltammogram at scan rates from 5 mV s^{-1} to 1 V s^{-1} for the sample THC800-4, B and C): Dependence of capacitance to square of scan rate and its inverse to estimate electric double layer capacitance (C_{EDL}) and faradaic contributions (C_{PsC}).

In summary, it can be concluded that carbonaceous materials derived from tannins through hydrothermal carbonization, under the conditions evaluated, exhibit limitations in achieving electrochemical energy storage via the formation of the double electric layer. This limitation can be attributed to the hydrophobic nature of the materials, resulting from the lack of a substantial quantity of oxygenated functional groups where the major groups is the carboxylic, which are the undesirable given their strong polarity and steric hindrance, coupled with a limited development of porosity that hampers the efficient storage and transport of ions into the smallest pores. The observed challenges in electrochemical performance highlight the importance of addressing these material characteristics for enhanced energy storage capabilities.

On this context, the subsequent section will delve into the effects of doping on these carbons, exploring how this modification contributes to the development of the double electric layer and facilitates their fruitful performance as electrodes in double-layer capacitors. By investigating the impact of doping, we aim to uncover insights that could potentially overcome the current limitations and pave the way for the optimization of these materials for efficient electrochemical energy storage.

5.2.3 N-doped and B-doped tannins-derived carbon materials characterization

This section focuses on analyzing the electrochemical performance of the tannins-derived carbon materials described in **section 5.2.1**, which were doped using controlled concentrations of aqueous ammonia or boric acid. In order to develop their surface area, these carbon materials were submitted to CO_2 activation at 800°C by 4 hours. Analyzing as a whole, the morphology, the textural properties, the surface chemistry, and the electrochemical behavior of these materials, there is still necessary to unravel the underlying mechanisms that govern their performance, with a particular focus on the impact of dopants. This comprehensive investigation seeks to unravel the complexities of tailored modifications, providing crucial insights into the potential enhancements and functionalization of carbon materials.

On the same way that in **section 5.2.2**, the carbonized samples (THC800, B4THC800, B8THC800, N4THC800, and N8THC800) were considered as the raw material, and therefore assigning a burn-off (B.O.) value of 0 wt.% to these sample. This approach aims to clarify the specific impact of burn-off resulting from CO_2 activation. It is crucial to highlight that, for comprehensive characterization, the samples were synthesized multiple times under identical conditions. Additionally, while different activation times were explored, similarly to the THC800 series exposed on the previous section, the discussion is centered exclusively on the carbon materials activated for 4 hours. This ensures a well-defined and thorough examination of the pertinent aspects under consideration.

In

Table 5-7, a summary of the burn-off, chemical composition, and surface chemistry is provided for the carbon materials doped with nitrogen or boron, and subjected to a 4-hour physical activation. The reference sample (THC800 4), discussed in the previous section, is included for comparison. The results reveal that materials treated with boric acid exhibit a lower burn-off than the non-doped carbon material (THC800 4), reaching 9.5 wt. % for B4THC800 4 and 20.0 wt. % for B8THC800 4. Conversely, materials treated with aqueous ammonia solution show a significantly higher burn-off, reaching up to 42.9 wt.% and 27.8 wt.% for N4THC800 4 and N8THC800 4, respectively. Counterintuitively, it appears that a higher concentration of the doping agent leads to burn-off levels close to those of the reference sample (24.9 wt. %).

The elemental analysis reveals some differences respect to the carbonized samples (refer to **Table 5-4**). As discussed in **section 5.2.2**, physical activation leads to an increase in oxygen content for all samples, irrespective of the type of doping. Remarkably, the N-doped carbon materials exhibit a significant rise in oxygen content, increasing from 6.7 wt. % and 6.2 wt. % to 13.2 wt. % and 13.1 wt.% for the carbonized and physically activated N4THC and N8THC carbon materials, respectively.

Table 5-7 Burn-off, elemental analysis and XPS quantification of tannins-derived carbon materials doped with boron or nitrogen, submitted to CO_2 activation at 800°C by 4 hours.

Carbons	B.O. (wt. %)	Elemental analysis C (wt. %)	H (wt. %)	N (wt. %)	O (wt. %)	XPS C (at. %)	N (at. %)	O (at. %)	B (at. %)
THC800 4	24.9	92.8	0.8	0.2	6.2	97.8	N.D.	2.2	N.D.
B4THC800 4	9.5	95.2	0.8	N.D.	4.0	96.4	N.D.	3.3	0.28
B8THC800 4	20.0	95.4	0.9	N.D.	3.7	95.6	N.D.	4.4	N.D.
N4THC800 4	42.9	82.2	1.4	3.2	13.2	93.0	3.3	3.7	N.D.
N8THC800 4	27.8	81.8	1.6	3.5	13.1	92.8	3.9	3.3	N.D.

Similarly, the B-doped carbon materials show an elevation in oxygen content, rising from 0.4 wt. % and 1.7 wt. % for B4THC800 and B8THC800 to 4.0 wt. % and 3.7 wt. % for the CO_2-activated materials B4THC800 4 and B8THC800 4. The nitrogen path is different, showcasing a decrease in nitrogen content when comparing the activated carbon materials (3.2 wt. % and 3.5 wt. % for N4THC800 4 and N8THC800 4, respectively) with their carbonized counterparts (4.6 wt. % and 4.8 wt. % for N4THC800 and N8THC800, respectively), evidencing the high thermal reactivity of nitrogen functionalities [91]. Unfortunately, quantifying boron through ICP analysis was unfeasible due to insufficient material for conducting this analysis.

Nevertheless, the absence of boron quantification in the bulk material is compensated by the XPS quantification employed for surface characterization, revealing the presence of boron. Specifically, in the case of the B4THC800 materials, the carbonized material exhibits a moderate boron content of 0.31 at. %, while B4THC800 4 shows 0.28 at. %, indicating the successful doping of boron atoms into the carbon lattice under these conditions. However, the boron signals in the B 1s spectrum of the B8THC800 4 material were too faint for reliable quantification. In the case of nitrogen, the N 1s spectra area shows a relative content of 3.3 at. % and 3.9 at. % for N4THC800 4 and N8THC800 4, respectively.

The deconvolution of the C 1s spectrum were used to estimate the carbon nature onto the surface of the carbon materials, as shown in **Table 8-5**. Additionally, the original spectra of the B4THC800 and N4THC800 series are depicted in Figure 8-3 XPS deconvolution for N4THC800 series: A) C 1s spectra, B) O 1s spectra, and C) N 1s spectra.**Figure 8-3** and **Figure 8-4**, respectively. The peaks assignments were performed in a similar way to those described in section 5.2.2, utilizing results obtained from previous research [14,136–138]. On all cases, the main peak is associated with sp^2 hybridization of the carbon, evidencing the carbon layer formation.

It is important to highlight that the formation of a graphitizable structure is improbable in the absence of any graphitization catalyst, as elucidated in the comprehensive review by Celzard and Fierro [16]. As a matter of fact, the carbon structure derived from tannins, as evidenced by Raman spectra [183] and WAXS analysis [184], tends to exhibit characteristic consistent with glassy carbon.

Moreover, the nature of other elements such as oxygen, nitrogen and boron are of great interest, particularly in this research. In the case of N-doped materials, the O 1s and N 1s deconvoluted peaks assignment and optimized percentage area are shown in **Table 8-6**.

Unlike the undoped samples (THC800 series), the main contribution is made by the O_1, representing quinone-like groups, which are highly desirable in the electrochemical field due to their faradaic contributions [17,36,90], and excellent chemical stability that allows the expansion of potential windows [90]. Their contribution reaches a value of 61.4 at. % and 66.4 at. % for N4THC800 4 and N8THC800 4. The second main contribution for oxygen is the O_2 peak representing hydroxyl or ether groups and reach up to 16.8 at. % and 16.4 at. % for the same materials. These functionalities have been demonstrated to improve the wettability of electrolytes on the carbon surface, reducing mass transfer resistance [37], and also introducing faradaic contributions, although in smaller amounts than quinones [36]. The third peak at 533.1 eV, named O_3 and related to carboxylic acids, represents 14.9 at. % and 11.4 at. % of the total oxygen area. As discussed previously, these are undesirable functionalities that demote the electric double layer due to their strong polarity and steric hindrance [88]. Another peak at 534.1 eV was assigned in the O 1s spectrum due to the presence of nitrogen that form nitrogen oxides. The presence of this functionalities, in this case, cannot be neglected and reaches values between 3 and 4 at. %.

For the N 1s spectrum, it is recommended to assign four peaks according to the nature of nitrogen functionalities into the carbon matrix [137]. In this case, the N-doped materials have the main peak at 398.3 eV, named N_6, related to pyridinic groups present on the edge of the carbon layers. These groups are commonly linked to an increase in capacitance due to redox reactions, particularly in acid electrolytes [38,185]. Similarly, N_5, whose peak is assigned at 400.2 eV represents the third functionality, with values of 19.5 at. % and 24.0 at. % for N4THC800 4 and N8THC800 4, respectively. The second representative peak in area is named N_Q, assigned to nitrogen within the basal plane of the carbon lattice, representing close to 30 at. % on both N-doped carbon materials. This functionality is highly desired because it introduces one more electron on the system, enhancing the electronic structure of the carbon material by reducing the energy gap [185].

For B-doped materials, the O 1s and B 1s deconvoluted peaks assignment and optimized percentage area are shown in **Table 8-7**. In the O 1s spectrum, the same four peaks (O_1, O_2, O_3 and H_2O) are assigned in the same way as previously exposed, with an additional fourth peak at 531.5 eV assigned to oxygen bonded to boron [14].

Notably, there are remarkable differences in the nature of oxygen that can be useful for explaining variations in the electrochemical behavior between these two samples. For the B4THC800 4 material, the main peak area is associated with phenol or ether functionalities (O_2) reaching up to 61.3 at. %, followed by quinones-like groups (O_1) at 28.0 at. %. The curve was well-fitted without the inclusion of carboxylic acid functionalities. Additionally, oxygen bonded to boron (B-O) represents 10.7 at. %. Meanwhile, for the B8THC800 4 material, the primary functionalities are quinones-like groups (49.7 at. %), followed by carboxylic acids (42.1 at. %).

In this case, the deconvolution was well-fitted without the inclusion of the O_2 peak representing ether or hydroxyl functionalities, and also without the B-O peak. The latter observation aligns with the previously mentioned faint signal in the B 1s region. Concerning the nature of boron, it is primarily found in three forms: (1) BC_3, which indicates boron carbide bonded exclusively by carbon atoms within the inner structure of a carbon layer. This type of boron is particularly intriguing due to the electron deficiency, creating positively charged holes that facilitate electron transfer throughout the carbon structures, thereby enhancing electronic conductivity [39,182]. Additionally, boron can manifest as (2) BCO_2 and (3) BC_2O, which can generate extrinsic defects and active sites [138].

The deconvolution of the B1s spectrum (for detailed information, refer to **Table 8-7** in **Appendix 8.2.2**) was well-fitted assigning two main peaks at 190.1 eV and 192.1 eV, representing BC_2O and BCO_2, respectively [14,138,186,187]. Notably, physical activation promotes the formation of BC_2O over BCO_2, as evidenced by the relative area for B4THC800, where there is a distribution of 19.0 at. % and 81.0 at. %, respectively. Conversely, for the physically activated material (B4THC800 4), the percentage area shifts 40.2 at. % for BC_2O and 59.8 at. % for BCO_2. This could serve as evidence for the rearrangement of boron within the carbon matrix due to physical activation.

The textural properties of the physically activated materials were assessed through N_2 and H_2 adsorption-desorption isotherms using the 2D-NLDFT-HS model [156], as commonly employed in this research. The N_2 and H_2 adsorption-desorption isotherms at 77 K are illustrated in **Figure 5-17 A** and **B**, respectively. Notably, the isotherm shapes remain comparable to their respective carbonized samples (refer **to Figure 5-13** in **section 5.2.1**). The main distinction lies in an increase in the adsorbed volume at low pressures ($P/P^0 \approx 0$), indicating the development of microporosity [57,188,189]. In fact, all the materials exhibit a similar N_2 adsorbed volume at low pressures. Subsequently, differences become evident, with both B-doped carbon displaying a similar type I isotherm. On the other hand, THC800 4, along with both N-doped carbon materials, exhibits a combination of type I and II isotherms. Particularly, in the N4THC800 4 material, there is a broadening of the knee (also referenced as point B), indicative of widened pores [57,133], a slight tendence to increase the adsorbed volume in the partial pressure range between 0.1 to 0.8, suggesting mesopores development [57,190], and finally, the highest uptake indicative of macropores or interstitial condensation, typically from slit-like pores [188].

The H_2 adsorption isotherms, utilized as reference for ultra-micropores characterization [134], exhibit a similar curve for all the materials. In fact, as depicted in **Table 5-8**, nearly all the materials, with the exception of the N4THC800 4 sample, display comparable ultra-micropore volume, with values close to 0.210 $cm^3 g^{-1}$. Conversely, the N4THC800 4 material demonstrates a slightly lower ultra-micropore volume (0.178 cm^3 g^{-1}), aligning with the H_2 adsorption isotherms, where this material exhibits the lowest adsorbed volume.

The pore size distributions (PSD) presented in **Figure 5-17 C** highlight that the main peak for both B-doped and THC800 4 carbon materials is centered close to 0.4 nm, aligning with expectations for PSD in carbon materials derived from tannins [67,119,121]. Additionally, a secondary, subtle peak emerges near 0.7 nm. This secondary peak is more pronounced in both B-doped carbon materials compared to THC800 4.

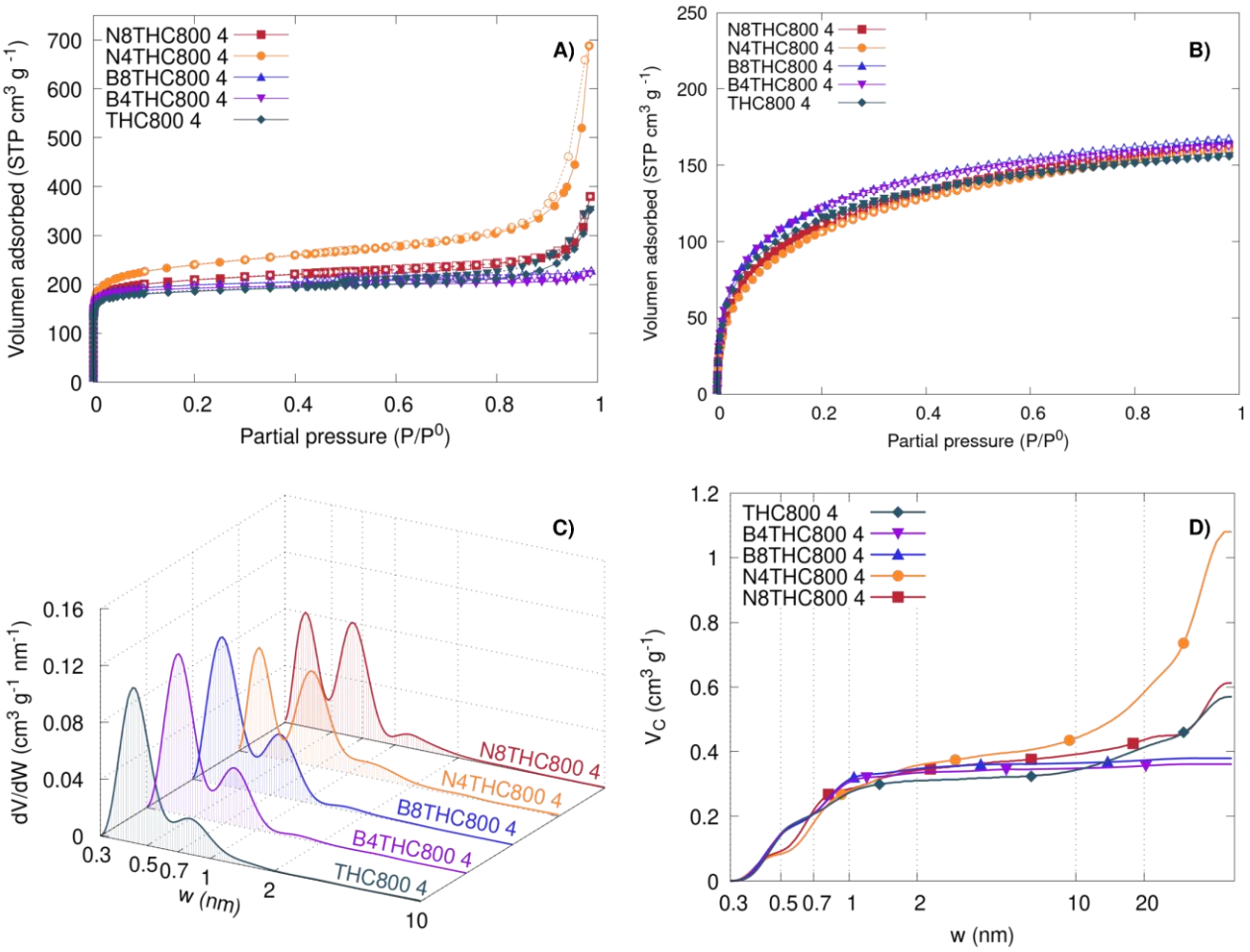

Figure 5-17 Textural characterization results for doped-carbon materials submitted to CO_2 activation by 4 hours: A) N_2 adsorption-desorption isotherms, B) H_2 adsorption isotherms, C) PSD and D) Cumulative volume obtained from N_2 and H_2 adsorption isotherms applying 2D-NLDFT-HS model.

Table 5-8 Summary of textural properties obtained to apply 2D-NLDFT-HS to N_2 and H_2 adsorption isotherms.

Carbons	A_{BET} (m^2g^{-1})	SSA (m^2g^{-1})	$V_{0.97}$ (cm^3g^{-1})	V_T (cm^3g^{-1})	$\langle w_{u\mu} \rangle$ (nm)	$V_{u\mu}$ (cm^3g^{-1})	$\langle w_{s\mu} \rangle$ (nm)	$V_{s\mu}$ (cm^3g^{-1})	$\langle w_{meso} \rangle$ (nm)	V_{meso} (cm^3g^{-1})
THC800 4	730	1150	0.304	0.570	0.5	0.206	1.0	0.104	24.9	0.260
B4THC800 4	766	1200	0.214	0.357	0.5	0.208	1.0	0.126	11.8	0.027
B8THC800 4	781	1237	0.223	0.379	0.5	0.206	1.0	0.140	11.3	0.034
N4THC800 4	905	1200	0.519	1.080	0.5	0.178	1.1	0.178	26.4	0.727
N8THC800 4	805	1180	0.316	0.613	0.5	0.216	1.1	0.125	27.0	0.272

[a]: V_T, $V_{u\mu}$, $V_{s\mu}$, V_{meso}, $\langle w_{s\mu} \rangle$, $\langle w_{u\mu} \rangle$, $\langle w_{meso} \rangle$ are total volume, ultra-micropore volume, super-micropore volume, mesopore volume, average super-micropore size, average ultra-micropore size, average mesopores size, respectively, obtained by applying 2D-NLDFT-HS model to N_2 and H_2 adsorption isotherms.

Conversely, the N-doped carbon materials display two main peaks of similar intensity, centered around 0.4 nm and 0.7 nm, with a third peak between 1 and 2 nm. Notably, the peaks observed for B-doped carbon materials are more prominent than those for N-doped carbon materials. Accordingly, the volume of supermicropores (0.7 nm <*w*< 2 nm) is less developed in the THC800 4 material, with a pore volume of 0.104 $cm^3\ g^{-1}$. Despite clear differences in the main peaks, B4THC800 4 and N8THC800 4 exhibit almost equal pore volumes, measuring 0.126 and 0.125 $cm^3\ g^{-1}$.

Following this, B8THC800 4 demonstrates a volume of 0.140 $cm^3\ g^{-1}$, while N4THC800 4 presents the most substantial volume in this zone, measuring 0.178 $cm^3\ g^{-1}$. This is attributed to the developed burn-off of N4THC800 4 at this condition, leading to the wide opening of existing pores rather than the generation of new pores [57].

Related to mesopore zone, there is a lack of prominent peaks indicative of a broad distribution of mesopores or, in some cases, their absence. These differences can be appreciated through the cumulative volume depicted in **Figure 5-17 D**, where is observed that B-doped materials have an absence of pore volume over the 2 nm. Actually, as observed in **Table 5-8**, the mesopore volume for these samples reach values of 0.027 and 0.034 $cm^3\ g^{-1}$ for B4THC800 4 and B8THC800 4, respectively. It can be seen that THC800 4 have a less pore development in the mesopore zone between 2 and 10 nm observed by the plateau in this zone, and their pore development is centered on pores close higher than 10 nm, aligning with observations made them from the N_2 adsorption-desorption isotherms. On a similar way and related to the high uptake at the final of the N_2 adsorption isotherms, the N-doped carbon materials present a highly developed mesopore zone, where a notably increases can be noticed over pore size of 10 nm on both cases, with a notably superiority for N4THC800 4. This leads to a mesopore volume of 0.272 $cm^3\ g^{-1}$ for N8THC800 4 and a notably 0.727 mesopore volume of 0.727 $cm^3\ g^{-1}$ for N4THC800 4 presenting close to 44% and 67% of mesopore/micropore ratio, respectively.

From these observations, it can be noticed that acquired carbon materials manifest diverse isotherm patterns, suggesting discernible differences in both microporosity and mesoporosity. Despite these differences, the estimated surface area for the materials closely approximates 1200 m^2 g^{-1}. Considering surface area as a pivotal parameter for assessing the electrochemical performance of carbon materials, the existence of dissimilar carbon materials with comparable surface area facilitates a comprehensive and discerning analysis.

The electrochemical characterization was performed using a carbon electrode made of 85 wt. % carbon material, 10 wt.% PTFE, and 5 wt. % black carbon. A symmetric two-electrode cell assembly was employed, using identical electrode material for both anode and cathode. The electrolytes were soaked in 1 M H_2SO_4 as electrolyte, with a porous quartz fiber serving as membrane separator. The mass of the electrode approached 2 mg, possessing a disc-shaped configuration with a 5 mm diameter to achieve an approximate carbon load of 10 mg cm^{-2} [191].

Electrochemical impedance spectroscopy (EIS) was employed to assess the kinetic and mass transport performance of the carbon materials in 1M H_2SO_4 electrolyte. The **Figure 5-18 A** and **B** depict the Bode and Nyquist plot, respectively, with detailed Nyquist plots for each material presented in the subsequent figures. In the Bode plot, it is evident that a low frequency, the phase angle approaches -90° for all doped materials, indicating capacitive behavior [34]. THC800 4 is the sole material showing non-capacitive performance, with a phase angle starting near -70°. Notably, both N-doped carbon materials exhibit an extended plateau close to -90°, indicative of behavior resembling an ideal capacitor. Conversely, the curves for B-doped carbon materials exhibit a rapid decline with increasing frequencies, revealing some resistance elements in the electrode, particularly noticeable in the B8THC800 4 material.

Furthermore, varying shapes and sizes of semicircles are observed at high frequencies, signifying charge-transfer resistances in the materials. THC800 4 materials exhibit prominent resistance, followed by B8THC800 4, B4THC800 4, N8THC800 4, and N4THC800 4, this las one with minimal resistance.

The THC800 4 material exhibited the largest semicircle, indicating a substantial charge-transfer resistance. Moreover, the sample displayed semi-infinite Warburg impedance behavior in the mass transfer control region, as evidenced by the slope close to 45° at high values of Z_r, suggesting high resistance to ion diffusion from the bulk to the surface. THC800 4 demonstrated an equivalent series resistance (ESR) value of approximately 251.5 Ω cm^{-2}. The hindered ion diffusion into the carbon surface is associated with the abundance of carboxylic acid species on the carbon surface, which impedes double layer formation [88] and restrict access to the already narrow pores [36].

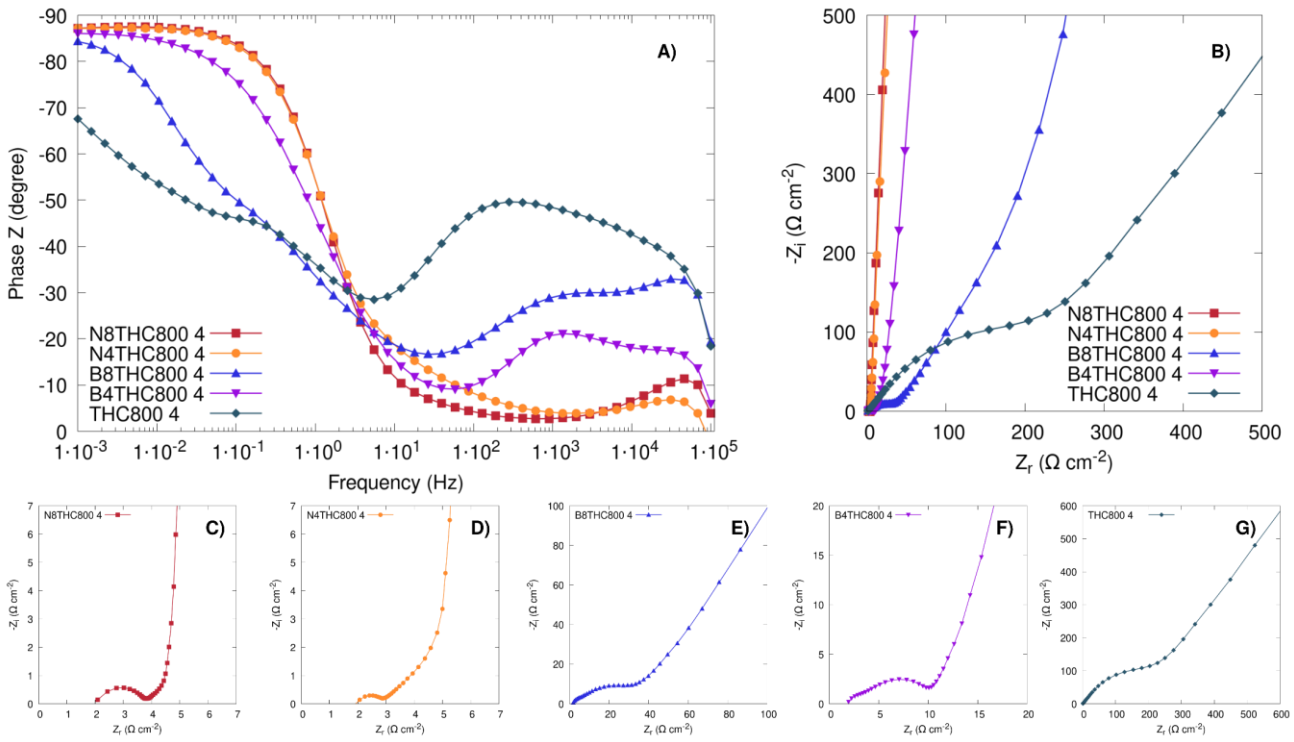

Figure 5-18 EIS results for symmetrical ECs using doped-carbon materials as electrodes and 1M H_2SO_4 as electrolyte: A) Bode plot, B) Nyquist plot at low frequencies; details of Nyquist plot on the kinetic control region for C) N8THC800 4, D) N4THC800 4, E) B8THC800 4, F) B4THC800 4, G) THC800 4.

The B-doped materials exhibit enhanced electrochemical features compared to THC800 4, particularly evident in the B4THC800 4 material, showcasing a significant reduction in charge-transfer resistance R_{CT}. Despite having similar textural parameters, both B-doped carbon materials exhibit distinct differences in EIS results, highlighting an improved electrochemical performance for B4THC800 4, attributed to its chemical surface characteristics. As indicated by XPS results, B8THC800 4 possesses a notable quantity of carboxylic acid species, similar to THC800 4, hindering electric double layer formation that explains the extended slope at 45° in medium frequencies. In contrast, B4THC800 4 predominantly features oxygen functionalities that enhance electrode surface wettability, thereby reducing mass-transfer resistance for ion diffusion. Additionally, the presence of boron may contribute to an improved electrical conductivity in the carbon structure [186], further decreasing charge-transfer resistance.

The N-doped carbon materials demonstrate superior electrochemical performance under the analyzed conditions, characterized by well-defined semicircles indicating charge-transfer resistance close to 3.0 Ω cm^{-2} for N4THC800 4, and 3.8 Ω cm^{-2} for N8THC800 4, accompanied by a subsequent straight line that tends to the infinite. Notably, both materials exhibit classic electrochemical capacitor curves, with a distinctive post-semicircle feature.

Following the semicircle, the N4THC800 4 material displays a slope close to 45°, indicative of mass-transfer resistance, while this tendency is slightly observed for N8THC800 4. Consequently, despite N4THC800 4 having a lower R_{CT}, both materials exhibit similar ESR values, reaching 4.8 and 4.6 Ω cm^{-2} for N4THC800 4 and N8THC800 4, respectively. The enhanced electrochemical performance of these materials can be attributed to the developed mesoporosity facilitating ion transport to the micropores [119], in conjunction with improved surface chemistry due to the presence of quinones and nitrogen functionalities.

Cyclic voltammetry (CV) was conducted over a range of scan rates, specifically from 5 mV s^{-1} to 1 V s^{-1}, utilizing a potential window spanning 0 V to 1 V. The corresponding curves for the doped carbon materials are illustrated in **Figure 5-19**. In agreement with the preceding EIS findings, it becomes evident that both N-doped carbon materials exhibit optimal performance, showcasing a square-shaped curve characteristic of electrochemical capacitors. Notably, no discernible peaks are observed. Furthermore, the voltammogram shape exhibits minimal variation with the escalating sweep rate, indicative of a predominant contribution from the electric double layer capacitance. Significant deviations from the idealized curve are only apparent at sweep rates of 500 mV s^{-1} and 1 V s^{-1}. These deviations are attributed to the constrained diffusion of ions [153] or the occurrence of irreversible polarization [192] at these elevated sweep rates.

This distortion agrees with the EIS results, highlighting a pronounced limitation related to ion diffusion. Consequently, there is an observable constraint on the electric double layer storage mechanism. Conversely, B4THC800 4 maintains a sustainable rectangular shape even as the sweep rate increases, with appreciable distortions emerging only at higher rates (500 mV s^{-1} and 1 V s^{-1}). This behavior is similar to that observed in both N-doped carbon materials. Although, notably distinctions exist between B4THC800 4 and the N-doped carbon materials, particularly in terms of the voltammogram's area, which emerges as a salient differentiating feature.

As discussed in **section 2.1**, energy can be stored in electrochemical capacitors through both the electric double layer and faradaic contributions. In this context, the capacitance nature of the doped materials was estimated using Trassatti's method [126], as illustrated in **Figure 5-19 E** and **F**. The y-axis intercept in **Figure 5-19 E** represents the electric double layer capacitance, while in **Figure 5-19 F**, represents the inverse of the total capacitance.

The total capacitance estimated for both N-doped carbon materials is notably similar, reaching values of up to 39.0 F g^{-1} and 40.1 F g^{-1} for N4THC800 4 and N8THC800 4, respectively. In each case, the electric double layer capacitance represents 88.8% and 88.3%, with the remaining differences attributed to Faradaic contributions. The resemblance between these two materials is expected due to their similar surface chemistry and textural properties, as previously elucidated.

However, as discussed in the following section, CO_2 activation reveals remarkable differences between these two carbon materials.

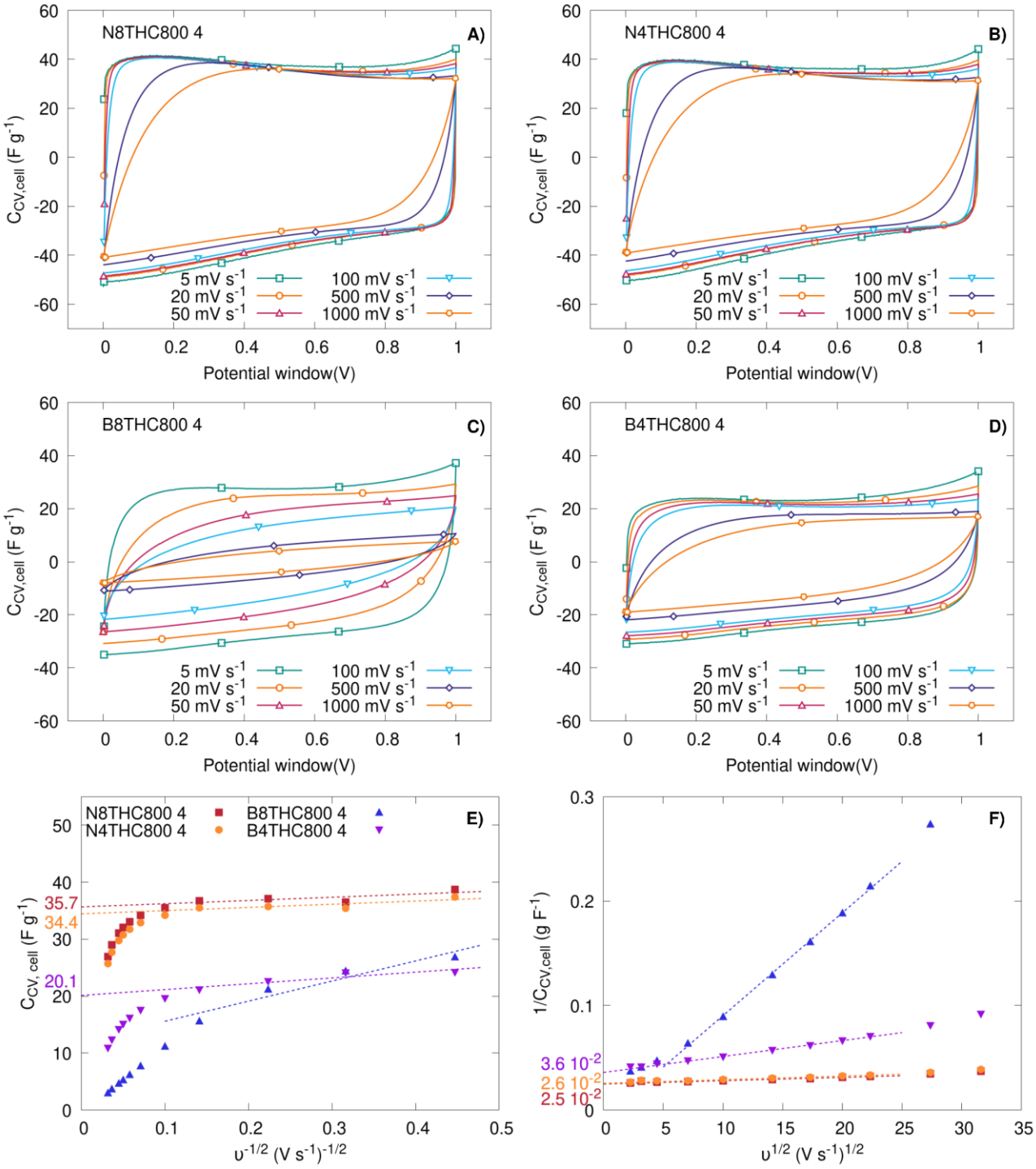

Figure 5-19 Cyclic voltammetry at scan rates ranging from 5 mV s-1 to 1 V s-1 using 1M H2SO4 as electrolytes and symmetrical electrolytes of the following carbon materials A) N8THC800-4, B) N4THC800-4, C) B8THC800-4, D) B4THC800-4; E) and F) refers to the dependence of capacitance as a function of the scan rate according to Trassatti's method.

For the B4THC800 4 carbon material, linear regression estimates a total capacitance of 27.8 F g^{-1}, whit 72% attributed to the electric double layer and the remaining percentage associated to faradaic contributions. It is noteworthy that not only is there a higher percentage of capacitance attributed to faradaic contributions compared to the N-doped carbon materials, but also a higher absolute value is achieved (7.6 F g^{-1}) in contrast to both N-doped carbon materials (4.5 F g^{-1}). This highlights the influential role of boron in enhancing the electrochemical activity of this material.

Finally, galvanostatic charge-discharge curves (GCD) were conducted across a range of specific currents ranging from 0.2 to 40 A g^{-1}. The GCD curves for each material, along with their respective fitted lines (in red) to estimate capacitance values, are presented in the **Appendix E**. To highlight differences between the materials, **Figure 5-20** illustrates the GCD curves at specific current of 0.5, 2, and 10 A g^{-1}, along with their respective ohmic potential drop (iR).

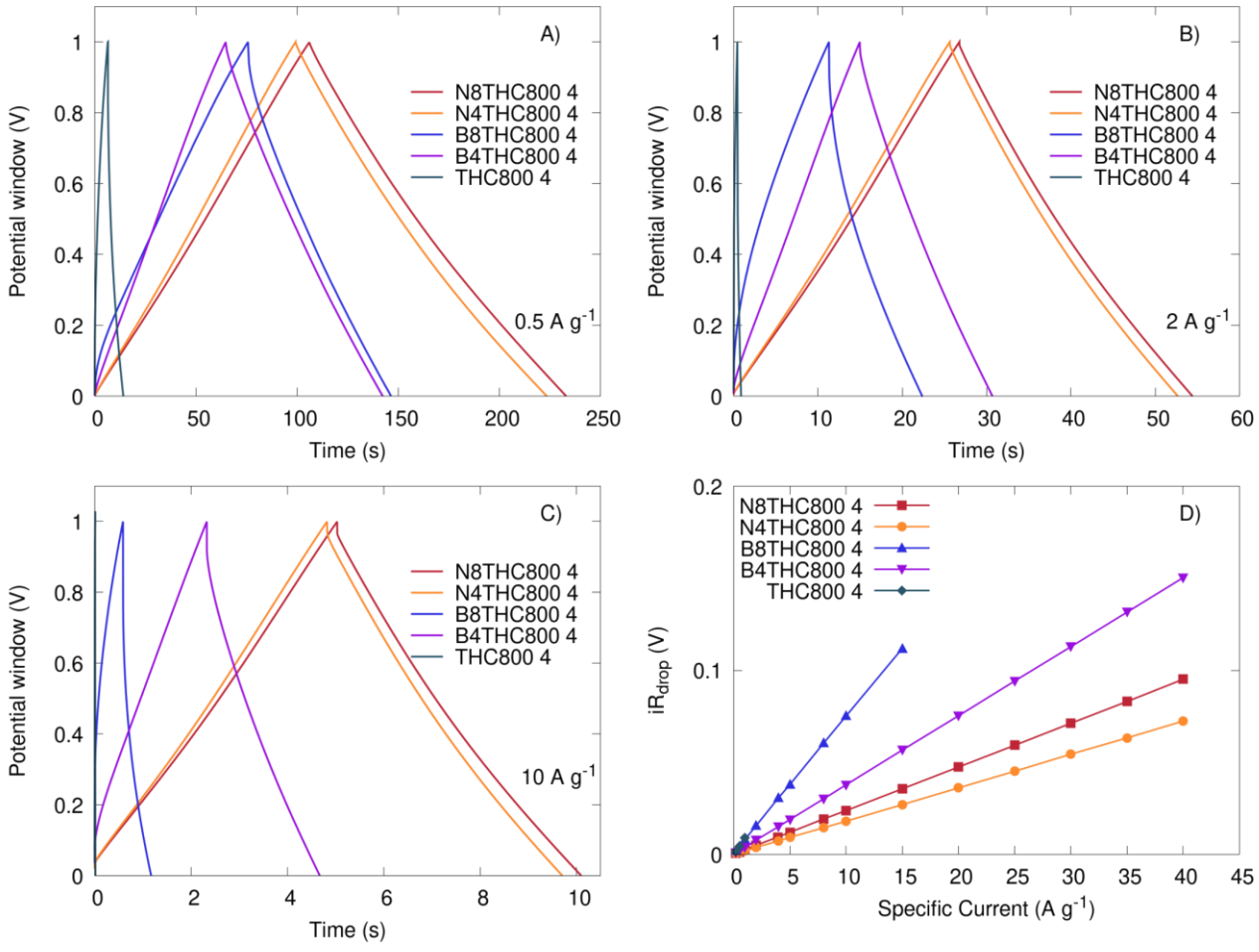

Figure 5-20 GCD curves at A) 0.5 A g^{-1}, B) 2 A g^{-1}, C) 10 A g^{-1}, and the respective IR drop as a function of the specific current for ECs using 1 M H_2SO_4 in symmetrical electrolytes of the hydrothermal doped-carbon materials submitted to CO_2 activation by 4 hours.

The GCD curves exhibit a rectangular shape for both N-doped carbon materials across the explored specific current, confirming their optimal performance in electrochemical capacitors, even under high-power conditions. Both B8THC800 4 and B4THC800 4 exhibit similar performance, exhibiting an extended discharge curve at low specific current (e.g. 0.5 A g^{-1}), resulting in coulombic efficiencies exceeding 100%. This phenomenon can be attributed to internal resistances that either delay the charge process or prolong the discharge process [140].

However, this effect diminishes with increasing specific current. In the case of B-doped materials, it is noteworthy that B8THC800 4 exhibits a charge-discharge time process similar to B4THC800 4 at a specific current of 0.5 A g^{-1}. Despite a clear distortion from the typical triangular shape, often associated with faradaic phenomena [140,193], as the specific current increases, the energy stored by the B8THC800 4 electrode cell significantly decreases compared to B4THC800 4, indicating its diffusion-limited performance, as mentioned earlier. The ohmic potential drop, illustrated in **Figure 5-20 D**, reveals electrical resistance in the cell increasing as the specific current rises for all materials, with lower values observed for the N-doped materials than the B-doped materials, aligning with the observed ESR values estimated from the Nyquist plot.

The **Figure 5-21** illustrates the cell capacitance values of the doped carbon materials, estimated from the discharge curve. Notably, following the approach recommended by Stoller et al. [139], these values were calculated utilizing the upper half of the discharge curve and were adjusted by subtracting the ohmic potential drop.

Aligning previous results, THC800 4 exhibit subpar performance, and the fitted line inaccurately represents its experimental discharge curve (refer to **Figure 8-7** on section **8.5**, **Appendix E**), suggesting capacitance overestimation. B8THC800 4 shows improved capacitance at low specific current ($C_{GCD,cell}$ of 24.7 F g^{-1} at 0.5 A g^{-1}) but diminishing rapidly at higher currents with 31.0% retention at 5 A g-1, and non-capacitive behavior at 10 A g^{-1}. Conversely, B4THC800 4 maintains similar capacitance at low current ($C_{GCD,cell}$ = 26.6 F g^{-1} at 0.5 A g^{-1}), and exhibits enhanced retention with values of 72% at 5 A g^{-1}, and even 52.5% at 20 A g^{-1}.

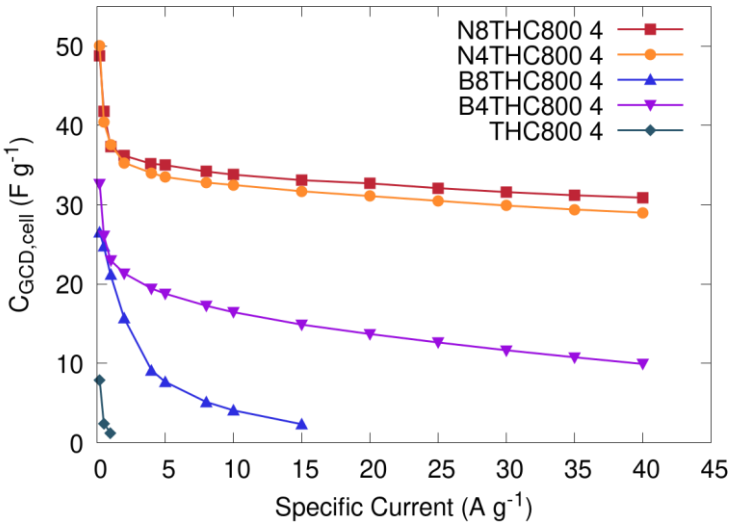

Figure 5-21 Capacitance as a function of the scan rate obtained from GCD discharge curves of the hydrothermal doped-carbon materials.

N-doped carbon materials (N4THC800 4 and N8THC800 4) showcase impressive capacitance values (40.4 F g-1 and 41.8 F g-1, respectively) despite their modest surface area (close to 1200 m^2 g^{-1}), underscoring the efficacy of nitrogen doping. Notably, these materials demonstrate formidable capacitance retention, reaching 82.9%, 77.1%, and 71.7% at 5 A g^{-1}, 20 A g^{-1}, and 40 A g^{-1} for N4THC800 4, and 83.7%, 78.1%, and 74.0% for N8THC800 4, respectively.

In summary, the doping method for nitrogen and boron significantly influences the surface chemistry and textural properties of the resulting carbon materials. Notably, the addition of doping agents, coupled with the specific nature of oxygen, brings about substantial alterations in the surface chemistry, ultimately enhancing the electrochemical performance of these carbon materials.

5.3 An extension analysis on N-doped tannins-derived carbon materials

The preceding section underscores the substantial impact of boron and nitrogen doping on the surface chemistry of the developed carbon materials, with notable performance enhancements observed for N-doped carbon materials. Both N4THC800 4 and N8THC800 4 exhibit comparable electrochemical performance, attributed to their similar surface chemistry and microporosity. However, as detailed in **section 5.2.1**, the morphology and textural parameters of the resulting N-doped carbon materials undergo modifications based on the use of aqueous ammonia and its concentration in the hydrothermal step. In this context, this section aims to elucidate the influence of aqueous ammonia and its concentration on the electrochemical performance of N-doped carbon materials, with a particular focus on the textural development and surface chemistry modifications arising from physical activation.

5.3.1 Surface chemistry and chemical composition

The chemical composition of the ACs in the bulk and on the surface was obtained through elemental analysis and XPS, respectively. **Table 5-9** shows a summary of these results as a function of the burn-off (BO) obtained to each AC. The elemental analysis of the materials revealed some notable features with increasing BO. For instance, the use of ammonia during the HTC step resulted in the incorporation of very similar N content, 4.6 and 4.8 wt.% in N4THC and N8THC, respectively. N content decreased after CO_2 activation to values of 3.0 – 3.7 wt.% for the N4THC-derived ACs and 3.3 – 4.2 wt.% for the N8THC-derived ACs. An increase in O content was observed as well, with the undoped material exhibiting approximately 4.5 wt. %, while N4THC800 and N8THC800 displayed an O content close to 6.7 and 6.2 wt.%, respectively.

The C content in the bulk decreased after 4 h activation with CO_2 at 800°C. This decrease was more pronounced for N-doped samples, suggesting a catalytic effect during the activation process, which aligns with the observed increase in the BO for the samples submitted to CO_2 activation for 4 h. In addition, these N-doped series exhibit a remarkable increase in O content, 13.2 and 13.1 wt.% for N4THC800-4 and N8THC800-4, respectively. Similarly, the series of carbons activated at 900°C follow a similar trend, with a slight decrease in C content and an increase in O content.

In contrast, the non-activated N-doped samples (N4THC800 and N8THC800) display a lower C content than the non-doped THC800 sample. Simultaneously, the O content increased both in the bulk material, based on elemental analysis, and on the surface, based on XPS analysis. As expected, the N content was noticeably higher in the N-doped samples compared to the non-doped samples. However, the N content did not show significant differences between the two samples in either bulk or surface composition.

Table 5-9 Summary of burn-off (BO), elemental analysis and XPS quantification for N-doped carbon materials.

Carbons	B.O. (%)	Elemental analysis C (wt. %)	H (wt. %)	N (wt. %)	O (wt. %)	XPS C (at. %)	N (at. %)	O (at. %)
N4THC800	0 [a]	87.4	1.3	4.6	6.7	93.6	3.6	2.8
N4THC800-1	10.6	87.3	1.3	3.6	7.8	94.8	3.0	2.2
N4THC800-2	18.1	87.5	1.2	3.4	7.9	94.7	3.0	2.3
N4THC800-4	42.9	82.2	1.4	3.2	13.2	93.0	3.3	3.7
N4THC900-1	35.3	87.8	1.3	3.7	7.2	94.5	3.1	2.4
N4THC900-1.5	49.8	88.1	1.5	3.5	6.9	94.7	2.6	2.6
N4THC900-2	70.0	86.7	1.5	3.0	8.8	94.3	2.8	2.9
N8THC800	0 [a]	87.5	1.5	4.8	6.2	92.6	3.9	3.5
N8THC800-1	10.2	88.0	1.4	4.2	6.4	93.9	2.8	3.3
N8THC800-2	16.4	88.1	1.4	4.2	6.3	92.7	4	3.3
N8THC800-4	27.8	81.8	1.6	3.5	13.1	92.8	3.9	3.3
N8THC900-1	21.2	87.6	1.5	3.5	7.4	94.1	2.7	3.2
N8THC900-1.5	50.2	87.4	1.4	3.5	7.7	94.0	3.1	2.9
N8THC900-2	59.9	87.3	1.4	3.3	8.0	93.5	3.9	2.6

[a] This burn-off values were assumed for the non-activated samples for the sake of comparison. The burn-off obtained for samples pyrolyzed at 800°C for 1h were ca. 48 %, and 47 % for N4TCH800 and N8TCH800, respectively. The rest of burn-off values correspond to those obtained after CO_2 activation.

The XPS results presented in **Table 5-9** suggests that in absence of N, the non-doped carbons exhibit similar chemical surface composition, i.e., C and O remained nearly the same, regardless of the BO that increase from approximately 10 to 25%. It is evident that the C content on the surface of the doped materials decreased compared to that of the THC800 materials due to the introduction of N functionalities by the amination synthesis process. The O content on the surface showed minimal variation between the non-doped and the two N-doped series, being slightly higher for the N8THC-derived materials.

The interpretation of the XPS spectra is based on previous studies [136,137,194], which provide valuable insights into this matter. For a detailed analysis of the relative atomic composition of the deconvoluted peaks in the C 1s, O 1s, and N1s regions for both N-doped tannin-derived carbons series, please refer to **Table 8-8** and **Table 8-9** in **section 8.2.3 (Appendix B)**. These tables allow a comprehensive understanding of the atomic composition of the materials.

As an illustrative example, **Figure 5-22 A, B and C** shows the XPS spectra and deconvolution of peaks for C 1s, N 1s, and O 1s regions, respectively, for the N8THC900-2 sample. The main peak observed in the C 1s spectra (**Figure 5-22 A**) is located at 284.4 eV, and named C_{sp^2}, which corresponds to graphitic carbon, indicating the presence of carbon atoms arranged in a planar, hexagonal lattice structure. Additionally, a range of peaks associated with N or O bonding can be identified. These include the C_D peak at 283.5 eV, which is associated with defects in five-member rings and/or to the formation of graphitic carbon nitrides. The C_2 peak at 285.5 eV is assigned to carbon atoms out of the basal planes, exhibiting sp^3 hybridization. The peak C_3 at 286.4 eV assigned to ether or hydroxyl bonded or C bonded nitrogen oxides. The C_4 peak at 287.6 eV indicates the presence of lactones or pyridines. The C_5 peak at 289.2 eV is assigned to carboxylic acids, while the $C_{\pi\text{-}\pi^*}$ peak at 291 eV is assigned to HUMO-LUMO transitions associated to the C_{sp^2} peak. The **Figure 5-22 B** shows the XPS spectra in the N 1s region with the corresponding peaks deconvolution. The two N-doped series showed pyridinic species, N_6 peak at 398.3 eV, as the main contribution, followed by N_5 species, peak at 400.2 eV, which are associated with pyrroles and/or pyridones. These two nitrogen functionalities are located on the edge of the carbon layers and are commonly linked to an increase in capacitance of N-doped carbon materials due to redox reactions, particularly in acid electrolytes [38,185].

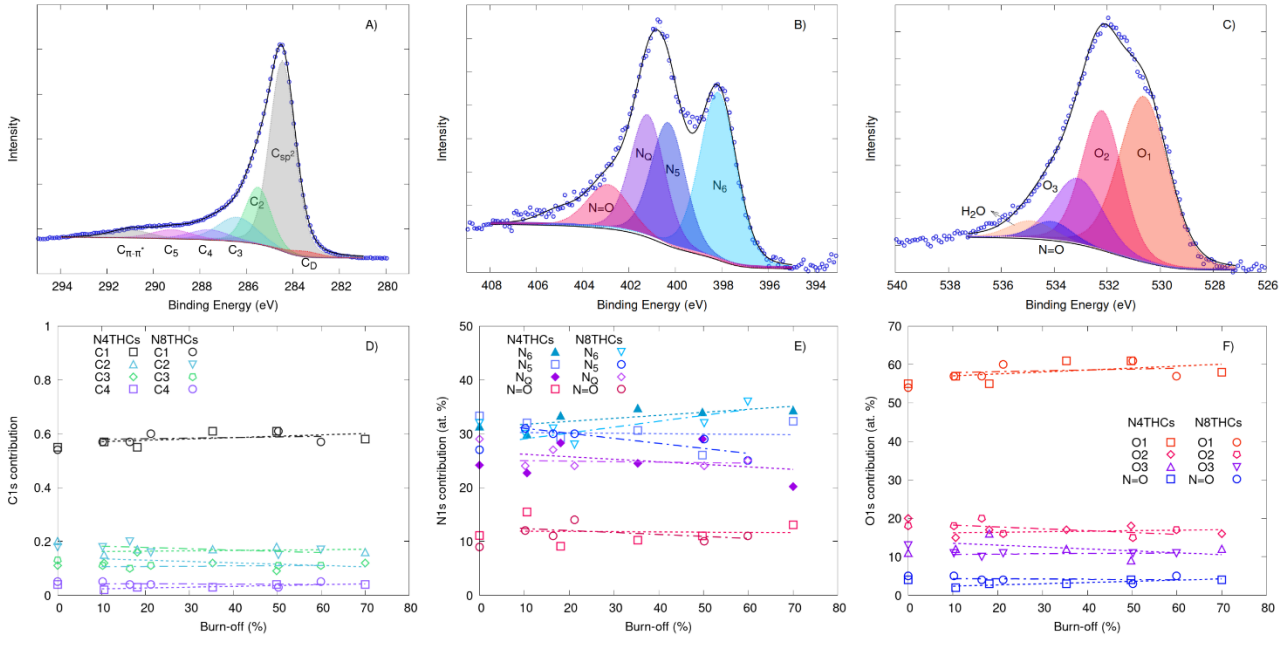

Figure 5-22 XPS spectra and deconvolution of C 1s, N 1s, and O 1s regions for the sample N8THC900-2. A): C 1s; B): N 1s; C): O 1s. D): Carbon functionalities contribution according to deconvolution of C 1s. E): Contribution of nitrogen functionalities according to deconvolution of N 1s region; and F): Oxygen functionalities contribution according to deconvolution of O 1s region for N4THCs (dashed trend line) and N8THCs series (dot-dashed trend line).

The N8THC series exhibited a slight increase in N_6 species over N_5 species for higher BO, which is consistent with data reported in literature [91,195]. However, it is important to note that this trend is not well-observed for the N4THC series. The presence of graphitic N, N_Q, peak at 401.2 eV, accounts for approximately 26 – 34 % in the N4THC series, and 26 – 32 % in the N8THC series. The presence of this nitrogen functionality is highly desired because it enhances the electronic structure of the carbon material by reducing the energy gap [185]. Finally, a peak at 402.9 eV corresponding to nitrogen bonded to oxygen, N=O, represents approximately 9 – 15 % in both cases without significant variations as the BO increases.

The **Figure 5-22 C** shows the deconvolution of the O 1s spectrum, revealing five distinct peaks. Among these, the quinone groups, O_1 peak at 530.9 eV, are the most prominent across, constituting approximately 60 at.%. This observation aligns with the characteristic catechol B-ring on the pine tannin precursor [132,196]. A smaller proportion of phenol/ether groups, O_2 peak at 532.3 eV, accounting for around 20 %, can be observed. Carboxylic acid groups, O_3 peak at 533.1 eV, comprising roughly 10 %, are also present. Additionally, there is a minor percentage of oxides bonded to nitrogen, N=O peak at 534.1 eV, and a small peak at 534.9 eV associated with chemisorbed water. The main difference among the series of materials is a slight increase in carboxylic acid groups (O3) at the expense of quinone-like groups (O_1) for both N4THCs and N8THCs compared to the THCs. This change is attributed to the amination of tannins [67,68].

However, as depicted in **Figure 5-22 E** and **Figure 5-22 F**, the atomic contributions of the specific N-containing and O-containing functional groups between both N-doped series do not exhibit significant variations with BO. The role of oxygen functionalities upon the capacitive performance of carbon materials has been extensively studied [36,37,87]. These functionalities play a crucial role as they enhance the wettability of the materials and induce faradaic contributions through electron transfer. However, it should be noted that the presence of oxygen functionalities lead to a decrease in surface conductivity [37]. Existing literature suggests that quinone groups (referred to as O_1) could be of crucial importance in high-energy density capacitors. Quinones are electrochemically active through reversible two-electron and proton-coupled electron transfers with hydronium ions, especially in acidic solutions, enhancing the faradaic contributions [17,36,90]. Besides, quinones allow for an expanded potential window, exhibit good chemical stability, and do not negatively impact the cycling stability of the electrode [90]. Furthermore, as suggested by previous studies [8,112], it is anticipated that there will be a modification in the surface chemistry of the carbon materials due to nitrogen incorporation in the carbon matrix during the HTC step involving ammonia.

It is worth noting that no significant differences in the atomic ratios of nitrogen to carbon (N/C) and oxygen to carbon (O/C) were observed with the ammonia concentration nor the physical activation conditions as the BO increases (**Figure 5-23**). Although, the inset figure in **Figure 5-23** shows that the ratio [$(N+O)/C_{at}$] decreases slightly as the BO increases.

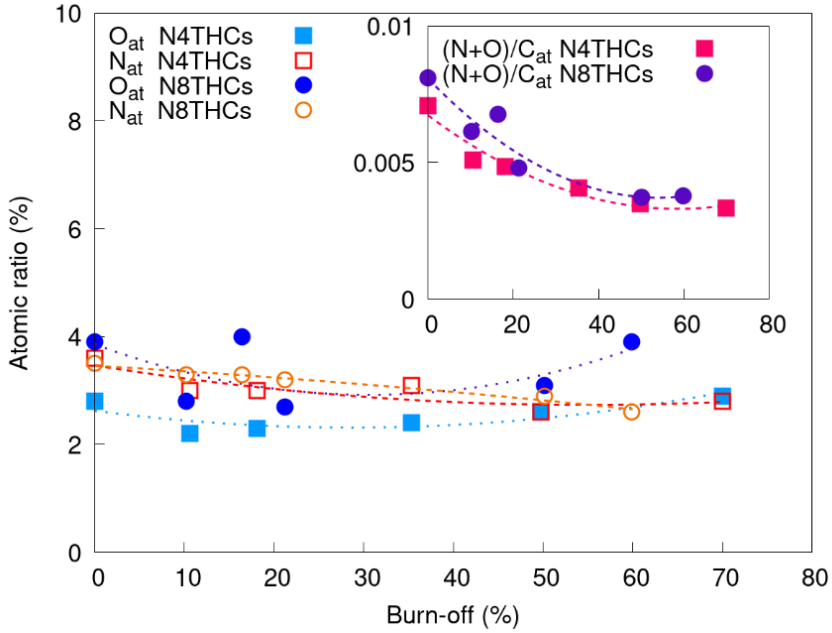

Figure 5-23 Nitrogen and oxygen atomic ratio estimated by XPS (inset: ratio N+O/C).

5.3.2 Textural properties

The N_2 and H_2 adsorption-desorption isotherms for both series of N-doped tannins are shown in **Figure 5-24**. All the materials showed a combination of type I and type II isotherms. The pronounced N_2 uptake at very low P/P° indicates the presence of significant microporosity [133], and as the activation intensity increases, the N_2 uptake also increases and the drop knee of the isotherms gradually widens, indicating an expansion of the micropores [133,190]. Additionally, a sharp increase in N_2 uptake close to P/P° = 0.97 is observed, indicating the presence of large mesopores or condensation within interparticle voids [190]. However, significant differences can be observed in the N_2 isotherms across the various materials. The N4THC-derived carbons (**Figure 5-24 A)** display a type H3 loop, which is often associated to capillary condensation [190]. Interestingly, the N_2 isotherms of the N8THC series (**Figure 5-24 C**) do not exhibit a noticeable loop. The H_2 adsorption isotherms (**Figure 5-24 B and D**) show an evolution of the quantity adsorbed as the CO_2 activation becomes intense indicating an evolution of micropores in the nitrogen-doped carbons. The textural parameters estimated from N_2 and H_2 isotherms at 77 K are reported in **Table 5-10**. The A_{BET} is presented solely for the purpose to compare data with another studies in the literature, given the limitations of the BET method [189]. The analysis is primarily discussed based on the results obtained from the application of the NLDFT model, which provides a more accurate representation of the surface [197].

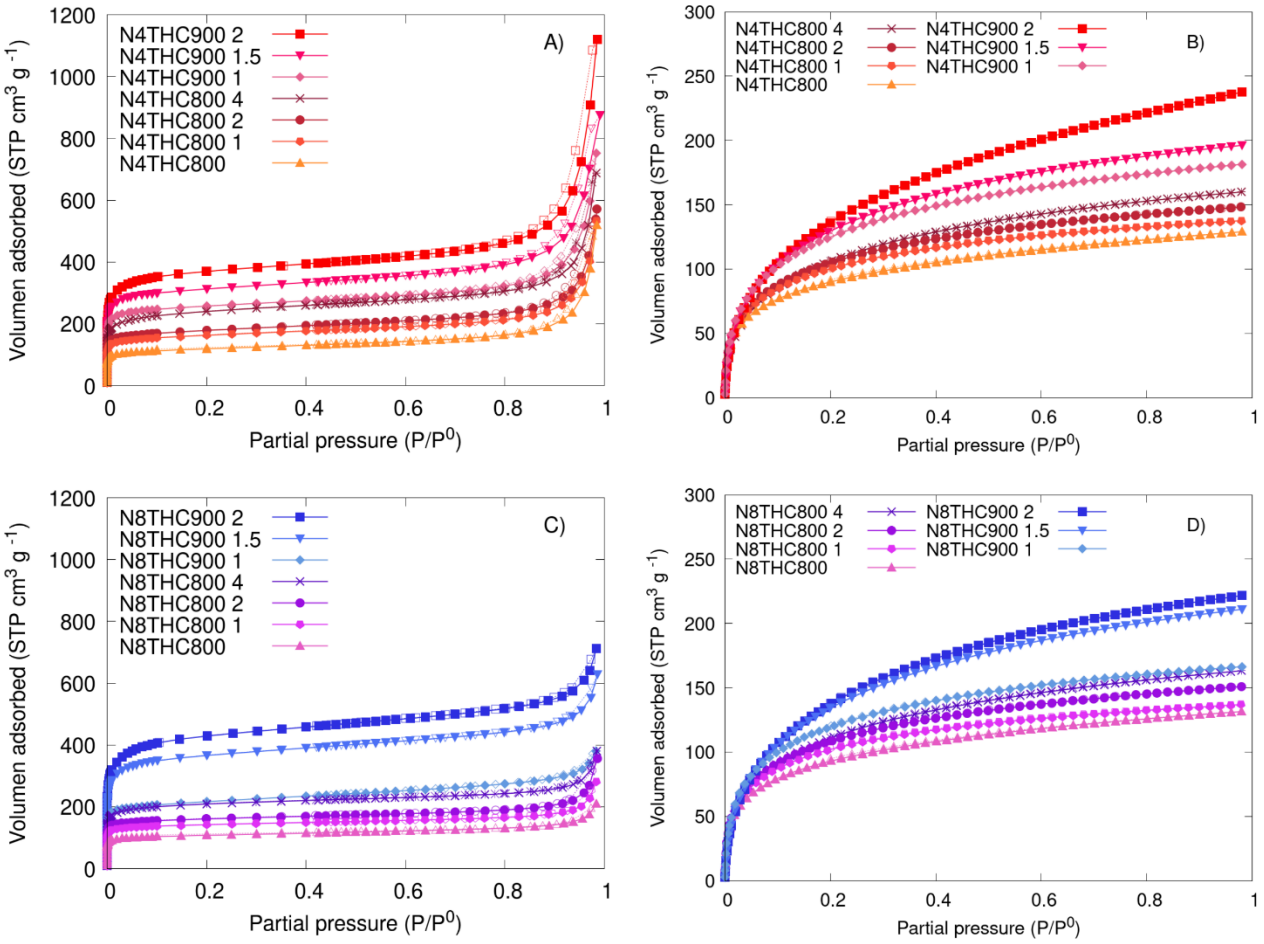

Figure 5-24 A, C) N_2 and B, D) H_2 adsorption (filled symbols)-desorption (empty symbols) isotherms at 77 K for N4THC and N8THC series.

As can be observed in **Figure 5-25 B and D,** all carbon materials have a similar pore size distribution (PSD) with peaks centered in the ultra-micropores, which is a characteristic feature of tannin-derived carbon materials [67,119,121]. For instance, two main peaks are observed on all the materials, one at ca. 0.4 nm and another at ca. 0.7 nm. For both N4THC and N8THC series, as the activation conditions become more severe, a broadening of the ultra-micropores occurs, leading to a widening of the aforementioned peaks. The appearance of a third broad peak between 1 to 2 nm is observed in the most severe conditions of activation. It should be noted that the third peak is also slightly observed for the non-activated N-doped samples (N4THC800 and N8THC800), suggesting that the HTC treatment using ammonia could be responsible for promoting the formation of larger micropores.

Table 5-10 Textural properties obtained to apply 2D-NLDFT-HS kernel to N_2 and H_2 adsorption isotherms.

Carbons	A_{BET} (m^2g^{-1})	SSA (m^2g^{-1})	$V_{0.97}$ (cm^3g^{-1})	V_T (cm^3g^{-1})	‹$w_{u\mu}$› (nm)	$V_{u\mu}$ (cm^3g^{-1})	‹$w_{s\mu}$› (nm)	$V_{s\mu}$ (cm^3g^{-1})	‹w_{meso} › (nm)	V_{meso} (cm^3g^{-1})
THC800	505	990	0.173	0.339	0.5	0.182	1.0	0.065	21.7	0.091
THC800-1	655	1100	0.214	0.380	0.5	0.203	1.0	0.084	19.0	0.093
THC800-2	680	1110	0.229	0.421	0.5	0.206	1.0	0.089	22.8	0.126
THC800-4	730	1150	0.304	0.570	0.5	0.206	1.0	0.104	25.0	0.260
N4THC800	450	905	0.378	0.848	0.5	0.170	1.1	0.043	28.5	0.636
N4THC800-1	620	1020	0.403	0.854	0.5	0.172	1.0	0.090	27.0	0.592
N4THC800-2	675	1090	0.420	0.866	0.5	0.180	1.0	0.100	25.7	0.586
N4THC800-4	905	1200	0.519	1.080	0.5	0.178	1.1	0.178	26.4	0.727
N4THC900-1	1000	1350	0.597	1.170	0.5	0.194	1.0	0.191	26.5	0.789
N4THC900-1.5	1210	1490	0.701	1.360	0.5	0.194	1.0	0.265	25.9	0.901
N4THC900-2	1415	1710	0.908	1.670	0.5	0.173	1.1	0.362	24.6	1.186
N8THC800	420	910	0.175	0.385	0.5	0.175	1.1	0.044	24.2	0.166
N8THC800-1	560	995	0.228	0.474	0.5	0.174	1.0	0.078	27.3	0.223
N8THC800-2	630	1080	0.268	0.589	0.5	0.196	1.0	0.083	28.3	0.310
N8THC800-4	805	1180	0.316	0.613	0.5	0.216	1.1	0.125	27.0	0.272
N8THC900-1	830	1230	0.339	0.611	0.5	0.186	1.0	0.148	19.1	0.277
N8THC900-1.5	1410	1610	0.553	0.970	0.5	0.196	1.1	0.353	23.4	0.422
N8THC900-2	1645	1720	0.641	1.080	0.5	0.180	1.1	0.447	21.2	0.449

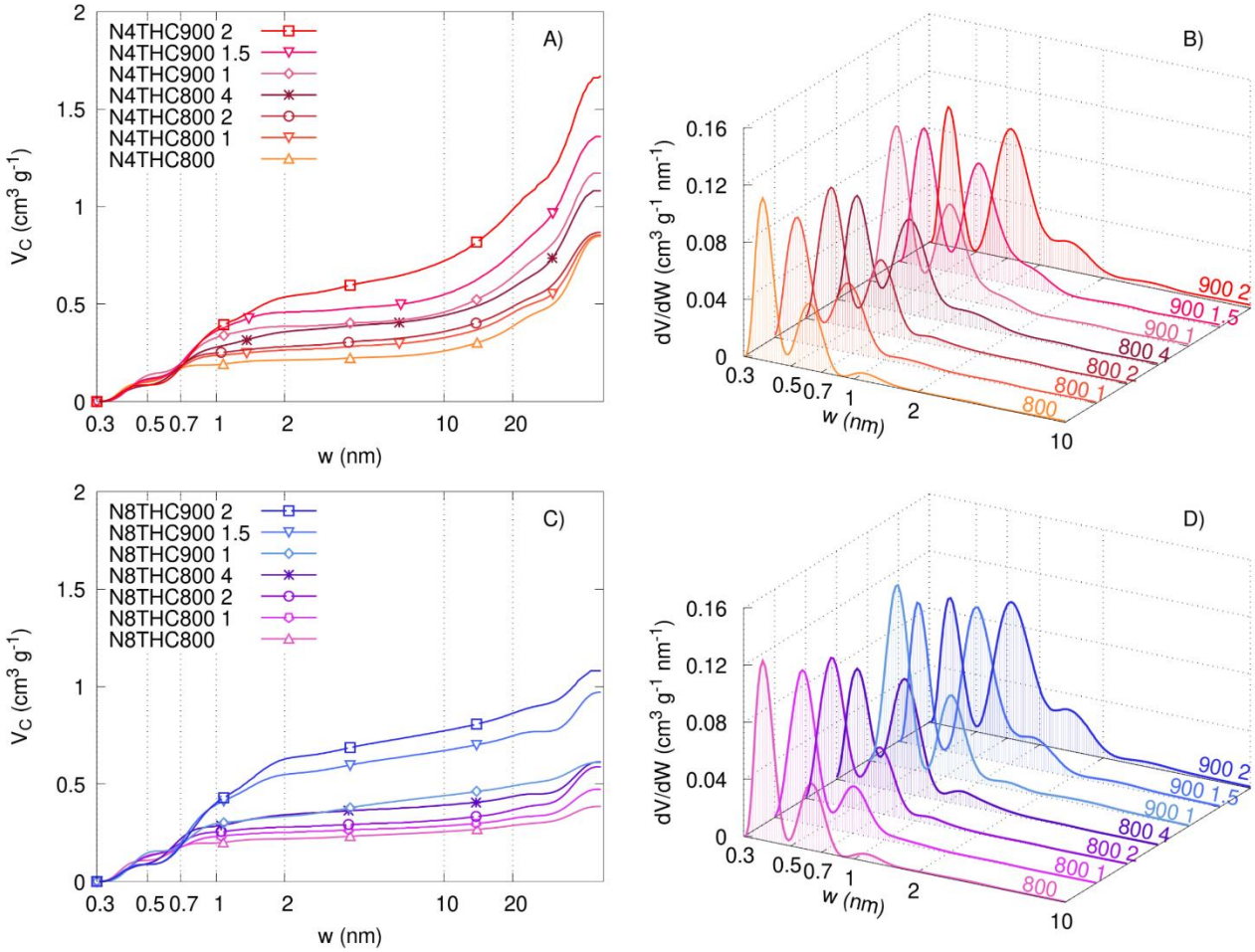

Figure 5-25 A, C) Cumulative volume and B, D) differential pore size distribution (PSD) estimated by 2D-NLDFT-HS for N4THC and N8THC series.

In **Figure 5-26 A**, the influence of the BO upon the specific surface area (SSA) is presented, revealing a linear relationship between BO and SSA. The non-activated materials exhibit relatively similar and low SSA values of 905, and 910 m^2g^{-1} for the N4THC800 and N8THC800, respectively. As the BO increases due to intensified activation conditions, the SSA follows the same trend.

For instance, N4THC900-2 and N8THC900-2, activated at 900°C for 2 hours, reached values of 1710 and 1720 m^2g^{-1}, respectively, corresponding to a BO of ca. 70 % and 60 %. The evolution of the ultra-micropore volume follows a negative parabolic pattern, as can be observed in **Figure 5-26 B.4**, and it is expected due to this pattern is well-documented for the pore volumes within this range [57,120]. In addition, **Figure 5-26 B.3** shows the monotonic increase of the supermicropore volume ($V_{s\mu}$) as a function of the SSA for both N-doped series, $V_{s\mu}$ increased up to 0.36 cm^3g^{-1} for N4THC900-2 and 0.43 cm^3g^{-1} for N8THC900-2.

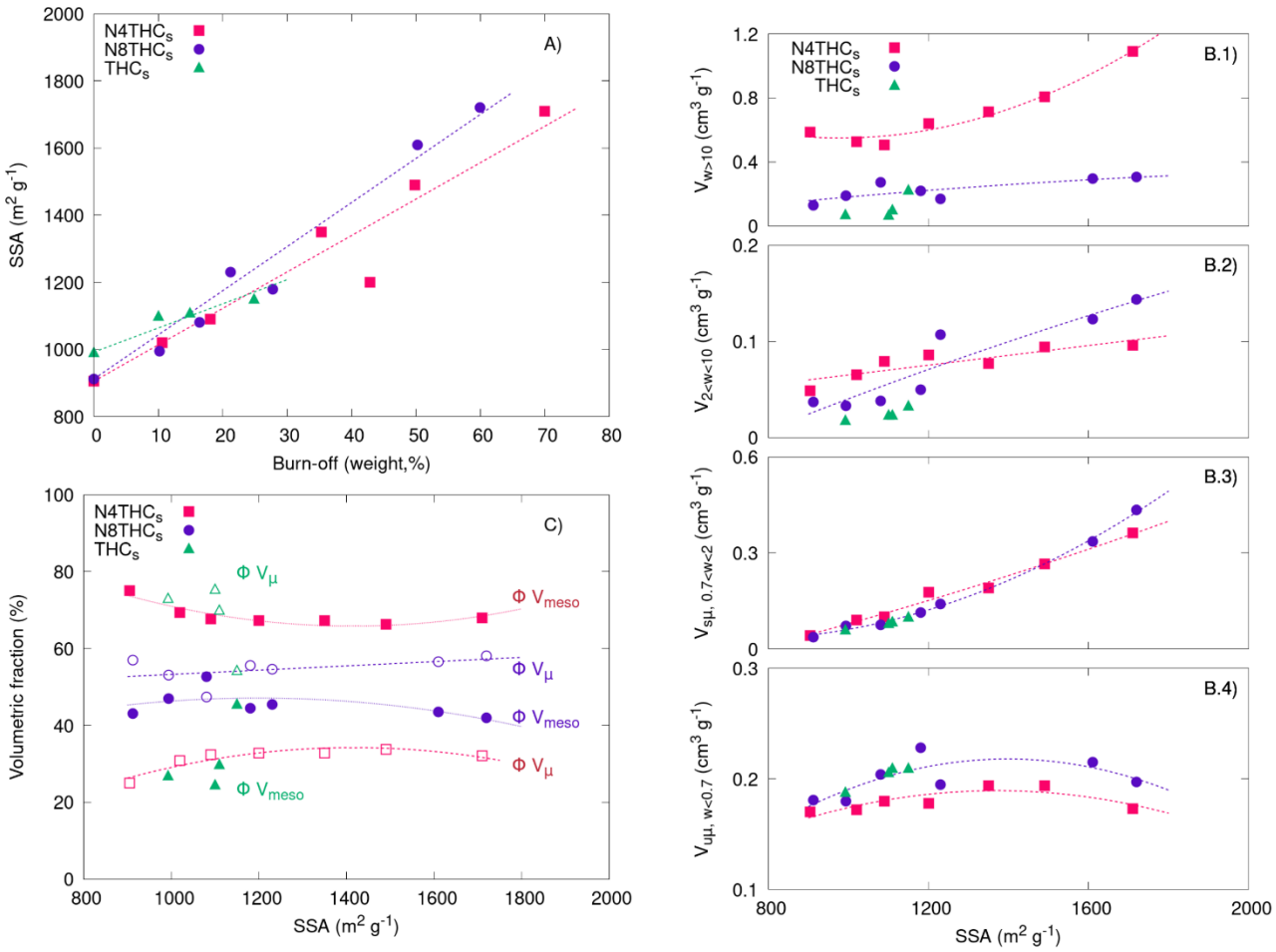

Figure 5-26 A): SSA as a function of the burn-off (BO). B.1): Large mesopore volume (10 < w < 50 nm); B.2): narrow mesopore volume (2< w < 10 nm); B.3): supermicropores (0.7 < w < 2 nm); and B.4): ultramicropores (w < 0.7 nm) as a function of SSA. C): Volumetric fraction of micropores and mesopores (Φ Vμ and Φ Vmeso, respectively) as a function of SSA.

In the case of mesopores, they are widely distributed throughout the range without significant peaks, but they represent a significant fraction of the total volume. To clarify the differences between N4THC and N8THC series, the mesopores region was divided into two zones, namely the narrow and the large mesopore ranges, 2 < w < 10 nm and 10 < w < 50 nm, respectively, as is observed in **Figure 5-26 B.1** and **B.2**. The samples of the N4THC series have a substantial volume increase in the large mesopore range, which parabolically increases with the SSA from ca. 0.64 cm^3g^{-1} (N4THC800) to a maximum of 1.19 cm^3g^{-1} (N4THC900-2). However, in the narrow mesopore range (**Figure 5-26 B.2**), the increase in volume is slightly noticeable. In contrast, the mesopore volume for the N8THC series evolved significantly in the narrow mesopore range, the volume increased from 0.04 to 0.14 cm^3g^{-1}, while for larger mesopores, the volume increased from 0.13 to 0.31 cm^3g^{-1}. Although the reasons for these differences in the porosity development are not evident, they are crucial in explaining the contrasting electrochemical behavior of both series, as discussed in the subsequent section.

5.3.3 Electrochemical performance

Electrochemical impedance spectroscopy (EIS) was used as a technique to evaluate the kinetic and mass transport performance of the carbon materials as electrodes for ECs using 1 M H_2SO_4 as electrolyte. **Figure 5-27 A** shows the Nyquist plot obtained in the two-electrode cell system. It can be seen that the graph did not start at the origin, but with a shift close to 1.8 Ω cm^2 along the Z_r axis, associated with the bulk electrolyte resistance (R_s) [122], as explained in **section 2.4.3**.

The N-doped carbon materials exhibited a finite-space Warburg impedance, characterized by a straight line at high frequencies and a phase angle close to 90°, as shown the Bode plot in **Figure 5-27 B**, which is typical of capacitive systems. Furthermore, the equivalent series resistance (ESR) can serve as a global parameter for comparing materials. For instance, THC800-4 had an ESR value of approximately 251.5 Ω cm^{-2}, which is almost two orders of magnitude higher than values estimated for N-doped carbon materials activated at the same conditions studied in this work. The materials not submitted to physical activation, N4THC800 and N8THC800, had similar ESR values of ca. 11.4 and ca. 10.0 Ω cm^{-2}. It is worth noting that, in both cases, around 68 % and 63 % of the ESR values could be attributed to the charge-transfer resistance (R_{CT}), after subtracting the electrolyte resistance value (R_S) to calculate the respective percentages. In this context, the physical activation process resulted in a decrease in materials electrical resistivity by improving charge transfer, as evidenced by the significant reduction in the arc size shown in **Figure 5-27**. For instance, N4THC900-2 and N8THC900-2, which underwent the most severe activation conditions in their respective series, had an ESR of ca. 4.2 and 3.8 Ω cm^{-2}, respectively, with R_{CT} accounting for only 37 % and 45 % of the total ESR.

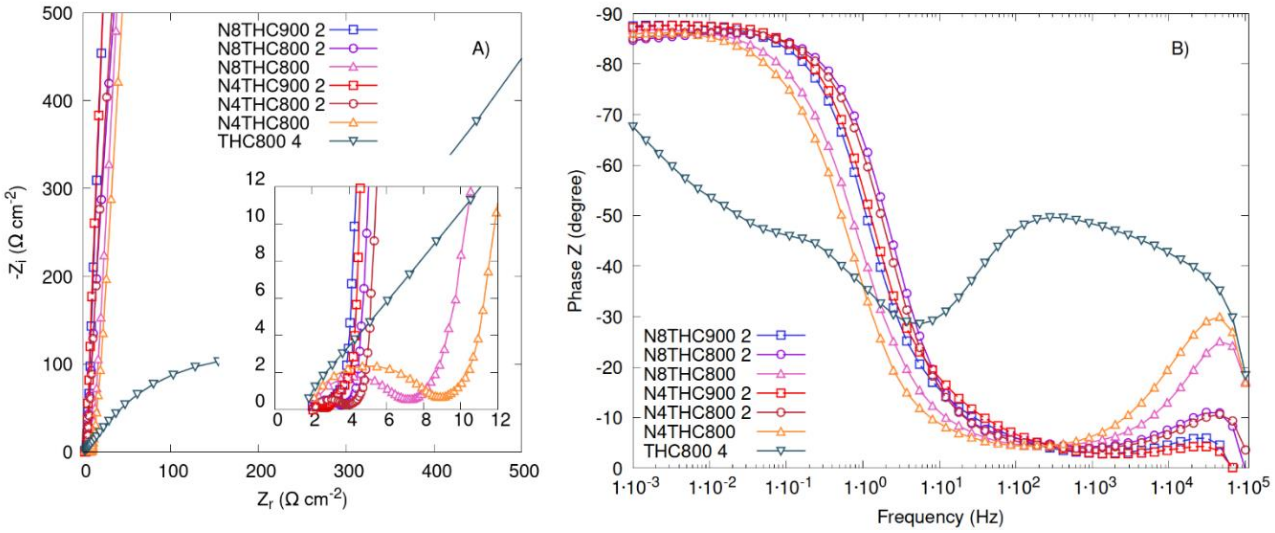

Figure 5-27 EIS results for representative N-doped and non-doped samples. For the sake of comparison, THC800-4 is selected as reference. A): Nyquist plot; B): Bode plot.

The overall reduction in ESR of N-doped carbon materials can be attributed to carbon surface modifications resulting from tannin amination, which improves water affinity, as discussed above. In addition, pore widening and improved pore connectivity, attributed to the higher degree of activation [120], contributed to a better charge transfer process but also to better mass transfer (ion diffusion), as evidenced by the absence of Warburg impedance for N-doped and activated samples.

Cyclic voltammetry (CV) was conducted at scan rates from 5 mV s^{-1} to 1 V s^{-1}, using a potential window of 0 – 1 V, which was chosen because an aqueous electrolyte was used in this study. The main results are presented in **Figure 5-28**, and further information is provided in the **section 8.4** (**Appendix D**). The amination process improved the electrochemical performance of the tannin-derived carbon materials, in line with the EIS results discussed above. The **Figure 5-28 A** and **B** show CV curves for representative carbon materials from the N4THC and N8THC series, respectively. A quasi-rectangular shape at a scan rate of 5 mV·s^{-1} can be observed, indicating near-ideal capacitive behavior. As the scan rate increased, an alteration on the shape of the curves is noticed, due to the gradual decrease in Faradaic contributions and limitation of the diffusion from the bulk electrolyte to the pore, so that the current aroused mainly from the formation of the electric double layer. In fact, at 5 mV·s^{-1} the specific cell capacitance ($C_{CV,cell}$) for N4THC800 and N8THC800 was approximately 37 F·g^{-1} and 34 F·g^{-1}, respectively, with 43 % and 50 % retention, respectively, when tested at 1 V·s^{-1}. The activation process improved $C_{CV,cell}$ values at low scan rates, with N4THC900-2 and N8THC900-2 exhibiting capacitance values of 43 F·g^{-1} and 51 F·g^{-1}, respectively, at 5 mV·s^{-1}.

Additionally, the capacitance retention reached remarkable values close to 65 % for both series when tested at a high scan rate of 1 V·s^{-1}. However, despite the relatively similar behavior in capacitance resulting from the activation process, there are still interesting features worth highlighting.

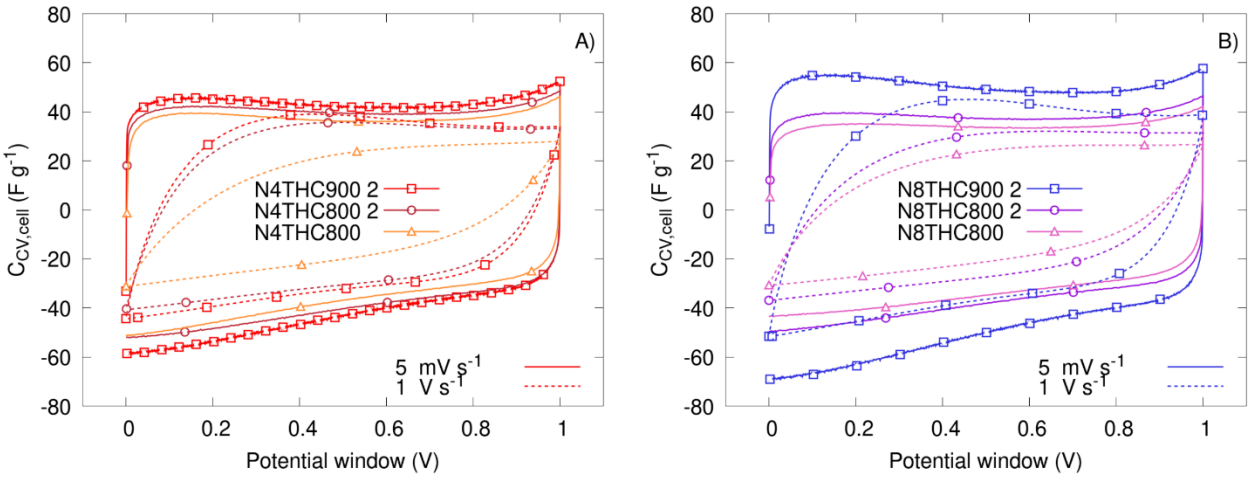

Figure 5-28 Cyclic voltammogram at 5 mV·s-1 (solid line) and 1 V·s-1 (dashed line). A): N4THCs. B): N8THCs.

In this context, Trassatti's method [126] was used to differentiate the double-layer capacitance (C_{EDL}) from the Faradaic contribution commonly referred to as pseudocapacitance (C_{PsC}). The dependence of the capacitance on the square root of the scan rate and its inverse ($v^{1/2}$ and $v^{-1/2}$, respectively) for the whole series is shown in **Figure 5-29**, with the main results plotted in **Figure 5-30** as a function of SSA. The pseudocapacitance arises from surface functionalities present in the material, which can improve mass or charge transfer [82]. It can be noticed that C_{PsC} has comparable values for both series, displaying a similar downward trend, followed by a stabilization of its contribution. This behavior is a consequence of the chemical evolution of the carbon surface, as discussed previously in **section 5.3.1** shown in **Figure 5-23**. When considering C_{EDL}, which originates from the textural properties of the carbon materials [76], it is essential to analyze the differences between the two series. Despite the noticeable increase in surface area for the N4THC series, from 905 $m^2\ g^{-1}$ to 1710 $m^2\ g^{-1}$ (see **Table 5-10**) for the most severe activation conditions, only a marginal enhancement in C_{EDL} was observed.

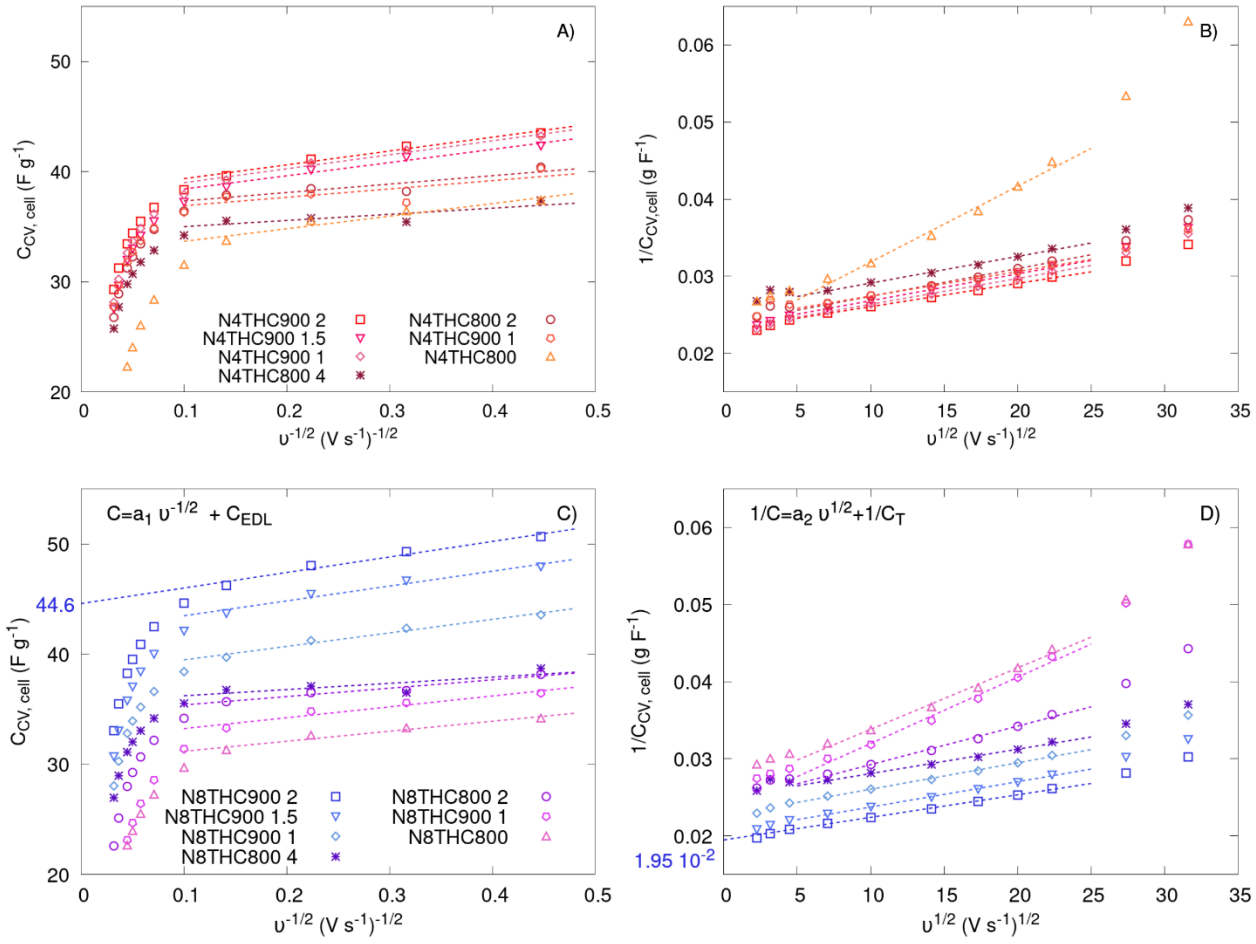

Figure 5-29 Dependence of capacitance as a function of the scan rate to differentiate pseudocapacitance (C_{PsC}) and double-layer capacitance (C_{EDL}) according to Trassatti's method for A) and B) N4THC series, and C) and D) N8THC series.

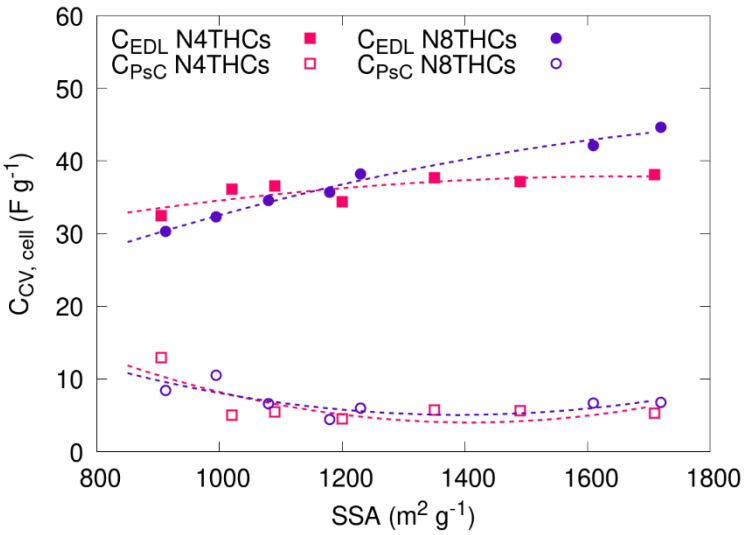

Figure 5-30 Contribution of electric double layer capacitance (C_{EDL}), and pseudocapacitance (C_{PsC}) estimated by Trassatti's method for both series of N-doped carbon materials.

Similar trends are observed in galvanostatic charge-discharge (GCD) tests performed by varying the applied specific current from 0.5 to 40 A g^{-1}. **Figure 5-31** shows the original charge-discharge curves within the 0 – 1 V potential window and at a specific current of 5 A g^{-1}, while **Figure 5-32 A** and **B** shows the calculated specific cell capacitance obtained from the corresponding discharge curves ($C_{GCD,cell}$). Remarkably, all curves, even at high specific current values, exhibited a triangular shape indicating capacitive behavior with a low potential drop ($\boldsymbol{iR}$). At a specific current of 0.5 A g^{-1}, $C_{GCD,cell}$ increased from 36 F·g^{-1} for N4THC800 to 45 F·g^{-1} for N4THC900-2.

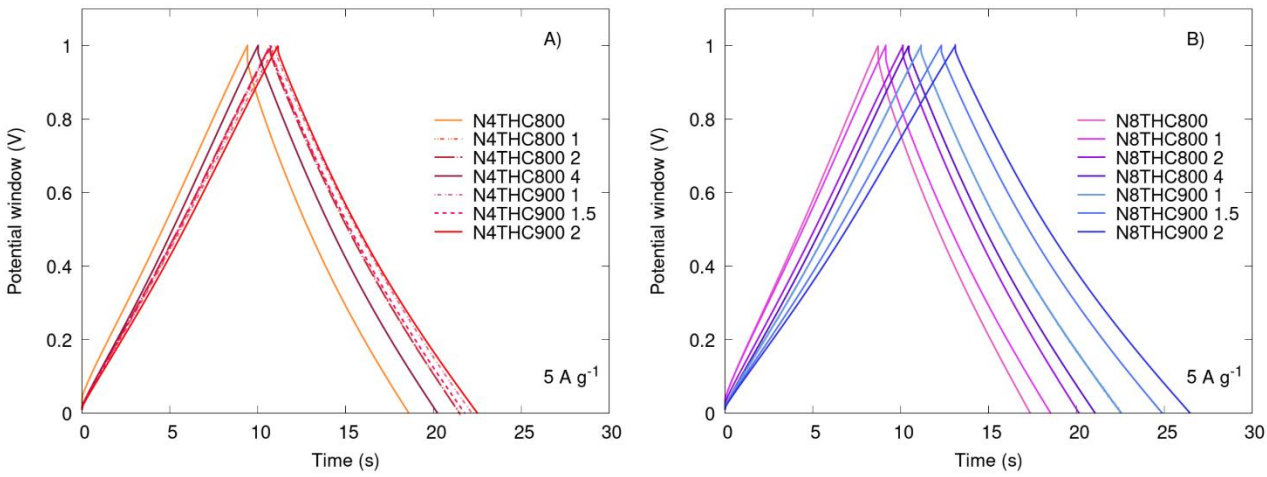

Figure 5-31 Charge-discharge curves at 5 A g-1. A): N4THC series. B): N8THC series.

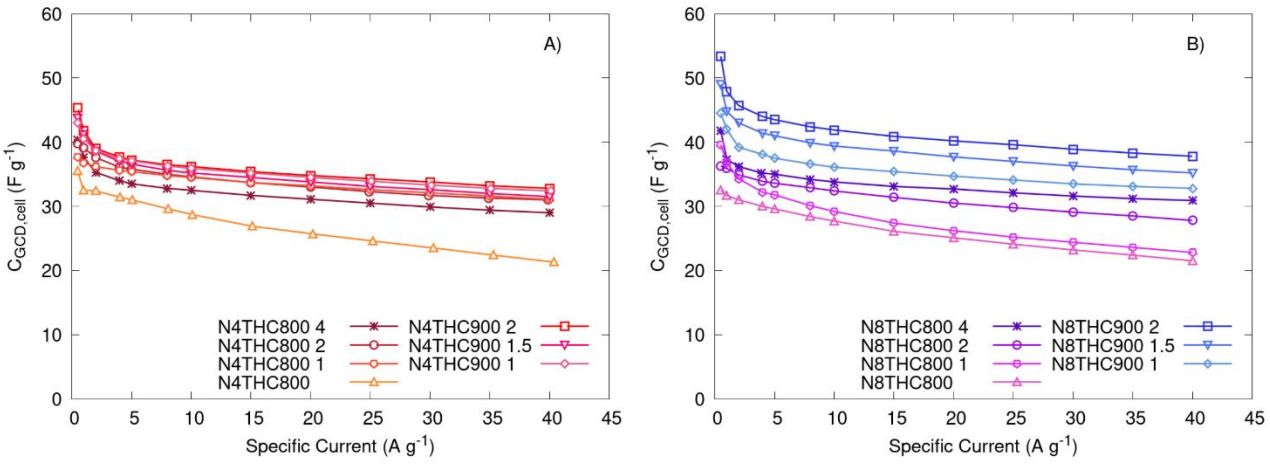

Figure 5-32 Specific cell capacitances calculated from GCD curves ($C_{GCD,cell}$) for A) N4THC and B) N8THC series.

As with the CV results, a significant increase in capacitance could be observed for the N8THC series compared with the N4THC series. Indeed, for the N8THC series, $C_{GCD,cell}$ ranged from 32 F·g^{-1} to 53 F·g^{-1} for the same activation conditions. Interestingly, as discussed above, there were no notable differences in N or O contents between the two series (**Table 5-9**) or in the proportions of surface functionalities (**Figure 5-22** E and **F**). Therefore, the observed increase in $C_{GCD,cell}$ could, once again, be attributed to the development of narrow mesopores.

It is worth noting that while the capacitance values obtained by GCD, at low specific current, and CV, at low scan rate, were comparable, the $C_{GCD,cell}$ retention was higher than that obtained from CV tests. For instance, N4THC900-2 and N8THC900-2, the best performing materials in their respective series, demonstrated impressive retention rates in GCD tests. At a specific current of 5 A g^{-1}, N4THC900-2 retained 82 % of its initial capacitance, while N8THC900-2 retained 81 %. Even at a higher specific current of 40 A g^{-1}, both materials maintained a high level of stability, with N4THC900-2 retaining 72 % of its initial capacitance and N8THC900-2 retaining 71 %. Therefore, to assess their cycling stability, N4THC900-2 and N8THC900-2 were subjected to 30,000 continuous GCD cycles at a specific current of 5 A g^{-1}.

Figure 5-33 depicts the cycling stability of both carbon materials, demonstrating a remarkable retention of ca. 96 % for N4THC900-2 and N8THC900-2 relative to their initial capacitance. The inset in **Figure 5-33** reveals that the triangular-shaped charge-discharge curve remained largely unchanged after the cycling test, indicating the excellent stability of the surface functionalities of these materials. It is worth noting that although pseudocapacitive contributions represented approximately 10 % of the total capacitance, as suggested by the CV results discussed earlier (**Figure 5-30**), they had no significantly impact on the stability of the materials.

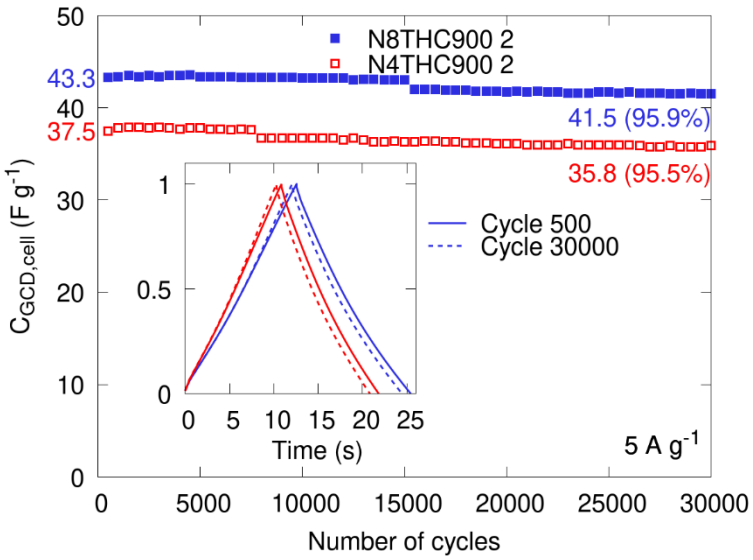

Figure 5-33 Cycling stability of N8THC900-2 and N4THC900-2 performed at 5 A g-1, inset corresponds to the GCD curves of cycle 500 (solid line) and cycle 30000 (dashed line).

5.4 Electrochemical performance summary

As exposed at the beginning of this manuscript in **section 2.1**, the Ragone plot is the main way used to compare the electrochemical performance of any energy storage system, where it can be observed both key parameters power and energy density. In this context, the electrochemical performance of the key carbon materials obtained from this research are compared in the Ragone plot depicted in **Figure 5-34**. The power density (P, W kg^{-1}), and specific energy (E, W-h kg^{-1}) were calculated from the GCD curves exposed in their respective sections.

For chemically activated carbon materials, the sample TBC K-2.8 with a specific surface area of 2190 $m^2\ g^{-1}$ and O_{XPS} = 7.5 at. %, with a similar abundance of both quinones and hydroxyl functionalities and less than 10 at. % of carboxylic acids was chosen due to its outstanding performance among the carbon materials studied in the **section 5.1**. To compare the doped effect of carbon materials the B4THC800 4 carbon material with a specific surface area of 1200 $m^2\ g^{-1}$ with B_{XPS} = 0.28 at. % consisting mainly in boron on the edge of the carbon lattice bounded to oxygen, and O_{XPS} = 3.3 at. % consisting mainly in hydroxyl functionalities (61.3 at. %), followed by quinones-like groups (28.0 at. %) and carboxylic acid species (10.7 at. %) was chosen to represent the boron doped materials described in **section 5.2**. Meanwhile, for N-doped carbon materials, two materials were chosen to do the comparative analysis. The N8THC800 4 material with a specific surface area of 1180 $m^2\ g^{-1}$, and a chemical surface involving N_{XPS} = 3.3 at. % and O_{XPS} = 3.9 at. %, and N8THC900 2 material with a specific surface area of 1720 $m^2\ g^{-1}$, and chemical surface involving N_{XPS}= 2.6 at. % and O_{XPS} = 3.3 at, where the nature of nitrogen is characterized by three main functionalities commonly founded in carbon materials and oxygen functionalities represented mainly by quinones (close to 60 %).

The sample TBC-K2.8 exhibit one of the highest specific energies across the entire specific power range for the chemically-activated carbon materials studied in this research with a value of 5.4 W-h kg^{-1} at the specific power close to 110 W kg^{-1} ($\hat{I}$ = 0.5 A g^{-1}). At the power output of 1 kW kg ($\hat{I}$ = 5 A g^{-1}), the specific energy is close to 4.4 W-h kg^{-1}, about twice the obtained from TBC-K0.6 (E=2.3 W-h kg^{-1}, data not represented in the figure) at similar power output, showing the importance of porosity development and pore widening during KOH activation. A similar curve was founded for chemically-activated chitosan at 750°C with a C:KOH ratio of 1:4, named ACRHC 750°C [198], with A_{BET} = 2807 $m^2\ g^{-1}$ (for comparison, TBC-K2.9 has an estimated A_{BET}=2417 $m^2\ g^{-1}$) and not informed XPS characterization.

The B-doped carbon materials were represented by B4THC800 4 described in **section 5.2.3** that shows a low performance with an energy density of 3.6 W-h kg^{-1} at the specific power of 16.7 W kg^{-1} ($\hat{I}$ = 0.5 A g^{-1}), which declines rapidly to values close 2.1 W-h kg^{-1} at 3.2 kW kg^{-1} due to their low specific surface, and highly microporosity without enough mesopores that allows an improved ion transport to the carbon surface.

In comparison, the N-doped carbon material N8THC800 4 shows a comparative superior performance with an energy density of 5.79 W-h kg^{-1} at 16.4 W kg^{-1} ($\hat{I}$ = 0.5 A g^{-1}) that slowly decreases at high-power demands reaching up to 4.75 W-h kg^{-1} at 1.6 kW kg^{-1} ($\hat{I}$ = 0.5 A g^{-1}). It is noteworthy, that even having a low surface area N4THC800 4 presents similar energy density values that TBC-K2.8 at low-power demand, and it has improved the values as the power demand increases. The superior capacity can be attributed to an improved combination of micropores with mesopores that allows fast ion transport to the carbon surface in conjunction with the enhanced surface chemistry due to the nitrogen incorporation.

As anticipated from the results provided in **section 5.3**, the material exhibiting the best electrochemical performance was N8THC900-2. This material shows a specific energy of approximately 6.6 W·h·kg^{-1} at a specific power of around 3.2 kW·kg^{-1}. The specific energy gradually decreased as the specific power increased, reaching approximately 4.6 W·h·kg^{-1} at about 12.1 kW·kg^{-1}. Although the specific energy of these ACs cannot exceed that obtained with N-doped reduced graphene oxide (N-RGO, A_{BET} = 355 m^2 g^{-1}, O_{XPS} = 12.6 at. %, N_{XPS} = 3.0 at. %) [38], it is noteworthy that they outperformed other N-doped ACs, especially at high rates, as the reported by Sahoo et al. [199], coded NAC-2. Similarly, an improvement in the electrochemical performance of N8THC900-2 (SSA = 1720 m^2 g^{-1}, O_{XPS} = 2.6 at %, N_{XPS} = 3.9 at. %) was observed compared to previously reported non-doped tannin-derived ACs obtained by CO_2 activation (SSA = 1614 m^2 g^{-1}, O_{XPS} = 5.0 at. %) [17], all tested under similar conditions, confirming the benefits of the nitrogen doping enhancing the electrochemical performance of materials.

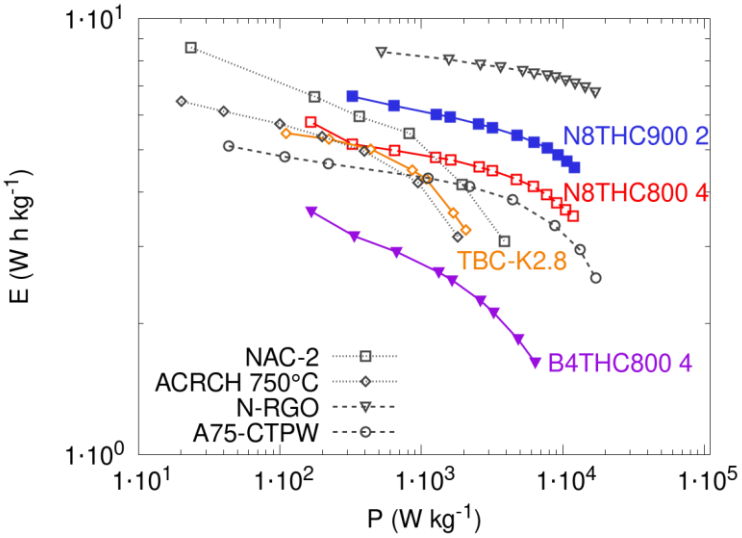

Figure 5-34 Electrochemical performance of key carbon materials obtained from this research and comparison with literature data obtained from similar electrochemical characterization, NAC-2 [199], ACRCH 750° [198], N-RGO [38], A75-CTPW. [17].

6 CONCLUSIONS

The research establishes tannin-derived carbon materials obtained from pine bark as viable electrodes for electrochemical capacitors, exhibiting competitive electrochemical performance compared to reported literature values under similar electrochemical characterization conditions.

The chemically activated tannins-derived carbon materials exhibit a linear correlation between capacitance and specific surface area development, attributed to an oxygen-containing surface chemistry conducive to efficient electric double layer formation. Employing KOH to biochar mass ratios of 2.8 and 3.6 achieved a balanced combination of high surface area and suitable pore size distributions. This optimization resulted in superior electrochemical performance, reaching energy densities values of 4.4 W-h kg^{-1} at 1.1 kW kg^{-1}. Notably, the materials demonstrated prolonged stability, retaining 92% of the initial energy storage after 10,000 cycles.

The hydrothermal carbonization doping method effectively incorporates nitrogen and boron into the tannins-derived carbon materials. This process introduces significant alterations to the specifically tailored chemical and morphological modifications induced by hydrothermal carbonization, achieved by employing controlled concentrations of aqueous ammonia or boric acid in each case.

The hydrothermal carbonization of tannins without doping agent results in a surface chemistry dominated by carboxylic acid species, which hinder the formation of the electric double layer, thereby limiting electrical storage. Conversely, the introduction of doping agents modified the surface chemistry of carbon materials. In the case of boron, the quantity incorporated onto the carbon surface is moderate but sufficient to introduce a moderate enhancement in electrochemical performance, primarily associated with changes in the oxygen functionalities present on the carbon surface.

Meanwhile, the research reveals that nitrogen doping through hydrothermal carbonization in aqueous ammonia not only altered the surface chemistry but also enhanced the textural properties of the resulting carbon materials after CO_2 activation. These modifications significantly improved the electrochemical performance of the N-doped carbon materials when employed as electrochemical capacitors. The concentration of ammonia used had no notable impact on the nitrogen content or the nature of the surface chemistry. However, it did influence the development of textural properties during CO_2 activation, with a more pronounced effect observed at higher ammonia concentration. The top-performing material achieved a remarkable energy density of 6.0 W-h kg^{-1} at a power-demand of 1.3 kW kg^{-1}, exhibiting exceptional stability by retaining nearly 96% of the initial energy storage after 30,000 cycles.

7 REFERENCES

[1] P. Simon, Y. Gogotsi, Perspectives for electrochemical capacitors and related devices, Nat. Mater. 19 (2020) 1151–1163. https://doi.org/10.1038/s41563-020-0747-z.

[2] T.M. Gür, Review of electrical energy storage technologies, materials and systems: challenges and prospects for large-scale grid storage, Energy Environ. Sci. 11 (2018) 2696–2767. https://doi.org/10.1039/C8EE01419A.

[3] M. Horn, J. MacLeod, M. Liu, J. Webb, N. Motta, Supercapacitors: A new source of power for electric cars?, Economic Analysis and Policy 61 (2019) 93–103. https://doi.org/10.1016/j.eap.2018.08.003.

[4] Z. Lin, E. Goikolea, A. Balducci, K. Naoi, P.L. Taberna, M. Salanne, G. Yushin, P. Simon, Materials for supercapacitors: When Li-ion battery power is not enough, Materials Today 21 (2018) 419–436. https://doi.org/10.1016/j.mattod.2018.01.035.

[5] J. Xie, P. Yang, Y. Wang, T. Qi, Y. Lei, C.M. Li, Puzzles and confusions in supercapacitor and battery: Theory and solutions, Journal of Power Sources 401 (2018) 213–223. https://doi.org/10.1016/j.jpowsour.2018.08.090.

[6] A. Burke, Ultracapacitors: why, how, and where is the technology, Journal of Power Sources 91 (2000) 37–50. https://doi.org/10.1016/S0378-7753(00)00485-7.

[7] B.K. Kim, S. Sy, A. Yu, J. Zhang, Electrochemical Supercapacitors for Energy Storage and Conversion, in: J. Yan (Ed.), Handbook of Clean Energy Systems, John Wiley & Sons, Ltd, Chichester, UK, 2015: pp. 1–25. https://doi.org/10.1002/9781118991978.hces112.

[8] A.G. Pandolfo, A.F. Hollenkamp, Carbon properties and their role in supercapacitors, Journal of Power Sources 157 (2006) 11–27. https://doi.org/10.1016/j.jpowsour.2006.02.065.

[9] F. Béguin, V. Presser, A. Balducci, E. Frackowiak, Carbons and Electrolytes for Advanced Supercapacitors, Advanced Materials 26 (2014) 2219–2251. https://doi.org/10.1002/adma.201304137.

[10] L.L. Zhang, X.S. Zhao, Carbon-based materials as supercapacitor electrodes, Chem. Soc. Rev. 38 (2009) 2520. https://doi.org/10.1039/b813846j.

[11] C.O. Ania, P.A. Armstrong, T.J. Bandosz, F. Beguin, A.P. Carvalho, A. Celzard, E. Frackowiak, M.A. Gilarranz, K. László, J. Matos, M.F.R. Pereira, Engaging nanoporous carbons in “beyond adsorption” applications: Characterization, challenges and performance, Carbon 164 (2020) 69–84. https://doi.org/10.1016/j.carbon.2020.03.056.

[12] S. Ghosh, S. Barg, S.M. Jeong, K. (Ken) Ostrikov, Heteroatom-Doped and Oxygen-Functionalized Nanocarbons for High-Performance Supercapacitors, Adv. Energy Mater. 10 (2020) 2001239. https://doi.org/10.1002/aenm.202001239.

[13] H. Shao, Y.-C. Wu, Z. Lin, P.-L. Taberna, P. Simon, Nanoporous carbon for electrochemical capacitive energy storage, Chem. Soc. Rev. 49 (2020) 3005–3039. https://doi.org/10.1039/D0CS00059K.

[14] G.S. Szymanski, Y. Suzuki, T. Ohba, B. Sulikowski, K. Góra-Marek, K.A. Tarach, S. Koter, P. Kowalczyk, A. Ilnicka, M. Zięba, L. Echegoyen, A.P. Terzyk, M.E. Plonska-Brzezinska, Linking the Defective Structure of Boron-Doped Carbon Nano-Onions with Their Catalytic Properties: Experimental and Theoretical Studies, ACS Appl. Mater. Interfaces 13 (2021) 51628–51642. https://doi.org/10.1021/acsami.1c12126.

[15] J. Castro-Gutiérrez, N. Díez, M. Sevilla, M.T. Izquierdo, J. Ghanbaja, A. Celzard, V. Fierro, High-Rate Capability of Supercapacitors Based on Tannin-Derived Ordered Mesoporous Carbons, ACS Sustainable Chem. Eng. 7 (2019) 17627–17635. https://doi.org/10.1021/acssuschemeng.9b03407.

[16] A. Celzard, V. Fierro, “Green”, innovative, versatile and efficient carbon materials from polyphenolic plant extracts, Carbon 167 (2020) 792–815. https://doi.org/10.1016/j.carbon.2020.05.053.

[17] J. Castro-Gutiérrez, A. Celzard, V. Fierro, Energy Storage in Supercapacitors: Focus on Tannin-Derived Carbon Electrodes, Front. Mater. 7 (2020) 217. https://doi.org/10.3389/fmats.2020.00217.

[18] J. Quílez-Bermejo, S. Pérez-Rodríguez, A. Celzard, V. Fierro, Progress in the Use of Biosourced Phenolic Molecules for Electrode Manufacturing, Front. Mater. 9 (2022) 810575. https://doi.org/10.3389/fmats.2022.810575.

[19] G. Tondi, V. Fierro, A. Pizzi, A. Celzard, Tannin-based carbon foams, Carbon 47 (2009) 1480–1492. https://doi.org/10.1016/j.carbon.2009.01.041.

[20] T.S. Mathis, N. Kurra, X. Wang, D. Pinto, P. Simon, Y. Gogotsi, Energy Storage Data Reporting in Perspective—Guidelines for Interpreting the Performance of Electrochemical Energy Storage Systems, Advanced Energy Materials 9 (2019) 1902007. https://doi.org/10.1002/aenm.201902007.

[21] P. Simon, Y. Gogotsi, B. Dunn, Where Do Batteries End and Supercapacitors Begin?, Science 343 (2014) 1210–1211. https://doi.org/10.1126/science.1249625.

[22] J.R. Miller, Valuing Reversible Energy Storage, Science 335 (2012) 1312–1313. https://doi.org/10.1126/science.1219134.

[23] J.R. Miller, P. Simon, Electrochemical Capacitors for Energy Management, Science 321 (2008) 651–652. https://doi.org/10.1126/science.1158736.

[24] E. Karden, S. Ploumen, B. Fricke, T. Miller, K. Snyder, Energy storage devices for future hybrid electric vehicles, Journal of Power Sources 168 (2007) 2–11. https://doi.org/10.1016/j.jpowsour.2006.10.090.

[25] W. Zuo, R. Li, C. Zhou, Y. Li, J. Xia, J. Liu, Battery-Supercapacitor Hybrid Devices: Recent Progress and Future Prospects, Advanced Science 4 (2017) 1600539. https://doi.org/10.1002/advs.201600539.

[26] D.P. Dubal, O. Ayyad, V. Ruiz, P. Gómez-Romero, Hybrid energy storage: the merging of battery and supercapacitor chemistries, Chem. Soc. Rev. 44 (2015) 1777–1790. https://doi.org/10.1039/C4CS00266K.

[27] M. Lu, F. Beguin, E. Frackowiak, Supercapacitors: Materials, Systems, and Applications, Wiley, 2013. https://books.google.cl/books?id=h3Yp8Llj6VcC.

[28] E. Frackowiak, Carbon materials for supercapacitor application, Phys. Chem. Chem. Phys. 9 (2007) 1774. https://doi.org/10.1039/b618139m.

[29] C. Zhong, Y. Deng, W. Hu, J. Qiao, L. Zhang, J. Zhang, A review of electrolyte materials and compositions for electrochemical supercapacitors, Chem. Soc. Rev. 44 (2015) 7484–7539. https://doi.org/10.1039/C5CS00303B.

[30] J. Chmiola, G. Yushin, Y. Gogotsi, C. Portet, P. Simon, P.L. Taberna, Anomalous Increase in Carbon Capacitance at Pore Sizes Less Than 1 Nanometer, Science 313 (2006) 1760–1763. https://doi.org/10.1126/science.1132195.

[31] C. An, Y. Zhang, H. Guo, Y. Wang, Metal oxide-based supercapacitors: progress and prospectives, Nanoscale Adv. 1 (2019) 4644–4658. https://doi.org/10.1039/C9NA00543A.

[32] Q. Jiang, Y. Lei, H. Liang, K. Xi, C. Xia, H.N. Alshareef, Review of MXene electrochemical microsupercapacitors, Energy Storage Materials 27 (2020) 78–95. https://doi.org/10.1016/j.ensm.2020.01.018.

[33] E. Frackowiak, Q. Abbas, F. Béguin, Carbon/carbon supercapacitors, Journal of Energy Chemistry 22 (2013) 226–240. https://doi.org/10.1016/S2095-4956(13)60028-5.

[34] B.E. Conway, Theoretical Treatment and Modeling of the Double Layer at Electrode Interfaces, in: B.E. Conway (Ed.), Electrochemical Supercapacitors: Scientific Fundamentals and

Technological Applications, Springer US, Boston, MA, 1999: pp. 125–168. https://doi.org/10.1007/978-1-4757-3058-6_7.

[35] A. Burke, R&D considerations for the performance and application of electrochemical capacitors, Electrochimica Acta 53 (2007) 1083–1091. https://doi.org/10.1016/j.electacta.2007.01.011.

[36] J.E. Zuliani, S. Tong, C.Q. Jia, D.W. Kirk, Contribution of surface oxygen groups to the measured capacitance of porous carbon supercapacitors, Journal of Power Sources 395 (2018) 271–279. https://doi.org/10.1016/j.jpowsour.2018.05.046.

[37] Y. He, Y. Zhang, X. Li, Z. Lv, X. Wang, Z. Liu, X. Huang, Capacitive mechanism of oxygen functional groups on carbon surface in supercapacitors, Electrochimica Acta 282 (2018) 618–625. https://doi.org/10.1016/j.electacta.2018.06.103.

[38] Y.-H. Lee, K.-H. Chang, C.-C. Hu, Differentiate the pseudocapacitance and double-layer capacitance contributions for nitrogen-doped reduced graphene oxide in acidic and alkaline electrolytes, Journal of Power Sources 227 (2013) 300–308. https://doi.org/10.1016/j.jpowsour.2012.11.026.

[39] Q. Abbas, R. Raza, I. Shabbir, A.G. Olabi, Heteroatom doped high porosity carbon nanomaterials as electrodes for energy storage in electrochemical capacitors: A review, Journal of Science: Advanced Materials and Devices 4 (2019) 341–352. https://doi.org/10.1016/j.jsamd.2019.07.007.

[40] J. Menzel, K. Fic, E. Frackowiak, Hybrid aqueous capacitors with improved energy/power performance, Progress in Natural Science: Materials International 25 (2015) 642–649. https://doi.org/10.1016/j.pnsc.2015.12.001.

[41] M. Gouy, Sur la constitution de la charge électrique à la surface d'un électrolyte, J. Phys. Theor. Appl. 9 (1910) 457–468. https://doi.org/10.1051/jphystap:019100090045700.

[42] J.A. Menéndez, M.J. Illán-Gómez, C.A.L. Y León, L.R. Radovic, On the difference between the isoelectric point and the point of zero charge of carbons, Carbon 33 (1995) 1655–1657. https://doi.org/10.1016/0008-6223(95)96817-R.

[43] J. Xia, F. Chen, J. Li, N. Tao, Measurement of the quantum capacitance of graphene, Nature Nanotech 4 (2009) 505–509. https://doi.org/10.1038/nnano.2009.177.

[44] J. Huang, B.G. Sumpter, V. Meunier, A Universal Model for Nanoporous Carbon Supercapacitors Applicable to Diverse Pore Regimes, Carbon Materials, and Electrolytes, Chem. Eur. J. 14 (2008) 6614–6626. https://doi.org/10.1002/chem.200800639.

[45] J. Huang, B.G. Sumpter, V. Meunier, Theoretical Model for Nanoporous Carbon Supercapacitors, Angew. Chem. Int. Ed. 47 (2008) 520–524. https://doi.org/10.1002/anie.200703864.

[46] X. Chen, R. Paul, L. Dai, Carbon-based supercapacitors for efficient energy storage, National Science Review 4 (2017) 453–489. https://doi.org/10.1093/nsr/nwx009.

[47] W. Gu, G. Yushin, Review of nanostructured carbon materials for electrochemical capacitor applications: advantages and limitations of activated carbon, carbide-derived carbon, zeolite-templated carbon, carbon aerogels, carbon nanotubes, onion-like carbon, and graphene, WIREs Energy & Environment 3 (2014) 424–473. https://doi.org/10.1002/wene.102.

[48] S. Vaquero, R. Díaz, M. Anderson, J. Palma, R. Marcilla, Insights into the influence of pore size distribution and surface functionalities in the behaviour of carbon supercapacitors, Electrochimica Acta 86 (2012) 241–247. https://doi.org/10.1016/j.electacta.2012.08.006.

[49] I. Yang, M. Jung, M.-S. Kim, D. Choi, J.C. Jung, Physical and chemical activation mechanisms of carbon materials based on the microdomain model, J. Mater. Chem. A 9 (2021) 9815–9825. https://doi.org/10.1039/D1TA00765C.

[50] C. Portet, Z. Yang, Y. Korenblit, Y. Gogotsi, R. Mokaya, G. Yushin, Electrical Double-Layer Capacitance of Zeolite-Templated Carbon in Organic Electrolyte, J. Electrochem. Soc. 156 (2009) A1. https://doi.org/10.1149/1.3002375.

[51] B. Yu, Z. Chang, C. Wang, The key pre-pyrolysis in lignin-based activated carbon preparation for high performance supercapacitors, Materials Chemistry and Physics 181 (2016) 187–193. https://doi.org/10.1016/j.matchemphys.2016.06.048.

[52] D. Momodu, M. Madito, F. Barzegar, A. Bello, A. Khaleed, O. Olaniyan, J. Dangbegnon, N. Manyala, Activated carbon derived from tree bark biomass with promising material properties for supercapacitors, J Solid State Electrochem 21 (2017) 859–872. https://doi.org/10.1007/s10008-016-3432-z.

[53] J. Wang, B. Ding, Y. Xu, L. Shen, H. Dou, X. Zhang, Crumpled Nitrogen-Doped Graphene for Supercapacitors with High Gravimetric and Volumetric Performances, ACS Appl. Mater. Interfaces 7 (2015) 22284–22291. https://doi.org/10.1021/acsami.5b05428.

[54] W. Lv, D.-M. Tang, Y.-B. He, C.-H. You, Z.-Q. Shi, X.-C. Chen, C.-M. Chen, P.-X. Hou, C. Liu, Q.-H. Yang, Low-Temperature Exfoliated Graphenes: Vacuum-Promoted Exfoliation and Electrochemical Energy Storage, ACS Nano 3 (2009) 3730–3736. https://doi.org/10.1021/nn900933u.

[55] M. Kaempgen, C.K. Chan, J. Ma, Y. Cui, G. Gruner, Printable Thin Film Supercapacitors Using Single-Walled Carbon Nanotubes, Nano Lett. 9 (2009) 1872–1876. https://doi.org/10.1021/nl8038579.

[56] J. Matos, M. Labady, A. Albornoz, J. Laine, J.L. Brito, Topological organization and textural changes of carbon macro-networks submitted to activation with N_2 and CO_2, Journal of Materials Science 39 (2004) 3705–3716. https://doi.org/10.1023/B:JMSC.0000030724.32255.b0.

[57] M.V. Navarro, N.A. Seaton, A.M. Mastral, R. Murillo, Analysis of the evolution of the pore size distribution and the pore network connectivity of a porous carbon during activation, Carbon 44 (2006) 2281–2288. https://doi.org/10.1016/j.carbon.2006.02.029.

[58] M. Sevilla, N. Díez, A.B. Fuertes, More Sustainable Chemical Activation Strategies for the Production of Porous Carbons, ChemSusChem 14 (2021) 94–117. https://doi.org/10.1002/cssc.202001838.

[59] J. Matos, M. Labady, A. Albornoz, J. Laine, J.L. Brito, Catalytic effect of KOH on textural changes of carbon macro-networks by physical activation, Journal of Molecular Catalysis A: Chemical 228 (2005) 189–194. https://doi.org/10.1016/j.molcata.2004.09.039.

[60] J. Wang, S. Kaskel, KOH activation of carbon-based materials for energy storage, J. Mater. Chem. 22 (2012) 23710. https://doi.org/10.1039/c2jm34066f.

[61] J. Matos, V. Fierro, R. Montaña, E. Rivero, A.M. de Yuso, W. Zhao, A. Celzard, High surface area microporous carbons as photoreactors for the catalytic photodegradation of methylene blue under UV–vis irradiation, Applied Catalysis A: General 517 (2016) 1–11. https://doi.org/10.1016/j.apcata.2016.02.031.

[62] C. Wang, T. Liu, Activated carbon materials derived from liquefied bark-phenol formaldehyde resins for high performance supercapacitors, RSC Adv. 6 (2016) 105540–105549. https://doi.org/10.1039/C6RA20373F.

[63] W. Xu, J. Liu, K. Sun, Y. Liu, C. Chen, A. Wang, H. Sun, Effect of activation temperature on properties of H3PO4-activated carbon, BioRes 16 (2021) 4007–4020. https://doi.org/10.15376/biores.16.2.4007-4020.

[64] W.S. Hummers, R.E. Offeman, Preparation of Graphitic Oxide, J. Am. Chem. Soc. 80 (1958) 1339–1339. https://doi.org/10.1021/ja01539a017.

[65] B. Hu, K. Wang, L. Wu, S. Yu, M. Antonietti, M. Titirici, Engineering Carbon Materials from the Hydrothermal Carbonization Process of Biomass, Advanced Materials 22 (2010) 813–828. https://doi.org/10.1002/adma.200902812.

[66] L. Wei, M. Sevilla, A.B. Fuertes, R. Mokaya, G. Yushin, Hydrothermal Carbonization of Abundant Renewable Natural Organic Chemicals for High-Performance Supercapacitor Electrodes, Adv. Energy Mater. 1 (2011) 356–361. https://doi.org/10.1002/aenm.201100019.

[67] A. Sanchez-Sanchez, M.T. Izquierdo, S. Mathieu, J. González-Álvarez, A. Celzard, V. Fierro, Outstanding electrochemical performance of highly N- and O-doped carbons derived from pine tannin, Green Chem. 19 (2017) 2653–2665. https://doi.org/10.1039/C7GC00491E.

[68] F.L. Braghiroli, V. Fierro, M.T. Izquierdo, J. Parmentier, A. Pizzi, A. Celzard, Nitrogen-doped carbon materials produced from hydrothermally treated tannin, Carbon 50 (2012) 5411–5420. https://doi.org/10.1016/j.carbon.2012.07.027.

[69] Y. Taluja, B. SanthiBhushan, S. Yadav, A. Srivastava, Defect and functionalized graphene for supercapacitor electrodes, Superlattices and Microstructures 98 (2016) 306–315. https://doi.org/10.1016/j.spmi.2016.08.044.

[70] E. Paek, A.J. Pak, K.E. Kweon, G.S. Hwang, On the Origin of the Enhanced Supercapacitor Performance of Nitrogen-Doped Graphene, J. Phys. Chem. C 117 (2013) 5610–5616. https://doi.org/10.1021/jp312490q.

[71] D. Hulicova-Jurcakova, M. Kodama, S. Shiraishi, H. Hatori, Z.H. Zhu, G.Q. Lu, Nitrogen-Enriched Nonporous Carbon Electrodes with Extraordinary Supercapacitance, Adv Funct Materials 19 (2009) 1800–1809. https://doi.org/10.1002/adfm.200801100.

[72] G. Pognon, C. Cougnon, D. Mayilukila, D. Bélanger, Catechol-Modified Activated Carbon Prepared by the Diazonium Chemistry for Application as Active Electrode Material in Electrochemical Capacitor, ACS Appl. Mater. Interfaces 4 (2012) 3788–3796. https://doi.org/10.1021/am301284n.

[73] W. Zhang, M. Zhao, R. Liu, X. Wang, H. Lin, Hierarchical porous carbon derived from lignin for high performance supercapacitor, Colloids and Surfaces A: Physicochemical and Engineering Aspects 484 (2015) 518–527. https://doi.org/10.1016/j.colsurfa.2015.08.030.

[74] D.E. García, W.G. Glasser, A. Pizzi, S.P. Paczkowski, M.-P. Laborie, Modification of condensed tannins: from polyphenol chemistry to materials engineering, New J. Chem. 40 (2016) 36–49. https://doi.org/10.1039/C5NJ02131F.

[75] M. Liu, X. Yang, X. Wu, X. Wang, Y. Li, F. Ma, J. Zhou, Understanding the pore-structure dependence of supercapacitive performance for microporous carbon in aqueous KOH and H2SO4 electrolytes, Electrochimica Acta 401 (2022) 139422. https://doi.org/10.1016/j.electacta.2021.139422.

[76] E. Raymundo-Piñero, K. Kierzek, J. Machnikowski, F. Béguin, Relationship between the nanoporous texture of activated carbons and their capacitance properties in different electrolytes, Carbon 44 (2006) 2498–2507. https://doi.org/10.1016/j.carbon.2006.05.022.

[77] C. Largeot, C. Portet, J. Chmiola, P.-L. Taberna, Y. Gogotsi, P. Simon, Relation between the Ion Size and Pore Size for an Electric Double-Layer Capacitor, J. Am. Chem. Soc. 130 (2008) 2730–2731. https://doi.org/10.1021/ja7106178.

[78] G. Lota, T.A. Centeno, E. Frackowiak, F. Stoeckli, Improvement of the structural and chemical properties of a commercial activated carbon for its application in electrochemical capacitors, Electrochimica Acta 53 (2008) 2210–2216. https://doi.org/10.1016/j.electacta.2007.09.028.

[79] Y. Duan, C.D. Stinespring, B. Chorpening, Electronic Structures, Bonding Configurations, and Band-Gap-Opening Properties of Graphene Binding with Low-Concentration Fluorine, ChemistryOpen 4 (2015) 642–650. https://doi.org/10.1002/open.201500074.

[80] Z.R. Ismagilov, A.E. Shalagina, O.Yu. Podyacheva, A.V. Ischenko, L.S. Kibis, A.I. Boronin, Y.A. Chesalov, D.I. Kochubey, A.I. Romanenko, O.B. Anikeeva, T.I. Buryakov, E.N. Tkachev, Structure and electrical conductivity of nitrogen-doped carbon nanofibers, Carbon 47 (2009) 1922–1929. https://doi.org/10.1016/j.carbon.2009.02.034.

[81] V. Augustyn, P. Simon, B. Dunn, Pseudocapacitive oxide materials for high-rate electrochemical energy storage, Energy Environ. Sci. 7 (2014) 1597. https://doi.org/10.1039/c3ee44164d.

[82] M. Seredych, D. Hulicova-Jurcakova, G.Q. Lu, T.J. Bandosz, Surface functional groups of carbons and the effects of their chemical character, density and accessibility to ions on electrochemical performance, Carbon 46 (2008) 1475–1488. https://doi.org/10.1016/j.carbon.2008.06.027.

[83] C. Song, J. Wang, Z. Meng, F. Hu, X. Jian, Density Functional Theory Calculations of the Quantum Capacitance of Graphene Oxide as a Supercapacitor Electrode, ChemPhysChem 19 (2018) 1579–1583. https://doi.org/10.1002/cphc.201800070.

[84] P. Hirunsit, M. Liangruksa, P. Khanchaitit, Electronic structures and quantum capacitance of monolayer and multilayer graphenes influenced by Al, B, N and P doping, and monovacancy: Theoretical study, Carbon 108 (2016) 7–20. https://doi.org/10.1016/j.carbon.2016.07.005.

[85] L.R. Radovic, B. Bockrath, On the Chemical Nature of Graphene Edges: Origin of Stability and Potential for Magnetism in Carbon Materials, J. Am. Chem. Soc. 127 (2005) 5917–5927. https://doi.org/10.1021/ja050124h.

[86] D. Chen, H. Feng, J. Li, Graphene Oxide: Preparation, Functionalization, and Electrochemical Applications, Chem. Rev. 112 (2012) 6027–6053. https://doi.org/10.1021/cr300115g.

[87] C.-T. Hsieh, H. Teng, Influence of oxygen treatment on electric double-layer capacitance of activated carbon fabrics, Carbon 40 (2002) 667–674. https://doi.org/10.1016/S0008-6223(01)00182-8.

[88] H. Oda, A. Yamashita, S. Minoura, M. Okamoto, T. Morimoto, Modification of the oxygen-containing functional group on activated carbon fiber in electrodes of an electric double-layer capacitor, Journal of Power Sources 158 (2006) 1510–1516. https://doi.org/10.1016/j.jpowsour.2005.10.061.

[89] C.-M. Chen, Q. Zhang, M.-G. Yang, C.-H. Huang, Y.-G. Yang, M.-Z. Wang, Structural evolution during annealing of thermally reduced graphene nanosheets for application in supercapacitors, Carbon 50 (2012) 3572–3584. https://doi.org/10.1016/j.carbon.2012.03.029.

[90] S.P. Ega, P. Srinivasan, Quinone materials for supercapacitor: Current status, approaches, and future directions, Journal of Energy Storage 47 (2022) 103700. https://doi.org/10.1016/j.est.2021.103700.

[91] J.R. Pels, F. Kapteijn, J.A. Moulijn, Q. Zhu, K.M. Thomas, Evolution of nitrogen functionalities in carbonaceous materials during pyrolysis, Carbon 33 (1995) 1641–1653. https://doi.org/10.1016/0008-6223(95)00154-6.

[92] G. Yuan, X. Zhao, Y. Liang, L. Peng, H. Dong, Y. Xiao, C. Hu, H. Hu, Y. Liu, M. Zheng, Small nitrogen-doped carbon dots as efficient nanoenhancer for boosting the electrochemical performance of three-dimensional graphene, Journal of Colloid and Interface Science 536 (2019) 628–637. https://doi.org/10.1016/j.jcis.2018.10.096.

[93] C. Ma, X. Chen, D. Long, J. Wang, W. Qiao, L. Ling, High-surface-area and high-nitrogen-content carbon microspheres prepared by a pre-oxidation and mild KOH activation for superior supercapacitor, Carbon 118 (2017) 699–708. https://doi.org/10.1016/j.carbon.2017.03.075.

[94] C. Zhan, Y. Zhang, P.T. Cummings, D. Jiang, Enhancing graphene capacitance by nitrogen: effects of doping configuration and concentration, Phys. Chem. Chem. Phys. 18 (2016) 4668–4674. https://doi.org/10.1039/C5CP06952A.

[95] D.-W. Wang, F. Li, Z.-G. Chen, G.Q. Lu, H.-M. Cheng, Synthesis and Electrochemical Property of Boron-Doped Mesoporous Carbon in Supercapacitor, Chem. Mater. 20 (2008) 7195–7200. https://doi.org/10.1021/cm801729y.

[96] R. Nankya, J. Lee, D.O. Opar, H. Jung, Electrochemical behavior of boron-doped mesoporous graphene depending on its boron configuration, Applied Surface Science 489 (2019) 552–559. https://doi.org/10.1016/j.apsusc.2019.06.015.

[97] N. Shcherban, S. Filonenko, P. Yaremov, V. Dyadyun, I. Bezverkhyy, V. Ilyin, Boron-doped nanoporous carbons as promising materials for supercapacitors and hydrogen storage, J Mater Sci 52 (2017) 1523–1533. https://doi.org/10.1007/s10853-016-0447-x.

[98] S.S. Balaji, M. Karnan, P. Anandhaganesh, S.M. Tauquir, M. Sathish, Performance evaluation of B-doped graphene prepared via two different methods in symmetric supercapacitor using various electrolytes, Applied Surface Science 491 (2019) 560–569. https://doi.org/10.1016/j.apsusc.2019.06.151.

[99] R. Bhushan, P. Kumar, A.K. Thakur, Catalyst-free solvothermal synthesis of ultrapure elemental N- and B-doped graphene for energy storage application, Solid State Ionics 353 (2020) 115371. https://doi.org/10.1016/j.ssi.2020.115371.

[100] K. Khanbabaee, T. van Ree, Tannins: Classifiaction and Definition, Nat. Prod. Rep. 18 (2001) 641–649. https://doi.org/10.1039/b101061l.

[101] H.P.S. Makkar, K. Becker, Isolation of Tannins from Leaves of Some Trees and Shrubs and Their Properties, J. Agric. Food Chem. 42 (1994) 731–734. https://doi.org/10.1021/jf00039a026.

[102] N. Meikleham, A. Pizzi, A. Stephanou, Induced accelerated autocondensation of polyflavonoid tannins for phenolic polycondensates. I. 13C-NMR, 29Si-NMR, X-ray, and polarimetry studies and mechanism, J. Appl. Polym. Sci. 54 (1994) 1827–1845. https://doi.org/10.1002/app.1994.070541206.

[103] C. Lacoste, M.C. Basso, A. Pizzi, M.-P. Laborie, D. Garcia, A. Celzard, Bioresourced pine tannin/furanic foams with glyoxal and glutaraldehyde, Industrial Crops and Products 45 (2013) 401–405. https://doi.org/10.1016/j.indcrop.2012.12.032.

[104] P. Jana, V. Fierro, A. Pizzi, A. Celzard, Biomass-derived, thermally conducting, carbon foams for seasonal thermal storage, Biomass and Bioenergy 67 (2014) 312–318. https://doi.org/10.1016/j.biombioe.2014.04.031.

[105] F.L. Braghiroli, V. Fierro, J. Parmentier, A. Pasc, A. Celzard, Easy and eco-friendly synthesis of ordered mesoporous carbons by self-assembly of tannin with a block copolymer, Green Chem. 18 (2016) 3265–3271. https://doi.org/10.1039/C5GC02788H.

[106] Braghiroli, Amaral-Labat, Boss, Lacoste, Pizzi, Tannin Gels and Their Carbon Derivatives: A Review, Biomolecules 9 (2019) 587. https://doi.org/10.3390/biom9100587.

[107] S. Schlienger, A.-L. Graff, A. Celzard, J. Parmentier, Direct synthesis of ordered mesoporous polymer and carbon materials by a biosourced precursor, Green Chem. 14 (2012) 313–316. https://doi.org/10.1039/C2GC16160E.

[108] J. Castro-Gutiérrez, A. Sanchez-Sanchez, J. Ghanbaja, N. Díez, M. Sevilla, A. Celzard, V. Fierro, Synthesis of perfectly ordered mesoporous carbons by water-assisted mechanochemical self-assembly of tannin, Green Chem. 20 (2018) 5123–5132. https://doi.org/10.1039/C8GC02295J.

[109] R. Romero, D. Contreras, M. Sepúlveda, N. Moreno, C. Segura, V. Melin, Assessment of a Fenton reaction driven by insoluble tannins from pine bark in treating an emergent contaminant, Journal of Hazardous Materials 382 (2020) 120982. https://doi.org/10.1016/j.jhazmat.2019.120982.

[110] F. Braghiroli, V. Fierro, A. Szczurek, P. Gadonneix, J. Ghanbaja, J. Parmentier, G. Medjahdi, A. Celzard, Hydrothermal Treatment of Tannin: A Route to Porous Metal Oxides and Metal/Carbon Hybrid Materials, Inorganics 5 (2017) 7. https://doi.org/10.3390/inorganics5010007.

[111] G. Amaral-Labat, A. Szczurek, V. Fierro, N. Stein, C. Boulanger, A. Pizzi, A. Celzard, Pore structure and electrochemical performances of tannin-based carbon cryogels, Biomass and Bioenergy 39 (2012) 274–282. https://doi.org/10.1016/j.biombioe.2012.01.019.

[112] F.L. Braghiroli, V. Fierro, A. Szczurek, N. Stein, J. Parmentier, A. Celzard, Electrochemical performances of hydrothermal tannin-based carbons doped with nitrogen, Industrial Crops and Products 70 (2015) 332–340. https://doi.org/10.1016/j.indcrop.2015.03.046.

[113] C. Liao, Q. Xu, C. Wu, D. Fang, S. Chen, S. Chen, J. Luo, L. Li, Core–shell nano-structured carbon composites based on tannic acid for lithium-ion batteries, J. Mater. Chem. A 4 (2016) 17215–17224. https://doi.org/10.1039/C6TA07359J.

[114] S.K. Ramasahayam, U.B. Nasini, A.U. Shaikh, T. Viswanathan, Novel tannin-based Si, P co-doped carbon for supercapacitor applications, Journal of Power Sources 275 (2015) 835–844. https://doi.org/10.1016/j.jpowsour.2014.11.020.

[115] A. Mukhopadhyay, Y. Jiao, R. Katahira, P.N. Ciesielski, M. Himmel, H. Zhu, Heavy Metal-Free Tannin from Bark for Sustainable Energy Storage, Nano Lett. 17 (2017) 7897–7907. https://doi.org/10.1021/acs.nanolett.7b04242.

[116] U.B. Nasini, V.G. Bairi, S.K. Ramasahayam, S.E. Bourdo, T. Viswanathan, A.U. Shaikh, Phosphorous and nitrogen dual heteroatom doped mesoporous carbon synthesized via microwave method for supercapacitor application, Journal of Power Sources 250 (2014) 257–265. https://doi.org/10.1016/j.jpowsour.2013.11.014.

[117] M. Seredych, A. Szczurek, V. Fierro, A. Celzard, T.J. Bandosz, Electrochemical Reduction of Oxygen on Hydrophobic Ultramicroporous PolyHIPE Carbon, ACS Catal. 6 (2016) 5618–5628. https://doi.org/10.1021/acscatal.6b01497.

[118] M.M. Abdi, N.F.W. Mohd Azli, H.N. Lim, P.M. Tahir, G. Karimi, Y.B. Hoong, M. Khorram, Polypyrrole/tannin biobased nanocomposite with enhanced electrochemical and physical properties, RSC Adv. 8 (2018) 2978–2985. https://doi.org/10.1039/C7RA13378B.

[119] J. Castro-Gutiérrez, N. Díez, M. Sevilla, M.T. Izquierdo, A. Celzard, V. Fierro, Model carbon materials derived from tannin to assess the importance of pore connectivity in supercapacitors, Renewable and Sustainable Energy Reviews 151 (2021) 111600. https://doi.org/10.1016/j.rser.2021.111600.

[120] J. Castro-Gutiérrez, R.L.S. Canevesi, M. Emo, M.T. Izquierdo, A. Celzard, V. Fierro, CO2 outperforms KOH as an activator for high-rate supercapacitors in aqueous electrolyte, Renewable and Sustainable Energy Reviews 167 (2022) 112716. https://doi.org/10.1016/j.rser.2022.112716.

[121] S. Pérez-Rodríguez, O. Pinto, M.T. Izquierdo, C. Segura, P.S. Poon, A. Celzard, J. Matos, V. Fierro, Upgrading of pine tannin biochars as electrochemical capacitor electrodes, Journal of Colloid and Interface Science 601 (2021) 863–876. https://doi.org/10.1016/j.jcis.2021.05.162.

[122] O. Gharbi, M.T.T. Tran, B. Tribollet, M. Turmine, V. Vivier, Revisiting cyclic voltammetry and electrochemical impedance spectroscopy analysis for capacitance measurements, Electrochimica Acta 343 (2020) 136109. https://doi.org/10.1016/j.electacta.2020.136109.

[123] N. Elgrishi, K.J. Rountree, B.D. McCarthy, E.S. Rountree, T.T. Eisenhart, J.L. Dempsey, A Practical Beginner's Guide to Cyclic Voltammetry, J. Chem. Educ. 95 (2018) 197–206. https://doi.org/10.1021/acs.jchemed.7b00361.

[124] D. Boonpakdee, C.F. Guajardo Yévenes, W. Surareungchai, C. La-o-vorakiat, Exploring non-linearities of carbon-based microsupercapacitors from an equivalent circuit perspective, J. Mater. Chem. A 6 (2018) 7162–7167. https://doi.org/10.1039/C8TA01995A.

[125] A.J. Bard, L.R. Faulkner, Electrochemical Methods: Fundamentals and Applications, Wiley, 2000. https://books.google.cl/books?id=kv56QgAACAAJ.

[126] S. Ardizzone, G. Fregonara, S. Trasatti, "Inner" and "outer" active surface of RuO2 electrodes, Electrochimica Acta 35 (1990) 263–267. https://doi.org/10.1016/0013-4686(90)85068-X.

[127] N.O. Laschuk, E.B. Easton, O.V. Zenkina, Reducing the resistance for the use of electrochemical impedance spectroscopy analysis in materials chemistry, RSC Adv. 11 (2021) 27925–27936. https://doi.org/10.1039/D1RA03785D.

[128] M. Itagaki, S. Suzuki, I. Shitanda, K. Watanabe, Electrochemical Impedance and Complex Capacitance to Interpret Electrochemical Capacitor, Electrochemistry 75 (2007) 649–655. https://doi.org/10.5796/electrochemistry.75.649.

[129] C. Arbizzani, Y. Yu, J. Li, J. Xiao, Y. Xia, Y. Yang, C. Santato, R. Raccichini, S. Passerini, Good practice guide for papers on supercapacitors and related hybrid capacitors for the Journal of Power Sources, Journal of Power Sources 450 (2020) 227636. https://doi.org/10.1016/j.jpowsour.2019.227636.

[130] L. Manjakkal, E. Djurdjic, K. Cvejin, J. Kulawik, K. Zaraska, D. Szwagierczak, Electrochemical Impedance Spectroscopic Analysis of RuO2 Based Thick Film pH Sensors, Electrochimica Acta 168 (2015) 246–255. https://doi.org/10.1016/j.electacta.2015.04.048.

[131] A. Moore, S. Park, C. Segura, M. Carrier, Fast pyrolysis of lignin-coated radiata pine, Journal of Analytical and Applied Pyrolysis 115 (2015) 203–213. https://doi.org/10.1016/j.jaap.2015.07.017.

[132] O. Pinto, R. Romero, M. Carrier, J. Appelt, C. Segura, Fast pyrolysis of tannins from pine bark as a renewable source of catechols, Journal of Analytical and Applied Pyrolysis 136 (2018) 69–76. https://doi.org/10.1016/j.jaap.2018.10.022.

[133] M. Thommes, K. Kaneko, A.V. Neimark, J.P. Olivier, F. Rodriguez-Reinoso, J. Rouquerol, K.S.W. Sing, Physisorption of gases, with special reference to the evaluation of surface area and pore size distribution (IUPAC Technical Report), Pure and Applied Chemistry 87 (2015) 1051–1069. https://doi.org/10.1515/pac-2014-1117.

[134] J. Jagiello, J. Kenvin, C.O. Ania, J.B. Parra, A. Celzard, V. Fierro, Exploiting the adsorption of simple gases O2 and H2 with minimal quadrupole moments for the dual gas characterization of nanoporous carbons using 2D-NLDFT models, Carbon 160 (2020) 164–175. https://doi.org/10.1016/j.carbon.2020.01.013.

[135] L.S. Blankenship, J. Jagiello, R. Mokaya, Confirmation of pore formation mechanisms in biochars and activated carbons by dual isotherm analysis, Mater. Adv. 3 (2022) 3961–3971. https://doi.org/10.1039/D2MA00141A.

[136] M. Smith, L. Scudiero, J. Espinal, J.-S. McEwen, M. Garcia-Perez, Improving the deconvolution and interpretation of XPS spectra from chars by ab initio calculations, Carbon 110 (2016) 155–171. https://doi.org/10.1016/j.carbon.2016.09.012.

[137] M. Ayiania, M. Smith, A.J.R. Hensley, L. Scudiero, J.-S. McEwen, M. Garcia-Perez, Deconvoluting the XPS spectra for nitrogen-doped chars: An analysis from first principles, Carbon 162 (2020) 528–544. https://doi.org/10.1016/j.carbon.2020.02.065.

[138] Q. Wang, Z. Xie, Y. Liang, L. Li, B. Liu, X. Li, C. Liu, X. Wu, Q. Huang, Facile synthesis of boron-doped porous carbon as anode for lithium–ion batteries with excellent electrochemical performance, Ionics 25 (2019) 2111–2119. https://doi.org/10.1007/s11581-018-2647-7.

[139] M.D. Stoller, R.S. Ruoff, Best practice methods for determining an electrode material's performance for ultracapacitors, Energy Environ. Sci. 3 (2010) 1294. https://doi.org/10.1039/c0ee00074d.

[140] A. Laheäär, P. Przygocki, Q. Abbas, F. Béguin, Appropriate methods for evaluating the efficiency and capacitive behavior of different types of supercapacitors, Electrochemistry Communications 60 (2015) 21–25. https://doi.org/10.1016/j.elecom.2015.07.022.

[141] M. Sevilla, R. Mokaya, Energy storage applications of activated carbons: supercapacitors and hydrogen storage, Energy Environ. Sci. 7 (2014) 1250–1280. https://doi.org/10.1039/C3EE43525C.

[142] D. Qu, Studies of the activated carbons used in double-layer supercapacitors, Journal of Power Sources 109 (2002) 403–411. https://doi.org/10.1016/S0378-7753(02)00108-8.

[143] Y.-R. Nian, H. Teng, Influence of surface oxides on the impedance behavior of carbon-based electrochemical capacitors, Journal of Electroanalytical Chemistry 540 (2003) 119–127. https://doi.org/10.1016/S0022-0728(02)01299-8.

[144] H. Lu, X.S. Zhao, Biomass-derived carbon electrode materials for supercapacitors, Sustainable Energy Fuels 1 (2017) 1265–1281. https://doi.org/10.1039/C7SE00099E.

[145] J. Singh, H. Bhunia, S. Basu, Adsorption of CO2 on KOH activated carbon adsorbents: Effect of different mass ratios, Journal of Environmental Management 250 (2019) 109457. https://doi.org/10.1016/j.jenvman.2019.109457.

[146] M.I. Nathan, J.E. Smith, K.N. Tu, Raman spectra of glassy carbon, Journal of Applied Physics 45 (1974) 2370–2370. https://doi.org/10.1063/1.1663599.

[147] A.C. Ferrari, J. Robertson, Interpretation of Raman spectra of disordered and amorphous carbon, Phys. Rev. B 61 (2000) 14095–14107. https://doi.org/10.1103/PhysRevB.61.14095.

[148] W. Qian, F. Sun, Y. Xu, L. Qiu, C. Liu, S. Wang, F. Yan, Human hair-derived carbon flakes for electrochemical supercapacitors, Energy Environ. Sci. 7 (2014) 379–386. https://doi.org/10.1039/C3EE43111H.

[149] N. Guo, M. Li, X. Sun, F. Wang, R. Yang, Enzymatic hydrolysis lignin derived hierarchical porous carbon for supercapacitors in ionic liquids with high power and energy densities, Green Chem. 19 (2017) 2595–2602. https://doi.org/10.1039/C7GC00506G.

[150] G. Xu, J. Han, B. Ding, P. Nie, J. Pan, H. Dou, H. Li, X. Zhang, Biomass-derived porous carbon materials with sulfur and nitrogen dual-doping for energy storage, Green Chem. 17 (2015) 1668–1674. https://doi.org/10.1039/C4GC02185A.

[151] J.V. Nabais, P. Carrott, M.M.L. Ribeiro Carrott, V. Luz, A.L. Ortiz, Influence of preparation conditions in the textural and chemical properties of activated carbons from a novel biomass precursor: The coffee endocarp, Bioresource Technology 99 (2008) 7224–7231. https://doi.org/10.1016/j.biortech.2007.12.068.

[152] L. Jiang, J. Yan, L. Hao, R. Xue, G. Sun, B. Yi, High rate performance activated carbons prepared from ginkgo shells for electrochemical supercapacitors, Carbon 56 (2013) 146–154. https://doi.org/10.1016/j.carbon.2012.12.085.

[153] F. Xu, R. Cai, Q. Zeng, C. Zou, D. Wu, F. Li, X. Lu, Y. Liang, R. Fu, Fast ion transport and high capacitance of polystyrene-based hierarchical porous carbon electrode material for supercapacitors, J. Mater. Chem. 21 (2011) 1970–1976. https://doi.org/10.1039/C0JM02044C.

[154] T.A. Centeno, F. Stoeckli, The assessment of surface areas in porous carbons by two model-independent techniques, the DR equation and DFT, Carbon 48 (2010) 2478–2486. https://doi.org/10.1016/j.carbon.2010.03.020.

[155] S. Brunauer, P.H. Emmett, E. Teller, Adsorption of Gases in Multimolecular Layers, J. Am. Chem. Soc. 60 (1938) 309–319. https://doi.org/10.1021/ja01269a023.

[156] J. Jagiello, C. Ania, J.B. Parra, C. Cook, Dual gas analysis of microporous carbons using 2D-NLDFT heterogeneous surface model and combined adsorption data of N2 and CO2, Carbon 91 (2015) 330–337. https://doi.org/10.1016/j.carbon.2015.05.004.

[157] J. Landers, G.Yu. Gor, A.V. Neimark, Density functional theory methods for characterization of porous materials, Colloids and Surfaces A: Physicochemical and Engineering Aspects 437 (2013) 3–32. https://doi.org/10.1016/j.colsurfa.2013.01.007.

[158] M. Sevilla, A.B. Fuertes, Direct Synthesis of Highly Porous Interconnected Carbon Nanosheets and Their Application as High-Performance Supercapacitors, ACS Nano 8 (2014) 5069–5078. https://doi.org/10.1021/nn501124h.

[159] S. Pérez-Rodríguez, G. García, M.J. Lázaro, E. Pastor, DEMS strategy for the determination of the difference in surface acidity of carbon materials, Electrochemistry Communications 90 (2018) 87–90. https://doi.org/10.1016/j.elecom.2018.04.014.

[160] Z. Qiu, Y. Wang, X. Bi, T. Zhou, J. Zhou, J. Zhao, Z. Miao, W. Yi, P. Fu, S. Zhuo, Biochar-based carbons with hierarchical micro-meso-macro porosity for high rate and long cycle life

supercapacitors, Journal of Power Sources 376 (2018) 82–90. https://doi.org/10.1016/j.jpowsour.2017.11.077.

[161] M.-H. Kim, K.-B. Kim, S.-M. Park, K.C. Roh, Hierarchically structured activated carbon for ultracapacitors, Sci Rep 6 (2016) 21182. https://doi.org/10.1038/srep21182.

[162] T.A. Centeno, F. Stoeckli, Surface-related capacitance of microporous carbons in aqueous and organic electrolytes, Electrochimica Acta 56 (2011) 7334–7339. https://doi.org/10.1016/j.electacta.2011.06.040.

[163] A.B. Fuertes, G.A. Ferrero, M. Sevilla, Commentary: Methods of calculating the volumetric performance of a supercapacitor, Energy Storage Materials 4 (2016) 154–155. https://doi.org/10.1016/j.ensm.2016.05.002.

[164] B.-A. Mei, O. Munteshari, J. Lau, B. Dunn, L. Pilon, Physical Interpretations of Nyquist Plots for EDLC Electrodes and Devices, J. Phys. Chem. C 122 (2018) 194–206. https://doi.org/10.1021/acs.jpcc.7b10582.

[165] M.F. El-Kady, V. Strong, S. Dubin, R.B. Kaner, Laser Scribing of High-Performance and Flexible Graphene-Based Electrochemical Capacitors, Science 335 (2012) 1326–1330. https://doi.org/10.1126/science.1216744.

[166] A. Sanchez-Sanchez, M.T. Izquierdo, J. Ghanbaja, G. Medjahdi, S. Mathieu, A. Celzard, V. Fierro, Excellent electrochemical performances of nanocast ordered mesoporous carbons based on tannin-related polyphenols as supercapacitor electrodes, Journal of Power Sources 344 (2017) 15–24. https://doi.org/10.1016/j.jpowsour.2017.01.099.

[167] L. Chang, Y.H. Hu, Breakthroughs in Designing Commercial-Level Mass-Loading Graphene Electrodes for Electrochemical Double-Layer Capacitors, Matter 1 (2019) 596–620. https://doi.org/10.1016/j.matt.2019.06.016.

[168] C. Ruan, K. Ai, L. Lu, Biomass-derived carbon materials for high-performance supercapacitor electrodes, RSC Adv. 4 (2014) 30887. https://doi.org/10.1039/C4RA04470C.

[169] Y.S. Yun, S.Y. Cho, J. Shim, B.H. Kim, S. Chang, S.J. Baek, Y.S. Huh, Y. Tak, Y.W. Park, S. Park, H. Jin, Microporous Carbon Nanoplates from Regenerated Silk Proteins for Supercapacitors, Advanced Materials 25 (2013) 1993–1998. https://doi.org/10.1002/adma.201204692.

[170] C. Falco, J.M. Sieben, N. Brun, M. Sevilla, T. van der Mauelen, E. Morallón, D. Cazorla-Amorós, M. Titirici, Hydrothermal Carbons from Hemicellulose-Derived Aqueous Hydrolysis Products as Electrode Materials for Supercapacitors, ChemSusChem 6 (2013) 374–382. https://doi.org/10.1002/cssc.201200817.

[171] C. Wu, X. Wang, B. Ju, Y. Bai, L. Jiang, H. Wu, Q. Zhao, J. Gao, X. Wang, L. Yi, Supercapacitive behaviors of the nitrogen-enriched activated mesocarbon microbead in aqueous electrolytes, J Solid State Electrochem (2013). https://doi.org/10.1007/s10008-013-2038-y.

[172] X. Zhang, X. Wang, L. Jiang, H. Wu, C. Wu, J. Su, Effect of aqueous electrolytes on the electrochemical behaviors of supercapacitors based on hierarchically porous carbons, Journal of Power Sources (2012).

[173] M. Haque, Self-discharge and leakage current mitigation of neutral aqueous-based supercapacitor by means of liquid crystal additive, Journal of Power Sources (2020). https://doi.org/10.1016/j.jpowsour.2020.227897.

[174] B. Gu, H. Su, X. Chu, Q. Wang, H. Huang, J. He, T. Wu, W. Deng, H. Zhang, W. Yang, Rationally assembled porous carbon superstructures for advanced supercapacitors, Chemical Engineering Journal 361 (2019) 1296–1303. https://doi.org/10.1016/j.cej.2019.01.007.

[175] F.L. Braghiroli, V. Fierro, M.T. Izquierdo, J. Parmentier, A. Pizzi, A. Celzard, Kinetics of the hydrothermal treatment of tannin for producing carbonaceous microspheres, Bioresource Technology 151 (2014) 271–277. https://doi.org/10.1016/j.biortech.2013.10.045.

[176] J. Kaal, K.G.J. Nierop, P. Kraal, C.M. Preston, A first step towards identification of tannin-derived black carbon: Conventional pyrolysis (Py–GC–MS) and thermally assisted hydrolysis and methylation (THM–GC–MS) of charred condensed tannins, Organic Geochemistry 47 (2012) 99–108. https://doi.org/10.1016/j.orggeochem.2012.03.009.

[177] M. Gaugler, W.J. Grigsby, Thermal Degradation of Condensed Tannins from Radiata Pine Bark, Journal of Wood Chemistry and Technology 29 (2009) 305–321. https://doi.org/10.1080/02773810903165671.

[178] F.-X. Collard, J. Blin, A review on pyrolysis of biomass constituents: Mechanisms and composition of the products obtained from the conversion of cellulose, hemicelluloses and lignin, Renewable and Sustainable Energy Reviews 38 (2014) 594–608. https://doi.org/10.1016/j.rser.2014.06.013.

[179] A.V. Bridgwater, Renewable fuels and chemicals by thermal processing of biomass, Chemical Engineering Journal 91 (2003) 87–102. https://doi.org/10.1016/S1385-8947(02)00142-0.

[180] D. Neves, H. Thunman, A. Matos, L. Tarelho, A. Gómez-Barea, Characterization and prediction of biomass pyrolysis products, Progress in Energy and Combustion Science 37 (2011) 611–630. https://doi.org/10.1016/j.pecs.2011.01.001.

[181] K.A. Trick, T.E. Saliba, MECHANISMS OF THE PYROLYSIS OF PHENOLIC RESIN IN A CARBON/PHENOLIC COMPOSITE, (n.d.).

[182] A.K. Thakur, K. Kurtyka, M. Majumder, X. Yang, H.Q. Ta, A. Bachmatiuk, L. Liu, B. Trzebicka, M.H. Rummeli, Recent Advances in Boron- and Nitrogen-Doped Carbon-Based Materials and Their Various Applications, Adv Materials Inter 9 (2022) 2101964. https://doi.org/10.1002/admi.202101964.

[183] M. Letellier, A. Szczurek, M.-C. Basso, A. Pizzi, V. Fierro, O. Ferry, A. Celzard, Preparation and structural characterisation of model cellular vitreous carbon foams, Carbon 112 (2017) 208–218. https://doi.org/10.1016/j.carbon.2016.11.017.

[184] K. Jurkiewicz, Ł. Hawełek, K. Balin, J. Szade, F.L. Braghiroli, V. Fierro, A. Celzard, A. Burian, Conversion of Natural Tannin to Hydrothermal and Graphene-Like Carbons Studied by Wide-Angle X-ray Scattering, J. Phys. Chem. A 119 (2015) 8692–8701. https://doi.org/10.1021/acs.jpca.5b02407.

[185] G. Lota, K. Lota, E. Frackowiak, Nanotubes based composites rich in nitrogen for supercapacitor application, Electrochemistry Communications 9 (2007) 1828–1832. https://doi.org/10.1016/j.elecom.2007.04.015.

[186] O. Mykhailiv, K. Brzezinski, B. Sulikowski, Z. Olejniczak, M. Gras, G. Lota, A. Molina-Ontoria, M. Jakubczyk, L. Echegoyen, M.E. Plonska-Brzezinska, Boron-Doped Polygonal Carbon Nano-Onions: Synthesis and Applications in Electrochemical Energy Storage, Chemistry A European J 23 (2017) 7132–7141. https://doi.org/10.1002/chem.201700914.

[187] Y. Lin, S. Wu, W. Shi, B. Zhang, J. Wang, Y.A. Kim, M. Endo, D.S. Su, Efficient and highly selective boron-doped carbon materials-catalyzed reduction of nitroarenes, Chem. Commun. 51 (2015) 13086–13089. https://doi.org/10.1039/C5CC01963J.

[188] J. Lykiema, K.S.W. Sing, J. Haber, M. Kerker, E. Wolfram, J.H. Block, N.V. Churaev, D.H. Everett, R.S. Hansen, R.A.W. Haul, J.W. Hightower, R.J. Hunter, Prepared for publication by the Subcommittee on Reporting Gas Adsorption Data Consisting of K. S. W. SING (UK, Chairman); D. H. EVERETT (UK); R. A. W. HAUL (FRG); L. MOSCOU (Netherlands); R. A. PIEROTTI (USA); J. ROUQUEROL (France); T. SIEMIENIEWSKA (Poland), (1984).

[189] J. Rouquerol, P. Llewellyn, F. Rouquerol, Is the bet equation applicable to microporous adsorbents?, in: Studies in Surface Science and Catalysis, Elsevier, 2007: pp. 49–56. https://doi.org/10.1016/S0167-2991(07)80008-5.

[190] F.J. Sotomayor, K.A. Cychosz, M. Thommes, Characterization of Micro/Mesoporous Materials by Physisorption: Concepts and Case Studies, (2018) 17.

[191] Y. Gogotsi, P. Simon, True Performance Metrics in Electrochemical Energy Storage, Science 334 (2011) 917–918. https://doi.org/10.1126/science.1213003.

[192] X. Xi, D.D.L. Chung, Dynamics of the electric polarization and depolarization of graphite, Carbon 172 (2021) 83–95. https://doi.org/10.1016/j.carbon.2020.09.081.

[193] A. Allagui, T.J. Freeborn, A.S. Elwakil, B.J. Maundy, Reevaluation of Performance of Electric Double-layer Capacitors from Constant-current Charge/Discharge and Cyclic Voltammetry, Sci Rep 6 (2016) 38568. https://doi.org/10.1038/srep38568.

[194] Y. Yamada, H. Tanaka, S. Kubo, S. Sato, Unveiling bonding states and roles of edges in nitrogen-doped graphene nanoribbon by X-ray photoelectron spectroscopy, Carbon 185 (2021) 342–367. https://doi.org/10.1016/j.carbon.2021.08.085.

[195] J. Quílez-Bermejo, M. Melle-Franco, E. San-Fabián, E. Morallón, D. Cazorla-Amorós, Towards understanding the active sites for the ORR in N-doped carbon materials through fine-tuning of nitrogen functionalities: an experimental and computational approach, J. Mater. Chem. A 7 (2019) 24239–24250. https://doi.org/10.1039/C9TA07932G.

[196] C.S. Ku, S.P. Mun, Characterization of proanthocyanidin in hot water extract isolated from Pinus radiata bark, Wood Sci Technol 41 (2007) 235. https://doi.org/10.1007/s00226-006-0103-8.

[197] J.E. Zuliani, J.N. Caguiat, D.W. Kirk, C.Q. Jia, Considerations for consistent characterization of electrochemical double-layer capacitor performance, Journal of Power Sources 290 (2015) 136–143. https://doi.org/10.1016/j.jpowsour.2015.04.019.

[198] K. Lota, I. Acznik, A. Sierczynska, G. Lota, The capacitance properties of activated carbon obtained from chitosan as the electrode material for electrochemical capacitors, Materials Letters 173 (2016) 72–75. https://doi.org/10.1016/j.matlet.2016.03.031.

[199] M.K. Sahoo, G.R. Rao, A high energy flexible symmetric supercapacitor fabricated using N-doped activated carbon derived from palm flowers, Nanoscale Adv. 3 (2021) 5417–5429. https://doi.org/10.1039/D1NA00261A.

8 APPENDICES

8.1 Appendix A: Particle size distribution of carbon materials.

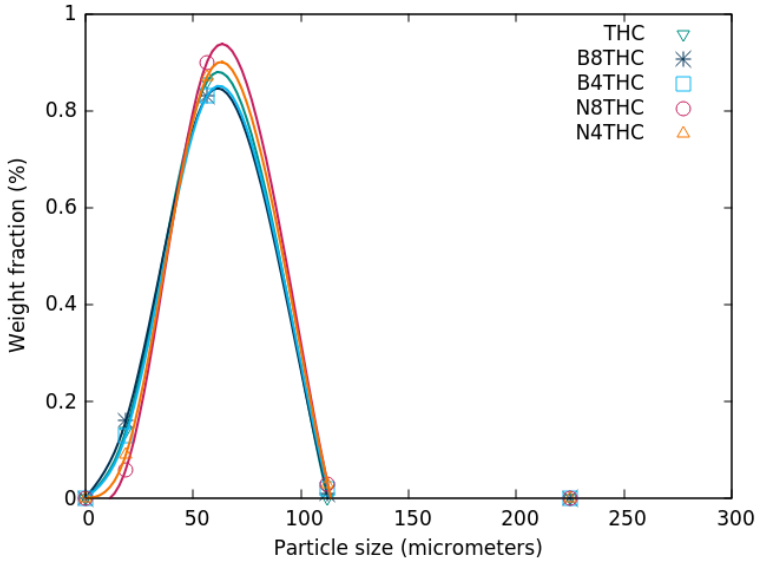

Figure 8-1 Particle size distribution of hydrothermal tannins-derived samples doped with boron or nitrogen previous to thermal and activation treatment.

8.2 Appendix B: XPS deconvolutions for tannins-derived chemically activated carbon materials.

8.2.1 XPS deconvolution for tannins-derived chemically activated carbon materials.

Table 8-1 Relative atomic composition (at. %) of the deconvoluted C 1s for the chemical activated tannins-derived carbon materials.

Carbon sample	C 1s[a]				
	C_{sp^2} 284.4	C_2 285.5	C_3 287.6	C_4 289.2	$C_{\pi-\pi^*}$ 290.4
TBC	73.3	21.1	4.7	0.9	-
TBC-K0	74.3	19.7	3.7	1.3	-
TBC-K0.3	63.8	25.3	8.6	2.3	-
TBC-K0.6	64.5	24.4	8.8	2.2	-
TBC-K1.1	64.7	24.6	8.9	1.8	-
TBC-K1.9	63.5	26.2	8.7	1.6	-
TBC-K2.8	62.1	25.3	8.5	2.7	1.5
TBC-K3.6	62.4	26.6	7.8	2.0	1.3

a: Csp^2: graphitic carbon with sp2 hybridization, C_2: C-C sp3 carbon and C-O single bonds associated to ethers, phenols and anhydrides; C_3: C=O double bonds as in carbonyls and quinones; C_4: C-O single bonds in carboxyls; $C\pi-\pi^*$: HUMO-LUMO transitions associated to Csp^2 peak. HUMO-LUMO transitions associated to Csp^2 peak.

Table 8-2 Relative atomic composition (at. %) of the deconvoluted O 1s for the chemical activated tannins-derived carbon materials.

Carbon sample	O 1s [b]			
	O_1 530.9	O_2 532.3	O_3 533.1	H_2O 534.9
TBC	39.9	60.1	-	-
TBC-K0	44.2	54.6	1.2	-
TBC-K0.3	48.5	43.4	6.7	1.4
TBC-K0.6	65.7	29.3	5.0	-
TBC-K1.1	65.6	28.8	5.6	-
TBC-K1.9	54.4	38.1	7.5	-
TBC-K2.8	43.6	50.0	6.4	-
TBC-K3.6	24.9	67.7	7.4	-

[b]: O_1: C=O double bonds in quinone-type groups, and carbonyls, O_2: -OH bonds in phenols, C–O–C ether groups and C=O bonds in ester and anhydride groups, O_3: C-O aromatics as in carboxylic acids, H_2O: chemisorbed water.

8.2.2 XPS deconvolutions for doped tannins-derived carbon materials.

Table 8-3 Relative atomic composition (at. %) of the deconvoluted peaks of C 1s for doped tannins-derived nanoporous carbons.

Carbon sample	C 1s[a]						
	C_D	C_{sp^2}	C_2	C_3	C_4	C_5	$C_{\pi-\pi^*}$
	283.5	284.4	285.5	286.4	287.6	289.2	291
THC800	N.D.	64.2	25.5	N.D.	0.8	6.3	3.2
THC800 1	N.D.	66.3	25.1	N.D.	0.7	5.7	2.3
THC800 2	N.D.	67.4	24.1	N.D.	0.9	5.4	2.3
THC800 4	N.D.	67.1	23.80	N.D.	0.8	5.4	2.9

[a] CD: carbon associated to defects like in five-member rings and/or to graphitic carbon nitrides, Csp^2: graphitic carbon, C2: carbon with sp3 hybridization, C3 : ether or hydroxyl bonded C, C bonded to nitrogen oxides, C4: carbon in lactones, pyridones, C5: carboxylic acids, $C\pi-\pi^*$: HUMO-LUMO transitions associated to Csp^2 peak.

Table 8-4 Relative atomic composition (at. %) of the deconvoluted peaks of O 1s for tannins-derived carbons and N-doped tannins-derived nanoporous carbons.

Carbon sample	O 1s[a]			
	O_1	**O_2**	**O_3**	**H_2O**
	530.9	532.3	533.1	534.9
THC800	26.6	N.D.	66	7.4
THC800 1	37.9	N.D.	49.6	12.5
THC800 2	30.3	N.D.	58.7	11.0
THC800 4	37.0	N.D.	56.2	6.8

[a] O_1: C=O double bonds as quinone-type groups, O_2: C-O aliphatic as bonds in phenols, ether groups, O_3: C-O aromatics as in carboxylic acids, H_2O: chemisorbed water.

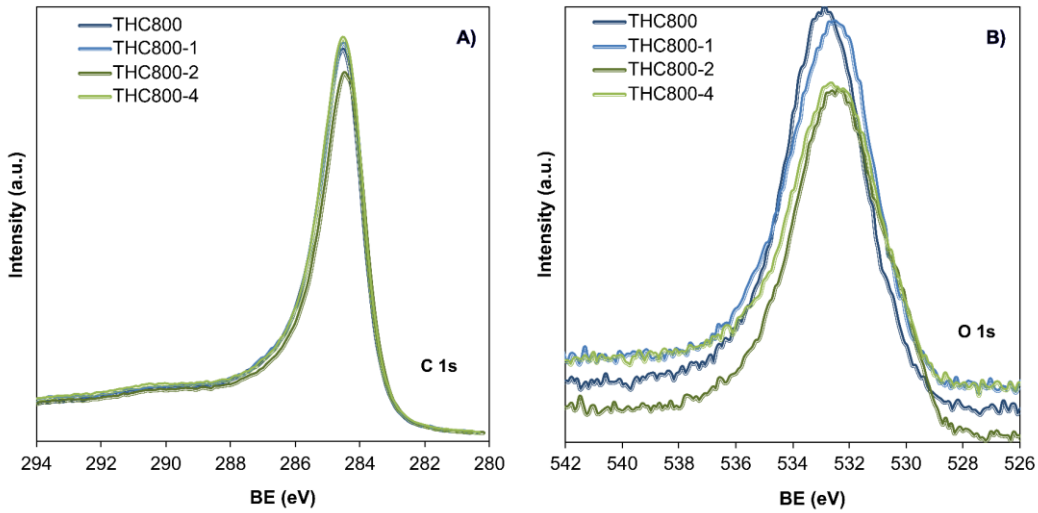

Figure 8-2 XPS spectra for THC800 series: A) C 1s spectra, and B) O 1s spectra.

Table 8-5 Relative atomic composition (at. %) of the deconvoluted peaks of C 1s for doped tannins-derived nanoporous carbons.

Carbon sample	C 1s[a]						
	C_D	C_{sp^2}	C_2	C_3	C_4	C_5	$C_{\pi-\pi^*}$
	283.5	284.4	285.5	286.4	287.6	289.2	291
THC800	N.D.	64.2	25.5	N.D.	N.D.	0.8	3.2
N4THC800	5	55.1	19.7	11.5	3.6	3.1	1.9
N8THC800	2.4	54.5	17.7	13.1	5	3.9	3.3
B4THC800	N.D.	66.1	23.9	N.D.	5.7	0.9	3.4
B8THC800	N.D.	64.5	25.1	N.D.	7.4	1.1	1.9
THC800 4	N.D.	67.1	23.8	N.D.	N.D.	0.8	3.2
N4THC800 4	5.5	56.5	15.5	13.7	3.4	2.9	2.5
N8THC800 4	4.3	62.9	15.5	10.8	2.8	2.7	1.1
B4THC800 4	N.D.	64.3	26.8	N.D.	5.4	1.0	2.5
B8THC800 4	N.D.	66.9	25.5	N.D.	4.7	1.3	1.5

[a] CD: carbon associated to defects like in five-member rings and/or to graphitic carbon nitrides, Csp^2: graphitic carbon, C2: carbon with sp3 hybridization, C3: ether or hydroxyl bonded C, C bonded to nitrogen oxides, C4: carbon in lactones, pyridones, C5: carboxylic acids, $C\pi-\pi^*$: HUMO-LUMO transitions associated to Csp^2 peak.

Table 8-6 Relative atomic composition (at. %) of the deconvoluted peaks of O 1s and N 1s for tannins-derived carbons and N-doped tannins-derived nanoporous carbons.

Carbon sample	O 1s[a]					N 1s[b]			
	O_1	**O_2**	**O_3**	**N=O**	**H_2O**	**N_6**	**N_5**	**N_Q**	**N=O**
	530.9	532.3	533.1	534.1	534.9	398.3	400.2	401.2	402.9
THC800	26.6	N.D.	66	N.D.	7.4	N.D.	N.D.	N.D.	N.D.
N4THC800	61.4	16.8	14.9	3.7	3.2	35.2	19.5	34.3	11.0
N8THC800	57.9	18.8	13.9	5.3	4.1	32.9	30.3	27.6	9.2
N4THC800 4	61.4	16.8	14.9	3.7	3.2	35.2	19.5	34.3	11.0
N8THC800 4	66.4	16.4	11.4	3.0	2.9	32.6	24.0	30.1	13.2

[a] O_1: C=O double bonds as quinone-type groups, O_2: C-O aliphatic as bonds in phenols, ether groups, O_3: C-O aromatics as in carboxylic acids, N=O: oxygens bounded to nitrogen, H_2O: chemisorbed water. [b] N_6: pyridinic groups, N_5: pyrrole or pyridones groups, N_Q: graphitic carbon nitrides, N=O: nitrogen bonded to oxygens.

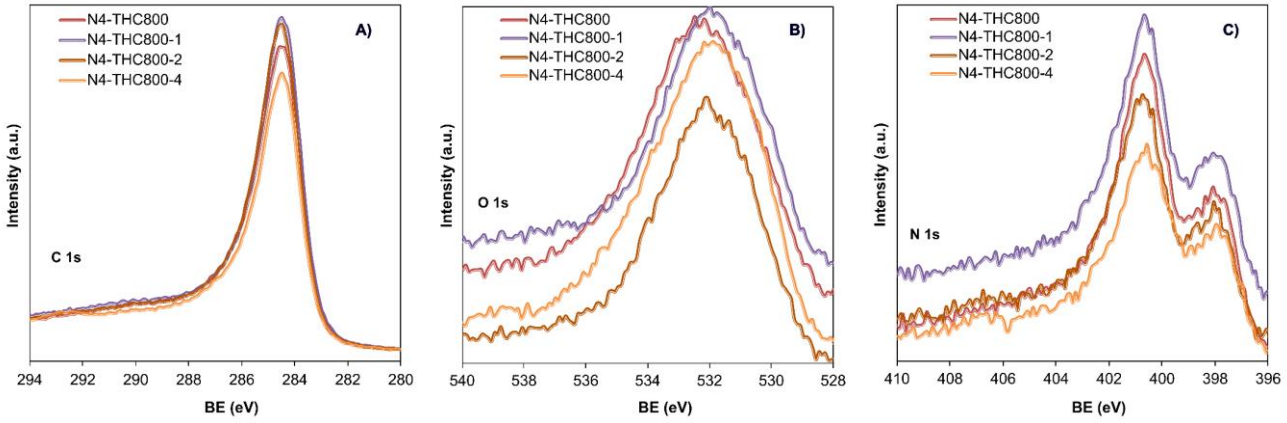

Figure 8-3 XPS deconvolution for N4THC800 series: A) C 1s spectra, B) O 1s spectra, and C) N 1s spectra.

Table 8-7 Relative atomic composition (at. %) of the deconvoluted peaks of O 1s and B 1s for tannins-derived carbons and B-doped tannins-derived nanoporous carbons.

Carbon sample	O 1s[a]					B 1s[b]	
	O_1	**O_2**	**O_3**	**B-O**	**H_2O**	**BC_2O**	**BCO_2**
	530.9	532.3	533.1	531.5	534.9	190.1	192.1
THC800	26.6	N.D.	66	N.D.	7.4	N.D.	N.D.
B4THC800	29.9	62.1	N.D.	4.3	3.7	19.0	81.0
B8THC800	31.2	N.D.	59.9	N.D.	8.8	N.D.	N.D.
B4THC800 4	28.0	61.3	N.D.	10.7	N.D.	40.2	59.8
B8THC800 4	49.7	N.D.	42.1	N.D.	8.1	N.D.	N.D.

[a] O_1: C=O double bonds as quinone-type groups, O_2: C-O aliphatic as bonds in phenols, ether groups, O_3: C-O aromatics as in carboxylic acids, B-O: oxygens bounded to nitrogen, H_2O: chemisorbed water, [b].

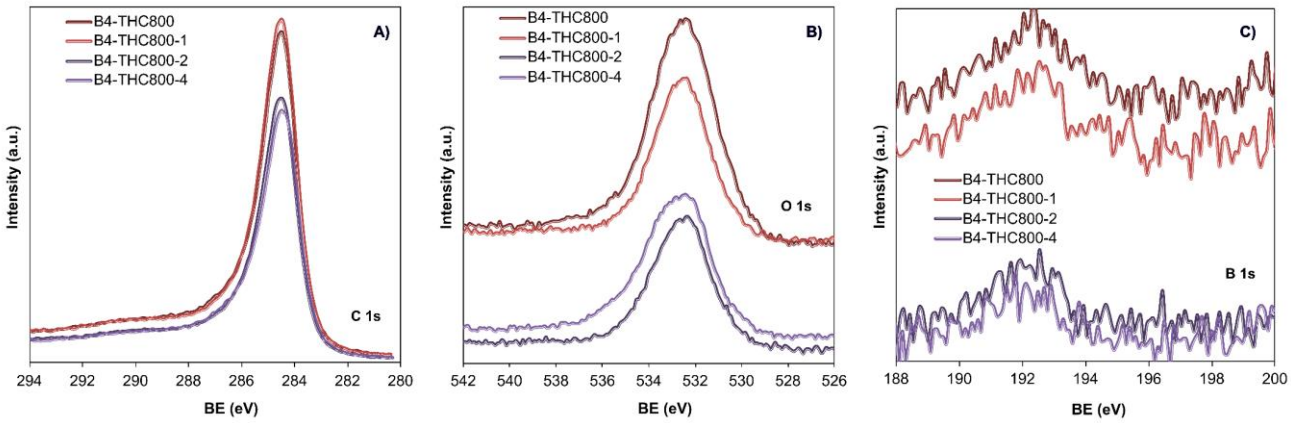

Figure 8-4 XPS spectra for B4THC800 series: A) C 1s spectrum, B) O 1s spectrum, and C) B 1s spectrum.

8.2.3 XPS deconvolutions for N-doped tannins derived carbons materials.

Table 8-8 Relative atomic composition (at. %) of the deconvoluted peaks of C 1s for N-doped tannins-derived nanoporous carbons.

Carbon sample	C 1s[a]						
	C_D	C_{sp^2}	C_2	C_3	C_4	C_5	$C_{\pi-\pi^*}$
	283.5	284.4	285.5	286.4	287.6	289.2	291
N4THC800	5	55.1	19.7	11.5	3.6	3.1	1.9
N4THC800-1	8.2	56.9	15.2	12.1	2.1	3.5	2.1
N4THC800-2	3.9	55	16.6	15.8	2.6	3.9	2.2
N4THC800-4	5.5	56.5	15.5	13.7	3.4	2.9	2.5
N4THC900-1	1.5	60.6	16.5	12	3	3.6	2.8
N4THC900-1.5	0.7	61.1	18.1	9.4	4.1	3.6	3
N4THC900-2	1.2	58.3	15.6	12.2	4.2	4.3	4.3
N8THC800	2.4	54.5	17.7	13.1	5	3.9	3.3
N8THC800-1	2.7	57.3	17.8	10.6	4.7	3.7	3.2
N8THC800-2	2.8	56.6	20	10.3	4.4	3.4	2.5
N8THC800-4	4.3	62.9	15.5	10.8	2.8	2.7	1.1
N8THC900-1	2.4	60.5	16.4	10.6	3.5	3.8	2.9
N8THC900-1.5	2.7	61.2	15.2	11.1	3.3	3.7	2.8
N8THC900-2	2.1	57	17.1	11.2	4.7	4.2	3.7

a CD: carbon associated to defects like in five-member rings and/or to graphitic carbon nitrides, Csp^2: graphitic carbon, C2 : carbon with sp3 hybridization, C3 : ether or hydroxyl bonded C, C bonded to nitrogen oxides, C4: carbon in lactones, pyridones, C5: carbo xylic acids, $C\pi-\pi^*$: HUMO-LUMO transitions associated to Csp^2 peak.

Table 8-9 Relative atomic composition (at. %) of the deconvoluted peaks of O 1s and N 1s for tannins-derived carbons and N-doped tannins-derived nanoporous carbons.

Carbon sample	O 1s[a]					N 1s[b]			
	O_1	**O_2**	**O_3**	**N=O**	**H_2O**	**N_6**	**N_5**	**N_Q**	**N=O**
	530.9	532.3	533.1	534.1	534.9	398.3	400.2	401.2	402.9
N4THC800	59.2	21.2	12.4	3.9	3.3	31.3	24.2	33.6	11.0
N4THC800-1	63.4	16.9	13.5	2.3	3.9	29.5	23.1	31.9	15.4
N4THC800-2	58.6	17.7	16.8	2.8	4.2	32.9	28.2	29.4	9.4
N4THC800-4	61.4	16.8	14.9	3.7	3.2	35.2	19.5	34.3	11.0
N4THC900-1	63.3	17.2	12.5	3.1	3.8	34.0	24.7	30.8	10.5
N4THC900-1.5	63.4	18.8	9.8	4.3	3.7	33.6	29.3	25.7	11.3
N4THC900-2	61.6	16.5	12.9	4.4	4.5	34.6	20.2	32.4	12.7
N8THC800	57.9	18.8	13.9	5.3	4.1	32.9	30.3	27.6	9.2
N8THC800-1	60.9	18.9	11.3	5.0	3.9	30.8	25.2	31.5	12.6
N8THC800-2	59.8	21.1	10.9	4.6	3.6	31.3	27.1	30.6	11.0
N8THC800-4	66.4	16.4	11.4	3.0	2.9	32.6	24.0	30.1	13.2
N8THC900-1	63.8	17.3	11.2	3.7	4.0	28.9	25.0	31.2	14.9
N8THC900-1.5	64.8	16.1	11.7	3.5	3.9	33.5	25.1	31.0	10.3
N8THC900-2	60.5	18.2	11.9	5.0	4.5	37.3	25.6	25.7	11.3

[a] O_1: C=O double bonds as quinone-type groups, O_2: C-O aliphatic as bonds in phenols, ether groups, O_3: C-O aromatics as in carboxylic acids, N=O: oxygens bounded to nitrogen, H_2O: chemisorbed water. [b] N_6: pyridinic groups, N_5: pyrrole or pyridones groups, N_Q: graphitic carbon nitrides, N=O: nitrogen bonded to oxygens.

8.3 Appendix C: Nominal presence of the doping agent in the hydrothermal carbonization of tannins.

The presence of the doping agent is calculated from their molecular weight. In the case of boron, the reagent used is boric acid, which chemical formula is H_3BO_3, considering the molecular weight of each element is:

Mw_H = 1.008 u

Mw_B = 10.811 u

Mw_O = 15.999 u

Thus, the molecular weight of the boric acid is 61.83 u, and the percentage by weight of boron in boric acid is given by:

$$\%B_{H_3BO_3} = \frac{Mw_B}{Mw_{H_3BO_3}} \times 100 = 17.48\% \qquad \textbf{Eq. 8-1}$$

The masses of boric acid used are 0.500 and 0.250 g according to shown in **Table 4-1**, and the mass of boron is calculated by:

$$m_B = m_{H_3BO_3} \times \%B_{H_3BO_3} \qquad \textbf{Eq. 8-2}$$

Thus, the mass of boron used as doping agent are 8.74 g and 4.37 g, respectively. Additionally, using the molecular weight of boron, it is possible to calculate the quantity of boron moles given by:

$$n_B = \frac{m_B}{Mw_B} \qquad \textbf{Eq. 8-3}$$

Therefore, the nominal moles of boron in the aqueous solution used on the hydrothermal carbonization step are $8.08 \cdot 10^{-3}$, and $4.04 \cdot 10^{-3}$, respectively.

In the case of nitrogen, this is doped in the tannin matrix using an ammonia solution ($NH_4^+OH^-$) as reagent. To compare the results obtained from both boron and nitrogen doped materials, the quantity of nominal moles for each one is intended to be as similar as possible. In this case, a back forward calculation is used to calculate the equivalent mass of the ammonia solution. Take into account that the molecular weights of the elements present in the reagent are:

Mw_N = 14.007 u

Mw_H = 1.008 u

Mw_O = 15.999 u

Using the molecular weight of nitrogen, it is possible to calculate the mass of nitrogen given the quantity of moles:

$$m_N = n_B \times Mw_N \qquad \textbf{Eq. 8-4}$$

Given that the nitrogen moles intended to use are $8.08 \cdot 10^{-3}$, and $4.04 \cdot 10^{-3}$, so the mass of nitrogen are 0.113 g and 0.057 g, respectively. Also, the molecular weight of the NH_4^+OH- is 35.046u, and the percentage by weight of nitrogen is given by:

$$\%N_{NH_4^+OH^-} = \frac{Mw_N}{Mw_{NH_4^+OH^-}} \times 100 = 39.97\ \% \qquad \textbf{Eq. 8-5}$$

And the quantity of ammonia solution in mass are 0.283 and 0.146 g, respectively. Considering that the ammonia solution concentration is 26.2 wt. %, according to the supplier, the quantities of ammonia solution required are 1.08 and 0.557 g. Since the ammonia solution is easier and safer to handle by volume than by weight, a lineal regression was made it to determine the volume of aqueous ammonia solution. Based on the above, and due to the accurate of the micropipette, the volumes of ammonia solution used were 1.3 mL and 0.65 mL, respectively. Recalculating the mass according to the volumes used, the mass of reagent added were 1.09 g and 0.54 g, which in mass of NH+4 OH− are 0.285 and 0.142 g, respectively. Also, the quantities of nitrogen moles were $8.12 \cdot 10^{-3}$ and $4.06 \cdot 10^{-3}$, respectively. Beyond that, the summarize results of both boron and nitrogen nominal presence are summarized in the

Table 8-10 Mass and moles of the reagent (r) and doping agent (DA) used in the HTC synthesis of doped tannins-derived carbon materials

Code	Reagent	Presence	Doping agent	m_r (g)	n_r (mmol)	m_{DA} (g)	n_{DA} (mmol)
B8THC	H_3BO_3	Powder (99.5 wt. %)	Boron	0.500	8.08	8.74	8.08
B4THC	H_3BO_3	Powder (99.5 wt. %)	Boron	0.250	4.04	4.37	4.04
N8THC	$NH_4^+OH^-$	Solution (26.2 wt. %)	Nitrogen	0.285	8.12	0.114	8.12
N4THC	$NH_4^+OH^-$	Solution (26.2 wt.%)	Nitrogen	0.142	4.06	0.057	4.06

8.4 Appendix D: Cyclic voltammetry for tannins-derived carbon materials.

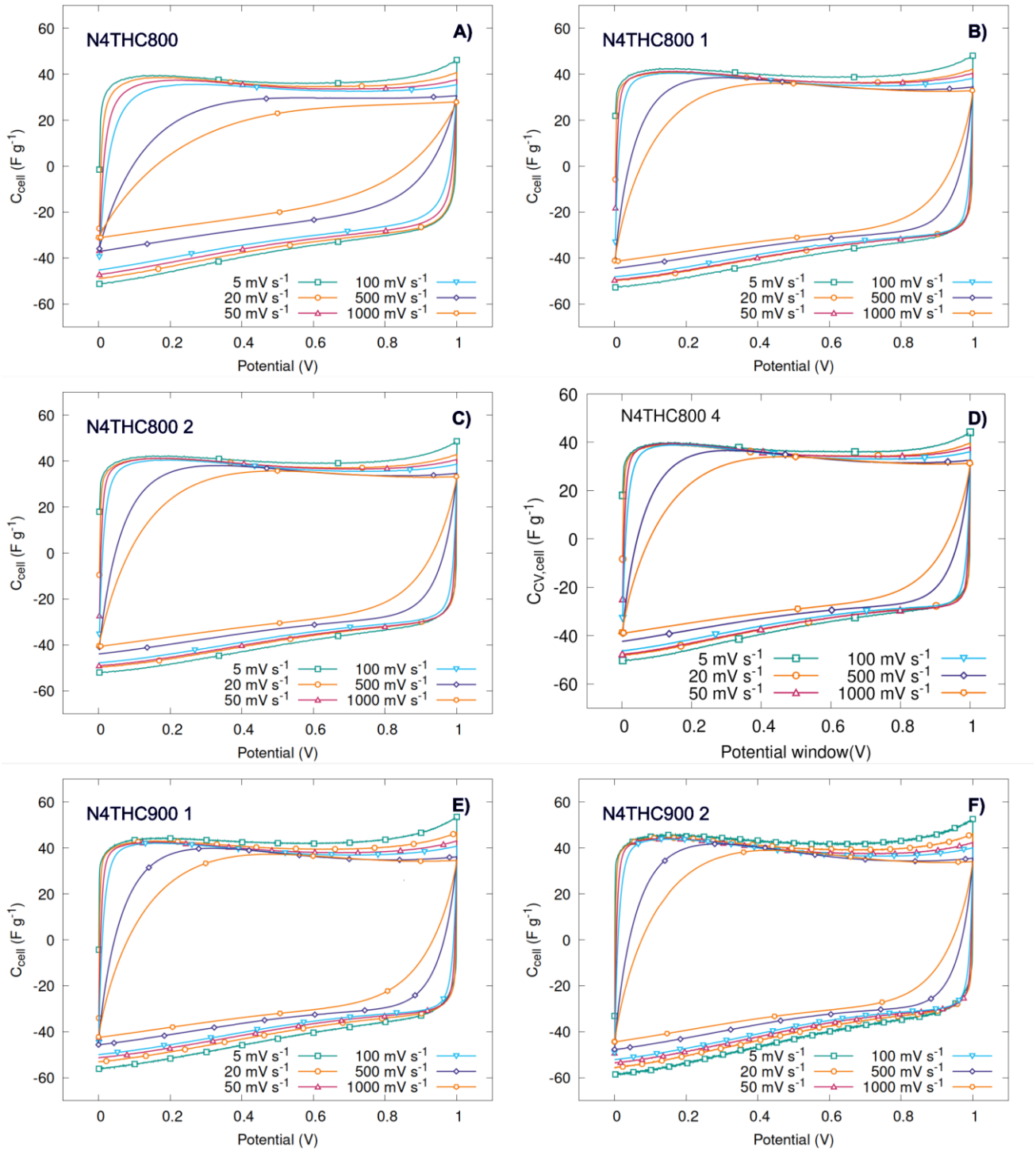

Figure 8-5 Cyclic voltammograms at scan rate ranging from 5 mV s^{-1} to 1 V s^{-1} for N4THC carbon materials series in 1M H_2SO_4 as electrolyte.

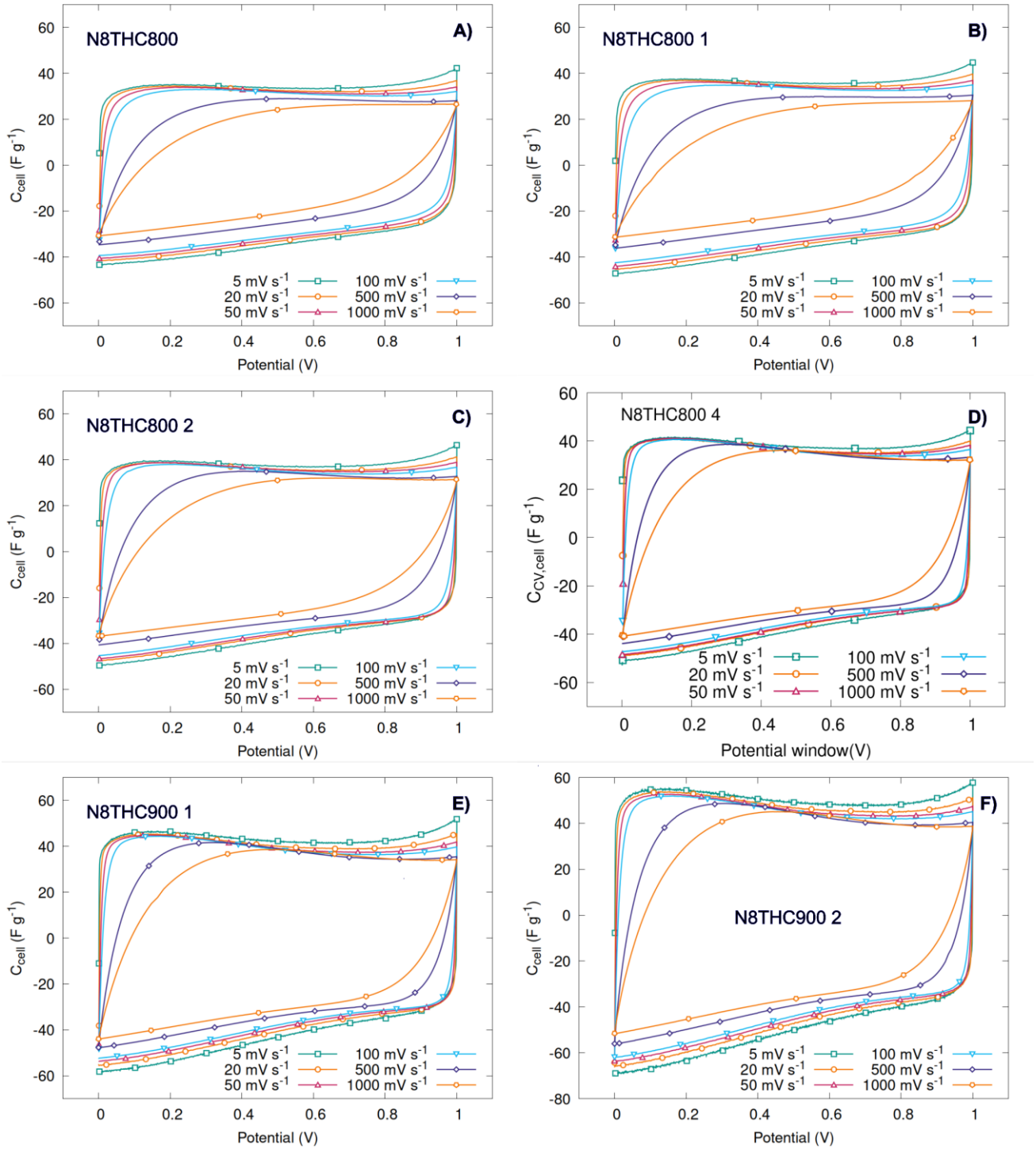

Figure 8-6 Cyclic voltammograms at scan rate ranging from 5 mV s^{-1} to 1 V s^{-1} for N8THC carbon materials series in 1M H_2SO_4 as electrolyte.

8.5 Appendix E: Galvanostatic charge-discharge curves.

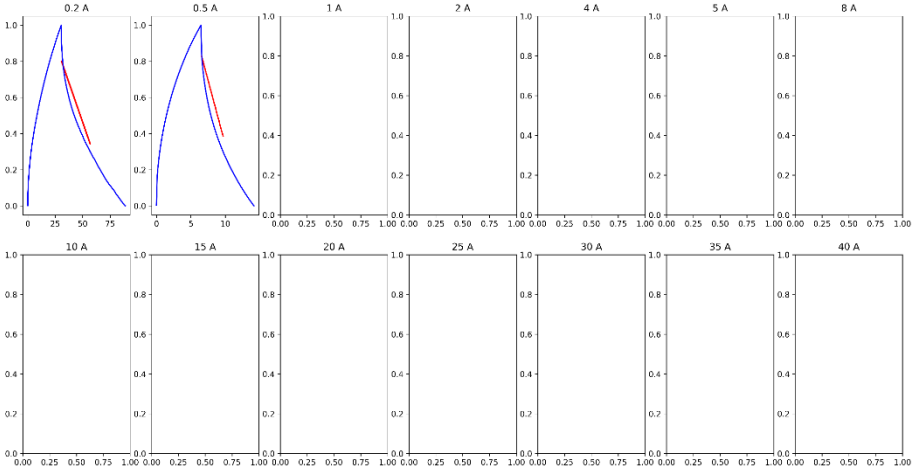

Figure 8-7 Charge-discharge curves for THC800-4 at specific current from 0.2 A g^{-1} to 40 A g^{-1} (blue line) and estimated slope at discharge curve to estimate capacitance (red line).

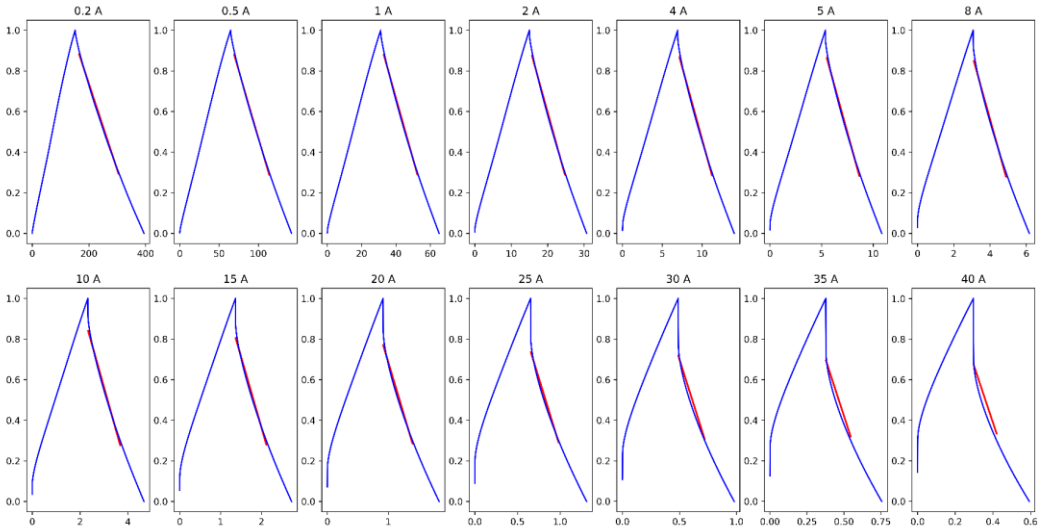

Figure 8-8 Charge-discharge curves for B4THC800-4 at specific current from 0.2 A g^{-1} to 40 A g^{-1} (blue line) and estimated slope at discharge curve to estimate capacitance (red line).

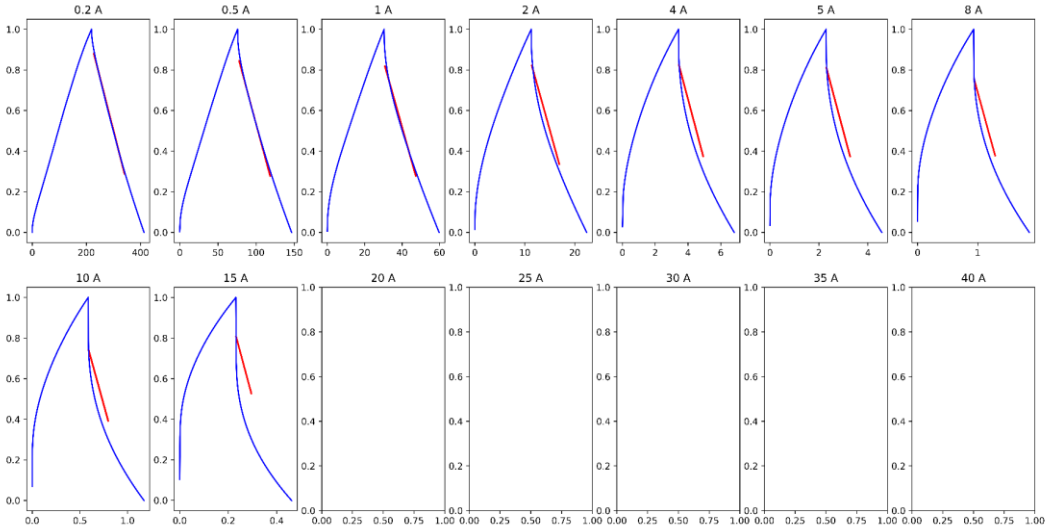

Figure 8-9 Charge-discharge curves for B8THC800-4 at specific current from 0.2 A g^{-1} to 40 A g^{-1} (blue line) and estimated slope at discharge curve to estimate capacitance (red line).

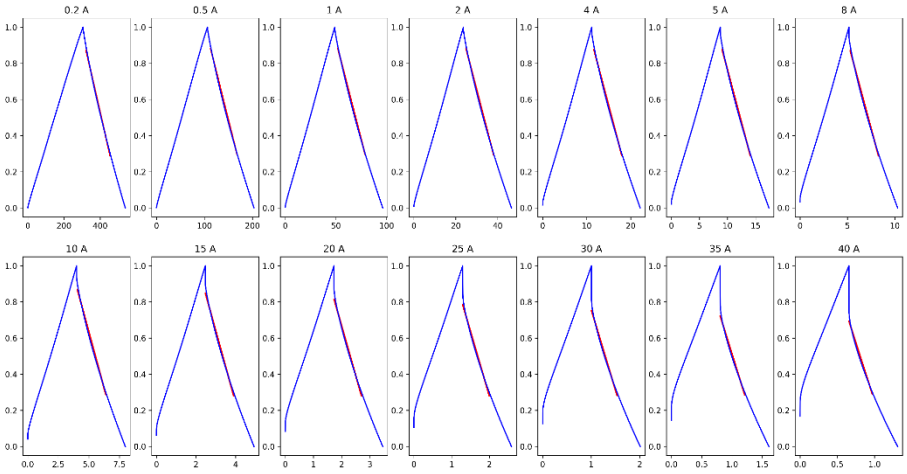

Figure 8-10 Charge-discharge curves for N8THC800 at specific current from 0.2 A g^{-1} to 40 A g^{-1} (blue line) and estimated slope ofdischarge curve to estimate capacitance (red line).

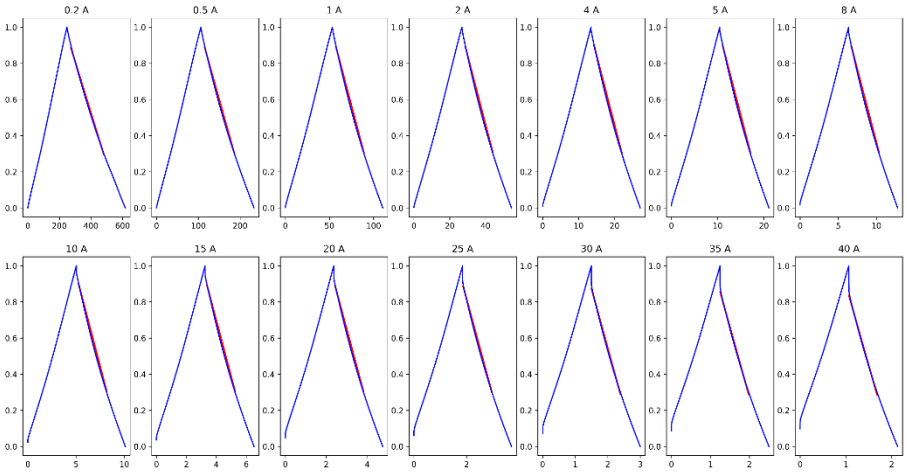

Figure 8-11 Charge-discharge curves for N8THC800-4 at specific current from 0.2 to 40 A g^{-1} (blue line) and estimated slope of discharge curve to estimate capacitance (red line).

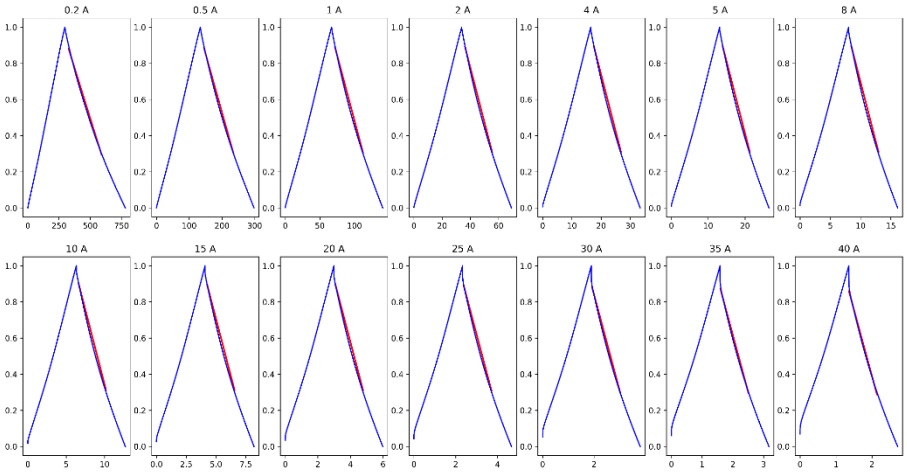

Figure 8-12 Charge-discharge curves for N8THC900-2 at specific current from 0.2 to 40 A g^{-1} (blue line) and estimated slope of discharge curve to estimate capacitance (red line).

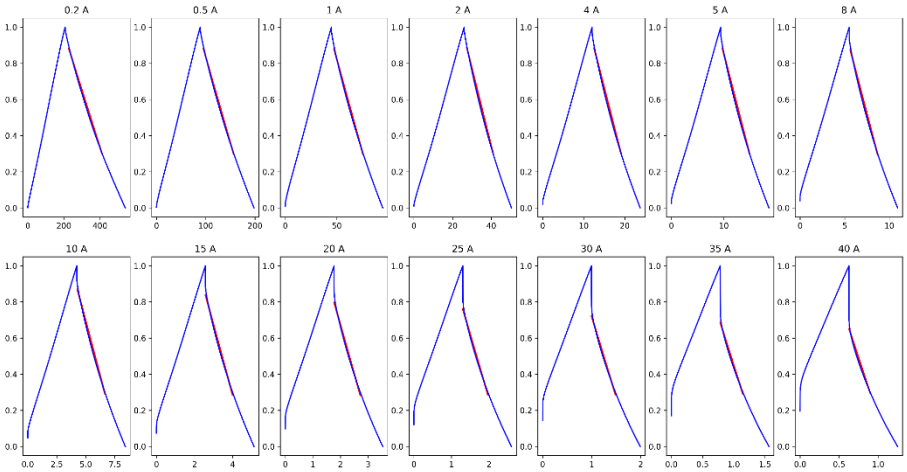

Figure 8-13 Charge-discharge curves for N4THC800 at specific current from 0.2 to 40 A g^{-1} (blue line) and estimated slope of discharge curve to estimate capacitance (red line).

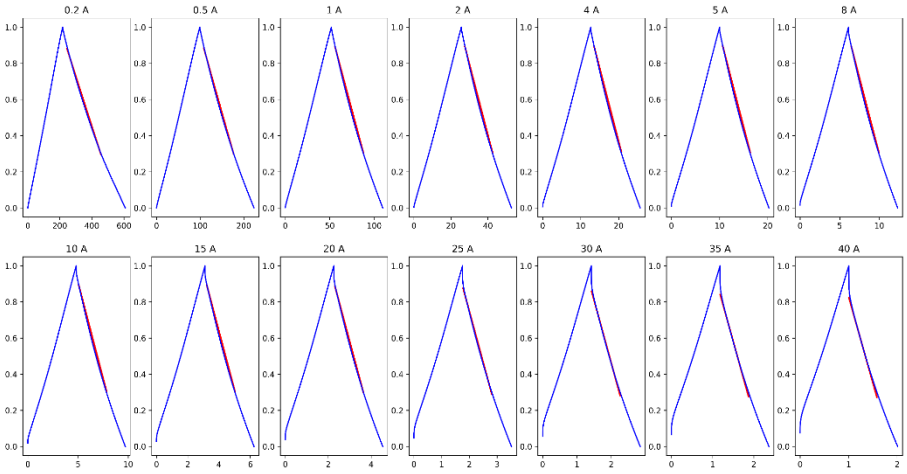

Figure 8-14 Charge-discharge curves for N4THC800-4 at specific current from 0.2 to 40 A g^{-1} (blue line) and estimated slope of discharge curve to estimate capacitance (red line).

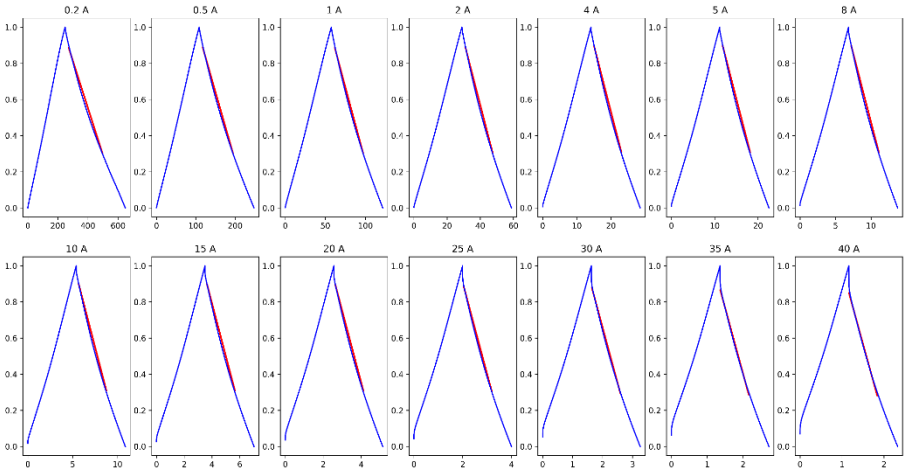

Figure 8-15 Charge-discharge curves for N4THC900-2 at specific current from 0.2 to 40 A g^{-1} (blue line) and estimated slope of discharge curve to estimate capacitance (red line).